Advanced Monitoring and Parameter Estimation Techniques for Doubly Fed Induction Generator Drives

A thesis submitted to

The University of Manchester

for the degree of

Doctor of Philosophy

in the

Faculty of Science and Engineering

2020

Yingzhao Wang

School of Science and Engineering

Table of Contents

List of Figures

List of Tables

Total word count:43167

List of Abbreviations

DFIG	Doubly-Fed Induction Generator
MMF	Magnetic Motive Force
FBG	Fibre Bragg Grating
WT	Wind Turbine
O&M	Operation and Maintenance
COE	Cost Of Energy
CM	Condition Monitoring
SCIG	Squirrel Cage Induction Generator
WRIG	Wound-Rotor Induction Generator
PMSG	Permanent Magnet Synchronous Generator
EESG	Electrically Excited Synchronous Generator
SSB	Spectral Search Based
SFOC	Stator Flux Oriented Control
SSE	Sensorless Speed Estimation
CMFD	Condition Monitoring Fault Diagnosis
VSWT	Variable Speed Wind Turbine
AC	Alternating Current
DC	Direct Current
VSCF	Variable-Speed Constant-Frequency
VSC	Voltage Source Converter
RSC	Rotor Side Converter
GSC	Grid Side Converter
GVOVC	Grid Voltage Oriented Vector Control
PWM	Pulse-Width Modulation
SVOC	Stator Voltage Oriented Control
DTC	Direct Torque Control
DPC	Direct Power Control
P-DTC	Predictive Direct Torque Control
P-DPC	Predictive Direct Power Control
SCADA	Supervisory Control And Data Acquisition
SHM	Structure Health Monitoring
MCSA	Motor Current Signature Analysis
RF	Radio-Frequency
ETD	Embedded Temperature Detectors
EMI	Electromagnetic Interference

FFT	Fast Fourier Transform
STFT	Short-time Fourier Transform
HHT	Hilbert-Huang Transform
EMD	Empirical Mode Decomposition
IMF	Intrinsic Mode Function
FMB	Fundamental Model Based
MRAS	Model Reference Adaptive Systems
ADC	Analogue To Digital
DAC	Digital To Analogue
PLL	Phase Locked Loop
PD	Phase Detector
LF	Loop Filter
VCO	Voltage Controlled Oscillator
WRIM	Wound Rotor Induction Machine
EMF	Electromotive Force
MPPT	Maximum Power Point Tracking
SSU	Stator Supply Unbalance
DFT	Discrete Fourier Transform
RPM	Revolutions Per Minute
VI	Virtual Instrument
DMA	Direct Memory Access
FPGA	Field-Programmable Gate Array
FIFO	First In First Out
FBG-A	Fibre Bragg Grating-Axial
FBG-R	Fibre Bragg Grating-Radial
FBG-C	Fibre Bragg Grating- Circumferential
ACC-R	Accelerometer-Radial
ACC-A	Accelerometer-Axial
FEA	Finite Element Analysis
RTI	Real-Time Interface
SG	Synchronous Generator
AI	Artificial Intelligence

Abstract

This thesis investigated the development of condition monitoring techniques for generator mechanical fault diagnosis and sensorless speed estimation in a doubly fed induction generator (DFIG) utilizing the DFIG closed loop controller signals. The DFIG harmonic model was first implemented in the MATLAB/Simulink platform to investigate shaft misalignment fault signatures for fault diagnosis as well as harmonic content selection for sensorless speed estimation. Conductor distribution function approach was employed to predict the frequency content of the electrical signals including terminal signals and control loop signals of a DFIG. By analysing the characteristics of DFIG signals, the fault-specific spectral signatures and speed related harmonic contents could be effectively recognized thus further employed for DFIG condition monitoring.

To validate the findings in the DFIG harmonic model and evaluate the experimental performance in research, a DFIG test-rig facility using industrial converters along with associated sensors and real-time platform was developed. The frequency contents of the DFIG terminal signals and control loop signals in different operating load and speed conditions acquired from experimental tests were examined and cross-correlated with the DFIG harmonic model.

After identifying the spectral nature of the DFIG control loop signals, their potential to be used as a signature for shaft misalignment recognition and sensorless speed estimation in DFIG system were investigated. Fault identification capability of the control loop signals were examined in a range of different load and speed operating points and indicated better performance compared to typically used machine terminal signal. The spectral based searching algorithm based on control loop signal MMF harmonic identification was validated with real-time DFIG constant and variable speed scenarios, which manifested a considerable potential for actual speed estimation for wind turbine applications. Moreover, a novel DFIG shaft misalignment diagnostic technique utilizing Fibre Bragg Grating (FBG) to monitor machine frame strain was developed. Practical strain sensing tests in different load, speed and severities were undertaken and cross-correlated with vibration sensing. It was shown to have the capability to provide a sufficient means of monitoring misalignment induced effects.

Declaration

No portion of the work referred to in this thesis has been submitted in support of an application for another degree or qualification of this or any other university or other institute of learning.

Copyright

Acknowledgements

First, I would like to express my most sincere gratitude to my supervisor Dr Siniša Djurović for his invaluable advice, guidance and dedication throughout my PhD study, especially the constant and patient encouragements in this difficult pandemic graduation year.

I would like to express my warmest gratitude to my parents for their love and support they have always given to me, and to my wife Yiran Chen for her accompany and inspiration throughout my PhD.

Finally, I would like to thank all the academic stuff, research associates and PhD students of the Power Conversion Group, as well as the staff from mechanical support workshops for their constant and patient assistance. My PhD journey were greatly enjoyed thanks to my colleagues and friends. Their friendship is very special to me: Dr Juan Ignacio Melecio Ramírez, Dr Anees Mohammed, Dr Xiaotao Zhang, Mr Jonathan Hunte, Dr Nur Sarma and Dr Kavul Tshiloz.

Chapter 1 Introduction

1.1 Background

The modern human society is highly dependent on electrical energy generation and transmission; the energy consumption and demand have been increasing continuously in the past decades and are set to continue a steady increase trend in the foreseeable future. The conventional energy sources based on fossil fuels generally dominate the total global gross electricity production, catering for 44.3% percent of UK demand in year 2019 and in the process leading to a considerable production of greenhouse gas emissions [1]. The consequent growing environmental concerns on climate change and pollution have thus inspired a large-scale development of renewable energy generation, such as wind, solar and tidal power, which contributed 72% of all new capacity globally in 2019 [2].

Wind generation in particular, as a mature, commercially competitive and virtually pollution-free energy source is increasingly seen as a dominant factor in decarbonizing our power supply [3]. The global onshore wind cumulative installed capacity reached

602GW in 2019, and is estimated to grow more than three-fold by 2030 and nearly ten-fold by 2050, relative to 2018 levels [4, 5]. In addition, the offshore wind power deployment capacity was 29GW in 2019 and is expected to grow gradually to nearly a 1000GW of total installed capacity by 2050 [5]. Offshore wind generation is increasingly seen as a key factor in decarbonizing our power supply and is set to become the largest source of electricity in the European Union by 2040, with the UK amongst the leaders in this attractive field [6].

Wind power has become the one of the fastest growing renewable energy sources and it is predicted to remain so for some time [7]. The comparatively high operation and maintenance (O&M) cost is the major issue in making these systems more commercially competitive – largely caused by the fact that wind turbines (WT) are remotely located and hard-to-access, which imposes considerable further expenses in maintenance and operation related duties [8]. O&M costs can account for approximately $10 - 20\%$ of the total COE (Cost of Energy) for a wind project [9]. Larger size offshore WTs though may reduce the cost per unit power of electricity produced, however more lost energy, longer downtime and more costly facilities required for their repair increase the O&M cost for these, which has been reported to be as high as 20-25% of total income over asset lifetime [8, 10]. A considerable contributor to this is the wind turbine drivetrain faults, while the drive train is regarded as one of the most critical components of modern WTs. The control strategy and uncertain operating environment makes WTs operating under unsteady and complicated load. In consequence, WT drivetrains have a relatively high failure rate. Corresponding, maintenance costs and drivetrain downtime are also considerable thus reducing the net economic gain of using wind power [11, 12].

To reduce the O&M cost, condition monitoring (CM) and fault diagnosis techniques are

developed for WT drivetrains and other subassemblies in an attempt to provide an effective means of early mechanical or electrical fault warning, as well as awareness of the turbine operating conditions. The relevant maintenance could hence be pre-scheduled and deployed before a further more serious or potentially catastrophic failure occurs, with the aim to achieve a reduction in the associated economic loss and downtime. Online CM techniques are of particular interest here as these enable unattended fault detection while WTs are in service. To reduce the O&M cost and increase the monitoring reliability, many different techniques and tools are researched for WT CM and particularly so for its drivetrain components [11, 12, 13]. To enable these, a variety of sensors are utilized to measure the diagnostically relevant signals like speed, torque, vibrations, temperature, flux density, etc. The sensors are coupled with suitable algorithms (e.g. spectral analysis) to monitor any identifiable fault relevant signatures in the monitored signals and thus derive effective diagnosis and trending of fault [7]. Present CM techniques, especially for mechanical fault recognition, are highly dependant on relatively costly vibration sensors and associated data conditioning platforms. This PhD research will focus on investigation of novel techniques for WT generator and drivetrain CM.

WT concepts could be generally classified depending on the drive train components: gearbox (geared or gearless), electric generator (synchronous or asynchronous) and power converter (partial scale, full scale or none). The WT generators can generally be classified in following types: [14]

- Type A: Geared and high-speed SCIG (Squirrel Cage Induction Generator)
- Type B: Geared and high-speed WRIG (Wound-Rotor Induction Generator)
- Type C: Geared and high-speed DFIG (Doubly-Fed Induction Generator)
- Type D: Direct drive configuration and low speed PMSG (Permanent Magnet

Synchronous Generator) or EESG (Electrically Excited Synchronous Generator) with full power converter.

- Type E: Geared and medium/high-speed PMSG or EESG with full power converter.
- Type F: Geared and high-speed SCIG with full power converter.

To further illustrate the variety of commercially available WT design the Table 1.1 summarises the WT generator type and their market penetration on-shore and off-shore in 2016 [14]. The data show that, while newer alternatives are emerging, and particularly offshore, the DFIG WTs remain the most dominant installed generator type until now; with the WT estimated lifetime of 20-25 years these components require much improved methods for health monitoring and diagnosis to realise their service life at minimal cost. This PhD project thus focuses on analysis of improved CM techniques for DFIG systems.

Table 1-1 Classification of WT generator types [14, 15].

Type	Operating speed	Gearbox	Generator	Grid connection	Usage onshore (%)	Usage offshore (%)
Type A	Fixed	Yes	SCIG	Direct	7%	0
Type B	Variable	Yes	WRIG	Direct	6%	0
Type C	Variable	Yes	DFIG	Via partially rated converter	58%	54%
Type D	Variable	No	SG	Via fully rated converter	17%	5%
Type E	Variable	Yes	SG	Via fully rated converter	4%	14%
Type F	Variable	Yes	SCIG	Via fully rated converter	5%	27%

1.2 Overview of the PhD project

This PhD project aims to research improved CM techniques for WT DFIG systems. The project aim is twofold: to explore the possibility of intelligent utilization of the information embedded in the DFIG control loop signals for generator mechanical fault diagnosis and its operating parameter (shaft speed) spectral search based (SSB) sensorless estimation, and to investigate the application and usage of advanced fibre optic sensing for monitoring and diagnosis of the generator shaft misalignment fault condition.

Considerable research has been done and is ongoing that explores the exploitation of the generator terminal current signals for CM and diagnostics [16, 17, 18].However, modern electric machine drive system consists of complex closed-loop control which can generally compromise the relevant signatures in terminal signals and suppress their manifestation, [19]. Controller signals themselves are readily available and require no addition sensing to be monitored – they could thus provide a readily available diagnostic medium if suitable signatures and methods for their extraction could be identified; however, while the analysis of controller signal application for electrical fault monitoring in DFIGs has received attention in the literature [20, 21, 19] their usage for the drivetrain mechanical fault monitoring remains largely unresearched to the best of the author's knowledge. Furthermore, while current practice favors the application of conventional and reasonably costly piezoelectric vibration sensing for monitoring the mechanical integrity of wind turbine drivetrains there is a need for improved sensing solutions in this area that could offer more flexibility and immunity to harsh operating conditions. The emergence of promising, but not yet proven or used in this area, fibre optic strain sensors could offer considerable advantages from practical usage perspective but requires research for its potential for application to be assessed. This project hence aims to assess the applicability

of control signal exploitation for mechanical fault diagnosis and DFIG operating parameter estimation purposes and to evaluate the requirements and the potential of novel fibre optic sensing to be applied for drivetrain mechanical integrity monitoring.

To this end, an in-depth study of DFIG controller signals inherent spectral nature and that with presence of mechanical fault is undertaken in a purpose developed harmonic model. This enabled the conception of suitable techniques whose validity is then examined in experimental tests on a dedicated purpose built vector controlled DFIG laboratory test rig. The test rig was also used for the development, deployment and performance analysis of novel fibre optic strain monitoring based drivetrain diagnostic schemes.

The following objectives were identified to achieve the project aims:

1. Develop a dynamic wound rotor induction machine (WRIM) harmonic model in Simulink interface to enable investigations of higher order harmonic spectral analysis of machine signals. Ideal switching controlled the stator flux oriented controlled (SFOC) controller with the developed WRIM harmonic model.

2. Develop a fully vector controlled laboratory DFIG test facility utilising commercial converters and a real time control platform to be used for experimental research.

3. Utilise the developed DFIG harmonic model to explore DFIG controller signal spectral contents for further fault diagnosis as well as SSB SSE algorithm development and correlate the findings with experimental measurements.

4. Introduce the mechanical shaft misalignment effects in the DFIG model to allow for modelling and analysis of the fault spectral signature in the controller loop signals and cross correlate the findings with experimental measurements.

5. Conceive a novel spectral search algorithm capable of effectively tracking the target controller signal spectral frequency to extract its frequency and this the rotor speed information. Based on that, implement the developed SSB SSE algorithm software/hardware and test its real time estimation performance in representative real time dynamic tests on the laboratory test rig.

6. Test the diagnostic performance potential of the developed fibre optic strain sensing system for monitoring and diagnosis of DFIG shaft misalignment fault conditions in real time test on the laboratory test rig and cross correlate the results with those obtained from a conventional vibration monitoring platform. Explore the means and methods for on-frame application of fibre optic strain sensors in DFIG systems, including installation, layout and cross-sensitivity effects.

1.3 Contributions of the research

A number of research aspects and knowledge related to modeling and condition monitoring of DFIG systems have been advanced in this research.

The established DFIG harmonic model formed through effective integration of a wound rotor induction machine harmonic model and that of its stator flux oriented controller provides a novel and effective means for analysis of controller signals spectral patterns and behavior [22]. This allowed for studies to be performed that have improved the understanding of the manifestation patterns of the spectral contents containing information on rotor speed in DFIG controller signals, with a view to their exploitation for spectral search based velocity estimation techniques development. Furthermore, combined with a shaft misalignment model utilizing a universal joint representation the resulting DFIG model enables the analysis of mechanical fault spectral signature origins,

propagation and trending in the DFIG controller signals.

This research has also established a unique DFIG laboratory test facility that enables the application of, closed controller access, commercial inverters in DFIG test systems while retaining the capability of stator flux oriented control application in a grid connected DFIG system [23]. This enables the user to utilize all of the inherent and considerable advantages of commercial off the shelf converter systems in built protection, while having the capability of DFIG active and reactive control flow.

This project also develops a novel controller signal embedded sensorless speed estimation scheme for DFIG drives that is underpinned by an intelligent high estimation rate spectral search algorithm utilizing parabolic interpolation and suited to the dynamics of a typical wind generator drive. The proposed scheme has been implemented on the test rig and tested real time showing good performance capability in dynamic operating conditions representative of field applications.

Finally, this research also explores the application, installation and layout features of a novel fibre optic strain sensing systems for DFIG misalignment fault monitoring through frame strain sensing [24]. The proposed method is experimentally examined and shown in tests to provide a comparable level of diagnostic performance to conventional vibration monitoring based systems, while offering the advantages of reduced sensor cost, improved ease of installation and flexibility, as well as the possibility for multiphysical sensing.

1.4 List of Publications

Journal Papers

- N. Sarma, P. Tuohy, J. Apsley, Y. Wang and S. Djurovic, "DFIG stator flux-oriented control scheme execution for test facilities utilising commercial

converters," *IET Renewable Power Generation*, vol. 12, no. 12, pp. 1366-1374, 2018.

- Y. Wang, A. Mohammed, N. Sarma and S. Djurović, "Double Fed Induction Generator Shaft Misalignment Monitoring by FBG Frame Strain Sensing," in *IEEE Sensors Journal*, vol. 20, no. 15, pp. 8541-8551, 1 Aug.1, 2020, doi: 10.1109/JSEN.2020.2984309.
- A. Al-ajmi, Y.Wang and S. Djurovic, "Doubly Fed Induction Generator Misalignment Fault Detection by Supervised Machine Learning of Controller Signals: a case study" in *energies,* vol. 14, 2021.

Conference Paper

- Y.Wang, N. Sarma, A.Mohammed, S. Djurovic "DFIG terminal and controller signal embedded shaft misalignment fault signature – an experimental study", *ICEM 2020*

1.5 Thesis structure

An overview of this PhD thesis structure and a brief summary of each chapter is presented in this section. The entire thesis is arranged into eight chapters apart from the introduction chapter, which is illustrated as follows:

Chapter 2: Literature Review: This chapter consists of a literature review focuses on the operating principles of WT applications. More focus is delivered to the most widely used DFIG based WTs with its structure and control scheme demonstrated. Common WT mechanical and electrical faults are explained along with the fault diagnostic techniques. Finally, the majority of existing sensorless speed estimation techniques are reviewed.

Chapter 3: Description of the experimental DFIG test rig: This chapter begins with a demonstration of the developed DFIG test-rig structure in the laboratory at the University of Manchester Power Conversion Group, which enables SFOC scheme employed for different load and speed conditions. A detailed step-to-step procedure illustration of how to approve testing DFIG SFOC control and grid synchronization utilizing existing commercial converters and sensors is provided. This chapter finishes with an experimental test to validate the implemented control scheme in DFIG system.

Chapter 4: Harmonic modelling of stator flux oriented controlled DFIG: This chapter introduces the theory and implementation process of a DFIG harmonic model to enable further theoretical analysis for DFIG investigation. It begins with demonstrating the theory of WRIM harmonic model utilizing coupled circuit theory. A detailed explanation of the deployed vector control scheme (a SFOC scheme) for DFIG drive and the controller Simulink model implementation are exhibited. By introducing the controller model to the WRIM harmonic model, the decoupled active power and reactive power DFIG control is enabled while the DFIG signals (controller loops signals and terminal signals) contains higher order harmonic contents. A number of derived equations are provided to predict possible theoretical spectral contents of DFIG signals. Meanwhile, the signals obtained from DFIG model are analyzed to identify the characteristic harmonic contents as a validation study. Lastly, a case study is illustrated to unfold how DFIG characteristic harmonic contents could be used for spectral searching based sensorless speed estimation.

Chapter 5: DFIG sensorless speed estimation utilizing controller embedded signal: This chapter demonstrates a novel technique for DFIG SSB SSE consisting of theoretical explanation, experimental signal validation and real-time algorithm

implementation. It begins with a spectral study to identify the harmonic contents of DFIG controller signals obtained from experimental tests. The signals are evaluated in varies of load scenarios to sort out the most proper one for SSE. Then spectral search technique consisting of parabolic interpolation is introduced. After explaining the mathematical theory of the algorithm, the algorithm is programmed in MATLAB and examined with recorded experimental signals. To enable real-time estimation, the algorithm needs to be implemented in LabVIEW interface to functionalize the routine with National Instrument hardware. The programming process is demonstrated in detail. Eventually, the experimental validation consisting of constant and variable speed in different load and estimation rate scenarios are demonstrated.

Chapter 6: Investigation of controller signals in DFIG system with shaft misalignment: This chapter consists of DFIG shaft misalignment model based investigation and an experimental test study. It begins with an introduction of a mechanical model (universal joint) to illustrate shaft misalignment effect. By introducing universal joint model into DFIG harmonic model, the shaft misalignment signature is capable to be observed in DFIG signal controller loop signals. The analysis based on experimental tests in DFIG healthy and faulty conditions is undertaken to cross-correlate with model findings. The limitations of the testing facilities and potential improve methods are presented in the end.

Chapter 7: DFIG shaft misalignment monitoring by FBG frame strain sensing: This chapter illustrates an experimental investigation to recognize shaft misalignment by frame strain signal obtained from FBG sensing. The FBG is an optical sensor recorded within the core of a standard, single-mode optical fibre using spatially-varying patterns of intense UV laser light [25]. This chapter begins with a brief

introduction of shaft misalignment mechanical effect and generally employed diagnostic tool (vibration sensing). Then followed with FBG sensing principle explanation and experimental test rig set up description. Three orientations of DFIG frame strain are tested and evaluated in different fault severities in a wide operating range (speeds and loads). Vibration signal recorded by commercial accelerometers are correlated with strain measurements. Lastly, a cross-sensitivity evaluation study is provided to demonstrate the FBG strain test is independent of thermal effect.

Chapter 8: Conclusions and recommendations for future work: This chapter provides a summary of the PhD project achievements. The suggestions for future research is also included.

Chapter 2 Literature Review

2.1 Introduction

The main topic of this PhD project is to investigate the novel monitoring and parameter estimation techniques for double fed induction generator (DFIG) condition monitoring (CM). A general review of the literature related to these topics is presented in this chapter. This chapter begins with the description of fundamental operating principles of wind turbines (WTs) and then proceeds to introduce the features of DFIG systems and their control. Common faults in the generator and state-of-the-art condition monitoring fault diagnosis (CMFD) techniques are then reviewed. Finally, the chapter ends with a review of modern machine sensorless speed estimation approaches.

2.2 Wind turbine operation

Wind turbine is a machine which converts the wind power into electricity. Typically, a wind turbine consists [26] :

- The rotor contains the blades and the supporting hub.
- The nacelle contains the drive train and the WT control system. The drive train consists of the rotating parts (excluding the turbine rotor): shaft, gearbox (but direct drive systems are also used), coupling, mechanical brake and the generator. The WT control system comprises sensors, controllers, power amplifiers, actuators and intelligences. The components inside the nacelle cover are protected from the weather.
- The main frame consists of turbine housing and bedplate. The mounting and proper alignment of the drive train components are secured by the main frame.
- The yaw system, whose primary component is the large bearing connecting the main frame to the tower, keeps the rotor shaft properly aligned with the wind direction.
- The tower and supporting foundation.
- The balance of electrical system consisting of cables, switchgear, transformers and the required power electronics.

The general WT layout is illustrated in Figure 2-1.

The kinetic energy contained in the wind stream is converted to mechanical power by the WT rotor; this mechanical power then drives the electrical generator enabling electrical power generation. The high torque low speed mechanical power is typically transferred to low torque high speed power via the gear box to actuate the electrical generator [27]. The kinetic energy P_v contained in the wind cross the WT rotor is expressed below: [28] [29] [26]

$$P_v = \frac{1}{2}\rho\pi R^2 V_v^3 \tag{2.1}$$

where:

ρ = the air density $[kg/m^3]$

R = the radius of WT rotor $[m]$

V_v = velocity of the air $[m/sec]$

Only part of the kinetic energy P_t can be recovered by WT: [28] [26] [29]

$$P_t = \frac{1}{2}\rho\pi R^2 V_v^3 C_p \tag{2.2}$$

where C_p is the power coefficient, which is often expressed as a function of tip speed ratio λ: [28] [26] [29]

$$\lambda = \frac{R\Omega_t}{V_v} \tag{2.3}$$

where Ω_t is the angular speed of the rotor $[rad/s]$. The theoretical maximum values of C_p is specified by Betz limit [28] as 59.3%.

For a variable speed wind turbine (VSWT), typically the WT starts generating power when wind speed reaches cut-in speed (usually around 5 m/s), which is the minimum wind speed required to drive the WT to deliver useful power. The output power keeps increasing with wind speed increase until the rated wind speed is reached, which corresponds to the WT rated power. WT delivered power is maintained at rated level until the wind speed exceeds cut-out wind speed, which is the high speed limit at which the WT stops working to prevent mechanical damage. Typically, the cut-out speed is approximately 25 m/s [26] [28] [27].

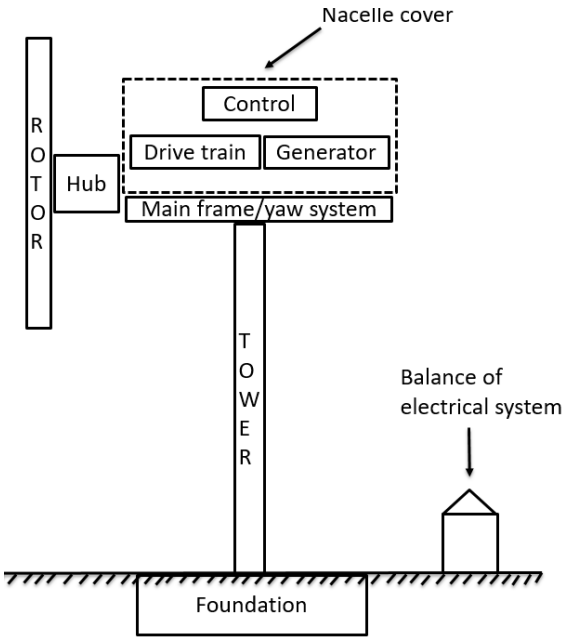

Figure 2-1 Major components of a wind turbine

In the wind speed range between rated wind speed and cut-out speed, the WT generated power is regulated at rated level utilizing pitch control or stall control or a combination of both to reduce the exceed power. The pitch control is basically the process of moving the rotor blades out of the wind (pitch angle) to regulate the mechanical power intake from the wind stream, i.e. to limit the power level. The stall control is a passive control method in which the rotor blades are designed to induce drag against lift while wind speed goes high [27] [28]. The ideal wind turbine power characteristic is illustrated in Figure 2-2. The cut-in speed and cut-out speed can vary in between specific WT designs however the general operating principles are identical.

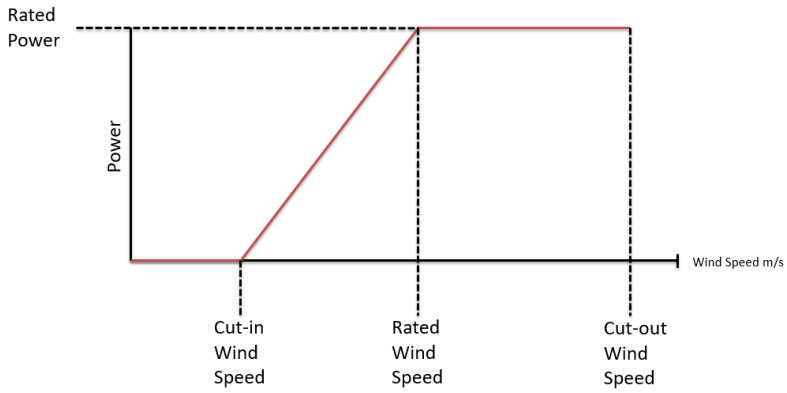

Figure 2-2 Ideal wind turbine power characteristic

The operating range of the DFIG WT corresponding to wind speed is shown in Figure 2-3 for illustrative purposes [28]. Here the nominal power of the turbine is reached at about 11m/s and 1800 rpm.

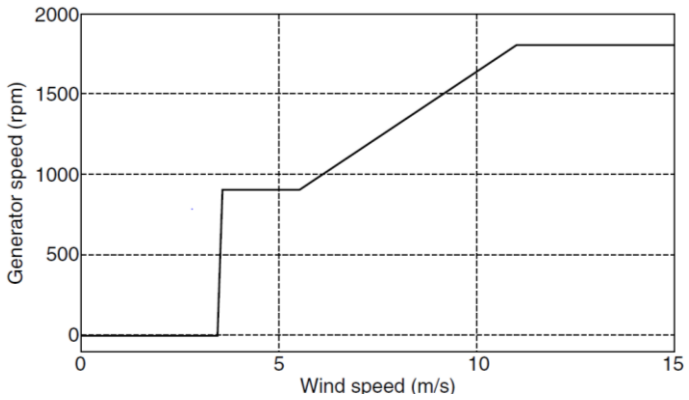

Figure 2-3 Wind turbine generator speed control [28]

The following parameters are assumed: [28]

1. The optimum tip speed ratio of 7.2.

2. The rotor radius is 42m.

3. The speed range of the generator from 900 rpm to 1800 rpm (this is a 4 pole 50 Hz DFIG system).

Four different control regions could be observed: [28]

1. Constant low speed region (900 rpm) for wind speed in the range of 3.5-5.5 m/s.

2. Maximum power tracking region (900-1800 rpm), corresponding to the wind speed range of 5.5-11m/s.

3. Constant nominal speed region for wind speed in the range of 11-12m/s. The stall mode is activated in this speed region.

4. For further increase in speed, the pitch control is employed to reduce the aerodynamic performance of WT and the power extraction.

A typical WT power curve is given in Figure 2-4.

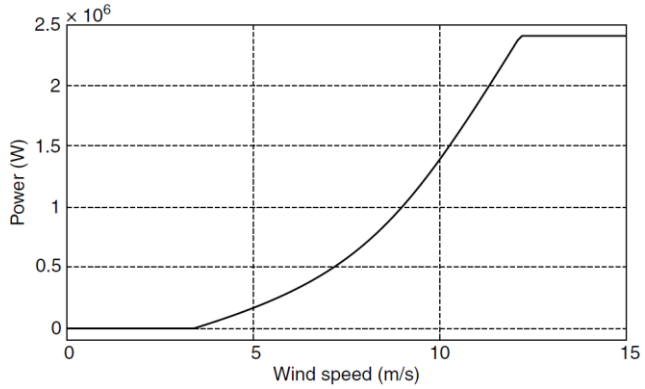

Figure 2-4 Wind turbine power versus wind speed

2.3 DFIG structure and control

The doubly fed induction generator (DFIG) consists of a wound rotor induction machine

(WRIM) and a back-to-back (AC-DC-AC) converter connected to the rotor windings. The stator windings of the generator are directly connected to the grid side thus relatively constant frequency and amplitude voltage is fed into stator side. The typical layout of DFIG based wind turbine is illustrated in Figure 2-5.

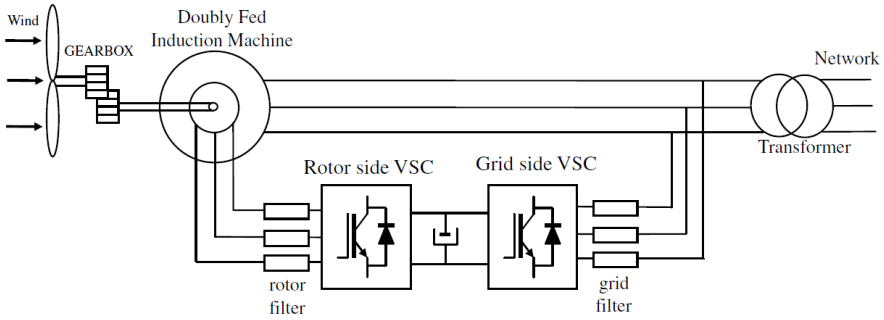

Figure 2-5 DFIG based wind turbine [28]

The low speed high torque mechanical power on the turbine rotor shaft is transferred to high speed low torque mechanical power driving the generator by a suitable gear box. The DFIG is a widely used WT generator accounting for 58% of onshore capacity and 54% of offshore installations [30] due to the following characteristics: [28] [15]

- The capability of variable-speed constant-frequency (VSCF) operation, where direct grid connection at supply frequency is facilitated.
- A reduced requirement for the power electronic converter rating, due to it being in the rotor circuit. Combined with a limited operating speed range (generally around ±30% slip) this yields reduced power loss and price.
- Complete control of active power and reactive power based on the grid demands.

The back to back converter in the DFIG rotor circuit is controlled in a specific routine to allow the generated power on the stator to be maintained at rated grid frequency and

voltage [28]; this converter consists of two three-phase bidirectional voltage source converters (VSC): the rotor side converter (RSC) and the grid side converter (GSC). Two converters are connected via a DC link. The RSC is responsible for the control of the rotor currents to allow stator flux oriented control for the DFIG while the GSC regulates the DC voltage of DC bus capacitor [31].

The DFIG limitation can be considerable since the stator is directly connected to the grid; a large rotor current can be transmitted from the stator side if there is a grid fault, which might lead to damage to the rotor side converter and hence adequate protection is needed for the device but also the grid in case of disturbances [15]. As the DFIG speed range is much narrower than that of the WT blade (usually 10-25 rpm), a multi-stage gear box is required to modulate the mechanical power flow into the electric generator, which can be problematic in these systems due to maintenance requirements/frequent failures but also heat dissipation from friction and noise [15].

2.3.1 DFIG wind turbine control strategy

Generally, the control strategy of a variable wind turbine is classified into three different levels illustrated in Figure 2-6.

Control level 3 is devoted to wind turbine–grid integration, which performs the same facilities as the wind farm control: [28]

- It caters for additional services: voltage (V_{grid}) and frequency (f_{grid}) control (droop characteristics), or inertial response.
- It reacts to active and reactive power references i.e. power factor (PF) from the grid operator or wind farm centralized control.

Control level 2 is used to manipulate wind energy conversion into mechanical energy,

which is the energy extracted from wind by the turbine rotor blades. The power references i.e. stator active power (P_s^*) or electromagnetic torque (T_{em}^*), stator reactive power (Q_s^*), DC bus voltage (V_{bus}) and grid reactive power (Q_g^*) for control level 1 are calculated at this level [28]. The wind turbines are designed to operate in a certain speed region, which is usually 5m/s-25m/s. The wind turbines can only extract part of wind energy, according to Betz's law, less than 59% of kinetic energy in wind can be converted into mechanical energy used in wind turbine. In practice, the wind turbines work at non-ideal condition, the ratio is reported in the range of up to 40% [27] [32]. The mechanical power extracted from wind was defined in equation (2.2).

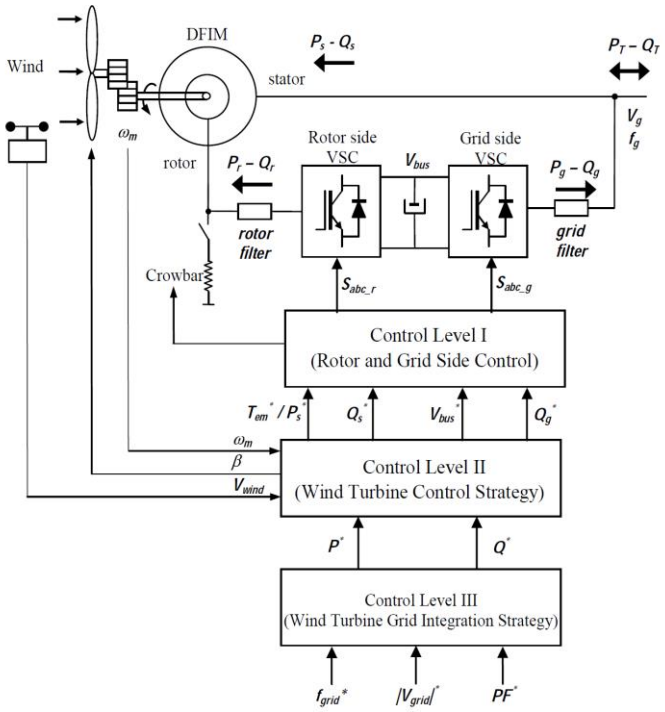

Figure 2-6 wind turbine control strategy based on DFIM [28]

There are two main operation modes usually used in control level 2: [33]

- The normal operating mode is to extract maximum power from wind, adjusting torque (stator power) and pitch angle (β) references. The speed is kept within speed limits.
- Future operation mode is to respond to active and reactive power references from higher level control (level III). This mode is employed in grid scenarios with a large dependence on wind power.

Control level 1 is to regulate the real power and reactive power flow between the grid and induction machine by employing a specific control scheme i.e. switching patterns for rotor side converter S_{abc_r} and grid side converter S_{abc_g} to the back-to-back converters [28]. The decoupled control of active power and reactive power flowing between the converter and the grid is enabled by GSC. The active power is exchanged between the DFIG rotor and the DC bus. Grid voltage oriented vector control (CVOVC) is the commonly used scheme to calculate the active power exchanged with the grid and keep the DC bus voltage constant [28]. A dq- reference frame controller is built for the GSC control, since this research project is more focused on DFIG machine side dynamics and performance. Detailed description of GSC control is not included in the thesis.

The induction machine excitation is provided by the rotor side converter. The PWM converter is able to provide rotor voltage signals with required frequency, magnitude and phase based on desired control scheme to control the power output at stator terminals output [6]. This is done by employing a vector control strategy and executed by implementing a dq- model for the vector control scheme, where 3-phase variables are transformed to dq-reference frame variables in synchronous reference frame, so that the reference current values of PI controllers are steady DC components [28]. To meet the

generated real power and reactive power output demand, stator flux oriented control (SFOC) is employed to enable DFIG decoupled power control, which is fixing the rotor current vector with the reference frame aligned with the stator flux in dq- model by aligning the d-axis with stator flux linkage space vector [34].

The stator flux position is obtained from stator voltage vector in this project, which is regarded as the most commonly used approach, due to its simple design and no requirement for dedicated sensing to achieve [34]. In stator flux oriented reference frame, stator active power and reactive power can be controlled by decoupled rotor side current I_q and I_d independently in dq- two axis controller model [31]. Apart from SFOC, another vector control scheme called stator voltage oriented control (SVOC) is also commonly employed for DFIG, similar to SFOC, by aligning the stator voltage space vector with q-axis of synchronous reference frame. In fact, since the stator resistance is neglected for stator voltage/ flux space vector estimation, the stator flux space vector is 90 degrees lagging of stator voltage vector. As a result, the reference frame d-axis is aligned with stator flux in both vector control schemes. SFOC is chosen among two options as it is the most widely used control scheme for WT generation system [35] [34]. More detailed descriptions of SFOC will be introduced in Chapter 4.

Other control schemes are available for DFIG RSC as well as generally available for other AC drives, which is different from the vector control schemes listed in last paragraph: Direct torque control (DTC) and direct power control (DPC). Both control schemes have the similar control structure but are designed to directly control different machine related components. DTC is aimed to manipulate the torque and rotor flux of the machine, while DPC controls the stator active and reactive powers [28]. The classic DTC and DPC have the following characteristics: fast dynamic response; on-line implementation simplicity;

reduced tuning and adjustment efforts on the part of controllers; robustness against model uncertainties; reliability; good perturbation rejection, however suffer from nonconstant switching frequency behaviour, which is the main drawback of classic DTC and DTC. [28]. To overcome this issue, the predictive direct torque control (P-DTC) and predictive direct power control (P-DPC) based on the same principles as direct control techniques but operating at constant switching frequency by slightly increasing the complexity of control. Compared with classic direct control schemes, predictive direct control requires three-level neutral point clamped converter while the classic direct control uses two-level voltage source converter [28].

In this research the widely used SFOC scheme is selected for DFIG control approach, due to its high performance control capability and the ability of decoupled active and reactive control [34], SFOC is implemented in model and experiment to enable the analysis of the relevant phenomena.

2.4 Wind turbine Condition monitoring

With wind turbines (WTs) growing in size and power capacity to exploit the higher and more consistent wind resource offshore, their exposure to harsh ambient conditions in remote offshore locations creates challenges for operation and maintenance (O&M): access is often limited and maintenance costly due to complicated repair infrastructure requirements imposed by the device location and scale. A good illustrative example of this is provided by General Electric Energy, where a $5000 bearing replacement could be easily turn into a $250000 project involving cranes, service crew, gear box replacements and generator rewinds without considering the downtime loss [8]. It has been reported in [36], that 1-3 failures per turbine per year are common for onshore turbines, and 0.5 failures per turbine per year for the offshore turbines. The development of WT in-service

monitoring techniques that can assist maintenance decisions is thus of considerable importance as it can improve availability and reduce the high O&M cost [11] – this is currently estimated to account for anywhere up to 35% of the total cost of the generated electricity [37].

The offshore wind O&M industry in the UK alone is anticipated to form an industry worth £2 billion/year nationally by 2025 [38] [39]: much of the needed cost savings in this area are believed to be possible through implementation of better proactive maintenance techniques underpinned by improved condition monitoring solutions [40]. In this regard, the relevant standards for wind turbine certification [41] require turbine drivetrains to be equipped with suitable monitoring systems to enable the understanding of its key components' integrity (e.g. bearings, generator, gearbox) with most manufacturers expanding these with proprietary systems aimed at enabling the monitoring of a wider array of drivetrain and associated device failure modes [40].

There are 3 maintenance approaches available for WT maintenance: Reactive maintenance, Preventive maintenance and Predictive maintenance [42].

- Reactive maintenance only fixes the problems after they occur. Although the upfront costs are not required, the cost of secondary damage, increased labor and unplanned downtime can be considerable with this approach.
- Preventive maintenance includes regular overhaul, regardless the condition of the parts. While this can often eliminate failures before they occur, the maintenance cost increases since the parts are more frequently changed and labor needed.
- Predictive maintenance involves the monitoring of the machine operating condition in an attempt to identify development of fault at the earlies stage possible. By predicting the likely to fail parts with symptoms, the maintenance

can be scheduled for only the parts exhibiting signs of damage. Therefore, it allows for an increased efficiency maintenance and the reduction of costly unplanned downtime.

To enable the third monitoring approach, condition monitoring techniques are essential for WT fault diagnosis, especially for offshore wind turbines. With the pre-programmed detection algorithms, the early warnings of mechanical and electrical faults can be observed while the defective component is operational, thus the repair actions can be planned with the consideration of weather conditions of offshore turbine and tower height. Correspondingly, the overall maintenance cost and downtime are optimised [7].

The monitoring systems in WTs are classified into different levels, which are illustrated in Figure 2-7.

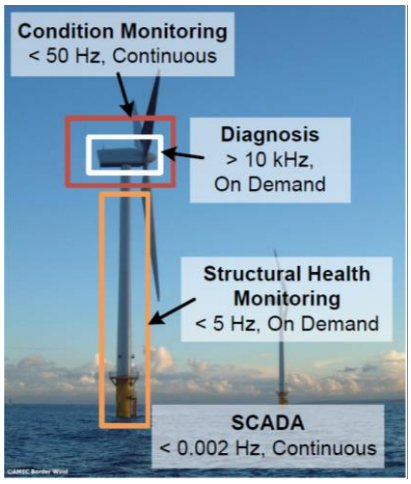

Figure 2-7 Structural health and condition monitoring of a wind turbine [43]

The supervisory control and data acquisition system (SCADA) offers the measurements of the wind turbine system. Every 5-10 minutes, the measured averaged values are

transmitted to a central database. The information like power output, wind speed and temperature is collected in this system [43]. The structure health monitoring (SHM) is designed to monitor the integrity of the wind turbine tower and foundations. Low sample frequency less than 5Hz is employed in SHM [43].

The condition monitoring (CM) system enables supervision of whether the wind turbine operates in a healthy condition. Reliable alarm and its severity are arranged by this system while a fault occurs, to enable the wind turbine operator to schedule maintenance. CM alarm are widely used in WT as an associated tool. CM signals are not sampled in high frequency considering the space of data storage [43]. Once there is a fault detected in CM system, the diagnosis system will be triggered either automatically or manually to sort out the fault part. In this case, intermittent high sample frequency signal is obtained by diagnosis system for fault analysis [43].

The components reliability in variable speed wind turbine are summarized in Figure 2-8 below: The presented data exhibited the annual downtime of variable speed WTs. The generator has the highest downtime among all components as it contains both complex electrical and high speed rotating mechanical components, moreover, other components related to generator such as bearing also contribute to down time of WT. As a result, the identification of generator faults are essential topics of CM to reduce the down time. Moreover, gearbox is reported as another major component causes failure in WT. In this PhD project, the diagnostic investigation for shaft misalignment fault in DFIG system and the DFIG condition monitoring technique implementation are some of key objectives of this research.

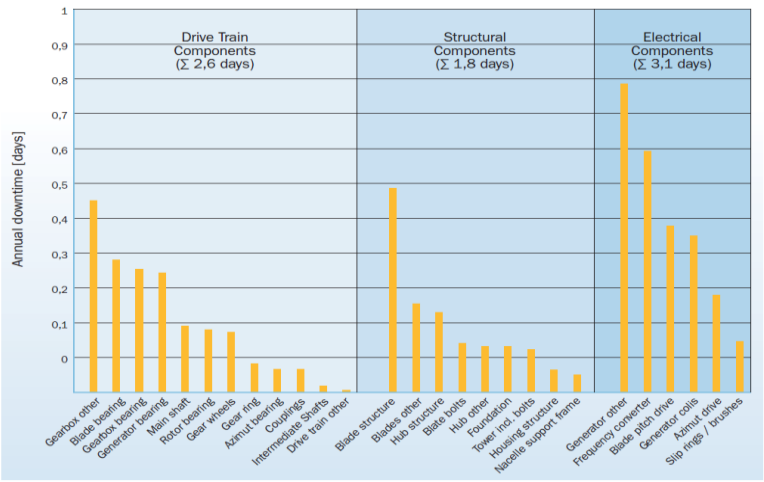

Figure 2-8 Components of variable speed wind turbines and their reliabilities [44]

2.4.1 Machine failure modes

The WT generator faults are generally classified in two categories: mechanical and electrical faults [45] [37]. Mechanical faults include: bearing fault, shaft misalignment, air gap eccentricity, bent shaft, broken rotor bar and rotor mass imbalance, etc. Electrical fault can be categorised as: stator or rotor insulation damage, open circuit fault and electrical imbalance.

The root causes of generator failures are summarized by [46] as:

- Defective design or manufacture; material or component; installation maintenance or operation
- Ambient conditions
- Over speed and overload
- Low cycle fatigue or shock load

- High cycle fatigue or excessive vibration
- Defective component
- Excessive temperature: in windings and in bearings
- Excessive dielectric stress: steady or transient
- Debris, dirt or corrosion

The following symptoms are reported to be possible in a WT induction generator when a mechanical or electrical fault occurs: [47] [48]

- Unbalanced air-gap voltages and line currents
- Increased torque pulsations and decreased average torque
- Increased losses and reduced efficiency
- Excessive heating
- Disturbances in the current/voltage/flux etc. waveform
- Specified harmonics in line current increased
- Leakage flux in axial direction

At present, a variety of sensors are employed to obtain signals from different sources for condition monitoring, which includes: stator voltages and currents, air-gap and external magnetic flux densities, rotor position and speed, output torque, internal and external temperature, and case vibrations, etc. [49].

A brief description of some general machine fault types is provided in the following subsection.

2.4.1.1 Shaft misalignment

Shaft misalignment is estimated to contribute to up to 50% of all rotating machinery breakdowns [50] and can result in considerable downtime and economic losses if it is not detected timely. Misalignment is defined as a condition in which the shaft of the driving machine and that of the driven machine do not align with the same centerline. While ensuring accurate alignment can in principle prevent a considerable number of breakdowns, including the associated unplanned downtime and production loss, in practice the alignment is challenging to sustain over extended service periods and ideally needs continuous monitoring, as it is unavoidably compromised by a number of drivetrain inherent factors. In WT systems in particular, shaft misalignment can give rise to undesirable forces leading to damage or destruction of bearings, seals, couplings, and eventually the gearbox and the generator [51]. Misalignment monitoring and diagnosis is thus especially important in contemporary WT drivetrains where due to additional issues associated with the remote and harsh operating environment misalignment issues have particularly significant downtime and repair cost implications [11] [52]. Shaft misalignment is also responsible for 30% of downtime [52]. Investigation of different approaches to recognize shaft misalignment fault in DFIG system for CM is one of the topics in this PhD project. The positional problems associated with shaft misalignment in a WT system are classified as following: [53]

- Extreme redial and axial vibrations
- Oil leakage at shaft seals and bearing seals
- Hot coupling or high casing temperatures at or near bearings
- Loosened coupling bolts or foundation bolts
- Premature bearing or shaft wear and failure

In general, the shaft misalignment fault can be classified into three different types: parallel, angular and combined. The different types of shaft misalignment are illustrated in Figure 2-9.

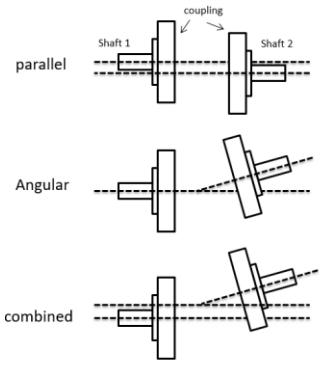

Figure 2-9 Types of shaft misalignment

In modern WT field applications drivetrain online monitoring systems are legally required [54]; these typically use piezoelectric accelerometers for distributed monitoring of the drivetrain vibration and can achieve misalignment detection through observation of vibration components at shaft rotational speed multiples [50] [55]. In addition, generator alignment is typically inspected once every twelve months using costly laser alignment tools as part of a maintenance program periodic checks to ascertain existing misalignment levels and identify any required corrective action; these laser sensors are however not fully suitable for continuous monitoring [56]. While effective, the expensive vibration based monitoring techniques can suffer in diagnostic reliability due to generator transient operation and limitations in dynamic range [52], hence alternative methods for shaft misalignment online monitoring are continuously researched: infra-red thermometers were applied in [52] to observe coupling temperature, but found to be sensitive to other heat sources in the drivetrain. Using generator current sensor

measurements for misalignment detection was also explored [57], but was shown to be challenging as other fault modes can be confused with misalignment. Strain gauge application to measure displacement in vicinity of couplings was researched in [58], but found to be constrained by the sensor location requirements. Fibre Bragg grating (FBG) was investigated as a diagnostic tool to monitor DFIG frame surface strain to explore the potential of shaft misalignment recognition and has been validated in [24]. Laser based shaft distance measurement was explored in [59], but requires further research to fully evaluate. Motor current signature analysis (MCSA) has been explored as a diagnostic tool for monitoring shaft misalignment in conventional electric machines [60, 61, 62] it is suggested that presence of misalignment can be demonstrated by additional content in the stator line current spectrum.

2.4.1.2 Bearing fault

Bearing fault is regarded as one of the most frequently occurred faults in electric motors (41%) [63]. Every bearing consists of two rings: inner one and outer one. A sets of balls or rolling elements are located in raceways rotates insides these rings [64]. Correspondingly, the bearing faults can be classified into three different types: outer raceway defect, inner raceway defect and other defects. Fatigue failures may occur even the machine operates in normal balanced condition with good alignment. These faults may be responsible for increased vibration and noise levels thus gradually lead to flaking or spalling of bearings [64]. The electro-mechanical symmetry in generator can be disturbed by bearing fault, which leads to dynamic or static changes in the generator air-gap and this field compared with those under healthy operation conditions [65]. A bearing failure example in practical machine is exhibited below:

Figure 2-10 Illustration of bearing failure [66]

Vibration analysis is the most widely used and investigated tool to diagnosis bearing fault. Typically fault diagnosis is conducted by recognizing spectral characteristic frequency components generated with bearing fault, which are listed in [63] [67] [64]. Apart from frequency domain analysis, vibration signal time domain analysis utilizing calculated Kurtosis value based on measured statistical parameters: crest factor, skewness, kurtosis, probability density curve, etc. As reported in [67], kurtosis value larger than 3 indicates the bearing fault occur. Alternative techniques have also been investigated to undertake bearing fault detection without expensive vibration sensors. MCSA as a diagnostic tool has been investigated in [63] [68], both researches built dynamic model of defect bearing and exhibited a compare spectrum study of healthy and faulty scenarios. MCSA indicated the potential of bearing fault diagnosis however the findings were reported less sensitive compared with vibration analysis in [69]. Acoustic analysis is able to show bearing fault frequencies clearly in acoustic spectra with fewer interferences and harmonics than vibration analysis but susceptible to external noise sources [69].

2.4.1.3 Eccentricity fault

Machine eccentricity is the unequal condition of air gap length between stator and rotor [70]. There are three types of eccentricity faults: static, dynamic and mixed. In static fault, the rotating part has the same rotation axis of the rotor, but displaced from the axis of the stator. In dynamic fault condition, the rotating part has the same axis of stator but it is not aligned with the rotor. In mixed fault, the rotation axis is different from either stator axis or rotor axis [71]. For a more visual view, the different types of eccentricity fault are illustrated in Figure 2-11

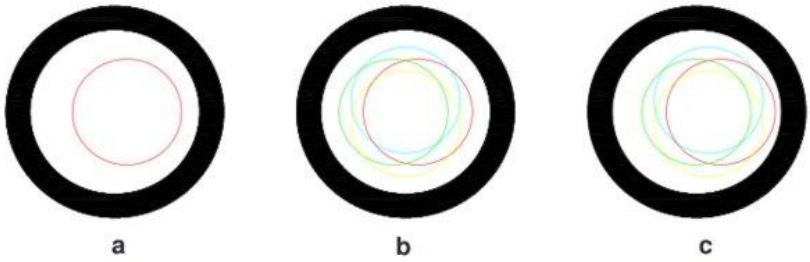

Figure 2-11 Different types of eccentricity fault [72]

Mechanical faults are common in electric machines which lead to 50%-60% of the faults, while 80% of the mechanical faults cause eccentricity [73]. Undesired impacts can be led by eccentricity like: accelerating the wear of bearings, undesirable vibrations, increased losses and heating. With the unsolved eccentricity fault, the stator core and winding can be damaged due to rotor-stator rub [71]. The dynamic simulation model was implemented in [74] Several approaches are reported to detect eccentricity fault: vibration signal, machine current [75] and reactive power [76] spectrum analysis were successfully investigated.

2.4.1.4 Stator winding fault

The stator or armature faults usually refer to insulation failure, which are known as phase-to-ground fault or phase-to-phase faults [70]. However, the root of phase-to-ground or phase-to-phase fault is the undetected turn-to-turn fault which propagated until machine failure occurs. Stator faults are responsible for 30%-40% of induction machine failures [77]. As a result, it is essential to detect the turn-to-turn fault at an early stage.

Various techniques have been investigated to detect stator winding faults. For large generators and motors with stator windings rated at 4kV and above, online partial-discharge test indicated good results [78]. For low-voltage motors, with the asymmetry in machine impedance caused by stator faults, the unbalanced phase current could be observed by monitoring the negative-sequence current flow. i.e. for example one turn fault out of 648 turns was reported possible to detect [77]. Additionally, the power decomposition technique and the statistical process control technique were also employed to detect stator fault, as reported in [70]. Some researches based on MCSA method were developed to detect stator fault as well, similar to previous sections, the characteristic frequency components can be observed when a fault occurs, however, further theoretical investigations are needed to demonstrate the root of spectral performance [70].

2.4.1.5 Rotor winding fault

Similar to stator fault, rotor fault in DFIG is mainly referring to turn-to-turn faults in rotor side. The rotor winding is originally symmetrical in the healthy condition, but the symmetry could be broken by inner turn short circuit [18]. Both power analysis and current signal analysis were investigated to detect rotor fault. The stator active power signal investigation was undertaken in [79] whilst similar research was conducted with stator current in [18]. A comparison test was carried out in [16], both power and current

sensing techniques were employed to detect rotor asymmetry. It was reported that the current spectrum signal has benefits of lower noise and clearer view while power spectrum signal benefits from the point of view of globality. Additionally, in [80], the controller error signals of a DFIG were validated as having potential for diagnostic application: Both the rotor side *d*-, *q*- current error signals contain the characteristic frequencies enabling fault diagnosis, with the e *q*- component signal signature exhibiting higher sensitivity to fault.

2.4.2 Condition monitoring techniques

Condition monitoring is a technical approach to forecast the potential faults in WT system thus reducing the maintenance cost and improve the reliability of WT. Some physical symptoms can occur exclusively with the electrical or mechanical fault present in the machine which are generally used as indicator for fault diagnosis: high temperature, noise, impulse harmonic components in electrical signals, vibration, torque etc. One or more unique attributes correspond to a specific type of fault which are commonly explored by comparing measured signals in fault condition with those in healthy condition. Until now, a number of techniques have been investigated to identify electrical or mechanical fault: [64] [46]

- Electromagnetic field monitoring
- Electrical discharge monitoring
- Temperature monitoring
- Radio-frequency (RF) emission monitoring
- Noise and vibration monitoring
- Chemical analysis

- Acoustic noise measurements
- Motor-current signature analysis (MCSA)
- FBG sensing
- Strain sensing
- AI techniques

In this section, the techniques involved in this PhD project are briefly introduced.

2.4.2.1 Temperature monitoring

The electrical machine maximum allowable operating temperature is limited by the capacity of the used insulation material to sustain high temperature [81]. Furthermore, some fault conditions like misalignment will generate heat at specific points, as will winding or bearing faults. Therefore, temperature sensing is essential in machine condition monitoring and has been applied as a tool to detect faults [29]. Three approaches are mainly employed to measure machine temperature: [81]

- Embedded temperature detectors (ETD) are used to measure local point temperatures, which are usually active parts like stator winding, stator core or bearings. The key point is to identify the hottest point that needs measuring.
- The thermal image is used to monitor the temperature and obtain the hottest spot. This technique is employed for thick extra high voltage insulation but have not widely used in rotation machine.
- Measure machine distributed temperatures or bulk temperatures of the coolant fluid.

2.4.2.2 Mechanical vibration monitoring

Vibration monitoring is the most commonly used condition monitoring technique especially for mechanical fault diagnosis due to its accuracy. The machine vibration stems from a variety of sources: bearings, gears and electrical/mechanical unbalance etc. [42]. Due to the nature of mechanical faults, vibration is the most directly affected component [82]. Thus vibration sensing as a diagnostic tool has been widely used to detect rotational machine mechanical related faults, such as: shaft misalignment, imbalance, looseness, bent shaft and bearing fault [50]. The common approach to measure the vibration signal is to mount accelerometers or velocimeters on the bearings, or proximeters mounted adjacent to bearings. Accelerometers are more suitable for higher frequencies while velocimeters and proximeters are more suited to lower frequencies [81]. Once collected, spectral analysis of the vibration signals needs to be performed to observe fault characteristic frequency components and thus diagnose the fault.

2.4.2.3 Electrical current monitoring

Considering the cost of sensors and the risk of sensor failure, the MCSA and generator output power analysis have received significant research attention, as these techniques are cost effective and non invasive. Compared with sensor monitoring, current signal is a multifunctional tool that has been reported to allow diagnosis of various faults, such as bearing fault, shaft misalignment, load unbalance, gearbox fault, winding fault et.al [63] [82] [83]. Furthermore, the fast development of signal processing techniques and hardware platforms reduces the cost and complexity of current monitoring. However, the current signal is affected by some other factors that can complicate its diagnostic employment and lead to error, such as electric power supply [84].

2.4.2.4 FBG sensing

The fibre optics were first employed for the purpose of high-quality, high capacity and long distance telecommunication [85]. The effect of the photo sensitivity for Germanium doped fibres was found by Ken O. Hill in 1978. The permanent change of the refractive index could be induced by exposure to ultraviolet light. With Bragg gratings written into fibers, which enables the reflections of very small wavelength peaks, the wavelengths of these peaks could change with temperature or when such fibres are strained [86]. Such features of fibre Gragg grating (FBG) spawned the applications of fibre optic sensing for electric machine condition monitoring is increasingly developing as a promising alternative to conventional techniques. This technology in particular presents a number of features which are attractive in this respect [85, 86]: Electromagnetic interference (EMI) immunity, small size (i.e standard optical fiber size is $\approx$ 125 µm in diameter, while FBG head length typically ranges from 2 to 20 mm) and light weight, multiplexing capability and that of multi-physical sensing: such as temperature, stress, electric field and magnetic field, long term stability (>25 years) and relatively easy installation. However, The disadvantages that can be attributed to the FBGs are: FBGs are highly dependent to temperature. The cross-sensitivity (temperature and strain) problem needs mitigating by special arrangements for temperature compensated strain sensing. The cost of interrogator is relatively high and the FBGs are also extremely fragile so it is easy damaged [86, 25, 87, 88].

A number of FBG applications for electrical machine condition monitoring have recently been researched demonstrating promising potential. For example, FBG strain sensing use was explored for dynamic eccentricity, winding and broken bar detection in induction machines in [89] [90] [91], while FBG thermal sensing application for winding temperature

monitoring and fault detection in permanent magnet and induction machines was studied in [92] [93] [94]. The development and application of FBG magnetic sensors for electric machine monitoring and diagnostic purposes was explored in [95] [96] [97], while [98] studies simultaneous use of single FBG head multiphysical sensing properties for machine bearing monitoring and [99] investigates the design of an FBG sensing suite for machine multi-parameter monitoring. The potential of FBG sensing application evaluation for misalignment monitoring in electric machine drivetrains however remains to be explored.

2.5 Signal processing techniques

Generally, signature analysis is the majority approach to distinguish which type of fault exist in DFIG [100, 64]. More specifically, since characteristic signal frequency corresponding to different faulty conditions could be observed in spectrum, the type of fault is identified via capturing these component. To this end, an appropriate signal processing technique is required to capture frequency components of interest from the acquired signal. A brief introduction to signal processing techniques employed in CM is given in this section.

2.5.1 The classical Fast Fourier Transform (FFT)

The acquired signals from machine side are generally time domain signal, to analysis the frequency component, the signal conversion from time domain to frequency domain is necessarily required. FFT is one of the most commonly used signal processing techniques. It is a faster implementation of DFT (discrete Fourier Transform), by reducing the n-point Fourier Transform to $(\frac{n}{2})log_2(n)$ points, the less complex algorithm is reached [101]. An example of FFT application in MCSA is illustrated in Figure 2-12 below:

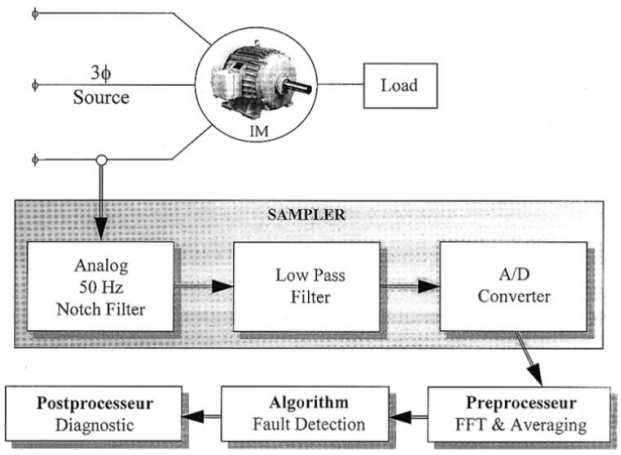

Figure 2-12 Single phase stator current monitoring scheme [28]

The whole process can be classified into four parts: sampler, pre-processor, algorithm and postprocessor. The stator current signal is obtained from induction machine stator side via current transducer, the fundamental frequency and higher frequency components are removed by notch filter and low pass filter correspondingly. The filtered signal is sampled by analogue to digital converter. Then the pre-processor converts the sampled signal from time domain to frequency domain, signal noise is reduced by averaging predetermined number of generated spectra. After that, the characteristic frequency components related to specific fault type are distinguished and extracted. Finally, the frequency components of interests are identified in postprocessor to determine if the fault exist or not [49].

Although FFT is commonly used for WT CM, the limitation is still crucial: it is not suitable for dealing with continuous non-stationary signals (i.e. the frequency content of those signals vary with time) [102]. However, in some situations, e.g. rolling bearing. The vibration signals are often non-stationary and the frequency components change

with respect of time [103]. Therefore Short-time Fourier Transform (STFT) is employed in non-stationary signal analysis, which is preferred for vibration signals to identify harmonic components [102]. In STFT, non-stationary signal (long time) is divided into several small sections (short time), the smaller sections can be regarded as stationary signal and then proceed with FFT. This technique enables a time and frequency based view of a signal. However, since the precision is determined by the size of window (i.e. the frequency resolution of spectrum) and the main drawback of STFT is the fixed size of the window [49].

2.5.2 Wavelet analysis

Time-frequency dimension analysis is widely used to detect fault since they can not only show the effected frequency range, but also the time of impacting occurs. The wavelet transform is regarded as one of the best time-frequency analysis methods [103]. The analysis is based on a special analyzing function, which is called the basic wavelet. The specific time range of the wavelet is selected while analyzing undertaken, then expanded or compressed by a scale parameter and shifted by time parameter. The expanded condition usually focuses on low frequency components while compressing condition is to observe high frequency components [102]. Compared to STFT, wavelet enables variable-size of windowing. As a result, the major advance of wavelet analysis is that the ability of providing multi-resolution diagrams in time and frequency domain. However, the limitations of wavelet transform are unneglectable as well:

- The data got from wavelet transform cannot be applied for feature extraction without further FFT analysis, which increases the complexity [86].
- Wavelet is affected by undesired spikes all over the frequency scales because of interference terms, border distortion and energy leakage [85].

- In some cases like bearing fault detection, the analyzed frequency range is large and requires high sample speed, would expect the method provides good computing efficiency. However, the wavelet transform, as a time consuming method, is not suitable for large size data analysis [85].

2.5.3 Hilbert-Huang transform

Hilbert-Huang transform (HHT) is another time-frequency analysis method which is suitable for non-stationary signal analysis. The analysed signal is proceeded by a time adaptive decomposition operation named empirical mode decomposition (EMD). One of the examples utilizing HHT for DFIG bearing fault detection was introduced in [104]. Then the signal is decomposed into a series of complete and orthogonal components called intrinsic mode function (IMF), which is nearly monocomponent. The full energy-frequency-time distribution of the signal can be obtained by applying Hilbert transform on the IMFs [103]

Compared with wavelet transform, HHT has the advantage of dealing with signal of large size, because the most complex computation step, EMD operation is not time consuming. Besides, the frequency resolution and time resolution concepts are not involved [103]. As a result, HHT is attacking more attention in condition monitoring, especially in the mechanical vibration aspect [105]. However, some drawbacks of HHT still exist: [103]

- Some undesired low amplitude IMFs at low-frequency region and unexpected frequency components are generated by EMD.
- If the first IMF covers a wide range of high-frequency region, the monocomponent definition cannot be satisfied perfectly.
- Some low-energy components from the analysis signal sometimes cannot be

separated by EMD operation, thus these components may lose in the frequency-time plane.

In this PhD project, the fault diagnosis is based on fixed speed condition (i.e. fixed frequency component of interest while operating) to help investigate and identify the characteristic frequency for fault analysis. Therefore, FFT is employed to identify the characteristic frequency from electrical, vibration and FBG measured signals in this project.

2.6 Sensorless speed estimation of rotational machine

Typically, the monitoring of rotating machinery speed and angle requires the use of incremental encoder. Such direct speed and position sensors require additional electronics, extra wiring, extra space, careful mounting, frequent maintenance is also required as the connection, electromagnetic interference, electronic circuit and optical disk damage may possibly affect the speed measurement result. In addition, it has been found that the cost of a speed sensor is close to an induction motor in the 2-5 kW range [106]. Correspondingly, the motor drives without direct speed sensors can provide reduced cost but also higher reliability, better noise immunity as getting rid of complicated wiring for encoder and less maintenance [107]. In WT applications, sensorless speed estimation (SSE) could be an alternative solution to keep the generator working normally if the encoder failure occurs. Therefore, SSE as an improved reliability and low cost drive solution has been investigated in many researches and aimed as a target in this PhD project. The SSE methods could be generally classified into two catalogues: the fundamental model based (FMB) estimation and the spectral search based (SSB) methods [107, 106, 108]. FMB techniques requires basic knowledge of machine parameters (such as stator resistance, inductance, rotor time constant, number of slots...etc.) and its

relevant control, moreover, these parameters are sensitive to inherent variations thus the estimation performance is affected [109]. The SSB is based on frequency components in the electrical or mechanical signal spectrum (e.g. stator current, power, vibration signals etc.), however extensive saliency is needed to visualize the characteristic harmonic component and utilize it for estimation purposes, which cannot always be guaranteed [110]. In this section, a brief explanation of SSE schemes for induction motor drives are illustrated.

2.6.1 Non-spectral sensorless speed techniques

FMB technique is the approach to obtain machine rotational speed or position utilizing electrical signal space vectors. In FMB methods, d-q reference frame equations are employed to express the electrical machine while other reference systems are also possible. The air-gap flux distribution is assumed sinusoidal, i.e. higher order harmonic components are neglected apart from the fundamental. As for DFIG system, the classic example of FMB sensorless control was introduced in [34]. To enable DFIG SFOC, one of the critical steps is to determine the transformation angle for the reference frame transformation. The corresponding phasor diagram is exhibited in Figure 2-13 as following:

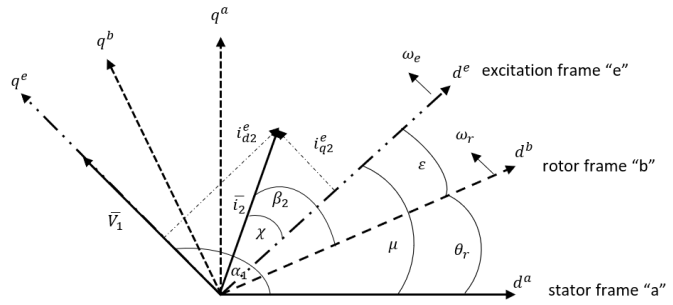

Figure 2-13 illustration of reference frames and angles for the DFIG

The angular difference between stator reference frame and stator flux (excitation frame "e") could be captured from stator voltage as μ, meanwhile, the angular difference among rotor reference frame "b" and rotor current vector $\overline{i_2}$ is β_2. Voltage vector $\overline{v_1}$ is aligned with q axis of excitation frame, which has the position difference α_1 from d axis stationary reference frame. Meanwhile, with the calculated rotor current vector component in excitation frame "e" via equations listed in [34], the angular difference among rotor current vector and stator flux could be worked out as χ. The rotor electrical angle $\theta_r$thus are deduced by $\mu - (\beta_2 - \chi)$. The differential $\theta_r$gives the rotor electrical rotational speed hence finally the mechanical speed could be determined with a pre-known machine pole-pairs. Unfortunately, the listed approach is highly sensitive to the machine parameter variation such as resistance. Non-constant parameters in machine would affect the precision of speed estimation. To mitigate this issue, a closed loop scheme was implemented to offer robustness and deal with dynamic characteristics [110].

Model reference adaptive systems (MRAS) is one of the most widely used approaches for sensorless induction motor drives due to its easy-to-implement system with high speed of adaptation for a wide range of applications [107]. MRAS generally contains a reference

model, an adjustable model and an adaptive mechanism. The reference model is to calculate a state variable x in a rotor speed independent approach such as terminal voltage and current. The adjustable model estimates the state variable $\hat{x}$ depend on rotor speed. The error ε is the difference between calculated state variable and the estimated one [107]. The rotational speed is generated from adaptation mechanism, which is a PI controller, utilizing error ε. As the error ε decreases, the estimated speed is closer to the actual rotational speed [110]. The structure diagram of MRAS is illustrated in Figure 2-14.

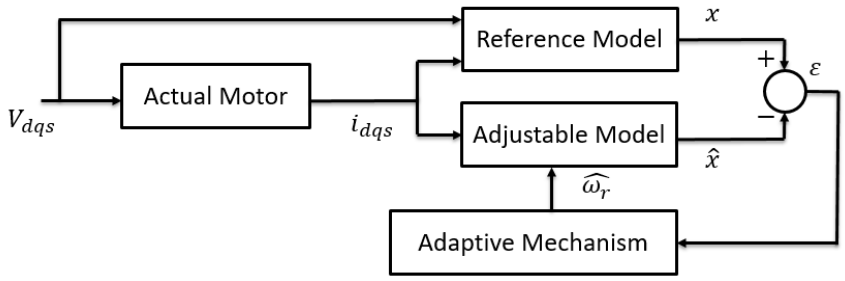

Figure 2-14 Structure block diagram of MRAS scheme

Different types of MRAS are classified with verities of state variable x employed into the scheme, the most commonly used are the rotor flux based MRAS, back emf-based MRAS, and stator current-based MRAS. The main advantages of MRAS algorithms are they are robust and fast convergence. Moreover, the implementation of adaptation mechanism block has to compromise between fast response and high robustness against noise and disturbances in the system [107].

2.6.2 Spectral based sensorless estimation

Unlike the FMB SSE scheme, SSB estimation offers an alternative approach without prior knowledge related to machine and is less sensitive to parameters. SSB SSE is usually

achieved by tracking the characteristic spectral component dependent on rotational speed in real-time. Stator current signal has been investigated for SSB SSE for induction motors. As the air-gap flux in induction motor is not perfectly sinusoidal- due to slotting - the slot effect harmonics can be induced in the stator current that can be employed for speed estimation purposes. Regarding DFIG systems, the spectral content induced in WRIM stator current could be observed in spectrum and demonstrated as following form: [111]

$$f_{current}^{k} = \left| kp\frac{n_r}{10} \pm f_s \right| \tag{2.4}$$

where: k=0,1,2,3…and represents the air-gap fields' pole-pair numbers, f_s is the supply frequency, p is the pole-pair number of the machine and n_r is the machine rotational speed in revolutions per minute (rpm).

Correspondingly, the machine rotational speed can be calculated from (2.4) as:

$$n_r = \frac{10}{k \times p}(f_{current}^{k} - f_s) \tag{2.5}$$

By capturing the real-time slot harmonic components' frequency from stator current signal, the machine rotational speed could be worked out with listed pre-known parameters (e.g. p, k). Signals other than the current have been explored for SSB SSE. Mechanical vibration was post-proceed utilizing zero-crossing detection technique to detect mechanical frequency in [112]. Active power has been evaluated to achieve SSE with its rotor speed dependant frequency component in [113].

The typical process of SSB SSE could be briefly summarized as follows [109]: The source signal (i.e. stator current) is acquired with a predefined sample rate. Generally, a band pass filter is employed to mitigate the effect of spectral interference. Besides, the algorithm usually consists a window function such as e.g. Hanning window to reduce the spectral leakage effect. Due to the limitation of spectral resolution, it is not possible to

obtain perfectly continuous spectrum but only discrete spectrum. The spectral leakage is the part between integer multiple of the spectral resolution. The spectral estimation technique is then employed to capture the frequency component of interest in the spectrum. Finally, the machine rotational speed could be calculated with the predicted speed dependent relationship. The flow chart of SSB SSE is exhibited in Figure 2-15. Stator current slot harmonic SSB SSE in WRIM is used as an example.

To extract the expected harmonic component from spectrum, the common approach is to capture the maximum amplitude harmonic in a specific frequency range. This frequency range required careful determination which can be challenging – its purpose is to isolate the other prominent spectral component like the fundamental frequency harmonic minimising interference with the target spectral frequency that is being monitored for SSE.

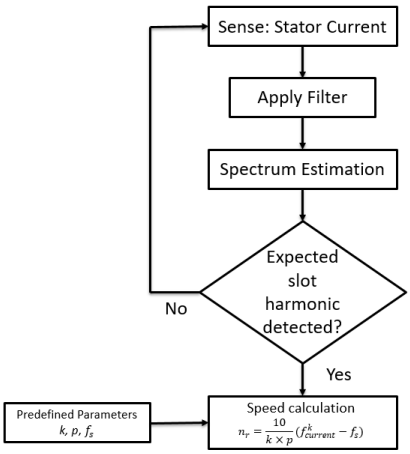

Figure 2-15 Simplified flowchart of SSB SSE

Several techniques were implemented to realize harmonic extraction. FFT is the common

approach to convert the signal from time domain to frequency domain. However, the resolution of FFT effects the estimation results. The error occurs while the estimated frequency lies between the integer multiple of resolution frequency, thus the accurate SSE requires high resolution FFT routine and hardware/software complexity, as introduced in [114] to achieve SSB SSE utilizing stator current signal. Another critical drawback is that the speed estimation rate is reduced by high resolution frequency. To balance the estimation rate and accuracy, various techniques were employed and are briefly reviewed next.

A combination of low resolution FFT and dichotomous technique was implemented in [111]. The slot harmonic of interest was first located within the low resolution frequency range by FFT coarse search, then fine search was deployed to capture the accurate position of slot harmonic by dichotomous scheme. Dichotomous searches the target frequency position in spectrum by reiteratively compare the larger components within halved coarse searched range, after numbers of iterations, a precision frequency estimation could be achieved with limited numbers of sample data and estimation speed is secured as around 10 estimations/second. In [106], the authors implemented a SSB SSE scheme with Hilbert transform and interpolated FFT. The acquired motor current signal is demodulated by Hilbert transform to obtain instantaneous amplitude and phase fluctuations, then the proceed instantaneous amplitude and phase fluctuations are calculated via FFT. To specify the speed related component within the resolution frequency range, the interpolation calculation is given to mitigate the estimation error to locate the frequency component in spectrum. Some other techniques like zero-crossing detection [115], maximum entropy spectral estimation [116] and Chirp-Z transform [108] were also reported in publications.

In this project, a novel SSB SSE scheme utilizing DFIG controller embedded signal with parabolic interpolation is implemented in LabVIEW FPGA interface to enable fast real-time estimation in laboratory testing. More detailed explanation will be demonstrated in Chapter 5.

2.7 Summary

This chapter first presented the general wind turbine structure and its operating region. Among all WT generator types, DFIG is the most widely installed due to its capability of variable-speed fixed-frequency operation and partial scaled back-to-back converter needed – this is challenged for large offshore systems which currently favors alternative technology, however DFIGs constitute the vast majority of currently of operating field devices. The DFIG structure and three-level WT control were explained to illustrate how DFIG associated WT operates in practice.

The chapter then discussed the importance of CM application in WT, CM is aimed to offer a forecast of faults at early stage to reduce the O&M costs as the WT especially offshore ones are remotely located in harsh environment. The common machine fault types and their relevant diagnostic methods were illustrated. Additionally, general CM fault diagnostic approaches and signal processing techniques were also reviewed as a part of CM system introduction. Investigate novel approaches for CM fault diagnosis is one of the targets in this PhD project.

SSE is another PhD research topic for improving machine reliability and cost reduction. Typical machine speed information was acquired via speed sensor, which requires power electronics, extra wiring, space and maintenance. In this chapter, a general review of FMB and SSB SSE were illustrated. Both main SSE classes were demonstrated in the

aspect of definition, control structure and examples.

The material presented in this chapter is aimed to provide a background introduction to the detailed condition monitoring and estimation studies for DFIG systems reported in the following chapter.

Chapter 3 Description of the experimental DFIG test rig

3.1 Introduction

This project explores new controller embedded and advanced sensing schemes for monitoring of operational and health parameters in DFIGs. For experimental research purposes a dedicated laboratory test system is used [117] [16]. The test system is controlled in a stator flux oriented control (SFOC) scheme and is capable of operating synchronised to the grid [118].

This Chapter presents the design and operational features of the purpose built laboratory test rig used in this work. First, the overall layout of the test rig is detailed, followed by a general description of its components (e.g. machines used, power converters, control platform, sensing etc.) and their interconnection and operation. The proprietary implementation of the rotor side converter SFOC scheme is then presented, including the

system run up and synchronisation procedure.

3.2 Test Rig Layout

The overall test rig layout is illustrated in Figure 3-1. A 30 kW wound rotor induction machine (four-pole, three-phase, 50Hz, 225 frame size by Marelli Motori) with a back-to-back converter system interfacing its rotor winding to the grid and its stator winding directly grid connected is employed to emulate a wind power DFIG system on an academic scale. The prime mover is a 40 KW DC motor, controlled by a commercial DC drive to provide a desired load characteristic, including pre-programmed torque-speed profiles representative of wind turbine generator dynamics. A commercial converter interfaced with a dedicated resolver feedback module is used in the test DFIG rotor circuit to allow practical SFOC scheme implementation while retaining the advantages of commercial protection. To execute the control routine and generate the reference signals to control the converter while also monitoring the relevant DFIG signals, a dSPACE real-time platform is used.

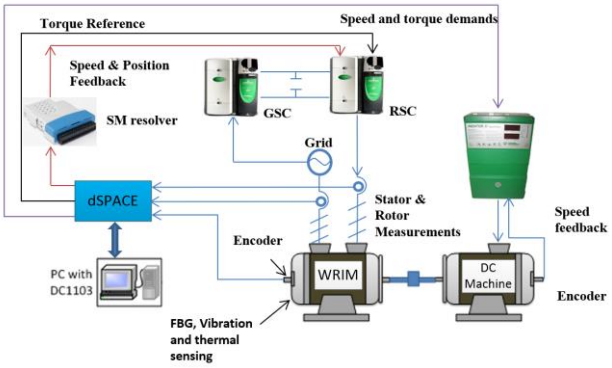

Figure 3-1 Layout of laboratory DFIG test-rig

Two incremental encoders are employed in the system: one is mounted on the rotor shaft of the induction machine to measure its rotor speed and position for real-time SFOC feedback purposes. The other is fixed on the DC machine shaft to provide rotational speed feedback to the DC drive and enable effective control of the DC load motor. A suite of LEM LA 55P/SP1 current and LV 25-600 voltage Hall sensors are fitted to the DFIG test system to sense the relevant electrical signals. To allow analysis of frame vibration signals for research purposes the test DFIG is also instrumented with a commercial Bruel and Kjaer (B&K) PULSE® vibration monitoring platform, including two (B&K) 4394 accelerometers mounted on the generator frame in a 90-degree spatial offset configuration connected to a vibration controller 3560-B-130.

3.3 dSPACE real time platform

The dSPACE 1103 real time platform is employed in test rig to enable implementation and execution of the SFOC. It is a software/hardware platform capable of compiling pre-programmed control routines in Simulink software into hardware control devices to enable development of real-time applications [119]. The user accessible system monitoring and control is provided by Control Desk software integrated with dSPACE. The used dSPACE system has 16 multiplexed analogue to digital (ADC) channels, 4 parallel ADC channels and 8 digital to analogue (DAC) channels are contained in dSPACE controller board. The operating signal range of the channels is -10V~10V DC. In addition, there are 6 digital incremental encoder interface connectors and 1 analogue incremental encoder interface channel capable to be connected with external encoders [120].

The dSPACE platform is employed in the experiments for the following objectives:

- To provide reference signals for the rotor side converter (RSC) to accomplish

SFOC.

- To control the mechanical output of the DC machine (speed and torque) by setting a desired static or dynamic operating profile reference for the DC drive.
- To monitor the system variables during experiments and collect signal information for further investigation.

The laboratory used dSPACE controller board is shown below:

Figure 3-2 dSPACE controller board

3.4 DFIG speed control and acquisition

3.4.1 DC motor control

DC motor is used as the prime mover to simulate the mechanical input of the DFIG test system and its speed and torque controlled for this purpose. The control is performed using a commercial DC drive (CONTROL TECHNIQUES MENTOR II), The characteristics and functions of DC drive control are regulated through a user interface menu allowing the relevant parameters to be set to achieve the desired functionality [121]. The DC drive is illustrated in Figure 3-3.

Figure 3-3 DC drive (MENTOR II)

The DC drive can operate in four distinct operating modes: speed control, torque control, torque control mode with speed override and coiler/uncoiler control mode [121]. The speed control mode is used in this project: a suitable speed reference is this provided to the drive using a dSPACE platform, determined based on the desired test conditions. The maximum torque limit is regulated by appropriately setting the controller current limit, defined by the particular test regime's requirements.

The DC drive operating point references are set remotely through the external reference input channels in this project: analogue references of voltage and current are generated from the dSPACE platform. To this end, the Simulink model in Figure 3-4 is built and compiled. The model is aimed to generate voltage signals (from DAC) as speed and torque limit references for the DC drive. The speed and torque (e.g. current) references are set in two constant blocks, with the actual reference values scaled by max limits with gain blocks to be mapped to the required 0-10Vs input voltage range of the drive, i.e. 10/max limits. The dSPACE scaling blocks (0.1) are necessary since the DAC channel tends to increase the original signal value by ten times [120]. Lastly, the scaled reference signals are sent to DAC blocks so that references can be generated for the DC drive via

the dSPACE DAC channels.

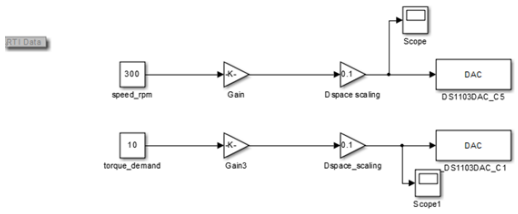

Figure 3-4 Simulink model layout for DC drive control

Since the DC drive requires speed feedback for closed loop speed control operation, an encoder (Hohner, E series, 15V, 1024 pulses per revolution encoder) is fitted to the DC machine to provide the necessary feedback signal.

3.4.2 DFIG rotor position and velocity measurement

To obtain the DFIG rotor speed and position information required for control and monitoring purposes, an encoder (Hengstler, R32, 5V, 1000 pulses per revolution) is installed on the rotor shaft of the wound rotor machine. The signal generated from the encoder is collected by the dSPACE platform by connecting encoder terminals to dSPACE digital incremental encoder interface connector. The following Simulink diagram is employed to obtain rotor speed and position information (provided via dSPACE defined block DS1103ENC_POS_C1).

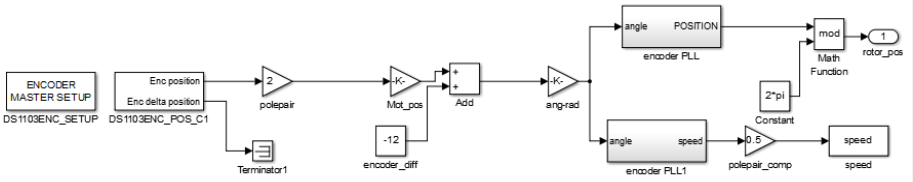

Figure 3-5 Simulink model layout for speed estimation

For the speed and position measurement, the ENCODER MASTER SETUP block must be built to establish the global specifications for channels of encoder interface. The input of dSPACE system is the pulse signal generated from encoder and the Simulink model above and counted in the system, which is the value of Enc Position output. Since the encoder is made by a disk with 1000 lines per revolution, each pulse count represents a 360/1000 degrees angular displacement. The "encoder_diff" block (-12) is the physical difference between the encoder index and the rotor reference frame *d*-axis position in degrees, which will be further discussed in section 3.6.1. The output of the "add" block provides the rotor reference frame *d*-axis position in degrees. Further scaling is provided by the "ang-rad" block to transfer the angular position to radian scale.

A phase locked loop (PLL) is employed to keep the coherence between the input (reference) signal frequency and the output signals via phase comparison. A PLL system generally consists of a phase detector (PD), a loop filter (LF) and a voltage controlled oscillator (VCO) [122]. In this project, the Simulink model for test rig control is executed at a high sampling frequency condition (50000Hz) to meet the requirements of the resolver feedback system, this will be further explained in SM resolver introduction part in section 3.5. Consequently, the available dSPACE platform capacity is not sufficient to process in real-time the relevant data to extract the encoder feedback in such high sample rate condition. To obtain the real time encoder feedback suitable for control purposes, the PLL model in Figure 3-6 is developed. The system input is the rotor position θ_i measured by encoder while its output is the rotational speed of WRIM ω_o and PLL proceed rotor position θ_o. The error signal is worked out as [123]:

$$error = sin\theta_i cos\theta_o - cos\theta_i sin\theta_o = \sin(\theta_i - \theta_o) \tag{3.1}$$

While $\theta_i - \theta_o \approx 0$, the error signal $\sin(\theta_i - \theta_o) \approx 0$ as well. It can hence be assumed that

$\sin(\theta_i - \theta_o) = \theta_i - \theta_o$ [123].

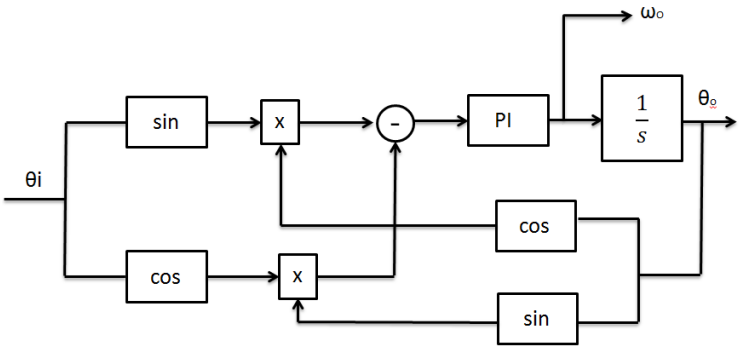

Figure 3-6 Structure of PLL

In this PLL system, the PI controller is behaving as the LF while the integrator is the VCO. The LF determines the dynamic performance of the PLL system; its key parameters are natural frequency (ω_n) and damping ratio (ζ). The calculation of controller parameters (K_p and K_i) is based on the transfer function below [122]

$$\frac{\theta o(s)}{\theta i(s)} = \frac{(K_p+\frac{K_s}{s})\times(\frac{1}{s})}{1+(K_p+\frac{K_s}{s})\times(\frac{1}{s})} \approx \frac{K_i}{s^2+sK_p+K_i} \tag{3.2}$$

In this work the PI controller parameters are set to K_i =685, K_p=60 [9].

3.5 Rotor side current control scheme

The DFIG current and voltage signals are measured via Hall sensors fitted to the test rig. Using these signals, the real-time control program in dSPACE works out the desired references for the rotor side converter so the SFOC scheme can be accomplished.

The DFIG back-to-back converter consists of two industrial CT UNIDRIVE SP-4401 units coupled by a DC link: the rotor side converter (RSC) and the grid side converter (GSC) [45]. The GSC is set to operate in Regen (regenerative) Mode as a sine rectifier

and maintains the dc link voltage. The DC bus set point is 700V in this project, corresponding to 400V rating drive [124]. The SFOC is accomplished on the test DFIG system by manipulating the RSC; while the used industrial converter has a high level of electrical protection and does not allow access to switching: its control capability for drives applications is limited to only standard control schemes and does not offer a readily available capability for execution of DFIG vector control (i.e. SFOC scheme). This posed a challenge to implement the SFOC scheme using the existing pre-set vector control schemes offered by the commercial converter. To overcome this limitation, a dSPACE platform with a commercial SM resolver model is employed to enable proprietary SFOC scheme implementation as described in [118]. In this project, the servo control mode is selected for the RSC converter, which is generally intended for PM motor control [125]. The commercial converter provides 6 kHz switching frequency for the testing DFIG. The control reference frame orientation in the servo mode is that the q axis is aligned with stator current vector [124]. In the ensuing text, this control reference frame is defined as the servo reference frame, which was illustrated in Figure 3-7.

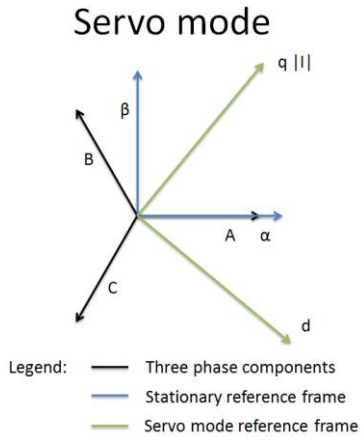

Figure 3-7 Servo mode current vector

However, in DFIG SFOC scheme, the servo reference frame, rotor current vector, has to be aligned with SFOC defined current vector, $\overline{I_r}$, while the vector is defined by SFOC frame d-q axis currents. Since the commercial RSC servo mode was pre-programmed for PM motors, the inherent servo reference frame was aligned with rotor reference frame. As a result, the proper orientation is required for RSC servo controller to implement SFOC with existing facilities, as illustrated on the corresponding phasor diagram in Figure 3-8.

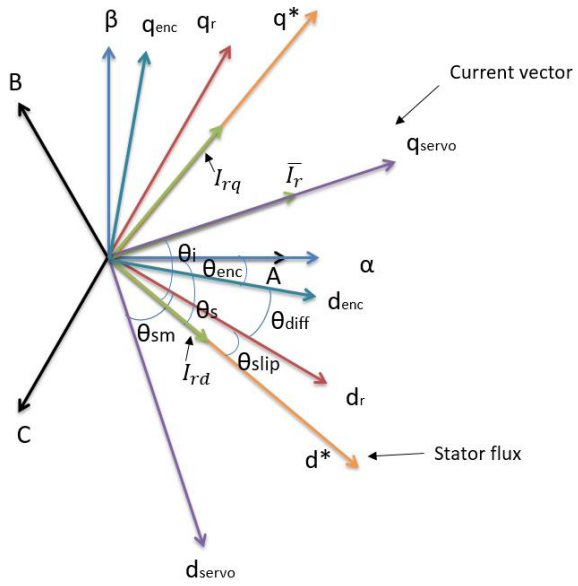

Figure 3-8 Phasor diagram

In Figure 3-8: the estimated rotor current vector, $\overline{I_r}$, is represented in green, as are the desired d-q axis rotor currents aligned with stator flux reference frame; the orange $d^* - q*$ axes and the red d_r –q_r axes denote the stator flux reference frame and the rotor reference frame, respectively. The desired servo reference frame, the q_{servo} axis is aimed to align with SFOC defined current vector $\overline{I_r}$ position, shown in purple. To implement

the DFIG SFOC scheme, the desired angular difference θ_{sm} between rotor reference frame d_r and servo reference frame d_{servo} needs to be provided to the RSC set servo control routine to ensure the SFOC appropriate current and flux orientation [118]. In fact, the sensed SFOC control reference frame angular position is defined by the stator flux position angle (derived from grid supply voltage vector angle -as detailed in section 3.6.2) and the rotor d axis position (derived from encoder position by adding the constant angle difference θ_{diff} between the encoder index axis and the rotor d axis). The θ_i is the angle difference of vector $\overline{I_r}$ (q_{servo}) and stator flux d^*, which can be obtained from $\overline{I_{rd}}$ and $\overline{I_{rq}}$ input. i.e. reference controller current value in SFOC reference frame. The slip angle is obtained from the stator flux position d^* minus that of the rotor position d_r. Therefore the angular reference $\theta_{sm} = \theta_i + \theta_{slip} - \frac{\pi}{2}$ is needed for the RSC to align the servo reference frame q axis with the SFOC defined reference rotor current vector $\overline{I_r}$. More details about the reference frames relationship is provided in the following sections for clarity.

Figure 3-9 back-to-back converter

The challenging part is to obtain the instantaneous angle θ_{sm} and provides the angular position information to the RSC. This is accomplished using an SM Resolver module [45].

A resolver can be regarded as a rotating transformer providing output voltages on a pair of SIN and COS secondary windings. The excitation voltage V_{exc}, provided by the SM-Resolver model, is the carrier signal sent to the primary winding to enable the generation of amplitude-modulated voltage waveforms on the secondary winding that carry positional information [45]. The control scheme to obtain θ_{sm} (θ_{conv} in graph) is presented below:

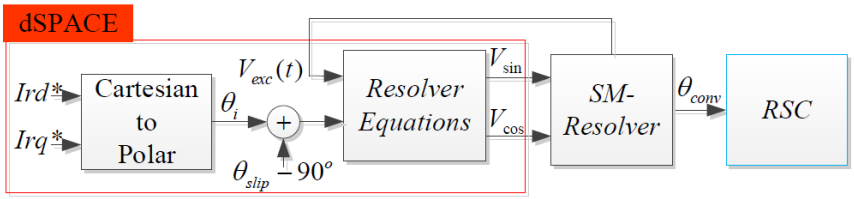

Figure 3-10 Real-time speed and position control scheme [126]

An emulated resolver output of the required angular reference for RSC to enable alignment with the SFOC reference frame is used and fed to the SM resolver module; the output sine V_{sin} and cosine V_{cos} signals are created in dSPACE. V_{sin} and V_{cos} are obtained from V_{exc} and θ_{sm} (i.e. $\theta_{sm} = \theta_i + \theta_{slip} - \frac{\pi}{2}$) as shown in (3.8) and generated from dSPACE: [126] [127]

$$V_{sin} = gV_{exc}\sin(\theta_{conv}(t))\sin(\omega_c t) \tag{3.3}$$

$$V_{cos} = gV_{exc}\cos(\theta_{conv}(t))\sin(\omega_c t) \tag{3.4}$$

where: g is the resolver turns ratio, V_{exc} and ω_c are the magnitude and angular frequency of the excitation signal, respectively. In this case, the resolver turns ratio is fixed as 2:1 and the excitation signal magnitude is set as 4 V_{rms} to ensure appropriate speed and position feedback from the SM Resolver model [126]. The excitation signal generated from the SM Resolver is configured at 6 kHz [45]. The V_{sin} and V_{cos} signals are sent from dSPACE DAC channel to the SM Resolver and V_{exc} signal is acquired from the SM

Resolver by the dSPACE ADC channel. The sampling frequency for the overall control model must be chosen appropriately, as a low sample frequency choice will lead to signal distortion while the dSPACE platform cannot execute real-time calculations for an excessively high choice of frequency. In this study, 50000Hz issued for the sampling frequency.

Using the position feedback provided through the emulated SM Resolver module, the DFIG rotor current control is established by the RSC, as illustrated in Figure 3-11:

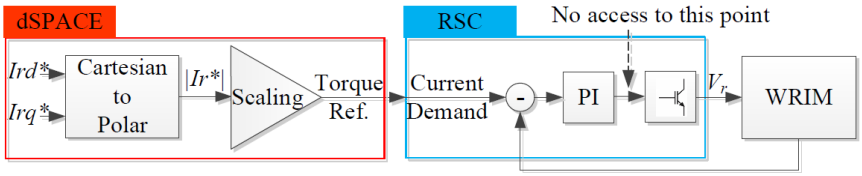

Figure 3-11 Rotor current magnitude control [126]

The magnitude of the rotor current vector is obtained from reference rotor current set I_{rd}^* and I_{rq}^*, which is defined as 'Torque reference' variable in the servo control mode setup on the commercial drive. The scaling factor here is to work out the reference for rotor current magnitude from dSPACE hence provides reference to RSC.

$$magnitude\ scaling = \frac{|I_r^*|}{rated\ rotor\ current} = \frac{|I_r^*|}{56A} \tag{3.5}$$

While this approach enables the establishment of a functional SFOC scheme some operative limitations remain: the cross coupling and effects are not catered for. Due to the limitation of commercial RSC units' accessibility, there is no access allowed to PI controller output in RSC [126]. As a consequence, higher gains in PI controller are required to compensate the disturbance, i.e. the feed forward term [34]. K_p and K_i were set as 34 $VA^{-1}S^{-1}$and $1VA^{-1}$, respectively, in previous published work [118] and this PhD project.

3.6 Synchronisation with the GRID

One of the key objectives to facilitate further research in this project is to enable the test DFIG to operate in SFOC control and in grid connected conditions. Recalling Figure 3.1, the DFIG stator and the grid must not be connected until the electrical potential between them is zero, i.e. their voltage magnitude, frequency and phase have to be as close to identical as possible before synchronisation is attempted. To enable this, a set of three synchronising lamps and a digital oscilloscope in Figure 3-12 are deployed to indicate and monitor the potential difference level between the DFIG stator winding and the grid.

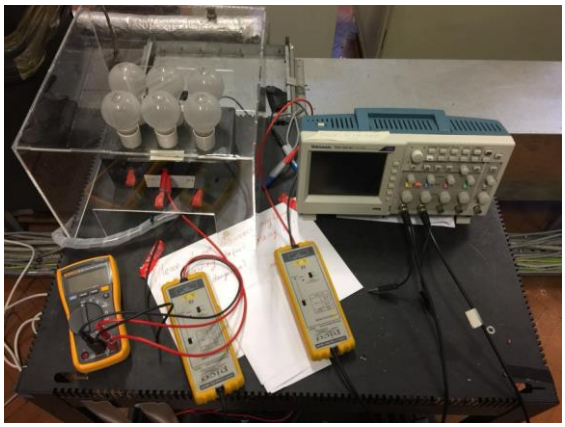

Figure 3-12 Stator and grid synchronisation tools

In the following section, the practical procedures of DFIG synchronisation and enabling SFOC on the test system are described.

3.6.1 Encoder initial position estimation

To accomplish the stator flux oriented control, it is essential to align the rotor current components I_{dr} and I_{qr} with the stator flux reference frame. The ideal stator flux position could be obtained from grid voltage, however the reference rotor winding position (d-axis

of the rotor reference frame) cannot be estimated directly. Therefore, an encoder is deployed as a reference to track the rotor position. The incremental encoder inherently measures only the relative movement of the rotor shaft but can also observe the rotor absolute position if a reference signal is provided, as illustrated in Figure 3-13. To obtain the rotor winding position from the encoder signal, the angle θ should be identified, which represents the rotor d axis position with reference to encoder index pulse. The actual position of the encoder readings is defined by the location of its index pulse, and thus by recoding the encoder outputs from Control Desk, the encoder's absolute angular position can be obtained. Since the rotor coil is rotating at the same speed as the encoder, its physical position can be estimated by referring to encoder index position and offsetting it by θ.

To estimate angle θ the following procedure was followed:

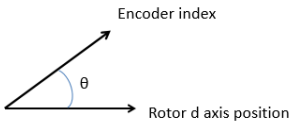

Figure 3-13 Encoder position and rotor position

a. Disconnect the machine rotor winding from the rotor side converter and the stator winding from the grid. Connect DC power supply to the rotor side windings as shown in Figure 3-14; keep the stator windings open circuited.

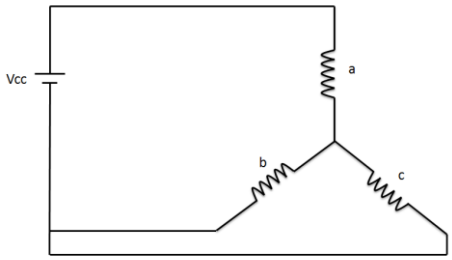

Figure 3-14 Rotor side connections for testing

b. Rotate the WRIM rotor using the in-line coupled DC motor at constant speed. To identify rotor *d*-axis position, the back e.m.f. induced in a stator phase winding by rotational DC current field on the rotor was captured. The identification of rotor flux and reference position is explained in step c.

c. Since the back e.m.f is lagging the magnetic flux by 90 degrees, the rotor flux position (reference rotor position) could be captured from induced voltage vector's angle on stator side. With the help of voltage sensor and dSPACE platform, the stator voltage vector angle are acquired by following procedure:

The three-phase stator voltage was converted by Clark's transform then the voltage vector was identified in terms of polar coordinate. After subtracting the voltage vector angle with 90 degrees, the rotational flux angle position can be obtained, assuming the stator resistive voltage drop is neglected. For a more convenient presentation for application in future steps, the estimated angle is converted to a periodic waveform of 2π.

d. The encoder position can be gathered from dSPACE Control Desk as described in previous section, and is for convenience of manipulation also converted to a periodic function of 2π.

e. Subtract the waveforms obtained in step **c** and step **d**: a resultant square wave is generated since the encoder and rotor are rotating at the same speed. The angular difference between the encoder index position and the d-axis of the rotor reference frame can now be obtained by comparing the two signals to extract their angular offset.

The described procedure is illustrated in a flowchart in Figure 3-15 for further clarity.

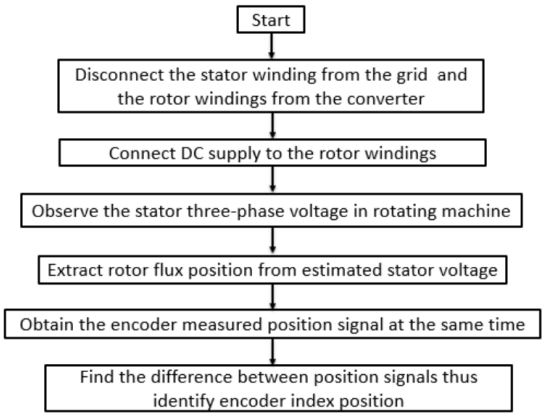

Figure 3-15 Initial encoder position identification process flowchart

3.6.2 Stator flux oriented control implementation and verification

After identifying the angular difference between d-axis of the rotor reference frame and the encoder index position, the rotor position can readily be observed from the encoder signal. The steps to implement DFIG SFOC are detailed in the following text, along with the validation tests of the RSC generated current.

The main requirement initially is to obtain the stator flux reference frame position for control purposes. This could be extracted from the grid voltage signal since stator voltage will be synchronised with that of the grid. The block diagram of overall controlling scheme is shown in Figure 3-16. A set of voltage sensors are employed to measure the

grid side three phase voltages V_{ga}, V_{gb} and V_{gc}. Proceeded by Clark's transformation and Cartesian to polar transformation, the grid (and stator) voltage vector angle is obtained. As the flux vector is 90 degrees lagging to this, the reference stator flux position for the system can be captured, which is the angle θ_s in the phasor diagram shown in Figure 3-8. This holds valid with the assumption that the stator resistance is sufficiently small for its effects to be neglected [34]. By subtracting the rotor reference frame d-axis angular position, the angular difference between rotor and reference stator flux can be concluded as θ_{slip}. As explained before, the angular input for the SM resolver is set as $\theta_{sm} = \theta_i + \theta_{slip} - \frac{\pi}{2}$ to align the rotor reference frame q axis with the SFOC defined rotor current vector $\bar{I_r}$ The rotor current magnitude and θ_i are obtained from the adjustable $i_{dr}^*$and i_{qr}^* reference values by following equations:

$$|\bar{I_r}| = \sqrt{{i_{dr}^*}^2 + {i_{qr}^*}^2} \tag{3.6}$$

$$phase\ angle = \tan^{-1}\frac{i_{qr}^*}{i_{dr}^*} \tag{3.7}$$

To verify the stator flux oriented control implementation and allow synchronisation, another set of voltage sensors are fitted on the stator side to monitor the stator three phase voltage. Following the procedure describer earlier in this chapter the actual stator flux position can be obtained as θ_s^*. After the rotor current is processed by Clark's and Park's transformation, the rotor current in stator flux reference frame I_{rd} and I_{rq} can be measured. If the measured values (I_{rd} and I_{rq}) are identical to the reference values ($i_{dr}^*$and i_{qr}^*), it can be concluded that the DFIG stator flux oriented control is accomplished and appropriate control of rotor current established.

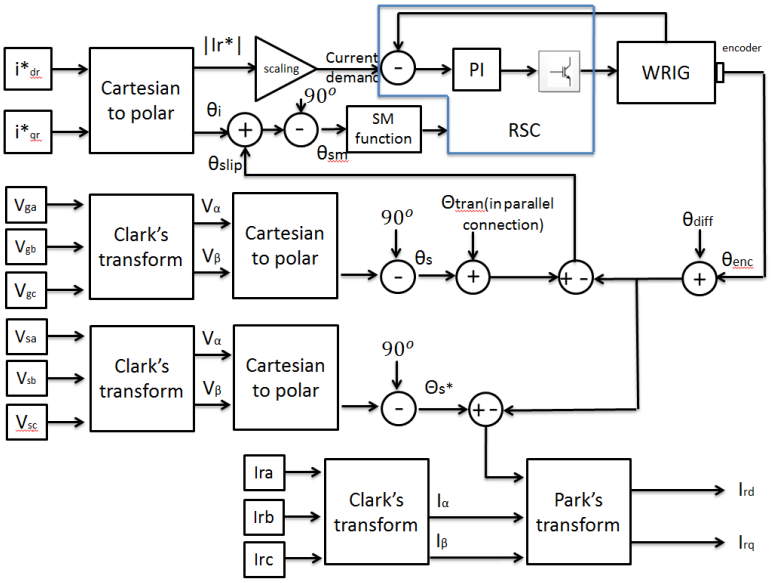

Figure 3-16 Overall control scheme

An illustrative test was undertaken to verify the built control scheme. In this case, the reference currents were set as $I_{dr}^{*} = 15.47A$ and $I_{qr}^{*} = 3.42A$. The generator speed is 1400 rpm. Figure 3-17 provides the corresponding rotor current measurements (I_{dr}, I_{qr} and three phase rotor current, the numerical values in the figures are the instantaneous value of the signal while taking snapshots) from dSPACE. The three phase currents are recorded from dSPACE ADC input channels directly, which are connected with current sensors in machine rotor side. I_{dr} and I_{qr} were worked out based on the pre-programmed algorithm as Figure 3-16 presented before. As the original signals in the dSPACE plotter were very noisy, to get a better view of signals, the measurements shown below were averaged for clarity (mean of every 1377 points). As the figures show, the mean values of generated rotor currents are in very good agreement with the reference rotor current settings, indicating that the SFOC of rotor current was successfully implemented based

on the presented methodology.

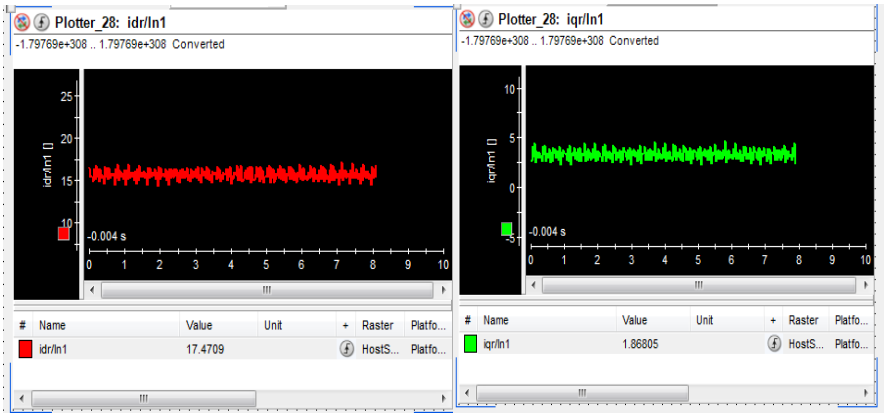

(a) Idr measured current (b) Iqr measured current

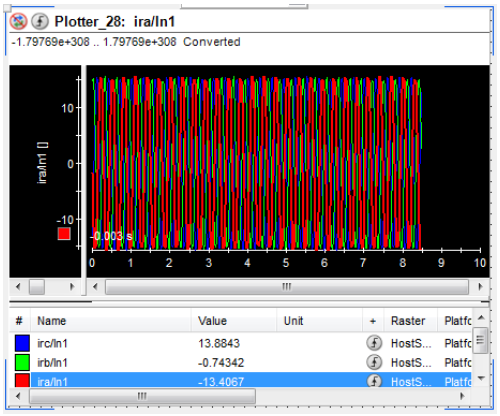

(c) Three phase rotor current

Figure 3-17 Rotor current measured from dSPACE

3.6.3 Synchronisation of a DFIG with the grid supply

After implementing the SFOC scheme, the next step is to synchronise the DFIG stator with the grid. With the help of two differential probes and an oscilloscope, the grid side

voltage and stator side voltage can be observed while testing. The following steps were performed to run up the test DFIG and accomplish its synchronisation.

First, start up the DC motor until reaching constant operating speed for DFIG. The rotor side current (i_{dr}^* and i_{qr}^*) is kept zero during shaft fun up. Then adjust the values of $i_{dr}^*$and i_{qr}^* from dSPACE platform to manipulate the stator voltage magnitude and phase as mentioned in last section. The voltage frequency is inherently synchronised through application of the SFOC scheme. The remaining part is to regulate the magnitude and phase of the stator voltage to match that of the grid. To this end, the value of $|\bar{I}_r|$ is manipulated until the stator side line voltage reaches a value of 415Vrms. The stator voltage phase angle (θ_i) was adjusted by keeping the $|\bar{I}_r|$ value constant and modifying the value of $i_{dr}^*$and i_{qr}^* (via equations 3.6-7). The synchronisation lamps in Figure 3-12 and an oscilloscope to synchronously monitor the stator open circuit voltage and that of the grid were used to assist in process of synchronisation. The typical measured stator and grid voltage signals during synchronisation are illustrated in Figure 3-18.

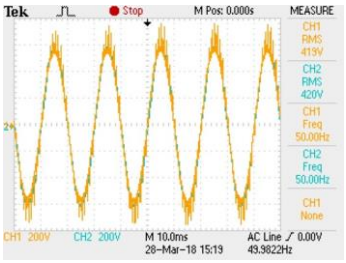

Figure 3-18 Stator voltage and grid voltage before closing the synchronisation contactor

In Figure 3-18, the channel one signal is the open circuited stator line voltage while the channel two signal is the grid line voltage; these are seen to be of very close magnitudes and of matching frequency and phase. The measured stator voltage can be seen to exhibit

considerable ripple arising from spectral noise due to various harmonic and interharmonic components inherent to the DFIG system. By closing the circuit breaker between the grid and stator terminals the DFIG is synchronised with the grid: the measured stator voltage after synchronisation is shown in Figure 3-19. At this point, the DFIG system reference frame is oriented with stator flux and has been synchronised with the grid.

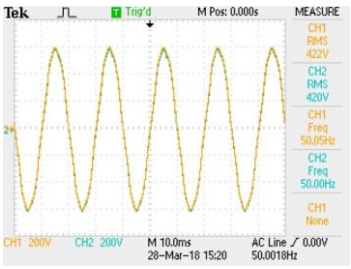

Figure 3-19 Stator voltage and grid voltage after switching on circuit breaker

3.7 SFOC close loop control implementation

After accomplishing the DFIG synchronisation with the grid with the reference frame aligned with stator flux, the power loop control is introduced to enable the close loop decoupled control of real power and reactive power. Based on the previous existing current loop control scheme in Figure 3-16, an outer loop is added to the system to provide the reference rotor current I_{dr}^{*} and I_{qr}^{*} into the current control system. The relationship between rotor current and stator power in SFOC are:

$$P_s = -\widehat{V_g}\frac{L_m}{L_s}i_{qr} \tag{3.8}$$

$$Q_S = \frac{\widehat{V_g}^2}{\omega_s L_s} - \widehat{V_g}\frac{L_m}{L_s}i_{dr} \tag{3.9}$$

Referring to the equations above, if a SFOC scheme is employed on DFIG, the active power and reactive power of stator side can be decoupled and linearly controlled by

regulating I_{qr}^{*} and I_{dr}^{*}, respectively. To make the stator voltage synchronized with the grid supply, the initial $P_s^*$and Q_s^* values corresponding initial value i_{qr}^{*} and i_{dr}^{*} (identified in last section) needs setting for the outer loop at the beginning of the test.

In theory, the reference $I_{qr}^{*}$and I_{dr}^{*}can be directly calculated using equations above based on the active and reactive power demand settings. However, the reality of a practical system is not as straight forward as the equation describes. The grid voltage is not as stiff as it is assumed to be in the real system [128]. Besides, the existing resistance inside the machine is ignored, and as a result, the reference I_{dr}^{*} and I_{qr}^{*} calculated with equation (3.8) and (3.9) are slightly different from the real references needed in the system [34]. Furthermore, the parameter values used in the equations alter due to temperature and saturation level variation hence affecting the reference current calculation as well [129]. To minimise these effects, the linear power calculations to extract inner controller reference current values are replaced by a simplified outer control loop design containing PI controller in this project, as illustrated in Figure 3-20. The active power and reactive power references are controlled via two constant blocks at left side. Since the reference controller loop signals are the output of outer control loops, these signals are highly effected by environmental noise from outer loop measurements and might cause instability due to strong correlation of the signals in both loops. As a consequence, feedback smoothing low pass filters with a 5Hz cut-off frequency are employed to avoid such effects [130]. The flited reference signals are sent to the inner current loops for further processing.

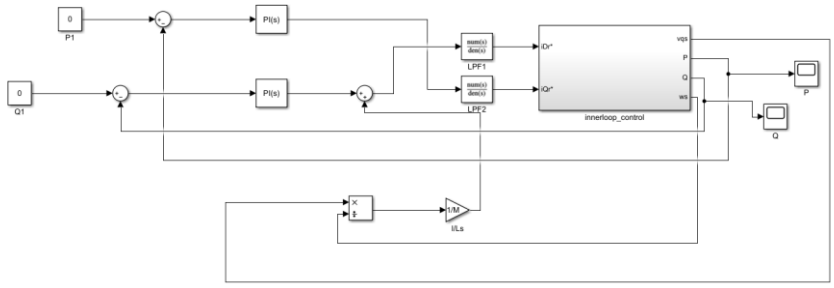

Figure 3-20 Simulink model for outer loop control

The implemented SFOC performance was evaluated by two different tests illustrated in Figure 3-21 and Figure 3-22 below.

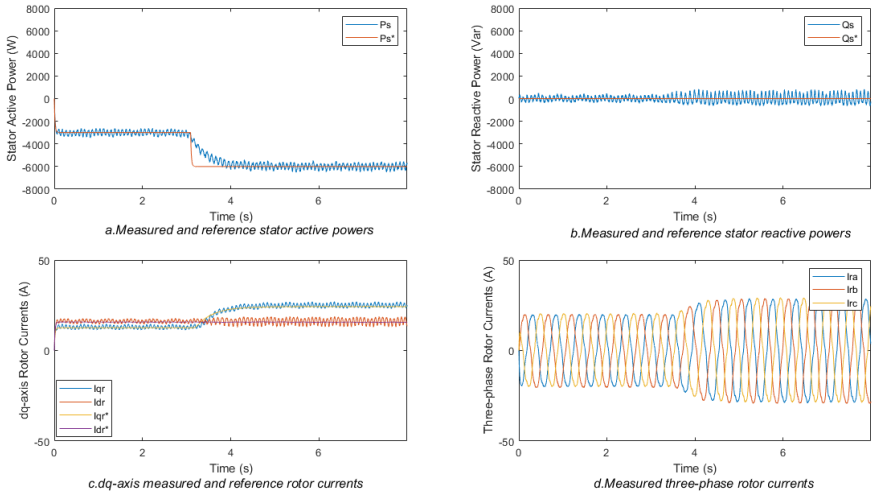

Figure 3-21 Stator active power step change implementation

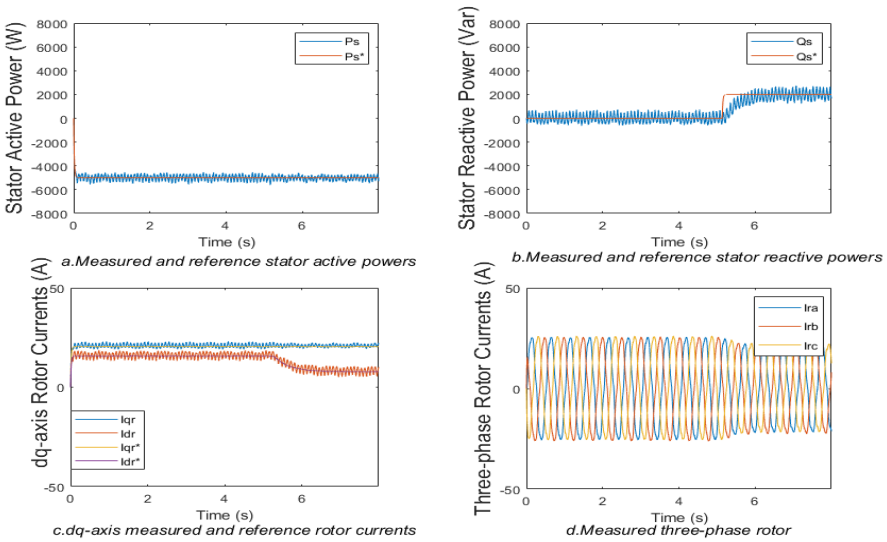

Figure 3-22 Stator reactive power step change implementation

The machine rotational speeds in both cases were 1560 rpm. In Figure 3-21, a step change of active power demand P_s^* was introduced at 3 seconds, varying from -3kW to -6kW, while the reactive power demand Q_s^* was kept unchanged. The corresponding active power P_s is seen to have followed the set reference, doubling with P^*change with a response delay. As generally expected, it could be clearly observed that the controller signal I_{qr} as well as its reference signal I_{qr}^* doubled at 3 second whilst I_{dr} and I_{dr}^* remained the same.

Similarly, in Figure 3-22, reactive power demand was set to change at 5s from 0 Var to 2kVar, whilst the active power demand was kept at a constant -5kW. d axis controller related signals responded to the reactive power demand change, while those of the q axis controller remained the same. The illustrative results shown in Figure 3-21 and Figure 3-22 show that the test DFIG active and reactive power has been achieved through

decoupled control of I_{qr} and I_{dr} respectively, thus validating that the SFOC is successfully employed.

3.8 Conclusion

The DFIG test system structure, the implementation of its SFOC scheme utilizing commercial converters and it experimental validation were reported in this chapter. Firstly, an overview of the overall DFIG system and its sensing scheme was given. Then, a brief introduction of the dSPACE real time platform was provided. The real time control schemes utilized for the laboratory DC load motor and the DFIG rotor side converter were then detailed and the DFIG synchronization procedure explained Finally, the SFOC outer loop implementation method was presented along with its experimental validation. The control scheme employed in this chapter has been applied in DFIG harmonic investigation and validation in this Ph.D project. The resulting test system enabled a range of experimental activities to be undertaken that were key to this research project.

Chapter 4 DFIG harmonic model and its implementation

4.1 Introduction

The key purpose of this project is to establish a suitable dynamic model that can enable the study on double fed induction generator (DFIG) condition monitoring. To enable higher order MMF harmonic effect analysis in DFIG signals, a wound rotor induction machine (WRIM) harmonic model is integrated with a standard stator flux oriented control (SFOC) scheme two-axis (dq) controller model. The resulting DFIG dynamic model is implemented in MATLAB Simulink environment.

In this Chapter, firstly, the mathematical harmonic WRIM model is introduced and a detailed procedure of its implementation demonstrated. The SFOC controller model, consisting of cascade control loops, is then developed and integrated with the machine model to provide a harmonic DFIG model. A model study is undertaken to demonstrate

how outer loop active power and reactive power decoupled controlled by inner loop controller current signals. Power demand step changes are introduced in the outer loop for model testing to observe the controller signal variation. The analytical expression that define the possible spectral content of DFIG electrical signals are then summarised and cross correlated with the established model's predicted signals spectra in sub-synchronous speed and super-synchronous operating conditions. Finally, a case study is provided to explore the feasibility of sensorless speed estimation based on utilizing DFIG signals' spectral contents.

4.2 Induction machine harmonic model and its implementation

4.2.1 Mathematic modelling of harmonic induction motor

Higher order MMF harmonic effects in WRIM model are catered for through evaluating harmonic coupling between any two stator and /or rotor windings. Considering the MMF harmonic effects while calculating the windings self and mutual inductances, the higher order MMF harmonic effects in electrical signals can be represented in the standard electrical and mechanical machine equations [27]. A more detailed explanation of the process of harmonic self and mutual inductance calculation is provided in Appendix B.

The induction machine mathematical model is constructed with following equations in matrix form: [27, 131]

$$[V] = [R][I] + \frac{d[\psi]}{dt} \tag{4.1}$$

$$[\psi] = [L][I] \tag{4.2}$$

$$T_e - T_{load} = J\frac{d\omega_{mech}}{dt} \tag{4.3}$$

$$\frac{d\theta_{mech}}{dt} = \omega_{mech} \tag{4.4}$$

$$T_e = \frac{1}{2}[I]^T \frac{d[L]}{dt}[I] \tag{4.5}$$

where:

$[V]$ =Voltage vector $[V]$

$[I]$ =Current vector $[A]$

$[\psi]$ =Flux linkage vector $[Wb]$

$[R]$ =Resistance matrix $[\Omega]$

$[L]$ =Inductance matrix $[H]$

T_e =Electromagnetic torque $[N.m]$

T_{load} =Load torque $[N.m]$

J = Rotor inertia $[kg.m^2]$

ω_{mech} =Rotor mechanical speed $[rad/s]$

θ_{mech} =Rotor mechanical position $[rad]$

The complete time domain equations are demonstrated in Appendix B.1

The machine parameters (J, R and leakage inductance L_l) can be identified from a given machine data sheet (see Appendix A). The expanded form of equation (4.1) and (4.2) could be written as:

$$\begin{bmatrix} V_s \\ V_r \end{bmatrix} = \begin{bmatrix} [R_s] & 0 \\ 0 & [R_r] \end{bmatrix} \begin{bmatrix} [I_s] \\ [I_r] \end{bmatrix} + \frac{d}{dt} [\begin{bmatrix} [\psi_s] \\ [\psi_r] \end{bmatrix} \tag{4.6}$$

$$\begin{bmatrix} [\psi_s] \\ [\psi_r] \end{bmatrix} = \begin{bmatrix} [L_{ss}] & [L_{sr}] \\ [L_{rs}] & [L_{rr}] \end{bmatrix} [\begin{bmatrix} [I_s] \\ [I_r] \end{bmatrix} \tag{4.7}$$

where:

$[L_{ss}]$ = stator self-inductance matrix $[H]$

$[L_{rr}]$ = rotor self-inductance matrix $[H]$

$[L_{sr}]$& $[L_{rs}]$= Mutual inductance between stator and rotor $[H]$

Besides, the subscripts 's' and 'r' represent stator and rotor correspondingly.

To solve the system of equations in (4.1)-(4.7), it is necessary to obtain the values of the inductance matrix parameters. There are two types of inductances that need calculating for this: one is the self-inductance between any two stator windings or any two rotor windings (i.e. the windings that are stationary with respect to each other), and the other is the mutual inductance between a stator and a rotor winding (i.e. the windings whose position with respect to each other is time varying). A brief calculating procedure for these is illustrated below, with detailed information on coupling impedance evaluation approach provided in Appendix B. Following assumptions are pre-defined here: [132] [27]

- The stator and rotor are modelled as smooth concentric cylinders and made of infinitely permeable iron.
- The stator and rotor windings are regarded as point conductors distributed on stator and rotor surface.
- The air-gap length is considered to be small enough to neglect curvature effects thus the flux across the gap is in straight radial lines.

For any two windings A and B, both either on the stator or on the rotor, the complex harmonic inductance can be calculated as: [27]

$$L_{AB} = \frac{w\pi d\mu_0}{g}\sum_{v=-\infty}^{v=+\infty}\frac{\overline{C_A^k}\dot{C_B^k}}{k^2} \tag{4.8}$$

where:

d = Mean air-gap diameter $[m]$

g= mechanical airgap length $[m]$

μ_0= permeability of vacuum $[H.m^{-1}]$

w = machine length $[m]$

v= space harmonic integer number v= 1,2,3…..

k= wave number of v^{th} order space harmonic

$\overline{C_A^k}$ = winding A v^{th} harmonic complex Fourier coefficient of conductor distribution function $[turns/m]$

$\overline{\dot{C}_B^k}$ = winding B v^{th} harmonic complex conjugate of Fourier coefficient of conductor distribution function $[turns/m]$

It is important to note that (4.8) can also be applied to calculate the harmonic self-inductance of a given winding, located either on the stator or the rotor. An arbitrary winding A v^{th} harmonic Fourier coefficient of conductor distribution function $\overline{C_A^k}$ can be obtained from: [27] The detailed derivation of this expression is given in Appendix B2

Commented [YW1]: Referred to Appendix B2

$$\overline{C_n^k} = -j\frac{2N_n}{\pi d}k_{bv}k_{pv}e^{jky_n} \tag{4.9}$$

where:

N_n= Conductor number in each slot

k_{bv} = v^{th} harmonic slot mouth width factor

k_{pv}= v^{th} harmonic coil pitch factor

y_n = Position centre of an n^{th} coil in a winding

For clarity, a more detailed procedure of calculating conductor distribution function

utilizing complex conductor distribution function approach is demonstrated in Appendix B.

The mutual inductance between a stator winding C and a rotor winding D can be calculated by the following equation:

$$L_{CD} = \frac{w\pi d\mu_0}{g} \sum_{v=-\infty}^{v=+\infty} \frac{\overline{c_A^k} \dot{c}_B^{\dot{k}}}{k^2} e^{-jk\beta(t)} \tag{4.10}$$

where:

$\beta(t)$= Rotor displacement from an arbitrary reference position $[m]$

With the harmonic inductance matrix obtained from equations (4.8) and (4.10), the higher order harmonic induction machine mathematic model can now be implemented and resolved for a given set of operating conditions and machine design parameters. The inductance calculation example is given in Appendix B4. Please note that some assumptions of machine characteristics such as skew and airgap coefficients are listed in Appendix B3.

Commented [YW2]: References to appendix B3 and B4 are added here.

4.2.2 Harmonic model implementation in Simulink

In this PhD project, the harmonic WRIM model introduced in the last section was implemented in the Simulink environment. The SFOC controller model will linked to the WRIM model to complete the DFIG harmonic model implementation. Simulink is chosen as it provide a versatile and robust software platform to implement the established dynamic model and resolve it to study the relevant electromagnetic and mechanical effects as well as those of machine faults of interests. Further investigations of DFIG shaft misalignment signature and controller embedded sensorless speed estimation are based on the signals' spectra analysis using the higher order DFIG harmonic model

implemented here.

The overall harmonic machine model in Simulink is illustrated in Figure 4-1 below. The induction model assumes that the stator is connected to a balanced 240V, 50Hz power supply in a pre-defined voltage input block. The harmonic inductance values are calculated via a MATLAB user defined function executing equations (4.8)-(4.10) for a given rotor position: the input of the block (theta) is provided by the subsystem "rotor speed and position calculation" to provide the rotor position for mutual inductance calculation. The motor parameters like wind pitch and slot positions are pre-defined in the function block. To meet the requirement of usage, the outputs of the harmonic inductance calculation block are inverse inductance matrix and differential inductance matrix calculated based on the inductance matrix, which will be employed further for current and electromagnetic torque calculation, respectively.

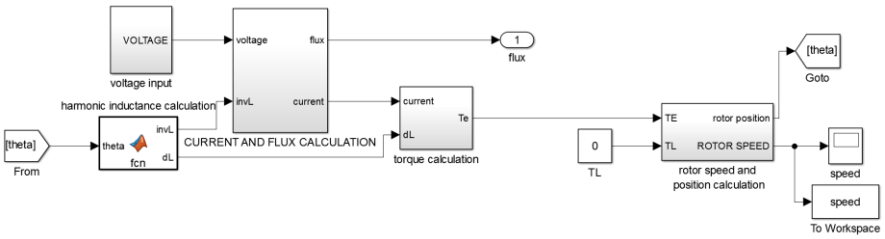

Figure 4-1 Harmonic induction machine model in Simulink

The inner diagram of the current and the flux calculation block is shown in Figure 4-2, corresponding to equations (4.1-4.2), to solve the motor current from voltage input. The block diagram below is constructed in forms of following equations:

$$[\psi] = \int_0^t [V] - [R][I]dt \tag{4.11}$$

$$[\mathrm{I}] = \frac{[\psi]}{[L]} \tag{4.12}$$

From the calculated currents the machine electromagnetic torque can be obtained based on equation (4.5). This is demonstrated in Figure 4-3, where the differential inductance matrix (dL) is necessary for (4.5) calculation. It is connected to the output of MATLAB user defined function in Figure 4-1. As explained before, the differential inductance matrix is worked out based on the calculated inductance matrix.

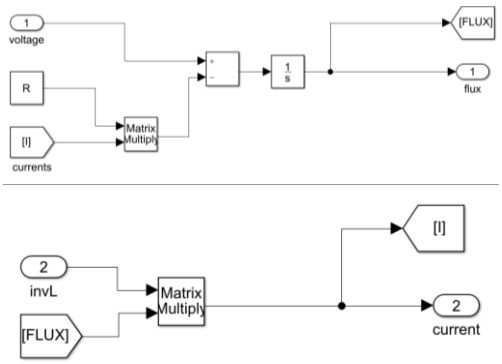

Figure 4-2 Flux and current calculation block components

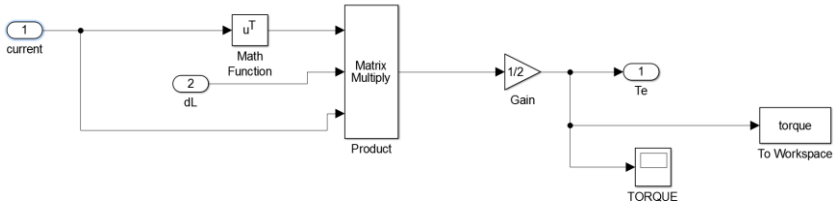

Figure 4-3 Electromagnetic torque calculation

Finally, using the obtained electromagnetic torque value, the rotor speed and position can be worked out from equations (4.3-4.4). The relevant Simulink block diagram is listed in Figure 4-4

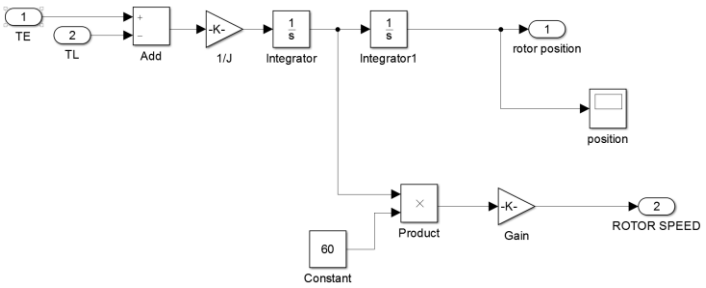

Figure 4-4 Rotor speed and position calculation

The calculated rotor speed from equation (4.3) and (4.4) is in the unit of rad/sec, and for a more convenient observation and future implementation, the following translation is utilized to change speed units from rad/sec to revolutions/minute (rpm).

$$\omega(revolutions/minute) = \omega(rads/\text{second}) \times 60/2\pi \tag{4.13}$$

The WRIM harmonic model has been successfully implemented in Simulink environment.

4.3 DFIG SFOC scheme

In wind power generation systems, the commonly employed DFIG vector control scheme is the stator flux oriented control (SFOC) [28] [133], due to its high performance control capability and the ability of decoupled active and reactive control [34]. Consequently, this control scheme was used to develop a harmonic DFIG model by merging the harmonic WRIM model and that of SFOC. The SFOC is a cascaded closed loop control scheme consisting of the power regulation in outer loops and current regulation in the inner loops, as well as orientation angle feedback, based on these, the rotor side converter (RSC)can provide modulated voltage to the WRIM. The illustration is demonstrated in Figure 4-5.

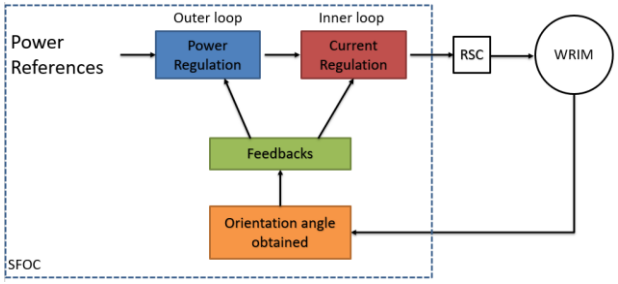

Figure 4-5 Block diagram of SFOC scheme

A typical two-axis (dq) synchronous rotating reference frame has been employed for SFOC, where the control frame d- axis is aligned with the stator flux. By defining decoupled rotor d- and q- axis components, the stator active power and reactive power can be independently controlled using d and q axis current controllers. Thus, the output power factor of wind turbine can be controlled to meet the farm operator/grid demand. The flow chart of SFOC scheme employed in the harmonic model is illustrated in Figure 4-6

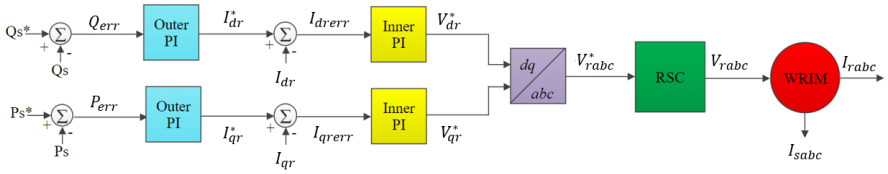

Figure 4-6 DFIG rotor side control flow chart

The active power P_s and reactive power Q_s are regulated in the outer loop, providing the reference controller currents I_{qr}^* and $I_{dr}^*$for the inner loops to maintain the actual power identical to reference power demand. Similarly, inner loop controllers are responsible for regulating the dq-axis rotor voltage. Processing the resulting voltage output reference with an inverse Clark's transform and Park's transform, the obtained three phase rotor voltage V_{rabc}^* can be fed into the harmonic WRIM model as rotor windings supply to

enable the emulation of a harmonic DFIG model; this in essence represents the DFIG rotor side converter (RSC) as an averaged model, neglecting any converter switching effects for the purpose of this study.

The bandwidths of outer loops and inner loops have to be appropriately chosen. Typically, the inner loops have to be 4-10 times faster than the outer loops to get accurate implementation in the outer loop [45]. In this PhD project, the inner loops are set as approximately 10 times faster than inner loops. The parameters of PI controllers utilized in this project are listed in Table 4-1; these provide the time constant of 0.54s in outer loops and 0.005s in the inner loop [118] [45].

Table 4-1 Tuning parameters for cascade loop

	K_i	K_p
Inner loop	0.09	0
Outer loop	34	1

In the stator flux oriented reference frame, the whole stator flux is aligned with d- axis while no flux component exists in q- axis. The relation between current and flux in corresponding axes are illustrated below: [28]

$$I_{ds}L_s + I_{dr}L_m = \Psi_s \tag{4.14}$$

$$I_{qs}L_s + I_{qr}L_m = 0 \tag{4.15}$$

where I_{ds} and I_{qs} are the stator current (in rms) component in d- and q- axis respectively, I_{dr} and I_{qr} are rotor d- axis and q- axis current component correspondingly, L_s is the stator self-inductance and L_m is the mutual inductance. Here, the inductance used here are in dq reference frame, which typically is a constant but not a harmonic value, to simplify the tuning process.

According to the equations above, the dq axis stator currents can be expressed as:

$$I_{ds} = \frac{\Psi_s}{L_s} - \frac{L_m}{L_s} I_{dr} \tag{4.16}$$

$$I_{qs} = -\frac{L_m}{L_s} I_{qr} \tag{4.17}$$

Since the stator flux is proportional to the grid voltage $\widehat{V_g}$ (in RMS), and neglecting stator resistance [28] we can write that.

$$V_{ds} = 0 \tag{4.18}$$

$$V_{qs} = \widehat{V_g} \approx \omega_e \Psi_s \tag{4.19}$$

where ω_e is the supply angular frequency ($\omega_e = 2\pi f_e$) $[rads]$ and f_e is the supply frequency $[Hz]$. V_{ds} and V_{qs} are RMS value of dq reference frame stator voltage.

With the control reference frame direct axis aligned with the stator flux, the stator active power and reactive power (in RMS) can be written as shown in equations (4.20-4.21) [28]. Here, a power invariant Clark's transform is employed.

$$P_s = \left(V_{ds} I_{ds} + V_{qs} I_{qs}\right) = V_{qs} I_{qs} \tag{4.20}$$

$$Q_s = \left(V_{qs} I_{ds} - V_{ds} I_{qs}\right) = V_{qs} I_{ds} \tag{4.21}$$

Substituting equations (4.16-4.19) into equations (4.20-4.21), the following equations are derived: [28]

$$P_s = -\widehat{V_g} \frac{L_m}{L_s} I_{qr} \tag{4.22}$$

$$Q_S = \frac{\widehat{V_g}^2}{\omega_e L_s} - \widehat{V_g} \frac{L_m}{L_s} I_{dr} \tag{4.23}$$

The equations above indicate that the stator active power and reactive power control can be decoupled via rotor current I_{qr} and I_{dr} respectively in the stator flux orientated reference frame – this is the essence of DFIG SFOC schemes.

4.3.1 Stator flux angle estimation

To implement SFOC in a DFIG system, the *d*- axis of the reference frame is set to align with the stator flux to enable decoupled control of stator active power and reactive power. As a result, the stator flux position capture is essential. There are several approaches listed in the literature to obtain the stator flux position, discussed in [34]. The approach applied in this work was selected due to its relatively straightforward implementation and requiring only the knowledge of the three phase stator voltage signal. The process is to capture the stator voltage vector position θ_v; the stator flux position is then secured since the flux vector is lagging 90 degrees behind that of voltage, assuming stator resistance can be neglected as is standard [28] [34]. The phasor diagram is illustrated in Figure 4-7.

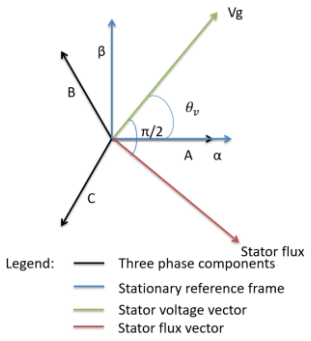

Figure 4-7 Stator voltage vector and flux position illustration.

The α axis of stationary reference frame (in blue) is aligned with a phase winding (in black). The stator flux (in red) is 90 degrees lagging the stator voltage vector (in green). The stationary reference frame $V_{\alpha\beta}$ is obtained by performing Clark's transform on the three phase stator voltage signal. The stator flux position measurement is then carried out with following Simulink block diagram.

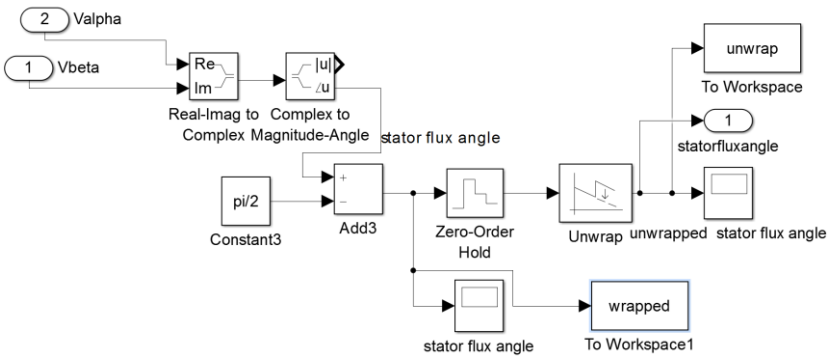

Figure 4-8 Stator flux angle estimation in Simulink model

As illustrated in Figure 4-8, the system inputs are the stator voltage α-β components in the stationary reference frame. Here, V_α and V_β are regarded as real and imaginary part of a complex number, respectively. By converting the complex number from Cartesian coordinates to Polar coordinates, the corresponding stator voltage vector position θ_v, can be obtained. Subtracting $\frac{\pi}{2}$ from this gives the stator flux position. However, this approach can only provide the position value within a periodic function of 2π; to obtain a continuous linear output angular signal, the unwrap block is employed to unfold the periodic position signal to a linear signal. Additionally, a zero-order-hold is needed since the unwrap function can only be deployed to process continuous signals, with a sample rate of $\frac{1}{20000}s$, which is identical to the fundamental sample rate of the Simulink model.

4.3.2 SFOC Outer loop implementation in Simulink

As illustrated in Figure 4-6, the outer loop of SFOC regulates the power demands P_s^* and Q_s^*. The reference rotor controller currents for inner loop I_{qr}^* and I_{dr}^* are worked out in the outer loop. The corresponding relationship is demonstrated by equations (4.22-23) in the SFOC condition. Here, the equations are written in terms reference signals with

superscript *:

$$P_s^* = -\widehat{V_g}\frac{L_m}{L_s}I_{qr}^* \tag{4.24}$$

$$Q_S^* = \frac{\widehat{V_g}^2}{\omega_e L_s} - \widehat{V_g}\frac{L_m}{L_s}I_{dr}^* \tag{4.25}$$

The relationships above indicate that decoupled control of DFIG reactive and active output power is realised by two axis rotor current control, i.e. $I_{qr}{}^*$ and $I_{dr}{}^*$, in a reference frames are chosen to align with the stator flux. Some assumptions are made here: the grid supply is relatively stiff and there is no variation of other parameters [45]. The SFOC implementation utilizing the listed relationship (4.24-4.25) directly solves the reference dq-axis rotor current for the inner loops and can be used to implement SFOC, as illustrated in [28]. However, the following limitation has to be acknowledged: with the stator resistance neglected, the calculated power would not be absolutely identical to the reference power setting. Moreover, other inaccuracies in values of machine parameters (such as L_s, L_m, etc.) also effects the loop system [28]. As a result, two outer power loops are usually employed with PI controllers to ensure accurate power flow in the stator.

The implementation of SFOC outer control loop in Simulink is shown in Figure 4-9. Time based switches for reference powers input are used for model validation to create a step change demand at a specific time. The reference powers P_s* and Q_s*. are subtracted by actual powers P_s and Q_s correspondingly. The error signals are fed into PI controllers and eventually the reference dq axis rotor current are generated as inputs for the inner loops. Additionally, two first order low pass filters are employed before the inner loop reference signals $I_{dr}{}^*$ and $I_{qr}{}^*$ send to the inner loop, because the noise level in reference signal can be relatively high in real-time applications [45]. To minimise the electrical noise level and thus reduce any noise associated issues in practical tests, low pass filters with a cut-off

frequency of 5Hz are introduced utilizing transfer functions in laboratory tests (described in section 3.7). The applied transfer function for low pass filters is: $\frac{1}{\frac{s}{2\pi\times5}+1}$ [130].

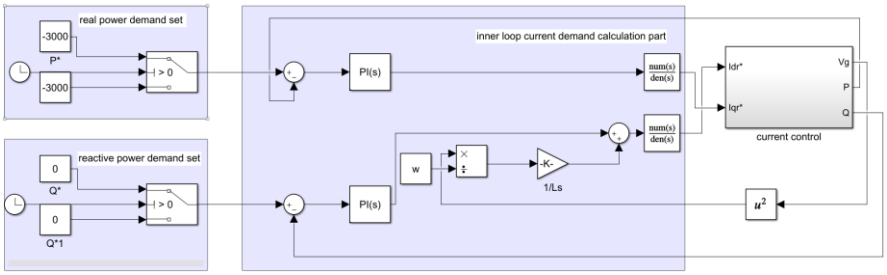

Figure 4-9 Outer loop implementation in Simulink

4.3.3 SFOC inner loop implementation in Simulink

The inner loops of SFOC regulate the dq-axis rotor controller via providing appropriate dq-axis rotor voltage values; these are then transferred to three phase axis voltage input and fed into rotor side windings of the WRIM. The equations of dq- axis rotor voltages are expressed as following: [28]

$$V_{dr}^{*} = R_r i_{dr} + \sigma L_r \frac{d}{dt} I_{dr} - \omega_r \sigma L_r I_{qr} \tag{4.26}$$

$$V_{qr}^{*} = R_r I_{qr} + \sigma L_r \frac{d}{dt} I_{qr} + \omega_r \sigma L_r I_{dr} + \omega_r \frac{L_m}{L_s} \Psi_s \tag{4.27}$$

Where $\omega_r$is the slip frequency, the angular speed difference between stator flux vector in synchronise reference frame and rotor quantity angular speed. σL_r is the leakage inductance $\left(L_r - \frac{L_m^2}{L_s}\right)$. In equations (4.26-4.27), the corresponding dq axis voltage and current variables relation on their own axis are illustrated in first and second terms of the equations. The third terms in the equations are dependent on the orthogonal/other axis currents and are thus usually referred to as the cross coupling terms. The cross

coupling terms are an order of magnitude smaller than the back e.m.f term so the minor influence upon control could be mitigated by PI controller. The final term in equation (4.27) is performed as a disturbance to the output of the PI controller in the q-axis, which referred as feed forward term. By compensating the cross coupling terms and feed forward terms, the controller loo is notably simplified [34, 28].

The SFOC inner loop implementation in Simulink is shown in Fig. 4.10.

After obtaining the reference values I_{qr}^{*} and I_{dr}^{*} from outer loop, the difference between these currents and measured currents will be fed into the PI controller, and the controller voltage V_{qr}^{*} and V_{dr}^{*} are then generated. As mentioned, the cross coupling terms and feedforward term are eliminated in the loops as well, the square areas represent the cross coupling terms demonstrated in equations (4.26-27). Once the dq axis reference rotor controller voltage signals are obtained, inverse Park's transformation and inverse Clark's transformation are employed to convert dq-axis voltage vector to three phase voltage then fed into harmonic induction machine model introduced in section 4.2. Since the dq axis rotor voltage are stator referred, they should be transferred to the rotor side using the turns ratio. The number of effective turns in the rotor and the stator windings are 42 per phase and 56 per phase, respectively [45]. With the implemented control scheme applied to rotor circuit, the harmonic WRIM model is now capable to operate with SFOC. The validation of DFIG harmonic model study will be given in the following sections.

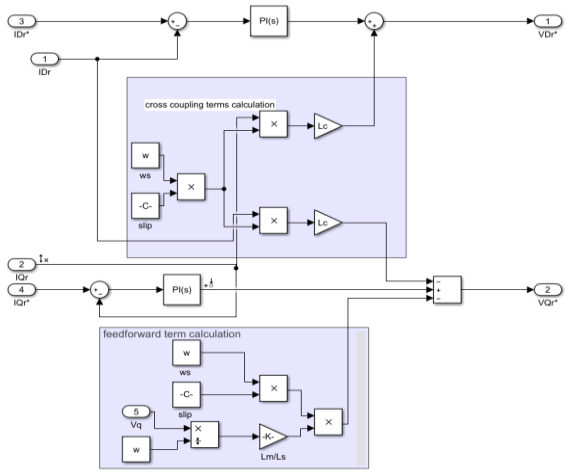

Figure 4-10 implementation of inner loop in Simulink

4.4 Time domain controller signal analysis

To validate the implemented DFIG SFOC scheme model, the stator active power and reactive power step changes are employed to check the corresponding rotor controller signal I_{qr} and I_{dr} behaviour. In Figure 4-11 below, the following power step changes are introduced: the initial reference powers (red) setting are P^* =5000W and Q^* =0. Q^* step change from 0 to -5000 Var at 3.5s while P^* changed from 5000W to -10000W at 5s. In reaction, the actual power signals (blue) P and Q vary as well to reach the power demand settings, the P and Q changes with respect of P^* and Q^* variation with little delay. In Figure 4-12, the reference rotor controller signals (red) $I_{qr}{}^*$ and $I_{dr}{}^*$ are dependently controlled by P and Q, respectively. As a result, a step change at 5s could be observed in $I_{qr}{}^*$ as well as $I_{dr}{}^*$ varies at 3.5s. The actual controller signals (blue) followed reference variation in plot. Little cross-coupling disturbances could be observed in the controller current signals ($I_{qr}{}^*$ at 3.5s and $I_{dr}{}^*$ at 5s), which was led by the reference frame orientation

error. As introduced in Section 4.3.1, the reference stator flux position was obtained from stator voltage vector angle subtracting $\frac{\pi}{2}$ [34]. However, it needs to be noted that the resistance in the machine is neglected and that thus the obtained reference stator flux position is not absolutely identical to that in reality, hence slight cross coupling disturbances appear in the plot. In general, the decoupled linear relationship between powers and *dq* axis currents indicated the SFOC scheme has been successfully employed in the presented harmonic DFIG model.

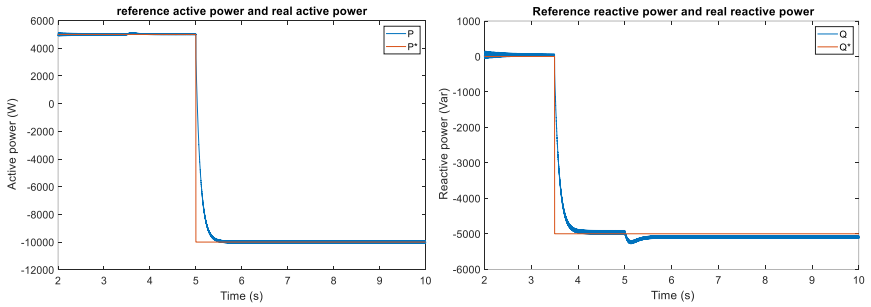

(a) Stator active power (b) Stator reactive power

Figure 4-11 Step changes in stator active power and reactive power in DFIG armonic model

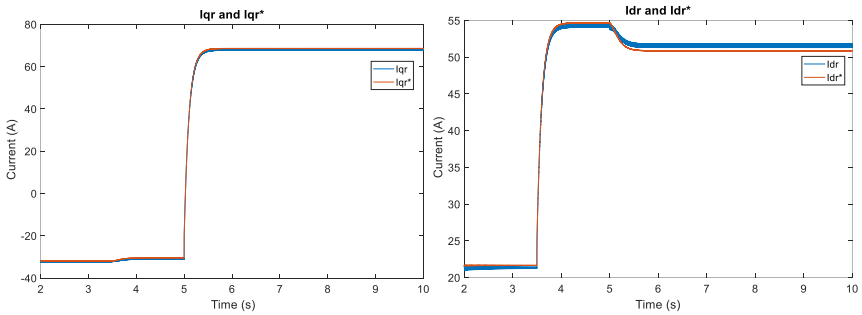

(a) Rotor q axis current (b) Rotor d axis current

Figure 4-12 Rotor dq-axis current respond with power step changes

4.5 Spectrum analysis of DFIG signals

Spectrum content analysis as a diagnostic tool in condition monitoring has been widely investigated. Machine current signature analysis (MCSA) has been employed for several different fault diagnostic scenarios and still attract considerable research interest [17] [82]. In this PhD project, DFIG shaft misalignment diagnosis and sensorless speed estimation feasibility studies are first performed based on spectral analysis of the DFIG model predicted electrical signals, thus a harmonic model study is first carried out here to demonstrate model validity in the spectral domain before further experimental analysis undertaken.

4.5.1 Electrical signals frequency component mathematical derivation

In this subsection, a sets of equations are summarised that predict the possible frequency components in stator current, rotor current, stator active and reactive powers, and controller related signals spectrum in DFIG operating in healthy conditions. Here, only the fundamental supply harmonic is taken into account and speed ripple effects are neglected in model study [83] [45].

The instantaneous time domain three-phase stator currents could be expressed in following equation: [83] [20]:

$$i_{sabc}(t) = \sum_k I_{sM}^k \cos\left([1 \pm 6k(1-s)]\omega_e t + \gamma_s\right) \tag{4.28}$$

where:

i_{sM}^k = Peak Value of the k^{th}harmonic stator current $[A]$

k = The number of air-gap magnetic field pole (k = 0,1,2,…)

s = Slip of induction machine

γ_s = Phase shift between three-phase stator currents $[rad]$

The frequency component f_{Cs} in stator current signal is :

$$f_{Cs} = |1 \pm 6k(1-s)|f_e \tag{4.29}$$

The rotor three phase instantaneous current can be expressed as following: [20]

$$i_{rabc}(t) = \sum_k I_{rM}^k \cos\left([s \pm 6k(1-s)]\omega_e t + \gamma_r\right) \tag{4.30}$$

where i_{rM}^k is the peak value of k^{th} harmonic rotor current $[A]$. γ_r is the phase shift between three-phase rotor current.

The corresponding possible frequency component f_{Cr} in rotor current is :

$$f_{Cr} = |s \pm 6k(1-s)|f_e \tag{4.31}$$

The stator total instantaneous active and reactive powers are listed below: [20]

$$p(t) = \frac{3}{2}\sum_k V_{sM} I_{sM}^k \cos\left([\pm 6k(1-s)]\omega_e t + \gamma_s\right) \tag{4.32}$$

$$q(t) = \frac{3}{2}\sum_k V_{sM} I_{sM}^k \sin\left([\pm 6k(1-s)]\omega_e t + \gamma_s\right) \tag{4.33}$$

where V_{sM} is the peak value of stator voltage.

According to the equations above, the frequency component is stator active power and reactive power could be summarized as:

$$f_{Cpowers} = |6k(1-s)|f_e \tag{4.34}$$

The dq axis rotor currents are calculated from three phase rotor current transformed by Clark's transformation and Park's transformation, the resultant equations for instantaneous dq-axis rotor currents are illustrated: [20]

$$i_{rd}(t) = \frac{3}{2}\sum_k I_{rM}^k \cos\left([\pm 6k(1-s)]\omega_e t + \gamma_r\right) \tag{4.35}$$

$$i_{rq}(t) = \frac{3}{2}\sum_k I_{rM}^k \sin\left([\pm 6k(1-s)]\omega_e t + \gamma_r\right) \tag{4.36}$$

Referring to the equations (4.35-36), the predicted frequency component in dq- axis rotor currents could be expected at:

$$f_{Cdqr} = |6k(1-s)|f_e \tag{4.37}$$

It could be observed that the frequency component locations in spectrum in stator powers (4.34) are identical to those in dq-axis rotor currents (4.37). Additionally, the error signal of these signals (as showed in Fig. 4.6) have the same frequency contents in spectrum apart from DC component (0Hz) because they are the result of DC value subtract higher order harmonic signals. Two cascaded control relevant signals: active and reactive powers, dq-axis rotor currents and all error signals' frequency component can be classified as following:

$$f_{SFOC} = |6k(1-s)|f_e \tag{4.38}$$

4.5.2 DFIG Harmonic model spectrum validation

With the help of harmonic modelling theory introduced in section 4.2, the higher order harmonic effect in DFIG model is capable to be observed. Considerable research of the stator current spectrum have been reported for fault analysis however little attention has been given to employing the signature analysis in controller signals to this end. One of the key aims of this project is to explore this are further to ascertain the feasibility of employing controller signals for diagnostic and parameter estimation purposes.

The DFIG harmonic model was implemented based on the known parameters of the laboratory Marelli Motori wound rotor induction machine, which is used for experimental

research in this study. The relevant parameters of the WRIM are listed in Appendix A. Here, healthy DFIG steady state operation performance is analysed. Two arbitrary operating speeds are observed for this purpose: 1340rpm and 1590 rpm, the load level of -6kW 0Var are set for both speed conditions. Fast Fourier transform (FFT) routine is carried out to post-process the time domain signal to frequency domain. The DFIG harmonic model step size is set to 1/20000Hz. With a rectangular window size of 2^{17} data points, approximately 0.15Hz resolution spectrum is provided. To illustrate the significant frequency components of interest, signal bandwidth of 0-700Hz is presented. The air-gap magnetic field pole number values for k=0,1 and 2 related frequency components demonstrated in equations (4.29), (4.31) and (4.37) are exhibited.

- Sub-synchronous speed operation (1340 rpm)

The predicted frequency components in stator current (equation 4.29 for f_{Cs}), rotor current (equation 4.31 forf_{Cr})and SFOC controller related components (equation 4.36 for f_{SFOC}) at 1340 rpm rotational speed are summarized in Table 4-2 below:

Table 4-2 Calculated frequency components of DFIG signals at 1340 rpm condition

Signal type	f_{Cs} (4.29)	f_{Cr} (4.31)	f_{SFOC} (4.36)
k=0	50	5.3	0
k=1	218,318	262.7,273.3	268
k=2	486,586	530.7,541.3	536

The results of the DFIG signals spectrum are illustrated in the Figure 4-13.

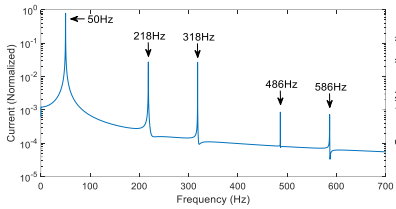

(a). Stator Current

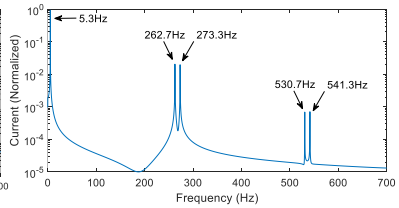

(b) Rotor Current

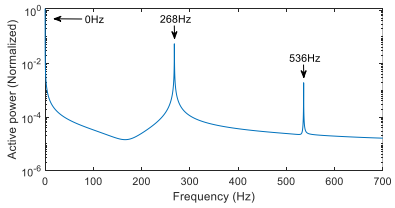

(c). Stator active power

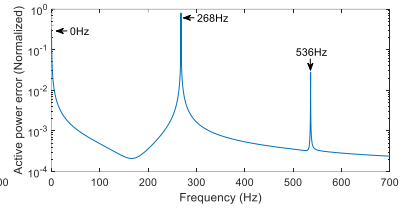

(d) Stator active power error signal

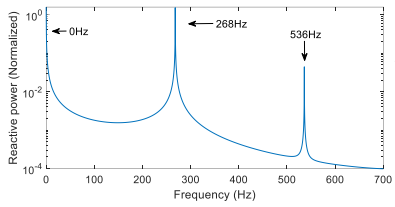

(e). Stator reactive power

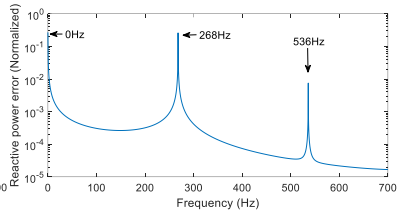

(f) Stator reactive power error signal

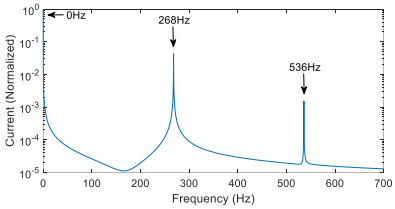

(g). I_{qr} current

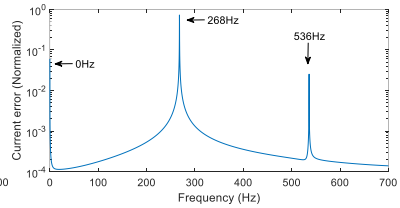

(h) I_{qr} error signal

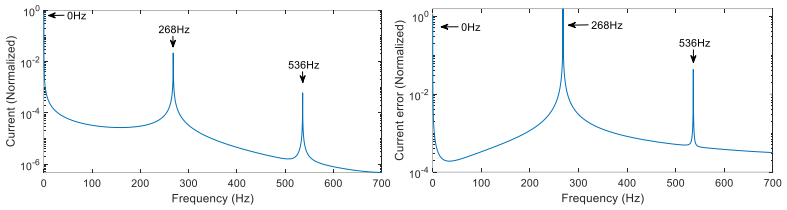

(i). I_{dr} current (j) I_{dr} error signal

Figure 4-13 DFIG signals spectrum for 1340 rpm condition

As the Figure 4-13 illustrated, the calculated frequency components in Table 4-2 could be observed in the DFIG signal spectrum. For stator current in plot (a), the fundamental component 50Hz (k=0) with the largest magnitude in spectrum (normalized 1), the higher order MMF harmonic components 218Hz, 318Hz (k=1) and 486Hz, 586Hz (k=2) are clearly showed in plot. In rotor current plot (b), the fundemental component at 5.3Hz (k=0), higher order MMF harmonic component 262.7Hz, 273.3Hz (k=1) and 530.7Hz, 541.3Hz (k=2) are exhibited. The SFOC controller related components, plot (c) to (h), the frequency components are located in the same position in spectrum. 0Hz (k=0) is the fundamental component for all signals, while the higher order component 268Hz (k=1) and 536Hz (k=2) are marked in the spectrm. There are some conditions in the plot where the fundamental frequency component is not the stronest in the spectrum. For example, in plot (e), the stator reactive power was set as 0 in the model thus the DC component is reasonably smaller than the relevant higher order spectral content. Besides, for the error signals: stator active power error in plot (d), stator reactive power error in plot (f), I_{qr} error in plot (h) and I_{dr} error in plot (j), their DC component may be smaller than the higher order spectral content since the DC components of these signals are inherently close to 0. In fact the magnitude of higher order components is dependent to the load level, as will be shwon in Chapter 5 with experimental signal spectra analysis. In this

sub-synchronous speed condition study, the frequency components in DFIG harmonic model are seen to match the therorethically predicted frequency components, demonstrating the validity of the model in spectral domain.

- Super-synchronous speed operation (1590 rpm)

A super-synchronous speed at 1590 rpm condition has been examined, the predicted frequency components of signals are summarized in Table 4-3 below.

Table 4-3 Calculated frequency components of DFIG signals at 1590 rpm condition

Signal type	f_{Cs} (4.29)	f_{Cr}(4.31)	f_{SFOC}(4.36)
k=0	50	3	0
k=1	268,368	315,321	318
k=2	586,686	633,639	636

The relevant DFIG signal spectrum is exhibited in Figure 4-14.

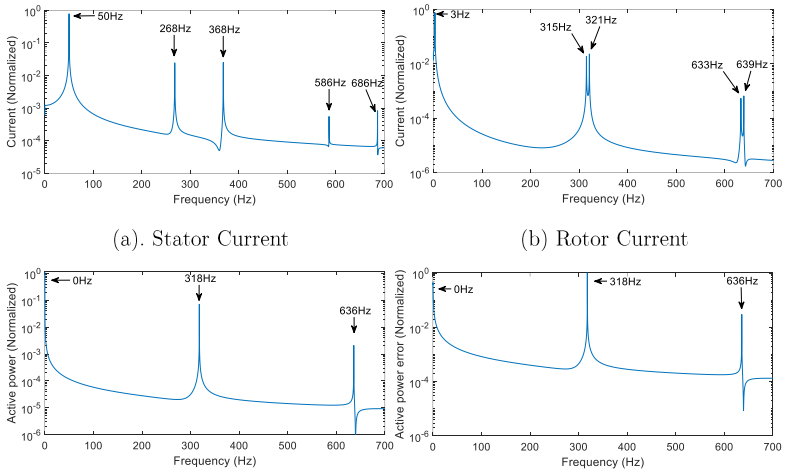

(a). Stator Current (b) Rotor Current

(c). Stator active power (d) Stator active power error signal

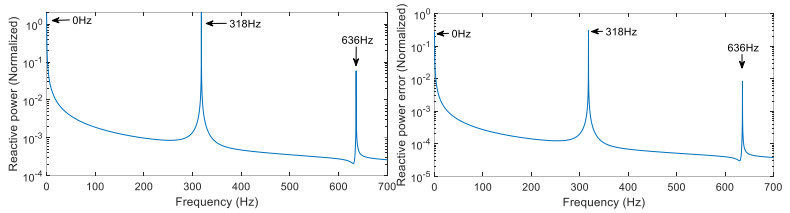

(e). Stator reactive power

(f) Stator reactive power error signal

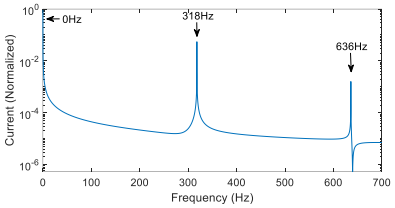

(g). I_{qr} current

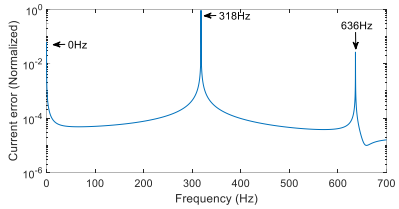

(h) I_{qr} error signal

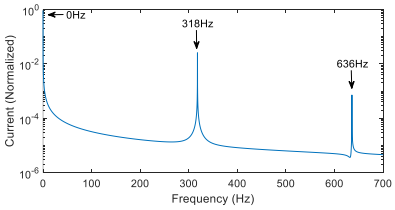

(i). I_{dr} current

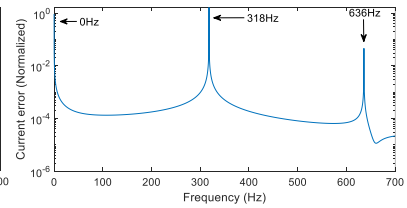

(j) I_{dr} error signal

Figure 4-14 DFIG signals spectrum for 1590 rpm condition

The second part of study investigates super-synchronous speed at 1590 rpm condition. The predicted frequency components listed in Table 4-3 could be witnessed in signal spectrum plot in Figure 4-14 clearly as showed in sub-synchronous speed scenario. As a result, the predicted frequency content of DFIG signals indicated a good agreement with FFT processed harmonic model results, this further demonstrating the validity of the established model.

4.5.3 Sensorless speed estimation utilizing frequency contents

One of the applications of DFIG harmonic model study is to explore the possibility of devising spectral search based controller signal embedded sensorless speed estimation methods. As per the equations listed in section 4.5.1, the frequency contents of DFIG signals are rotational speed related. If possible to capture a speed dependent frequency component in a specific bandwidth in spectrum, and extract its frequency in a timely fashion it would be possible to use this information for estimating rotor speed. Previous WRIM sensorless speed estimation researches utilizing stator current frequency contents [134] and active power frequency contents [135] have been successfully implemented.

Typically, the operating speed range of DFIG is approximately ±30% of synchronous speed [28]. However, due to the limitation of the test system used in this work, the maximum operation speed of the prime mover DC motor is 1700 rpm, therefore the DFIG maximum operating speed is set as 1700rpm. Recalling equation (4.38), the frequency contents for rotor controller signals are calculated as following:

$$f_{SFOC} = |6k(1-s)|f_e \tag{4.39}$$

For a WRIM with two pole pairs, the synchronise speed is:

$$synchronous\ speed = \frac{60\times f_e}{pole\ pairs} = \frac{60\times 50Hz}{2} = 1500rpm \tag{4.40}$$

Here, the frequency of interest is marked as F, the relationship between F and machine rotational speed ω_m (in rpm) is demonstrated below based on equation (4.38):

$$\omega_e = \frac{1500\times F}{6k\times 50} = \frac{5F}{k} \tag{4.41}$$

In this study, the frequency components up to k=3 are investigated. To get rid of bandwidth overlapping while identifying maximum peak in a specific bandwidth, e.g. the upper edge of k=2 bandwidth is smaller than lower edge of k=3 bandwidth, the speed

range 1150rpm to 1700rpm is selected as the speed varying range. The corresponding searched bandwidth spectral co-ordinates for different k values are: 230Hz to 340Hz (k=1), 460Hz to 680Hz (k=2), 690Hz to 1020Hz (k=3). I_{qr} signal spectrum (Figure 4-15) is illustrated below for demonstration purpose; it is important to note that this does not give a full picture of spectral content at this stage, as it ignores a number of relevant spectral effects that would be found on a practical system, as will be shown later in this thesis. However, the presented illustrative data allow for demonstration of the fundamental principle of the envisaged controller signal embedded speed estimation: by identifying the relevant frequency bandwidth (k=1,2,3) and identifying the strongest frequency component within the band, the frequency content marked in Figure 4-15 could be captured – assuming, of course, it can be shown that in practical application no stronger spectral components exist in the target bandwidth(s) that would interfere with this search. Then the corresponding machine rotational speed could be calculated with equation (4.41). The feasibility of band chosen and signal selection will be discussed in Chapter 5 based on experimental signal spectrum.

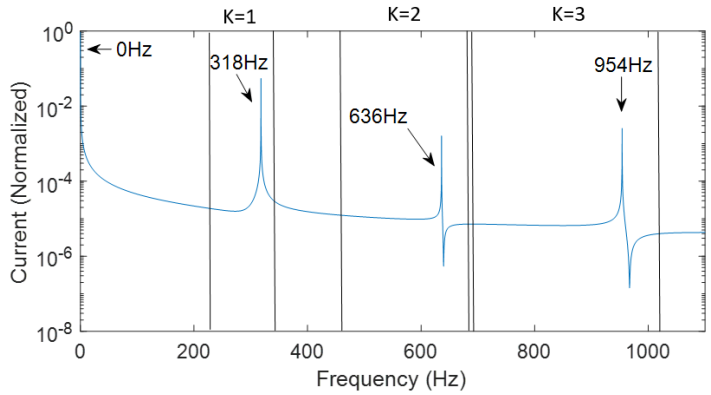

Figure 4-15 I_{qr} spectrum and spectral bandwidth that contain components carrying speed information

4.6 Conclusion

In this chapter, the WRIM model representing higher order field effects was integrated with a model of SFOC to form a harmonic DFIG model that is then implemented in Simulink environment. The mathematical theory of WRIM harmonic effect modelling and its Simulink implementation procedure were shown. A conventional SFOC scheme model was then established

To validate the DFIG model performance, both time domain and frequency domain analysis study were conducted: A time domain study was first undertaken via observing the performance of inner loop signals (controller currents) while outer loop demands (power demands) changing. The result manifested decoupled power control was successfully enabled in the implemented DFIG model. As for frequency domain: a spectrum study of DFIG signals had been presented to validate higher order MMF spectral effects representation in DFIG terminal and controller signals. The model predictions are cross correlated with theoretical closed form expressions defining possible spectral content of DFIG signals for a typical sub- and super-synchronous operating point. This showed close agreement, indicating the validity of the presented DFIG harmonic model in representing the relevant spectral effects in DFIG signals.

Chapter 5 Controller DFIG sensorless speed estimation utilizing controller embedded signal

5.1 Introduction

The wind turbine (WT) generator rotor velocity is a crucial parameter for power generation control and maximum power point tracking (MPPT). 14% of generator failures are directly related to motion sensors failure while 40% of generator failures are indirectly related [21, 136]. Typical rotational machine speed estimation is realized via rotor shaft connected physical measurement devices, often of incremental encoder type, which invariably require additional electronics, extra wiring and space, careful mounting and maintenance. Crucially, these devices become single failure points for the larger vector controlled rive system, as their failure inevitably renders the controller inoperative,

as the access to required positional and/or velocity information for its functioning is lost. Sensorless speed estimation (SSE) has therefore been widely been investigated in literature as a means of utilizing alternatives to dedicated measurement devices for inferring information on position and/or velocity – these can in theory provide features of lower cost, higher reliability, better noise immunity and lower maintenance compared with conventional, encoder or similar measurement device based, speed estimation approach [107]. In wind turbine applications, the SSE as an alternative approach for speed estimation could enable undisturbed generator operation when the encoder failure occurs, and thus undisturbed power production allowing expensive production loss and unplanned maintenance to be avoided. The implementation of a novel SSE technique embedded in the DFIG control system signals will be introduced in this chapter.

Recalling the SSE introduced in Chapter 2, the SSE techniques could be classified as fundamental model based (FMB) estimation and spectral search based (SSB) methods. SSB was chosen in this project rather than FMB because the latter is highly dependent on machine parameters, and hence its speed estimation accuracy could be affected by inherent machine parameters variations. The SSB estimation is fundamentally based on capturing the specific, speed dependent, harmonic content in the signal spectrum and thus deducing the machine rotational speed via a known frequency-speed relationship [135, 114]. There are two essential factors of SSB: the signal selection and the frequency content capturing algorithm. In this chapter, a SSB SSE approach utilizing DFIG controller signals and a parabolic interpolation spectral search algorithm will be devised and demonstrated.

This chapter commences with spectral analysis of experimental DFIG signals, reporting a comparative study of different DFIG signal types in various load conditions within the

nominal operating range, with the underlying aim being to determine those most suited to SSE application. The principle of real-time spectral search approach utilizing parabolic interpolation is then presented and the proposed DFIG SSE algorithm utilizing controller signals is detailed. The algorithm theoretical validation is first given in a MATLAB interface utilizing an experimentally recorded DFIG controller signal. Afterwards, the overview of parabolic interpolation SSB SSE scheme in LabVIEW platform as well as the detailed implementation procedure of LabVIEW code programming is illustrated. Finally, the performance of DFIG real-time SSE utilizing introduced algorithm is evaluated in a range of steady-state and transient practical tests.

5.2 Evaluation of practical DFIG controller signals harmonic contents

One of the critical factors for SSB SSE implementation is the ability to identify and select suitable speed dependent spectral content of a specific signal that can be unambiguously identified and used to extract speed information. To this end, a comparative study of experimentally recorded terminal and controller signals from the DFIG test rig is undertaken in this section: the first section illustrates the spectra of the acquired experimental signals to demonstrate the harmonic content of interest. The second part explores the spectral nature of the DFIG controller signals in different load conditions, hence specifying the optimal signal for SSB SSE application in this project.

5.2.1 Steady-state characterization of DFIG signals

Identifying optimal possible speed dependent spectral content to capture for SSB SSE is the first target of this research This builds on the DFIG signals spectral contents

theoretical study introduced in section 4.5. In the DFIG harmonic model chapter, an example controller signal spectrum predicted by the DFIG harmonic model was analyzed to demonstrate its possible potential for SSB sensorless speed estimation; this signal was however calculated in the harmonic model where a number of practical important spectral features such as higher order supply harmonics and other relevant spectral phenomena neglected [137, 138]. In this section, a case study examines the experimental DFIG controller signals spectra to ascertain their practical applicability potential in realistic, on-line operating conditions. For the sake of completeness, the conventionally analyzed terminal current signals for SSB SSE are also included in the analysis.

A typical DFIG operating point of 1340 rpm at 50% load is used for illustration purposes in the initial study condition. The investigation of experimental signal spectrum is undertaken to evaluate the spectral content characteristic of practical DFIG signals. The following measured signals are included in the study: the stator current and DFIG controller signals, including the stator active and reactive powers, the dq-axis rotor currents, the error signals of the outer and the inner controller loops and the reference dq-axis rotor currents. These signals were sensed via current and voltage sensors and acquired from within the dSPACE platform real-time control routine at a sample rate of 5000Hz. The recorded signals were then processed with a 2^{16} points FFT routine in MATLAB, giving a resolution of ~0.076Hz. The illustration bandwidth 0-1100Hz is chosen to present the spectral content found to be of interest on the practical system studied in this work.

The FFT spectrum of the stator active power signal is illustrated in Figure 5-1. Compared with model study spectrum in Chapter 4, the measured signal contains an evident increased spectral noise and additional contents, as is generally expected [22]. The

spectrum is analyzed to identify its potential for enabling SSB SSE. The fundamental frequency components in the spectra corresponds to 0Hz, which is the strongest component in the spectrum. The higher order magneto motive force (MMF) harmonics introduced in Chapter 4 (4.38) are labeled as k=1,2,3 in the spectra. The predicted harmonic contents from model study (Table 4-2) are stated in brackets in the following text. Spectral components corresponding to k=1,2,3, 267.9Hz (268Hz), 535.7Hz (536Hz) and 803.6Hz (804Hz) could be observed in the plot, which indicated a good match with the model study. These speed depend components are of potential interest for SSB SSE. Apart from the predicted contents, additional contents could be observed in the spectrum. Since the SSB SSE frequency component capture is generally established via detecting the strongest speed dependent component within a specific bandwidth, the undesired secondary spectral contents in the measured signal may affect this process. Some of the pronounces relevant spectral components are labelled in the spectrum, known to originate from the stator supply unbalance (SSU) (marked as A_i, where i = 1, 2, 3…) [45] and the rotor side converter (RSC) switching harmonics (marked as B_i, where i=1,2,3…) [20]. The SSU can gives rise to controller signal spectral contents defined as: [109] [45]

$$A = |2g \pm 6k(1-s)|f_s \tag{5.1}$$

Where: g is the side-band series order (g=0,1,2…). The equation indicates that the SSU introduces side bands of higher order MMF harmonics. The relevant contents are can be identified in the measured spectrum at following frequencies: A_1:99.72Hz (g=1, k=0); A_2: 199.4Hz (g=2, k=0); A_3: 299.1Hz (g=3, k=0); A_4:367.6Hz (g=1, k=1). In addition, the RSC switching harmonics appear at $6nsf_s$ (n=1,2,3..) sidebands of the MMF harmonics and SSU harmonics [20], and are observable in the measured spectrum at: B_1: 31.2Hz (k=0, g=0, n=1); B_2: 68.44Hz (k=0, g=1, n=1); B_3: 130.9Hz (k=0, g=2, n=1); B_4: 168.2Hz (k=0, g=2, n=1); B_5:236.7Hz (k=1, g=0, n=1). The listed SSU and switching harmonics

are those observed at pronounced magnitude levels in the examine spectrum: for example, the rotor supply unbalance related spectral components manifests $2nsf_s$ side band in the spectra contents (10.38Hz) are not significant in the spectral ranges.

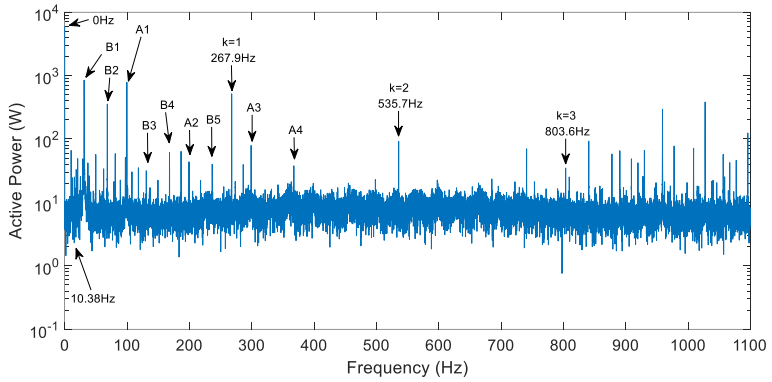

Figure 5-1 FFT spectra of the measured stator active power for 1340 rpm 50% load

The measured stator active power error signal spectrum is shown in Figure 5-2. The spectrum of the error signal coincides with the active power signal apart from the DC component (0Hz).

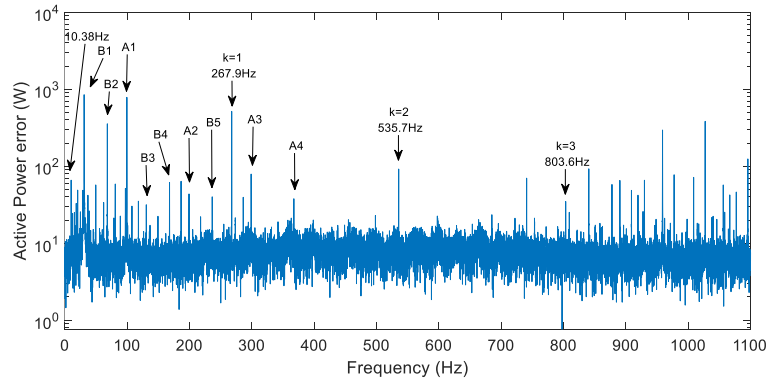

Figure 5-2 FFT spectra of the measured stator active power error P_{err} for 1340 rpm 50% load

Figure 5-3 and Figure 5-4 exhibit the spectrum of measured stator reactive power and its error signal. The error signal has the identical higher order harmonic contents as the reactive power spectra. Since the reactive power demand setting was 0 Var, the reactive power spectra DC component is not the dominant content in this case. The listed spectral content in the active power signal could be observed in the reactive power spectra: MMF harmonics, SSU effect harmonics, RSC switching harmonics.

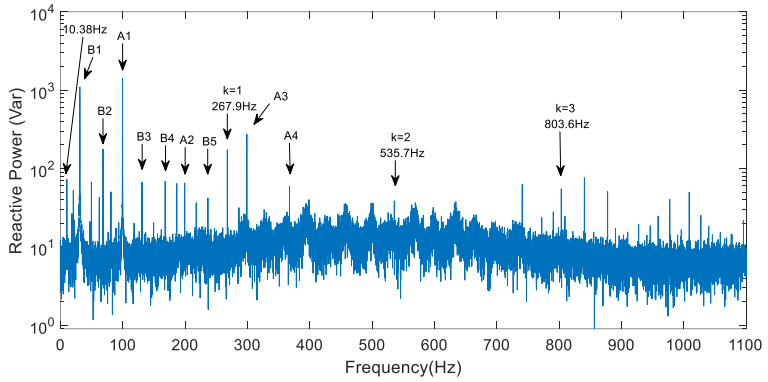

Figure 5-3 FFT spectra of the measured stator reactive power for 1340 rpm 50% load

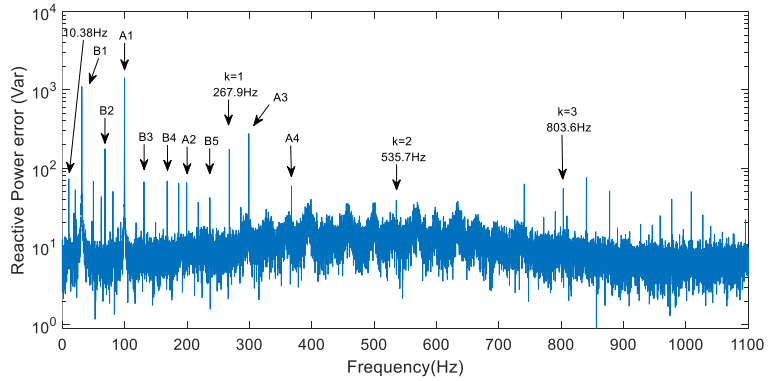

Figure 5-4 FFT spectra of the measured stator reactive power error Q_{err} for 1340 rpm 50% load

However, the speed depended spectral content is not as strong as observed in the stator

active power spectrum since the reactive demand setting was 0. The MMF contents are smaller than SSU and RSC harmonics so that the SSB approach would be interfered by the undesired contents.

Figures 5.5-10 illustrate the inner loop signals: dq-axis reference signals, controller signals and error signals. The q-axis related signals spectra are demonstrated in Figure 5-5 and Figure 5-6, and show the characteristic spectral the contents in the I_{qr} and I_{qrerr} signals. Nevertheless, the inner loop signals spectrum are less effected by noise thus the harmonic contents are more evident compared to those in outer loop. i.e., less undesired spectra peaks around MMF harmonic content k=3 appear in inner loop spectrum. Moreover, the error signal contains nearly the same spectral contents as the corresponding q axis controller current signal apart from the DC component. The error signal is the difference between the inner loop reference signal $refI_{qr}$ and I_{qr}, as illustrated in Figure 5-7, the DC component is the only significant spectral content in the $refI_{qr}$ spectra. Therefore the higher order harmonic characteristics in the inner loop controller signal and its error signal are almost the same in magnitude.

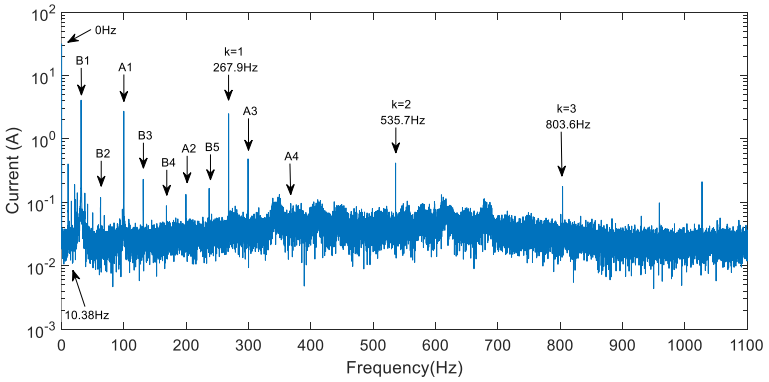

Figure 5-5 FFT spectra of the measured I_{qr} signal for 1340 rpm 50% load

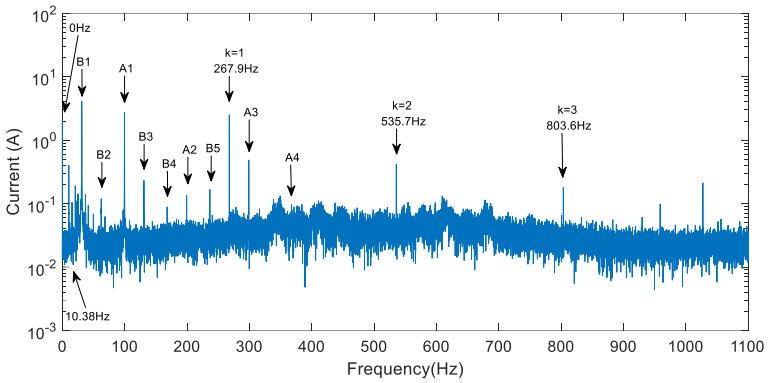

Figure 5-6 FFT spectra of the measured I_{qrerr} signal for 1340 rpm 50% load

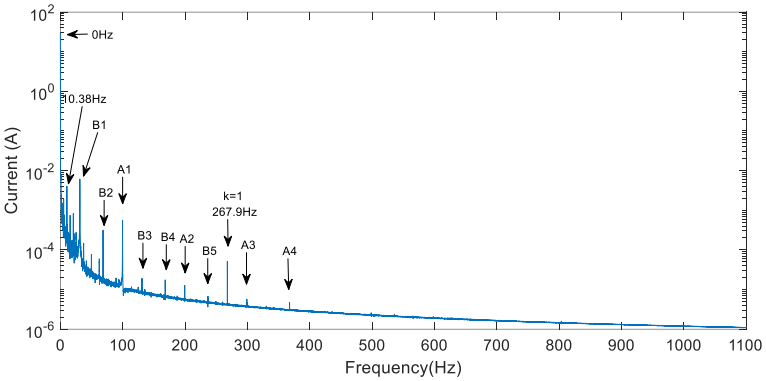

Figure 5-7 FFT spectra of the measured $refI_{qr}$ signal for 1340 rpm 50% load

The d-axis related signal spectrum are shown in Figures 5-8 to 5-10. The lower order speed dependent (MMF) content harmonic is less significant compared with I_{qr} spectra: the magnitude of k=1 content is not pronounced, and is seen to be smaller than the A3 SSU harmonic. The k=2 content is nearly invisible in spectrum. However, k=3 harmonic is significant and there are no other strong harmonic components near it. From SSB point of view, k=3 MMF harmonic in I_{dr} current would be an interesting prospect to explore. Concerning the reference signal $refI_{dr}$, strong SSU harmonic contents like A_1 could be

observed which result in the corresponding error signal SSU contents exhibiting a notable magnitude difference with those in the I_{dr} spectra. The magnitude difference between spectral effects in the d-axis and the q-axis signal spectra is due to the DC component difference in I_{dr} and I_{qr} current, which corresponds to the stator active power and reactive power in the outer loop.

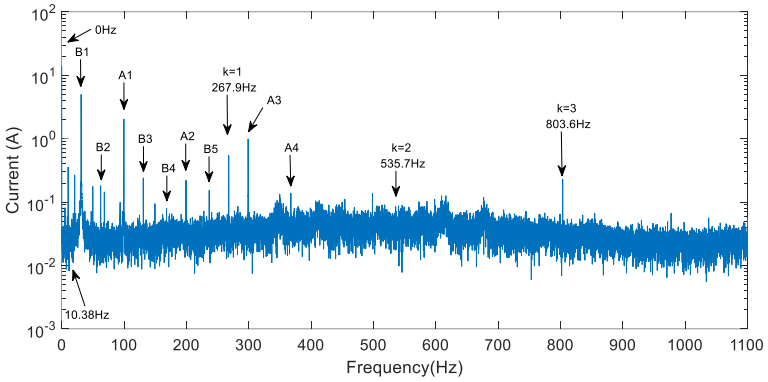

Figure 5-8 FFT spectra of the measured I_{dr} signal for 1340 rpm 50% load

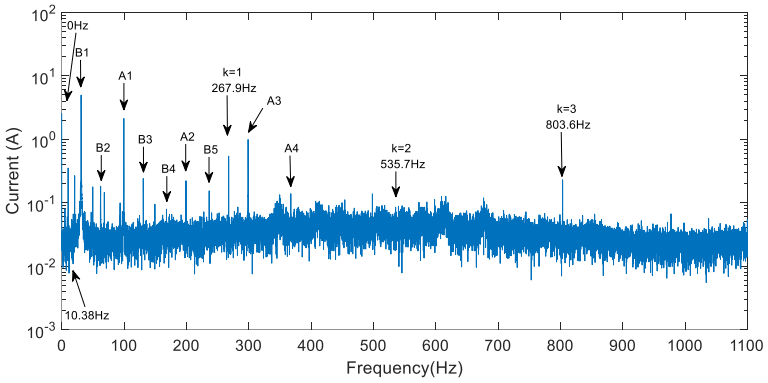

Figure 5-9 FFT spectra of the measured I_{drerr} signal for 1340 rpm 50% load

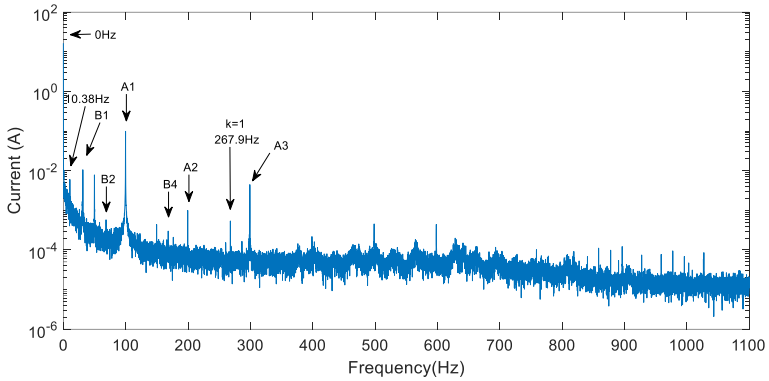

Figure 5-10 FFT spectra of the measured $refI_{dr}$ signal for 1340 rpm 50% load

The presented spectral measurements are intended to provide a general illustration of spectral contents manifestation patterns in signals measured on the practical system used in this research. The following section will report a load dependency study of these to enable further exploration of spectral component that could underpin the establishment of SSB SSE schemes.

Finally, for the sake of completeness, the stator current spectrum is investigated here for SSB SSE potential comparison purposes. As illustrated in Figure 5-11, the fundamental component is located at 49.82Hz (50Hz). Referring to Table 4-2, the actual higher order MMF contents and predicted contents are: 218Hz (218Hz) and 318 Hz (318Hz) (k=1), 485.8Hz (486Hz) and 585.6Hz (586Hz) (k=2); 753.7Hz (754Hz) and 853.4Hz (854Hz) (k=3). The SSU harmonic contents in stator current could be predicted via: [109] [45]

$$A = |(1 \pm 2g) \pm 6k(1-s)|f_s \tag{5.2}$$

The relevant SSU contents appeared in the spectrum: A_1:149.5Hz (g=1, k=0); A_2: 249.3Hz (g=2, k=0); Similarly, the RSC switching harmonics appear at $6nsf_s$ (n=1,2,3..) sideband of MMF harmonics and SSU harmonics: B_1: 18.62Hz (g=0, k=0, n=1); B_2: 81.1Hz (g=0, k=0, n=1); B_3: 118.3Hz (g=1, k=0, n=1); B_4: 186.8Hz (g=1, k=0, n=1); B_5: 286.5Hz

(g=1, k=1, n=1); B_6: 348.9Hz (g=1, k=1, n=1). Compared with controller signal spectra, each air-gap magnetic field pole number k corresponds to two significant speed dependent MMF harmonic contents. Compare with the MMF contents in I_{qr} signal spectra, the speed dependent spectral content in stator current is less significant, i.e. strong harmonic components like A_2 close to 218Hz in may effect SSB execution. As a consequence, the controller loop signals are deemed more capable for SSB SSE in SFOC DFIG system.

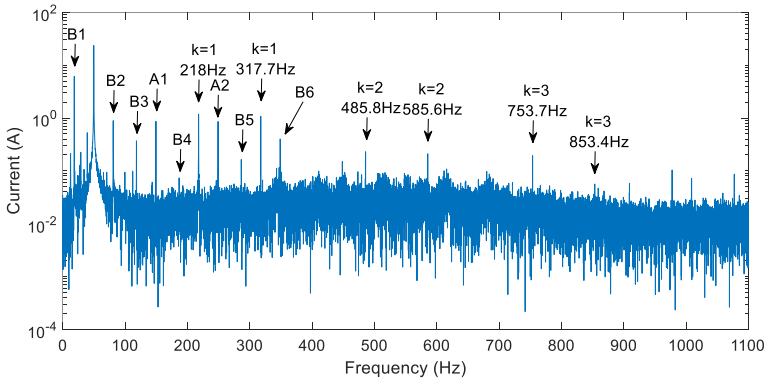

Figure 5-11 FFT spectra of the measured I_{sa} signal for 1340 rpm 50% load

5.2.2 Compare study for harmonic content of interest determination

In the previous section, an investigation was undertaken to evaluate the spectral characteristics of the DFIG controller loop and stator current signals, concluding that the controller signals seem more capable for DFIG SSB SSE compared with stator current. This section explores the spectral characteristics of controller loop signals in a range of different load levels in the nominal operating range with a view to identifying whether the manifestation and detectability of the spectral content of interest is consistent. The following load points are assessed in the study: 25%, 50% ,75% and 100% load. No load

condition is not examined as WTs typically operate at higher loads [28]. In fact, the DFIG would never operate at absolute no load condition but at very low level load even though setting the active power demand as zero. This section investigates the spectrum of the following controller loop signals: P_s, Q_s, I_{dr}, I_{qr} and their corresponding error signals P_{err}. Q_{err}. I_{drerr}, $I_{qrerr.}$ The specific suitable speed dependent harmonic content of a signal would be finally identified for SSB SSE in DFIG.

The measured stator active power spectrum in four assessed load points is illustrated in Figure 5-12 and Figure 5-13. For the sake of clarity, only the MMF harmonic contents with configured bandwidth for each air-gap magnetic field pole number k (introduced in Chapter 4) are labeled. The corresponding searching bandwidths for each k scenarios are as defined as following: 230Hz to 340Hz (k=1), 460Hz to 680Hz (k=2), 690Hz to 1020Hz (k=3). The key point of SSB SSE is to identify the labelled speed harmonic content within the pre-defined bandwidth. The observed magnitudes of MMF contents in assessed load conditions are summarized in Table 5-1: the magnitude of MMF contents in the active power signal have the same magnitude compared with the corresponding error signal. The harmonic content increasing tendency with load rise could be observed in k=1 and k=2 harmonic content, with a clear significant boost from 50% load to 75% for the former and a relative linear increase in the latter. No significant variations exist for k=3 contents. The identification of k=1 content bandwidth may be effected by undesired strong harmonic components. i.e. 300Hz (A_3). Compared with k=1, no consistent pronounced contents exist in k=2 corresponding bandwidth apart from MMF content, however the MMF content itself in 25% load is not sufficiently distinct in the spectrum so its identification lower loads may pose a challenge. As for k=3 scenario, the MMF content is not significant in its searching bandwidth, which is not capable for frequency identification.

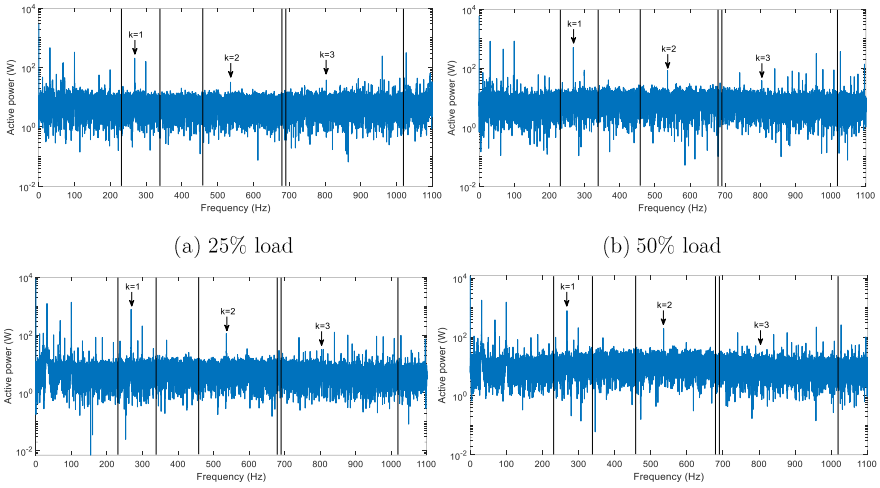

(a) 25% load (b) 50% load

(c) 75% load (d) 100% load

Figure 5-12 FFT spectra of the measured stator active power signal for 1340 rpm

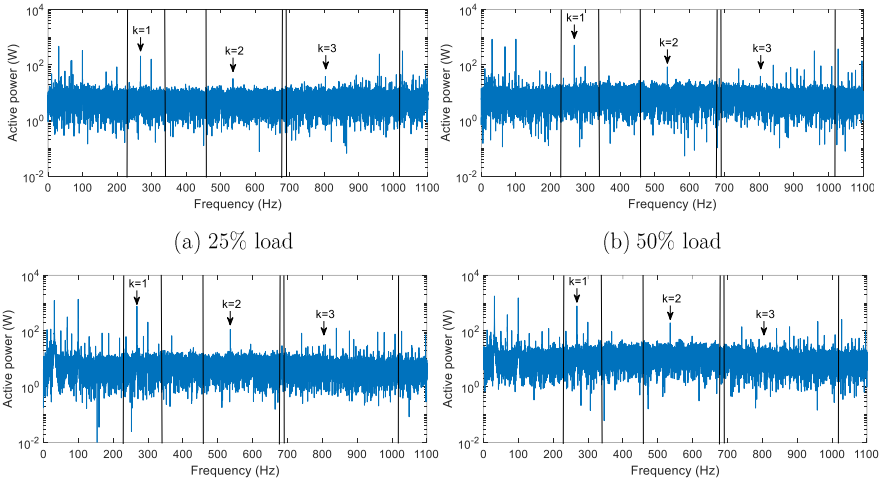

(a) 25% load (b) 50% load

(c) 75% load (d) 100% load

Figure 5-13 FFT spectra of the measured stator active power error signal for 1340 rpm

Table 5-1 Magnitude of MMF contents for P_s and P_{err} spectra with 1340 rpm DFIG in variety loads

Load level	P_s			P_{err}		
	k=1	k=2	k=3	k=1	k=2	k=3
25%	207.4	32.26	38.11	207.4	32.26	38.11
50%	267.9	84.25	38.82	267.9	84.25	38.82
75%	768.4	113.4	31.44	768.4	113.4	31.44
100%	779	193.9	21.61	779	193.9	21.61

The measured stator reactive power spectrum are shown in Figure 5-14 and Figure 5-15; the reactive power demand settings were 0 for all load conditions. Different reactive power level tests were not presented here as load level variation attracts are more deserved to be investigated for machine sensorless speed estimation researches [114, 134, 135]. The MMF contents in both reactive power and error signal spectrum are not evident enough for recognition. i.e. k=1 MMF content is not stronger than A_3 SSU harmonic in all load conditions; k=2 and k=3 MMF contents are not noticeable in their searching bandwidth. In consequence, the speed dependent contents in reactive power not capable for SSB identification in null reactive power condition.

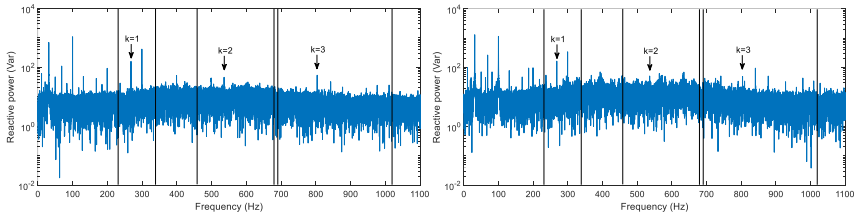

(a) 25% load (b) 50% load

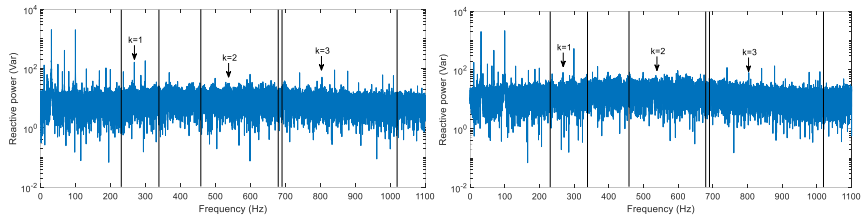

(c) 75% load (d) 100% load

Figure 5-14 FFT spectra of the measured stator reactive power signal for 1340 rpm

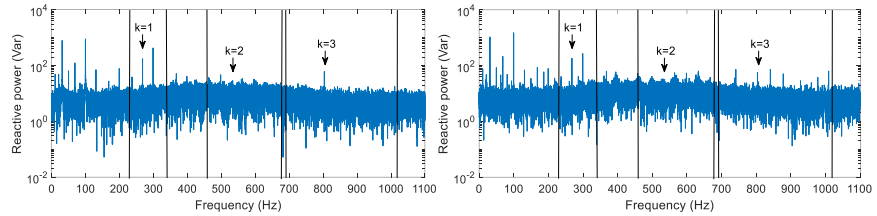

(a) 25% load (b) 50% load

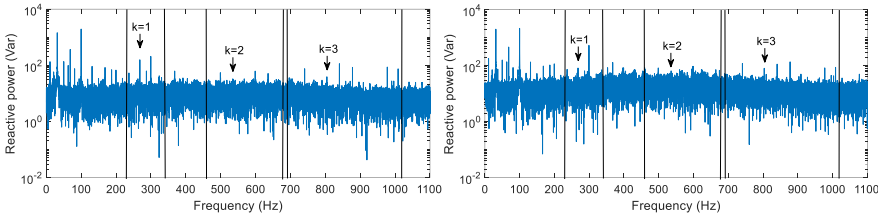

(c) 75% load (d) 100% load

Figure 5-15 FFT spectra of the measured stator reactive power error signal for 1340 rpm

Figure 5-16 and Figure 5-17 show the q-axis controller current signal and its corresponding error signal spectrum measured for the assessed load conditions. Compared with the outer loop signal spectrum, the speed dependent harmonics recognition would here be less effected by undesired harmonics, i.e. only the A_3 SSU content exists in k=1 searching bandwidth and k=3 MMF content is the observed as the sole strongly pronounced content in its search band.

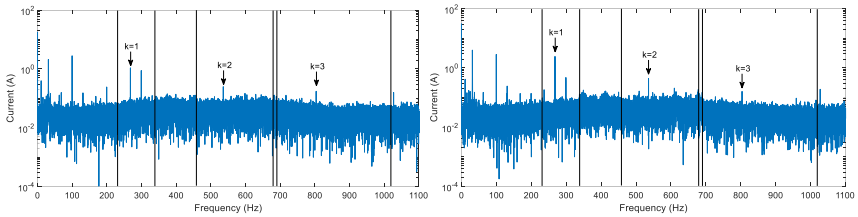

(a) 25% load (b) 50% load

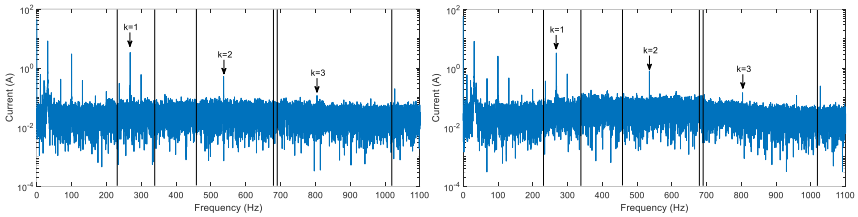

(c) 75% load (d) 100% load

Figure 5-16 FFT spectra of the measured I_{qr} signal for 1340 rpm

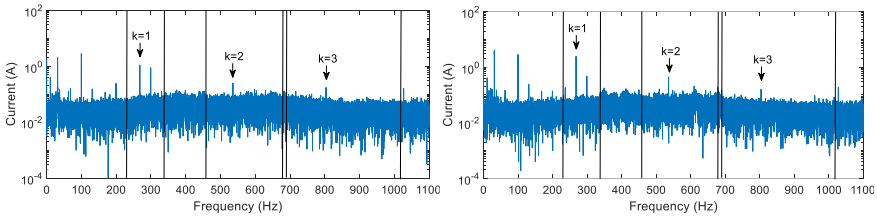

(a) 25% load (b) 50% load

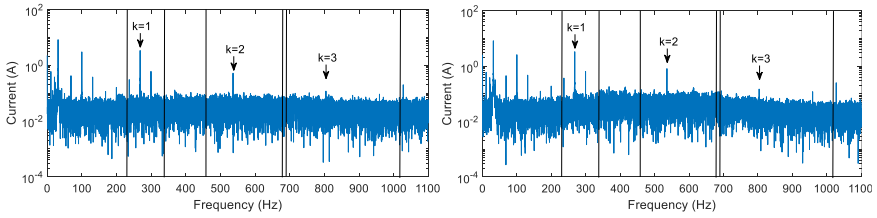

(c) 75% load (d) 100% load

Figure 5-17 FFT spectra of the measured I_{qrerr} signal for 1340 rpm

The magnitude of MMF contents in the I_{qr} signal have nearly the same magnitude

compared with the corresponding error signal. The magnitude of MMF harmonic contents are summarized in Table 5-2.

Table 5-2 Magnitude of MMF contents for I_{qr} spectra with 1340 rpm DFIG in variety loads

Load level	I_{qr}			I_{qrerr}		
	k=1	k=2	k=3	k=1	k=2	k=3
25%	1.088	0.2492	0.1737	1.088	0.2492	0.1737
50%	2.455	0.4439	0.1613	2.455	0.4439	0.1613
75%	3.371	0.52	0.118	3.371	0.52	0.118
100%	3.932	0.8176	0.1495	3.932	0.8176	0.1495

The magnitude of k=1 and k=2 speed dependent contents are increasing with the load level raising. As introduced in Chapter 4, in SFOC DFIG system, the I_{qr} current magnitude (fundamental) is proportional to the outer loop active power level. The magnitude of lower order relevant MMF harmonics vary with the fundamental content. Referring to the plots, k=1 searching band has undesired SSU harmonic, which may affect SSB SSE process especially in low load scenario. Compared with k=3 MMF content, k=2 content is more evident in its searching bandwidth with significant magnitude and less interference harmonics. In consequence, k=2 MMF content is suitable for speed dependent frequency identification for SSB SSE.

Finally the *d*-axis current spectrum in different load conditions are presented in Figure 5-17 and Figure 5-18. The magnitude of MMF contents in the I_{dr} signal have nearly the same magnitude compared with the corresponding error signal. As described in Chapter 4, the I_{dr} magnitude (DC component) is proportional to the outer loop reactive power level. Since the reactive power settings were defined as 0 for this set of tests, ideally there should be no magnitude change exist for I_{dr} current with active power load variation.

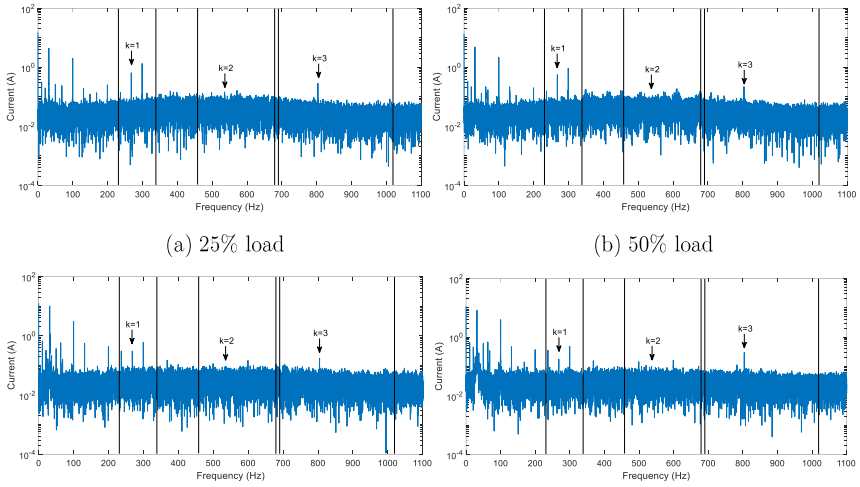

(a) 25% load (b) 50% load

(c) 75% load (d) 100% load

Figure 5-18 FFT spectra of the measured I_{dr} signal for 1340 rpm

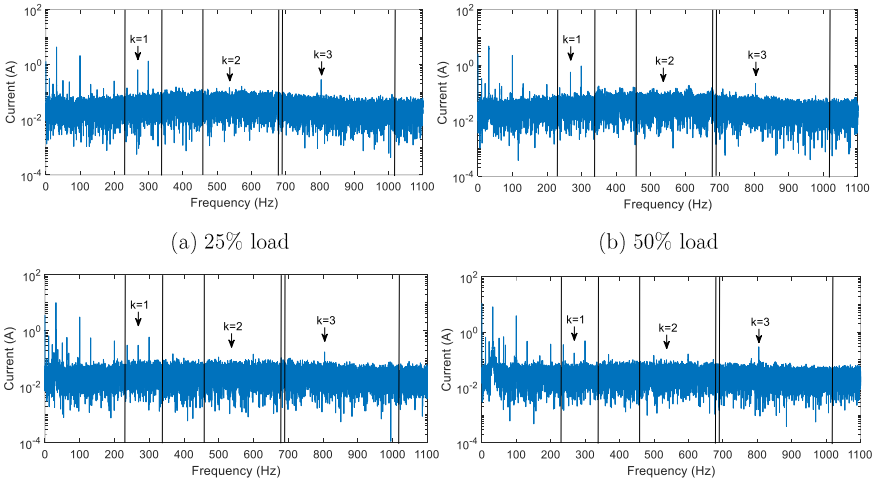

(a) 25% load (b) 50% load

(c) 75% load (d) 100% load

Figure 5-19 FFT spectra of the measured I_{drerr} signal for 1340 rpm

In practice, the decoupled linear relationship between outer loop contents (P_s and Q_s)

and inner loop contents (I_{qr} and I_{dr}) are not perfectly achieved due to the error inherent to the flux angle estimation. As the load level (i.e. active power demand) change is more focused investigated for DFIG sensorless control [134, 139, 140], reactive power level change is not presented here. The measured I_{dr} slightly dropped with load rising, i.e. 15.1A (25% load) decreased to 11.36A (100% load). The magnitude of speed dependent content in different load conditions are demonstrated in Table 5-3. It could be observed that the k=1 and 2 MMF contents magnitude are decreased with active power load incensement whilst k=3 contents have no significant tendency. As illustrated in Figure 5-17 and Figure 5-18, the k=1 MMF content is smaller than the SSU harmonic A_3 in magnitude for all load cases. Meanwhile, k=2 MMF content is not an evident harmonic in its searching bandwidth. However, an obvious k=3 MMF content is available for SSB identification. Compared with I_{qr} spectra, the MMF contents has stronger magnitude with no other disturbance harmonics exist in k=3 searching range, that makes its k=3 speed dependent harmonic a suitable choice for SSB frequency identification.

Table 5-3 Magnitude of MMF contents for I_{dr} spectra with 1340 rpm DFIG in variety loads

Load level	I_{dr}			I_{drerr}		
	k=1	k=2	k=3	k=1	k=2	k=3
25%	0.6485	0.1461	0.2864	1.088	0.2492	0.1737
50%	0.5589	0.1106	0.2207	0.5584	0.1106	0.2207
75%	0.3041	0.09338	0.1748	0.3034	0.09338	0.1748
100%	0.1768	0.1006	0.2961	0.1768	0.1006	0.2961

In summary, this section evaluated the controller loop signals' MMF harmonic contents in a variety of load conditions in the nominal range, compared with outer loop signal, the inner loop ones are less effected by noise and other non-relevant harmonics for speed dependent harmonic identification within searching bandwidth. After evaluating different load conditions, k=2 MMF harmonic in q axis controller signals (I_{qr} and I_{qrerr}) and k=3

in d axis controller signals (I_{dr} and I_{drerr}) spectra are assessed as the desired identification contents due to their obvious magnitude in spectra and less effected harmonics exist in the corresponding searching range. The former one with stronger magnitude is more evident in spectrum especially in the active power load varying conditions. As a result, the k=2 MMF harmonic in q axis controller signals is selected as the identification harmonic for SSB SSE in this research. To illustrate the consistency selected signal performance in other speed conditions, Figures 5-20 to 5-22 demonstrates the I_{qr} spectrum in 1440 rpm, 1550 rpm and 1590 rpm scenarios correspondingly. The error signal spectra are not demonstrated here as they have almost the same higher order spectra contents. The k=2 MMF content manifest an obvious magnitude in different load and speed signal spectra, which validated the purposed spectrum content is suitable for DFIG SSB SSE.

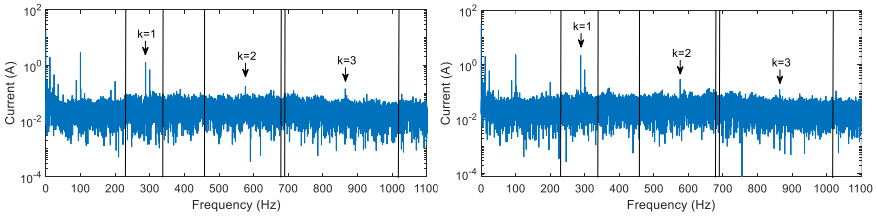

(a) 25% load

(b) 50% load

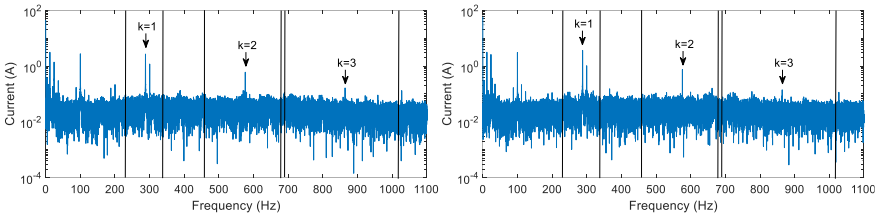

(c) 75% load

(d) 100% load

Figure 5-20 FFT spectra of the measured I_{qr} signal for 1440 rpm

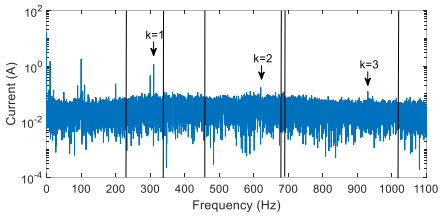

(a) 25% load

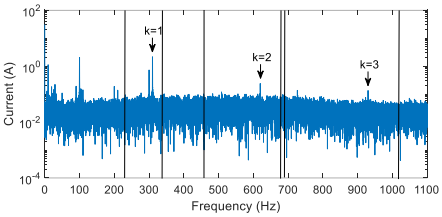

(b) 50% load

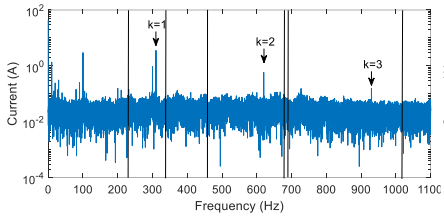

(c) 75% load

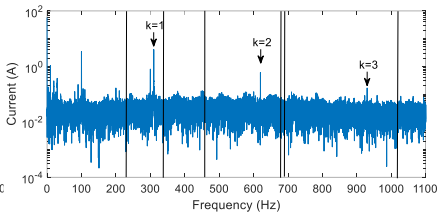

(d) 100% load

Figure 5-21 FFT spectra of the measured I_{qr} signal for 1550 rpm

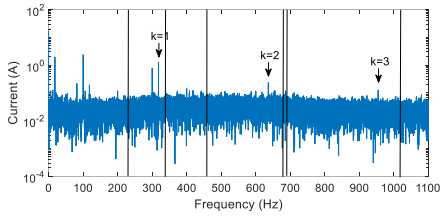

(a) 25% load

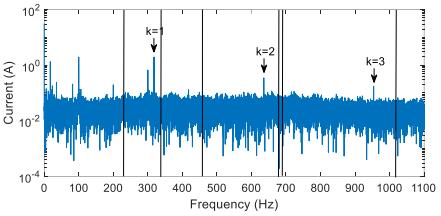

(b) 50% load

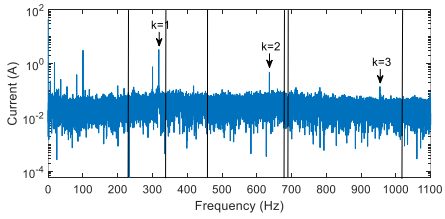

(c) 75% load

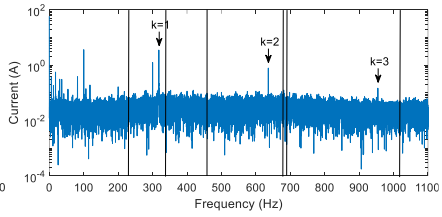

(d) 100% load

Figure 5-22 FFT spectra of the measured I_{qr} signal for 1590 rpm

5.3 Real-time frequency estimation scheme

The previous section evaluated the experimental DFIG signal spectrum in order to identify the suitable speed dependent harmonic contents for SSB frequency identification. To detect the target MMF harmonic content in real-time with sufficient fidelity and accuracy an adequate signal processing technique is required. In this section, the parabolic interpolation method is demonstrated as a tool suitable to identify MMF harmonic contents for DFIG SSB SSE in this research. The first introduces the theory and mathematical structure of the parabolic interpolation algorithm. Then the algorithm is validated in MATLAB platform utilizing an experimentally recorded signal in both constant speed and varying speed conditions. Finally a detailed introduction of the algorithm implementation in LabVIEW interface for real-time hardware execution is presented.

5.3.1 Overview of parabolic interpolation algorithm

The SSB speed estimation performance is highly dependent on the frequency tracking algorithm performance. To extract the harmonic content in the spectra, Fast Fourier Transfer (FFT) is the most commonly employed technique. However, the estimation results of these are highly affected by FFT resolution: a high resolution FFT routine requires hardware/software complexity and results in low estimation rate imposed by window time duration requirements, whilst a low resolution FFT results in low estimation accuracy. To secure both estimation rate and accuracy, different alternative frequency tracking techniques were examined in literature, as reviewed in Chapter 2.5.2. In this study, the parabolic interpolation algorithm is employed for SSB frequency identification due to its feature of low computational intensity and high resolution.

A periodogram of a signal is typically calculated by discrete Fourier transform (DFT). However, the DFT processed periodogram peak is generally displaced from the actual periodogram peak value since the continuous signal has to be discontinuous sampled while acquisition. As illustrated in Figure 5-23, an arbitrary periodogram is demonstrated: the DFT calculated peak is located at k_0 whilst the true maximum frequency is $f = (k_o + \delta)/N$, where δ is the frequency displacement meets the condition $-\frac{1}{2} \times resolution\ frequency < \delta < \frac{1}{2} \times resolution\ frequency$ and N is the sample length [141]. For illustration purposes, a typical DFT frequency maximum and two adjacent samples are named as $X(k_0)$, $X(k_0\text{-}1)$ and $X(k_0+1)$. The DFT located maximum is commonly called a coarse estimation and the estimation of actual displacement δ is referred as the fine frequency estimation [141].

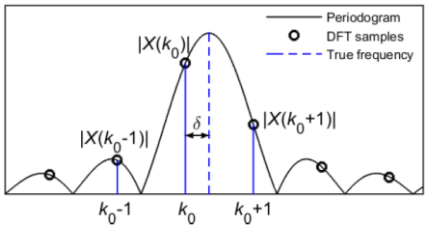

Figure 5-23 Illustration of displacement δ of true maximum position of periodogram from DFT [141]

Parabolic interpolation is an approach to refine the frequency estimation based on three DFT samples around the actual DFT maximum [141], and thus identify δ. It basically introduces a three points parabola fitting based on original DFT samples and then calculates the peak of periodogram from the interpolated points. Three samples with abscissa defined as $\theta_1, \theta_2, \theta_3$ are displaced with fixed distance (f_d) in periodogram, following definitions are made: $f_d = \delta_d \times \text{frequency resolution}, \theta_1 = f_{C2} - f_d, \theta_2 = f_{C2}, \theta_3 = f_{C2} + f_d$ while the center one θ_2 located at the DFT estimated periodogram

peak frequency f_{C2}. These samples are fitted by a parabola and the fine search is approved by obtaining parabola's vertex corresponding abscissa [141].

The calculation of the parabola vertex abscissa can be processed as follows: the three interpolation points are defined as $(\theta_1, P_1), (\theta_2, P_2)$ and (θ_3, P_3) in periodogram, the parabola that fits these points is $A\theta^2 + B\theta + C$. The vector of the parabola coefficients could be expressed as: [141]

$$\begin{pmatrix} A \\ B \\ C \end{pmatrix} = \begin{pmatrix} \theta_1^2 & \theta_1 & 1 \\ \theta_2^2 & \theta_2 & 1 \\ \theta_3^2 & \theta_3 & 1 \end{pmatrix}^{-1} \begin{pmatrix} P_1 \\ P_2 \\ P_3 \end{pmatrix}$$

The parabola coefficients could be calculated: [141]

$$A = \frac{\theta_3(P_2-P_1)+\theta_2(P_1-P_3)+\theta_1(P_3-P_2)}{(\theta_1-\theta_2)(\theta_1-\theta_3)(\theta_2-\theta_3)} \tag{5.3}$$

$$B = \frac{\theta_3^2(P_1-P_2)+\theta_2^2(P_3-P_1)+\theta_1^2(P_2-P_3)}{(\theta_1-\theta_2)(\theta_1-\theta_3)(\theta_2-\theta_3)} \tag{5.4}$$

$$C = \frac{\theta_2\theta_3(\theta_2-\theta_3)P_1+\theta_3\theta_1(\theta_3-\theta_1)P_2+\theta_1\theta_2(\theta_1-\theta_2)P_3}{(\theta_1-\theta_2)(\theta_1-\theta_3)(\theta_2-\theta_3)} \tag{5.5}$$

The abscissa of the vertex is then:

$$\theta_{ver} = -\frac{B}{2A} \tag{5.6}$$

$$= \frac{1}{2}\frac{\theta_3^2(P_1-P_2)+\theta_2^2(P_3-P_1)+\theta_1^2(P_2-P_2)}{\theta_3(P_1-P_2)+\theta_2(P_3-P_1)+\theta_1(P_2-P_3)}$$

The parabolic interpolation underpinned algorithm for DFIG SSB SSE could be illustrated by flowchart in Figure 5-24.

Step 0: A suitable DFIG signal narrowband maximised by a known speed dependent spectral component is identified for analysis and its pre-defined length time windows monitored for analysis

Step 1: First time fine search: The algorithm begins with excessively oversampled window

size FFT to obtain initial frequency peak location from high resolution periodogram.

Step 2: Parabolic points identification: Normal window size data set is employed for further calculation. Three parabola points, namely (x_1,y_1), (x_2,y_2) and (x_3,y_3), are interpolated in a regulated resolution periodogram (i.e. using the regulated window size but not oversampled one for parabolic interpolation), where x_2 is the maximum frequency position from high resolution periodogram and x_1 and x_3 are f_d away from x_2. Calculate the parabola values of three points. i.e. y_1,y_2 and y_3.

Step 3: Calculate the parabola coefficients A, B and C and hence identify the parabola vertex abscissa utilizing (5.6). The outcome is the maximum frequency f_{C2}.

Step 4: Work out the machine rotational speed with $\omega_e = \frac{5 f_{C2}}{2}$, which was introduced in chapter 4 equation (4.39).

Step 5: Provide the next set of data for following execution with overlapping window, i.e. push out **part** of data from previous window and integrate new data while keeping the window length constant. The implementation of overlapping window is aimed to increase the estimation rate, and involving the addition of only a part of the window size data set for every successive estimation.

Step 6: Define new parabola points for the new periodogram, where x_2 is the maximum frequency calculated from Step 3. Then calculate the parabola values, coefficients, new maximum frequency and eventually rotational speed.

Step 7: Repeat Step5 and Step 6 to keep tracking the machine rotational speed.

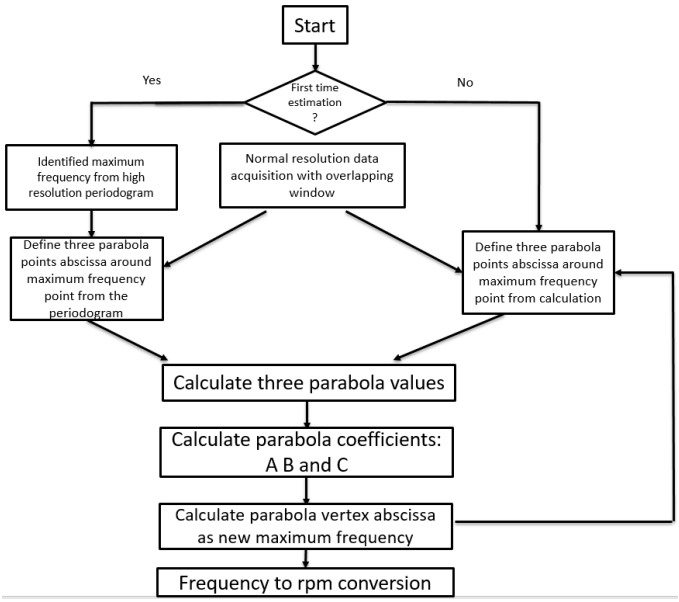

Figure 5-24 Parabolic interpolation involved SSB SSE algorithm

In this algorithm, the frequency displacement f_d has to be carefully selected as it affects the frequency tracking rate. The algorithm could tack the frequency change per second up to $f_d \times estimation\ speed$. i.e. Each iteration could identify the new periodogram peak within $\pm f_d$ range. However, large frequency displacement would result in a larger estimation error. To guarantee both estimation accuracy and feasible estimated speed variation rate, the displacement f_d is selected as $0.15 \times frequency\ resolution$ in this study, with an estimation rate of 40 *times/s* in a practically used 2.5Hz resolution frequency scenario, the frequency tracking algorithm could catch up with 15Hz per second variation. i.e. 37.5 *rpm/s* variation in speed.

5.3.2 Evaluation of parabolic interpolation algorithm in MATLAB interface

This subsection evaluates the illustrated algorithm's performance in a MATLAB interface. The q axis controller signal I_{qr}'s k=2 MMF harmonic component from experimental test is chosen for frequency extraction and speed tracking. Both constant speed test and variable speed test are performed following the same conditions: the selected normal window size is 2^{13} sample points with 2^8 window size shift. The over sampling window utilized for the initial maximum frequency identification is 128 times of normal window length, which takes both accuracy and process time consumption into account. The sampling frequency for experimental selected electrical signal is 50000Hz. The DFIG load condition for examined are selected as 100% full load.

A. Steady state speed estimation

A constant speed DFIG operation at 1550 rpm was firstly undertaken to examine the parabolic interpolation algorithm. The recorded experimental q-axis controller signal I_{qr} was sampled with 50000Hz (i.e. system required step size introduced in Chapter 3) from dSPACE platform. The recorded time duration is approximately 14.5s. In Figure 5-25, the estimation results are shown; each estimation is labeled with a circle in the plot with respect of reference operation DFIG rotational speed. Here the reference is the actual measured DFIG rotational speed. The SSB estimated speed is plotted in blue curve whilst the encoder measured speed is shown in orange curve. As illustrated in the plot, the 2812 estimated speed points from parabolic interpolation indicated a good match with reference rotational speed. i.e. 0.66% maximum error and 0.3% mean error.

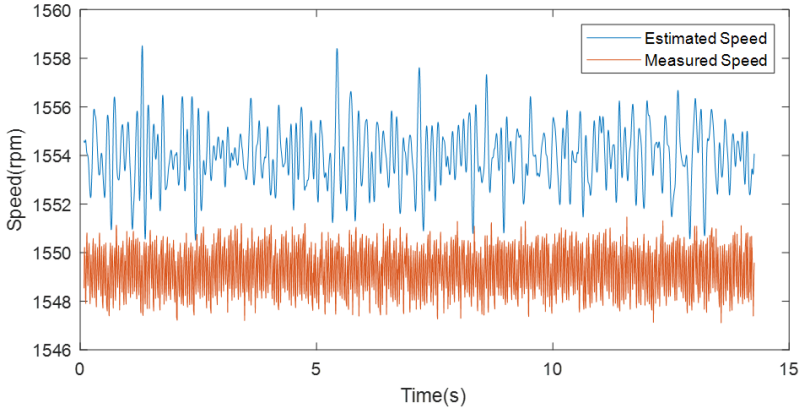

Figure 5-25 Parabolic interpolation SSB SSE at 1550 rpm DFIG

B. Variable speed estimation

A variable speed operation DFIG test was undertaken to evaluate the algorithm performance. A practical wind speed profile was employed to simulate the actual mechanical speed variation from generator side. Super-synchronous speed range 1520rpm-1650rpm was selected to emulate the DFIG high rated power generation scenario (see Figure 2-3 and Figure 2-4). Again, in Figure 5-26 and Figure 5-27. the q-axis controller signal I_{qr} was recorded for a minute and the algorithm executed speed estimations and it's instantaneous error. 11897 estimations are logged with blue in the plot whilst the actual DFIG measured rotational speed is exhibited with red line as a reference. The presented data are seen to be in good agreement, with the estimation maximum error rate being 1.05% and its average error rate 0.27 %. According to both constant and variable speed testing results, the feasibility of parabolic interpolation SSB SSE in DFIG system has been validated from theoretical point of view. The parabolic interpolation based real-time speed estimation system implementation procedure will be introduced in the following section.

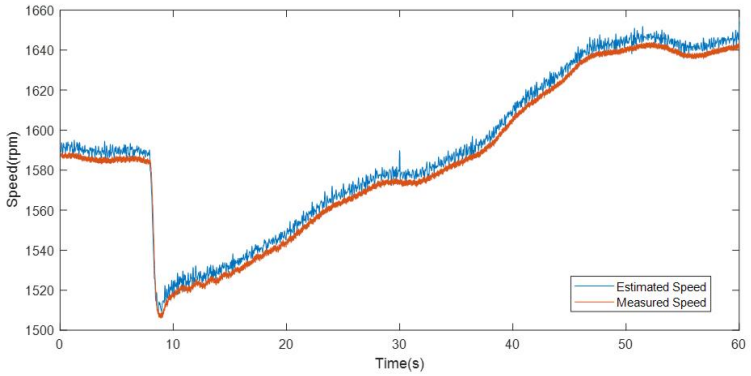

Figure 5-26 Parabolic interpolation SSB SSE in variable speed DFIG

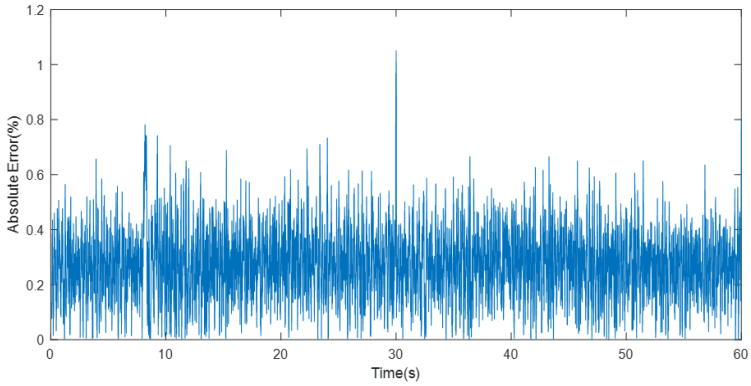

Figure 5-27 Parabolic interpolation SSB SSE real-time error recording in variable speed DFIG

5.3.3 Sensorless speed tracking algorithm implementation in LabVIEW interface

To enable practical real-time SSB SSE, LabVIEW codes are implemented on a national instrument NI-9024 compactRIO real-time platform to functionalize sensorless speed estimation algorithm introduced in previous section. This sub-section begins with real-time platform introduction, then the overall LabVIEW coding structure and FPGA based

signal acquisition are presented. The parabolic interpolation realization in LabVIEW interface is finally demonstrated.

A. Real-time platform overview

The compactRIO (cRIO) consists of the real-time controller, signal input and output modules and mounted on the chassis. The NI-9024 cRIO platform utilized in this study has a high performance processor and enables real-time operating system (RTOS) programming in LabVIEW interface [142]. The I/O modules could be directly connected to build in FPGA, which is an advanced and programmable hardware could be implemented in LabVIEW FPGA interface. The FPGA is connected to the processor by a high performance duplex peripheral component interconnect bus. The built in data transfer mechanisms in LabVIEW is responsible to obtain data from I/O modules to FPGA for data acquisition, processing as well as to link the FPGA to host computer for further real-time executions [109]. The NI-9024 platform is illustrated in Figure 5-28.

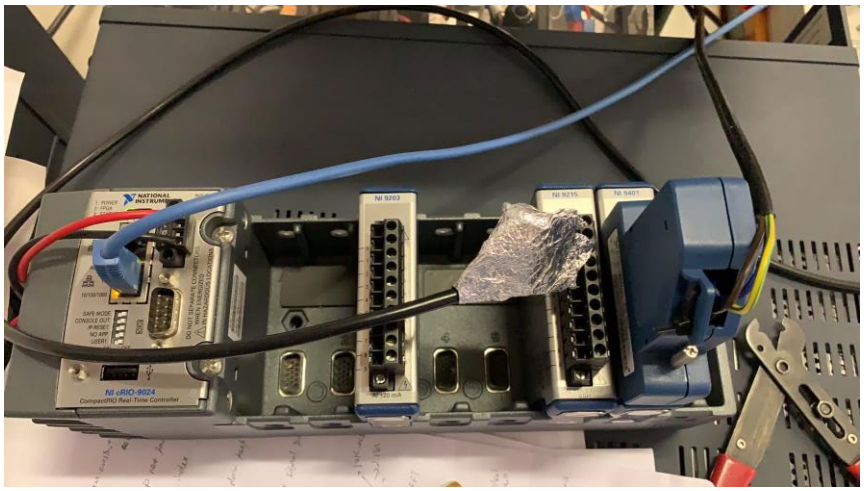

Figure 5-28 NI cRIO-9024 platform

The I/O NI-9125 analogue input module is employed for data acquisition in this research. NI-9125 is a 16-Bit resolution, 100kS/s/ch, 4 differential channels with ± 10V analogue input module [143]. It acquires DFIG q-axis controller signal I_{qr} from dSPACE DAC channel and send it to FPGA and eventually HOST program for spectrum extraction. A simplified shielding is employed to the terminal of cable connection part to mitigate the noise disturbance.

To assess the real-time speed estimation performance, the actual encoder measured speed is synchronously acquired with estimated speed. The measured speed is processed by phase locked loop (PLL) (introduced in Chapter 3) employed for DFIG system to secure precision instantaneous speed reference collection from dSPACE platform.

In this research, the LabVIEW FPGA is responsible for data acquisition and the post processing and real-time execution are offered by the Host program. The programming of both are based on LabVIEW virtual instrument (VI) code architecture, which is established by functional graphical block diagram coding. The system relevant configurations like sample rate are determined in corresponding blocks' settings.

B. Structural outline of LabVIEW code

The implementation of real-time SSB SSE system is based on LabVIEW interface. The structural flowchart is demonstrated in Figure 5-29.

The examined signal data is first acquired by NI-9215 and temporally stored in FPGA memory. The memory size is pre-defined as desired overlapping window shift size n_s. The stored data is then transferred to the HOST VI utilizing Direct Memory Access (DMA)-First In First Out (FIFO). By employing DMA, the calculation in HOST computer side could proceed while FPGA target sending data to the HOST. As illustrated in section 5.3.1, oversampled FFT is first executed to provide reference initial parabola point

position. Then further parabolic interpolation algorithm is deployed based on signal from overlapping HOST window to obtain the frequency component of interest and thus machine rotational speed.

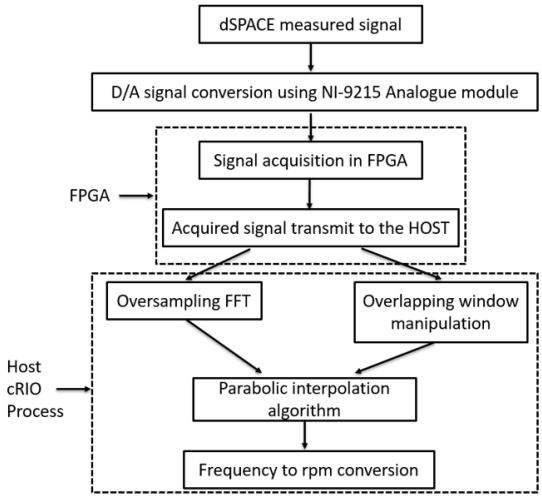

Figure 5-29 Structural flow chart of SSB SSE real-time system implementation

One of the challenges is to make the sampled normal size window overlapping in LabVIEW interface. To this end, the HOST window size (n_w) is defined integer a times of shift size (n_s) while a is determined by required overlap ratio. The following diagram Figure 5-30 is demonstrated to virtualize overlapping window development process for clarify.

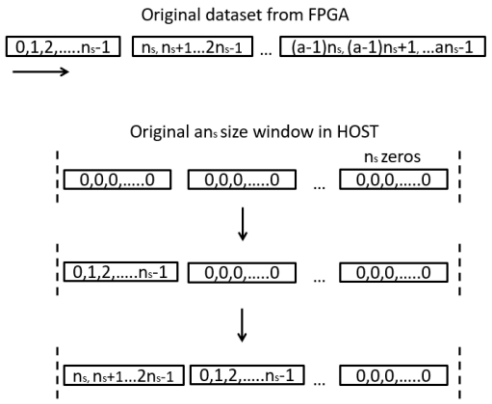

Figure 5-30 Overlapping window implementation principle

The acquired data is transmitted from FPGA to HOST VI in terms of n_s shift size window. The normal size HOST window utilized for parabolic interpolation is initially set as an_s zeros. The fundamental idea here is to fill in n_s new data in normal size window and push the earliest n_s data set out of the sample window. However, as illustrated in Fig.5.30, the demonstrated transmission process would make the order of data different from its original, i.e. in the HOST window, the data point n_s is supposed to be placed after n_s*-1* . Besides, the earliest data should be located at beginning part of the window. To get rid of these undesired effects, two reverse functions are employed to shift window and HOST window as shown in Figure 5-31.

Reversing every shift size window from FPGA makes the elements in HOST window placed in reversed order compared to the original data set. The other reverse action is deployed for HOST window to rebuild the order of elements so their layout is identical to the original signal data sequence. After all elements in HOST window are filled with FPGA transmitted elements, the elements would be employed for parabolic interpolation algorithm calculation to obtain frequency content of interest then provide machine

rotational speed. Afterwards, n_s new elements are fed into HOST window to replace the earliest n_s elements for next calculation. The overlapping ratio is determined by a.

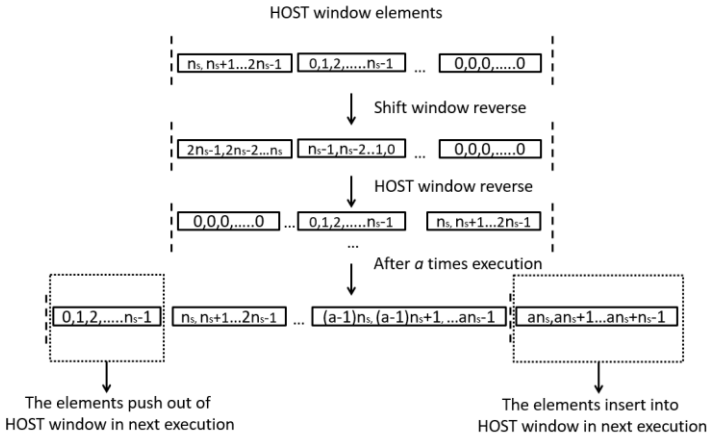

Figure 5-31 Overlapping window implementation principle with reverse fix

Regarding to the proposed overlapping window manipulation scheme, the LabVIEW shown in Figure 5-32 demonstrates how overlapping window are implemented in the HOST VI.

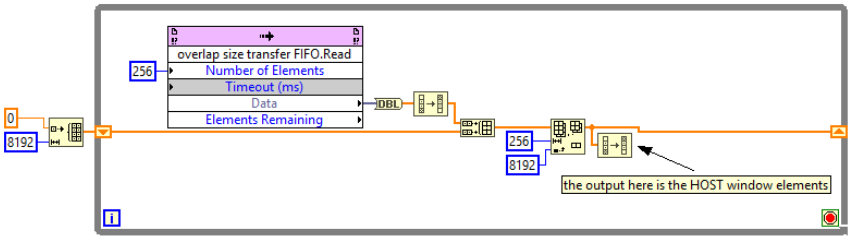

Figure 5-32 LabVIEW code of overlapping window implementation

The HOST window is regulated using fixed size array in LabVIEW code to enable

element manipulation needed in this algorithm and the elements are initialized as zeros at beginning. The acquired signal elements from FPGA side are transferred to HOST by DMA-FIFO, which sends 256 (n_s) elements for every loop calculation. The inversed FPGA transferred window shift size elements are added to the end of HOST array by the "build array" block thus offers an 8192 (an_s)+256 elements array. The resultant array is then processed by "delete from array" block to remove the earliest 256 elements from the array and a new array stored in the shift register for the next execution. Finally, the HOST window elements are reversed before sending elements for further calculation.

C. LabVIEW FPGA program implementation

In this study, FPGA VI is developed to acquire signal from NI 9215 for DFIG signal. The DFIG signal is stored in memory and transmitted to the HOST in 2^n element frames by DMA-FIFO. The elements are written in FIFO after checking the status of DMA-FIFO to get rid of FPGA DMA buffer overflow. With elements written in FPGA VI utilizing the write method of the FIFO method node, the HOST VI instantly reads the elements from the read method of the FIFO node at the same time using "invoke method" [109]. The LabVIEW code illustrated in Figure 5-33 shows how signals acquired in FPGA and transmitted to the HOST.

In the while loop shown in the figure below, the acquired data is written in a fixed size memory and the sample rate can be defined by the loop timer. The lower while loop reads the elements from memory and writes them into the DMA FIFO. The size of the DMA-FIFO should be at least twice of memory size to secure no data loss during transmission. The execution time of the loop can be checked by identifying the tick counts difference inside and outside the loop with the shift register storing previous value.

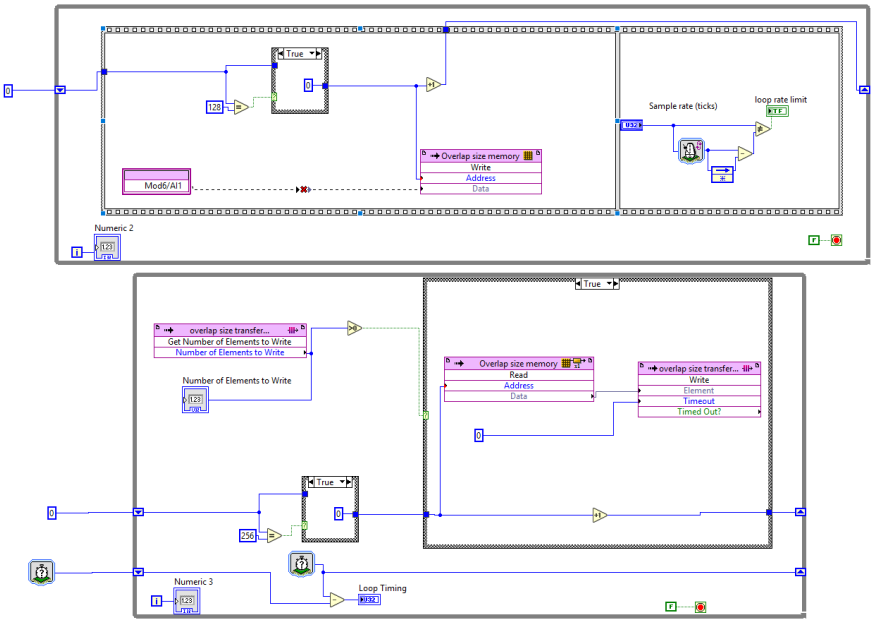

Figure 5-33 Coding for signal acquisition in FPGA

D. Parabolic interpolation in LabVIEW

After receiving the acquired signal from the FPGA and modifying data into overlapping windows, the main SSB SSE algorithm utilizing parabolic interpolation is employed for frequency extraction, which is the majority part of HOST VI. At the beginning of programming, the algorithm implementation is approved by MathScript RT module inFigure 5-34. The module enables text-based code in LabVIEW graphical coding interface to functionalize the algorithm introduced in section 5.3.1.

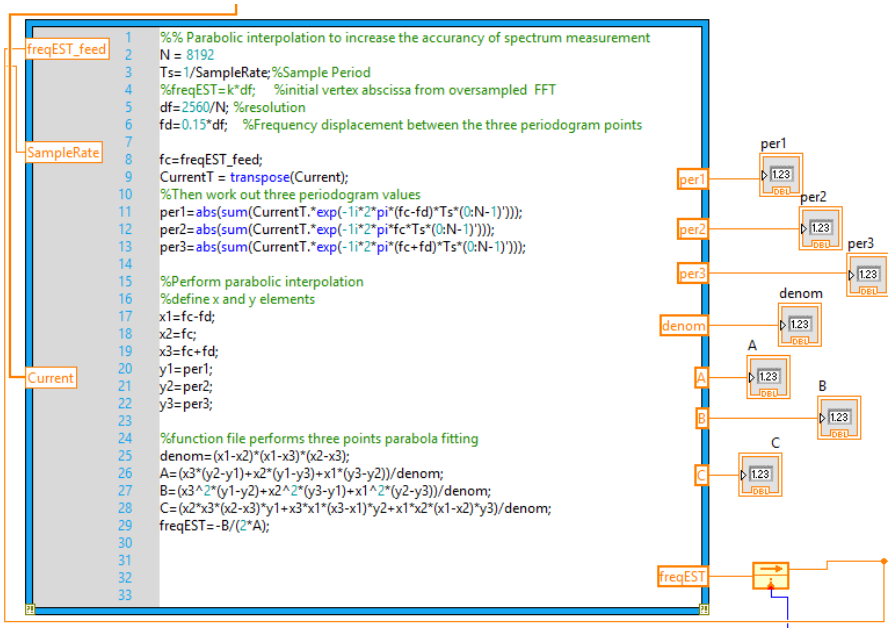

Figure 5-34 Real-time parabolic interpolation search algorithm

The following initial inputs are required for the listed code: window overlapping data, signal sample rate and initial estimated frequency from window oversampling FFT as a reference for first estimation. The window size and parabola points displacement are defined at the beginning of code. Then three parabola points identification and parabola vertex abscissa calculation are executed to work out the new maximum frequency as described in section 5.3.1. A feedback node is deployed to send the calculated frequency as a reference for the following iteration execution. The rotational speed is calculated from the estimated frequency via equation (4.39) in HOST VI. However, in real-time frequency observation tests, the illustrated LabVIEW code could not capture up-to-date frequency from signal due to the following limitation: the MathScript significantly slows the execution down, especially when large scale analysis needs processing. In consequence,

the algorithm processing speed could not keep up with the data acquisition rate while the system is running, and thus the accuracy of frequency estimation could not be guaranteed.

To speed up the execution, the parabolic interpolation algorithm is developed in LabVIEW code (i.e. graphical code) to avoid the need for utilizing MathScript node. Though a sizeable graphical code is required to achieve this when compared with MathScript code, the graphical code is executed significantly faster than MathScript due to the fact that the LabVIEW graphical code is strictly typed while MathScript is implemented on top of the native implementation. Referring to Figure 5-34, most of MathScript commands are easy to implement. The challenging part here is to develop the parabola values calculation in line 11-13. Literally the original command was to execute Discrete Fourier Transform, which requires a "For loop" to sum up all the involved iterations. Therefore, it would calculate elements from 0 to N-1 one by one then add them up. As a result, the execute of routine has to wait until all these iterations are finalized to then proceed with rest of the algorithm, which is time consuming. An alternative approach was implemented to replace the iteration process with one calculation: by modifying the signal data set and its corresponding element order number n in terms of matrix, the DFT parabola value could be regarded as the result of two matrix multiplication. Typed code line 12 is programmed with following LabVIEW code in Figure 5-35.

The original signal data is converted to matrix form by "build matrix" in column. The exponent of Euler's number is regarded as a constant with complex number multiplies number series from 0 to N-1 and converted to transposed matrix. The multiplication of two matrices makes the execution of the calculation procedure possible within a single

iterations, thus significantly reducing the computational requirement on the processor. The absolute parabola values are then processed for further calculations.

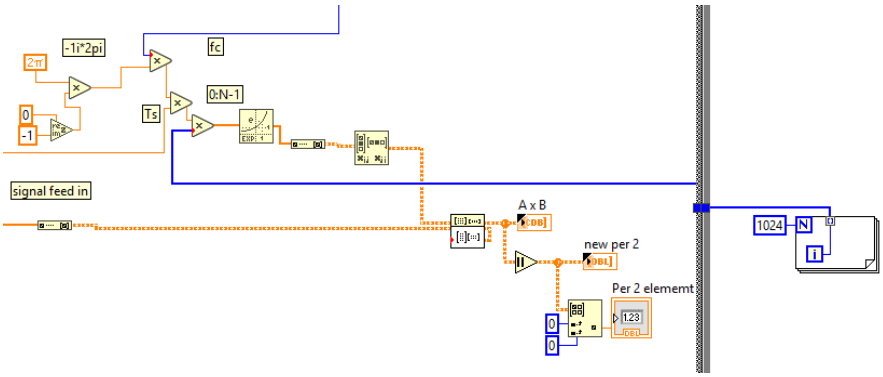

Figure 5-35 Typed code implementation in terms of LabVIEW coding

5.4 Real-time performance for DFIG sensorless speed estimation

In section 5.3, a detailed parabolic interpolation based SSB SSE algorithm was detailed, including background theory, algorithm off line evaluation and its real-time execution routine development in LabVIEW. A range of real-time experiments are undertaken in this section to evaluate the proposed algorithm's efficacy in SSE. The estimation is based on tracking of the k=2 harmonic component of the controller current I_{qr}, deemed to be an optimal component for tracking in the practical system analysed in this work referring to the spectral analysis in the previous section. Both constant and variable speed operation in different load conditions were examined. The measured speed from an encoder mounted on the machine shaft was synchronously cross-correlated with the estimated speed to ascertain the error rate margins and thus the feasibility and

performance potential of the proposed SSE scheme. The findings are presented in the following subsections.

5.4.1 Constant speed estimation

Speed estimation in steady-state conditions is firstly evaluated to explore the performance of the applied algorithm in a less dynamic set of operating conditions as a precursor to its evaluation in a fully transient generator operating regime. This subsection consists of two topics: the evaluation of the algorithm performance at different estimation rates, and the validation of its performance in a variety of operating load and speed conditions for a fixed estimation rate.

The speed estimation rate is regulated as following without overlapping window employed:

$$estimation\ rate = \frac{f_{sample}}{n_w} \tag{5.7}$$

where f_{sample} is the sample frequency, n_w is the window size (i.e. the number of data points for each execution).

With the overlapping window employed, as needed to increase the estimation rate, the estimation rate can be calculated as:

$$estimation\ rate = \frac{f_{sample}}{n_w} \times \frac{n_w}{n_s} \tag{5.8}$$

where n_s is the shift size of overlapping window in each algorithm iteration, giving:

$$estimation\ rate = \frac{f_{sample}}{n_s} \tag{5.9}$$

It could be concluded that the estimation rate is theoretically determined by f_{sample} and n_s. However, in a practical real-time LabVIEW routine, the algorithm execution rate is

also limited by the execution window size n_w (i.e. larger n_w consumes more time to execute due to an inherent increase in computational demand on the real-time platform). To guarantee both estimation accuracy and rate: larger window size result in higher frequency resolution thus reaches more accurate estimation however more time consuming in the algorithm execution. A window size 2048 was selected in real-time application. Moreover, it has also been tested shift window size 128 has the best performance: smaller shift window size like 64 would increase the computational complexity while the SSE accuracy can not be greatened in larger shift window size like 256. An investigation of different estimation rate performance evaluation was undertaken by testing the algorithm operation at a range of different values of $f_{sample.}$. A typical operating point (1550 rpm 100% load) was selected to illustrate the findings of this case study.

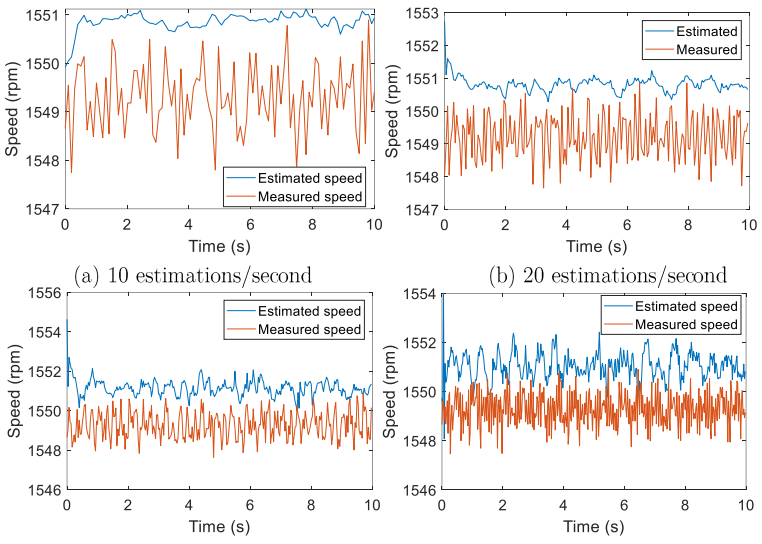

(a) 10 estimations/second (b) 20 estimations/second

(c) 30 estimations/second (d) 40 estimations/second

Figure 5-36 Real-time speed estimation vs measurement in different estimation rates

The obtained real-time results for different estimation rates are shown in Figure 5-36 and the corresponding error statistics are summarized in Table 5-4.

Table 5-4 Summary of estimation error in different estimation rates

Estimation rate (times/s)	Sample frequency (Hz)	Max error (%)	Mean error (%)
10	1280	0.21	0.10
20	2560	0.19	0.08
30	3840	0.38	0.12
40	5120	0.29	0.12

The real-time estimation rate is constrained by the LabVIEW algorithm inherent computing time, which is related to the hardware processor performance and the algorithm programming approach. With the window size of 2048, it takes 24ms to execute each iteration in the proposed real-time routine, which means the maximum attainable estimation rate with the real time hardware available for this work is approximately 42 estimations per second. In consequence, the estimation rates evaluated in this study range from 10 to 40 estimations per second. As illustrated in Figure 5-36, the estimated speed (blue) is instantaneously cross-correlated to the measured speed (orange) for a typical 10 second period. Although the estimated speed is slightly higher than measured speed due to inherent PLL speed measurement limitation described in Chapter 3. It could be generally observed a good match between measurement and prediction. Referring to Table 5-4, the obtained max error rate is in the range of 0.19% to 0.38% whilst the mean error rate is in the range of 0.08% to 0.12%. With the increase of sample frequency (i.e. estimation rate), the error is slightly increased but a good level of accuracy is still maintained, which manifests with better performance of real time estimators reported in literature [135, 144, 145]. This indicated that the proposed algorithm is competent in real time estimation at up to 40 estimates per second rate on the available test system,

but has strong potential for an even higher real time execution rate assuming availability of a more powerful real time execution platform. Also, the proposed algorithm shows higher real-time speed estimation rates compared with the published studies [135, 144, 145].

A range of experiments were undertaken to evaluate the algorithm performance in different DFIG operating conditions. The following four operating speeds consisting two sub- and two super- synchronous points were tested: 1340 rpm, 1440 rpm, 1550 rpm and 1590 rpm. For each considered speed point, four different load levels were examined by performing tests at 25%, 50%, 75% and 100% nominal current load. The estimation rate of 40 per second was selected for these tests. Figures 5-37 to 5-40 shown below demonstrate the speed estimation performance evaluated by synchronously estimating and measuring the rotor speed for 10 seconds in different load and speed operation points.

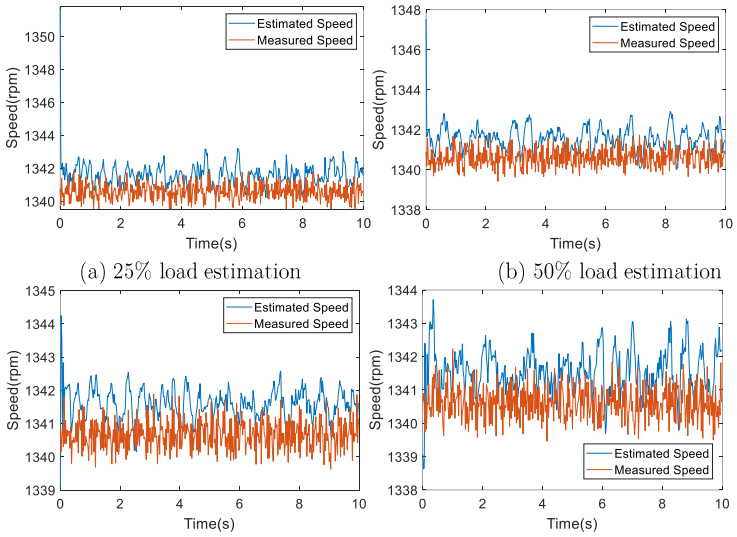

(a) 25% load estimation (b) 50% load estimation

(c) 75% load estimation (d) 100% load estimation

Figure 5-37 Different load conditions speed estimation vs measurement at 1340 rpm

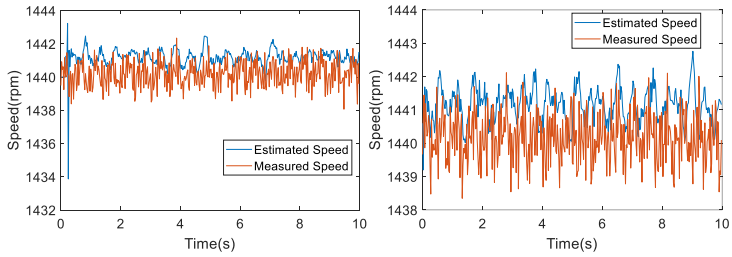

(a) 25% load estimation

(b) 50% load estimation

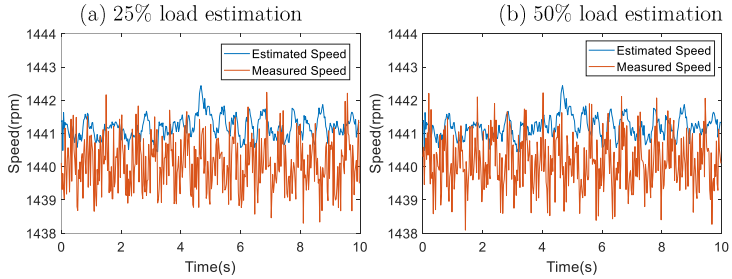

(c) 75% load estimation

(d) 100% load estimation

Figure 5-38 Different load conditions speed estimation vs measurement at 1440 rpm

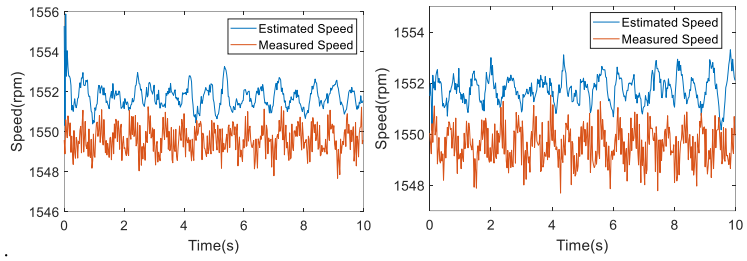

(a) 25% load estimation

(b) 50% load estimation

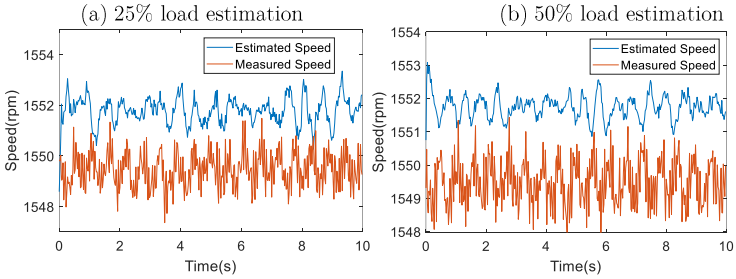

(c) 75% load estimation

(d) 100% load estimation

Figure 5-39 Different load conditions speed estimation vs measurement at 1550 rpm

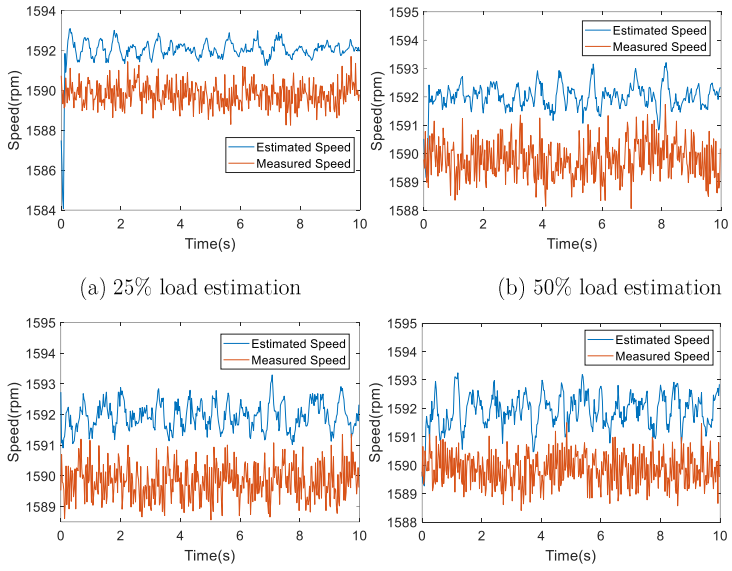

(a) 25% load estimation

(b) 50% load estimation

(c) 75% load estimation

(d) 100% load estimation

Figure 5-40 Different load conditions speed estimation vs measurement at 1590 rpm

The corresponding error statistics are summarized in Table 5.5.

Table 5-5 Summary of estimation error in different load and speed conditions

1340 rpm			1440 rpm			1550 rpm			1590 rpm		
Load level (%)	Max error (%)	Mean error (%)	Load level (%)	Max error (%)	Mean error (%)	Load level (%)	Max error (%)	Mean error (%)	Load level (%)	Max error (%)	Mean error (%)
25	0.824	0.082	25	0.433	0.078	25	0.368	0.151	25	0.373	0.144
50	0.490	0.077	50	0.277	0.078	50	0.310	0.146	50	0.269	0.139
75	0.300	0.075	75	0.226	0.082	75	0.300	0.143	75	0.249	0.135
100	0.262	0.079	100	0.239	0.080	100	0.283	0.139	100	0.271	0.131

The measurements indicated that the real-time speed estimation can be achieved in both super- and sub- synchronous speed points in all load level conditions: the maximum estimated error rate lower than 0.824% as well as the mean error rate less than 0.151%

for low load condition (25%), while the maximum estimated error is lower than 0.49% and the mean error rate less than 0.146% in the load levels ≥ 50%. In general, the accuracy of the estimation increases with the load level rising. Referring to Table 5-2, the magnitude of harmonic content of interest utilized for SSB SSE are positively related to load level. Therefore, the characteristic content is more obvious in higher load conditions and better accuracy is achieved in the SSB algorithm. Still, the obtained estimation result at low load 25% condition shows a tolerable error rate, with an average error smaller than 0.15% and a maximum error smaller than 0.824%.

5.4.2 Variable speed estimation

To evaluate the real-time performance for emulated wind-driven operation, an actual wind speed profile was employed at the prime mover side (i.e. DC machine) of the DFIG system. A transient speed profile in the generating region representative of generator operating dynamics employed in MW size variable speed, which was utilized in the literatures [146, 147, 148]. The transient profile was obtained from a detailed WT model developed in Supergen Wind Consortium, which was employed to emulate wind resource variation information [148, 147]. As mentioned in last section, the sampling frequency was selected as 5120Hz to enable 40 estimations per second, the maximum rate allowed by the available FPGA platform computational capacity. The real-time speed estimation and instantaneous error for 150 seconds of the DFIG are demonstrated in Figures 5-41 to 5-48. Table 5-6 shows the measured performance parameters for all the investigated load conditions.

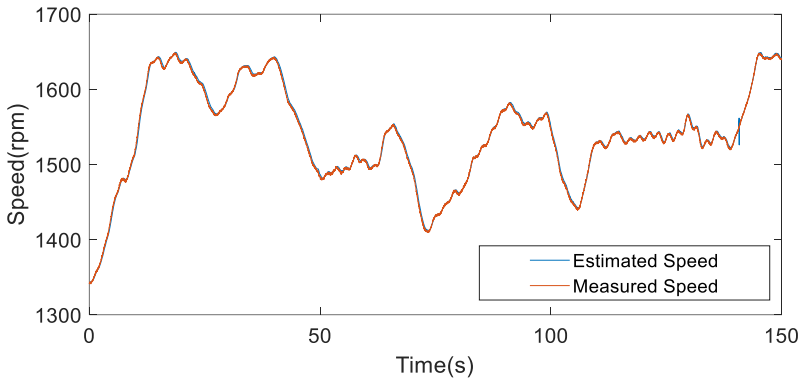

Figure 5-41 1340rpm-1650rpm speed profile estimation at 25% load

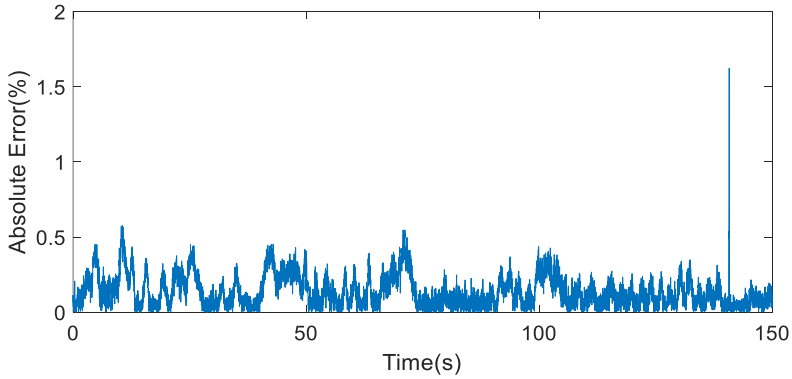

Figure 5-42 Error signal 1340rpm-1650rpm speed profile estimation at 25% load

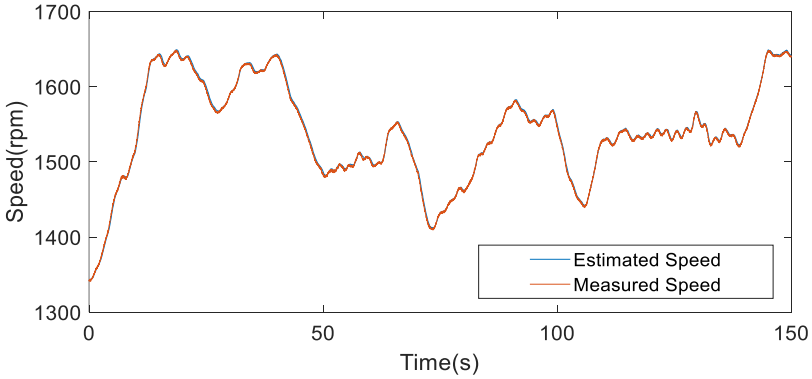

Figure 5-43 1340rpm-1650rpm speed profile estimation at 50% load

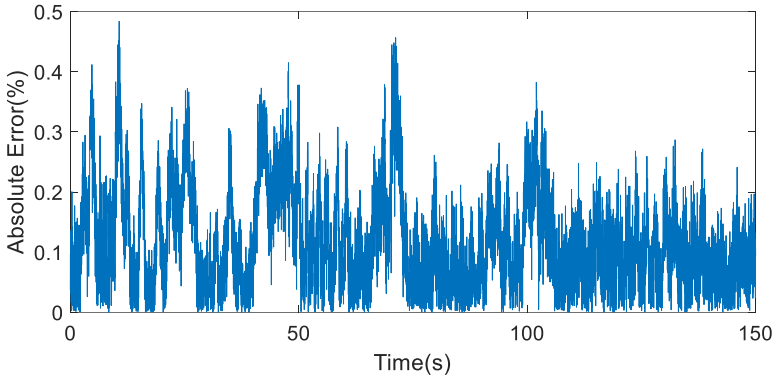

Figure 5-44 Error signal 1340rpm-1650rpm speed profile estimation at 50% load

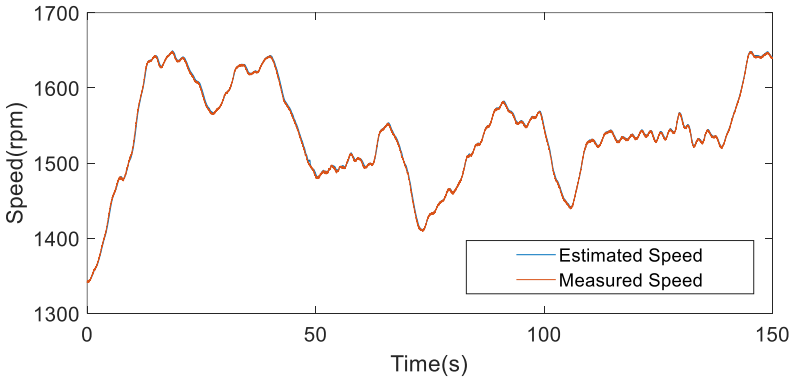

Figure 5-45 1340rpm-1650rpm speed profile estimation at 75% load

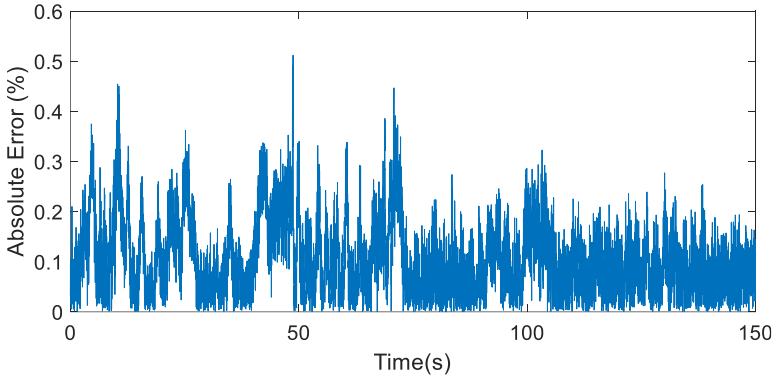

Figure 5-46 Error signal 1340rpm-1650rpm speed profile estimation at 75% load

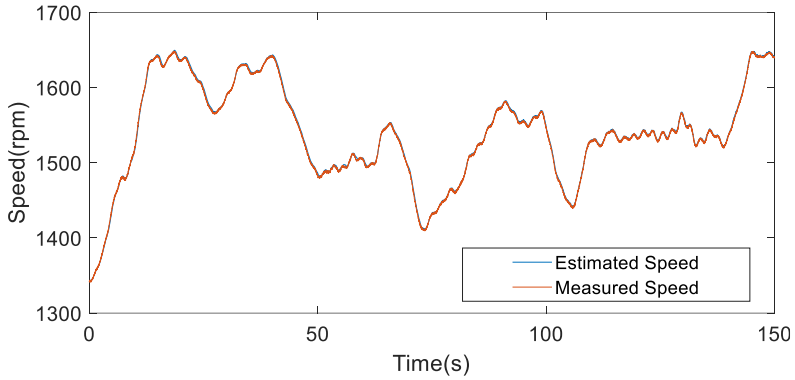

Figure 5-47 1340rpm-1650rpm speed profile estimation at 100% load

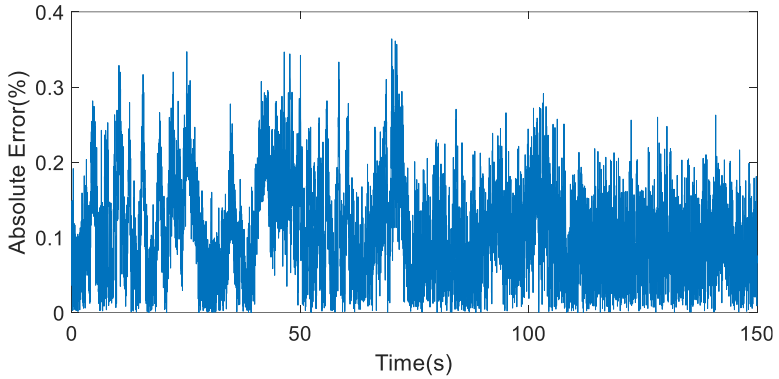

Figure 5-48 Error signal 1340rpm-1650rpm speed profile estimation at 100% load

Table 5-6 Summary of estimation error in different load conditions

Load level (%)	Max error (%)	Mean error (%)
25	1.63	0.19
50	0.48	0.12
75	0.51	0.10
100	0.36	0.10

The results demonstrate that real-time speed estimation is feasible for the operating ranges from sub-synchronous speed to super-synchronous speed of the DFIG in all load

conditions. The average estimation error is lower than 0.19% and maximum error is lower than 1.63% for all load conditions. Similar to constant speed estimation, more accurate estimation could be achieved in high load conditions, as the tracked spectral content will be more pronounced in these thus yielding higher estimation consistency. Recalling the previous spectrum analysis part, the magnitude of characteristic frequency component is nearly proportional to the load level, the identification of SSB SSE frequency component is more likely to be affected by the noise frequency (see the spike of estimated speed in low load condition). It is also important to point out that transient operation in higher load conditions is more typical of practical wind turbine generators operation, as these are designed to operate in as high average winds/loads as possible at the given location, hence the good estimation at higher loads could be deemed more pertinent to practical, field applications of generators.

5.5 Conclusions

Machine sensorless speed estimation (SSE) has been widely investigated by researchers due to its low cost, high reliability, better noise immunity and less maintenance required features. In WT system, SSE is an alternative approach to monitor generator rotational speed when encoder failure occurs. A novel DFIG SSE algorithm based on non invasive approach utilizing readily available signals embedded in the controller loops of the DFIG drive is therefore investigated in this chapter, which is spectral search based (SSB) SSE scheme utilizing parabolic interpolation. The proposed algorithm manifested good capability of high rate real-time estimation in both constant and variable speed scenarios. Compared with published researches, it has been shown this algorithm performs with a good degree of accuracy and higher estimation rate. Two main factors are essential to

approve the new technique: signal selection for spectrum search and SSB algorithm.

This chapter began with spectral analysis of experimental tested DFIG signals including terminal and controller signals. A typical load and speed condition was selected to evaluate DFIG signals' harmonic contents. The speed related harmonic contents in DFIG controller signals are clearer to obtain compared with terminal signals. To sort out the most appropriate controller signal's harmonic to track for SSB SSE, variable load conditions of controller signals were then assessed and eventually the q-axis controller signal I_{qr} is selected for DFIG SSE.

The second part of this chapter is the spectral harmonic content tracking scheme demonstration. A novel parabolic interpolation based SSB SSE algorithm was employed. The mathematical theory and structural overview of the algorithm was firstly exhibited. Then a validation study of the algorithm was proceed in MATLAB interface. Precision speed tracking could be observed in both constant and variable speed scenarios utilizing testing DFIG signal with parabolic interpolation. To approve the real-time speed estimation, the real-time platform NI-9024 cRIO platform with theoretical algorithm developed in LabVIEW interface are employed. The implementation process of FPGA and HOST LabVIEW code were demonstrated in detail.

Finally, the proposed LabVIEW algorithms were assessed and validated in real-time laboratory experiments on DFIG system. Both steady state and transient speed conditions tests were undertaken. The presented result indicate that the developed SSB SSE algorithm can provide a low error margin speed estimation in practical conditions, and particularly so at higher loads. To enable sensorless control of the DFIG, further development in shaft angular position estimation is required for the future research.

Chapter 6 Investigation of controller signals in DFIG system with shaft misalignment

Acknowledgement: The experimental study of this chapter was published in International Conference on Electrical Machines (ICEM2020). Some passages have been quoted verbatim from the following source [149].

6.1 Introduction

Shaft misalignment is characterized as a condition in which the shaft of the driving machine and that of the driven machine are not in the same center line. It is responsible for more than 50% of all rotating machinery problems [50] and can thus result in considerable downtime and economic losses, if a machine keeps running in misaligned condition. The operating life span of rotating machinery could be increased with accurate alignment [150]. As a result, the proper minoring of rotational machinery shaft alignment status is key to reduce the number of breakdowns, as well as the associated unplanned

downtime and economic losses. However, the alignment inspection is scheduled by extended service periods and ideally requires online monitoring due to a number of unavoidable drivetrain inherent factors. In a WT system, misalignment is a common problem reported to cause 30% of downtime [151], with the resulting undesired forces leading to damage or destruction of bearings, seals and couplings, and eventually having the potential to lead to gearbox and generator damage [152]. Correspondingly, misalignment monitoring and diagnosis are essential for contemporary WT drivetrains, and especially so where they are located in a remote and harsh operating environment, with more critical downtime and repair cost implications [153] [151].

Vibration monitoring is regarded as the typical approach that is widely used to forecast WT shaft misalignment. However, quality vibration sensors are generally costly and the required signal condition equipment to interpret their reading can also impose considerable expense. Furthermore, the different components of vibration signals and their relation highly depends on the flexible coupling type employed [154] hence diagnosis can sometimes be challenging. Alternative approaches for misalignment diagnosis were detailed in Chapter 2. In particular, the motor current signature analysis (MCSA) attracted much attention by researchers due to its inherent cost efficacy [60, 61, 62]. The presence of misalignment was shown to have the potential to manifest as additional content in the line current spectrum. For DFIG, the utilisation of controller signal to achieve condition monitoring has received little research attention. One of the few applications was reported in [80], where the DFIG controller signals were employed to monitor the rotor electrical asymmetry fault. Additionally, DFIG stator and rotor electrical asymmetry recognition utilizing controller signals was investigated in [45]. In this chapter, an investigation is undertaken to explore the feasibility of shaft misalignment diagnosis using DFIG controller signals.

The theoretical explanation of the relevant shaft misalignment effects will be presented to unfold how shaft misalignment influences machine mechanical performance. Then a DFIG model study undertaking a comparison of controller signal spectral signatures between a healthy DFIG and that operating with misalignment is illustrated to explore and identify potential fault signature characteristics in the controller signal spectrum. Finally, the experimentally measured DFIG signals are analysed to validate and analyse the observed phenomena.

6.2 Mechanical modelling of shaft misalignment

In general, the shaft misalignment condition can be classified in different types: parallel (or offset) misalignment, angular misalignment or the combination of the two. This section revises the mechanical features of coupled rotating shaft behavior in presence of angular misalignment (illustrated in Figure 6-1), with a view to identifying mechanical disturbances that can originate from this condition.

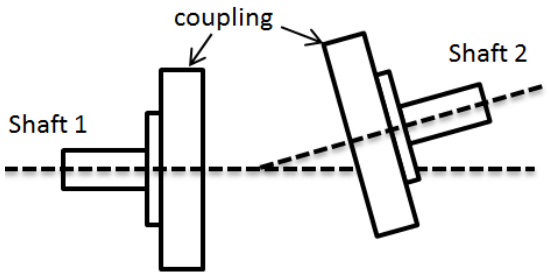

Figure 6-1 Angular shaft misalignment – illustration

Angular shaft misalignment can be represented by a simplified system that includes the universal joint model [62]. A general illustration of a universal joint is given in Figure 6-2 a, and the rotational angular position of both shaft ends is shown in Figure 6-2b [155].

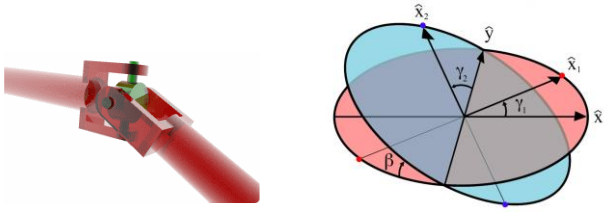

(a) Universal joint model (b) Universal joint motional variables

Figure 6-2 Universal joint model illustration

As illustrated in Figure 6-2(b), the drive shaft is perpendicular to the red plane (shaft initially mounted at $\hat{x}$) while the driven shaft is perpendicular to the blue plane (shaft fixed at $\hat{y}$; the angular difference of the planes is labelled as β, which is regarded as the angular misalignment angle for mechanical effect modelling. The angular displacement of the drive shaft is marked as $\gamma_1$with respect to vector $\hat{x}$ ($[0,0,1]$), thus the corresponding rotational position is defined as $\widehat{x_1}$ ($[\cos\gamma_1, \sin\gamma_1, 0]$). Similarly, the driven shaft is mounted at $\hat{y}$ of blue plane, $\widehat{x_2}$ is the driven shaft rotational position and γ_2 is the angular difference between $\widehat{x_2}$ and $\hat{y}$ on blue plane. If we set $\hat{x}$ as the reference position, $\widehat{x_2}$ with respect of $\hat{x}$ is $[-cos\beta sin\gamma_2, cos\gamma_2, sin\beta sin\gamma_2]$. The shaft fixing points on plane are fixed at pre-defined position, $\widehat{x_1}$ and $\widehat{x_2}$ must be located at right angle to each other, i.e. the dot product of $\widehat{x_1}$ and $\widehat{x_2}$ is zero. In consequence, the relationship between the drive shaft movement angle γ_1 and the driven shaft angle γ_2 connected by universal joint can be expressed as follows: [155]

$$\gamma_2 = tan^{-1}\left(\frac{1}{cos\beta} tan\gamma_1\right) \tag{6.1}$$

With the universal joint model, the simplified shaft misalignment model is exhibited in Figure 6-3.

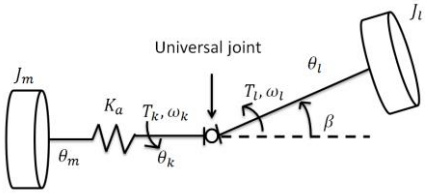

Figure 6-3 Shaft misalignment universal joint based model

Here, the misalignment angle, β, and the motor position angle, θ_m, are used to define angular misalignment. In Figure 6-3: θ_l is the load side shaft angular position, θ_k is the auxiliary angle defined to represent the joint transmitted rotational angular position on the motor side, ω_l and ω_k are the joint load side and motor side shaft angular speed, T_l and T_k are the joint load side and motor side shaft torque, J_m and J_l are the motor and load inertia, and K_a is the flexible coupling elasticity constant. Recalling equation (6.1), the fundamental kinematic relations for the universal joint are well established and give the relationship between load and motor shafts angular displacements, θ_l and θ_k, for a β degrees misaligned joint: [154]

$$\theta_k = tan^{-1}(\frac{1}{cos\beta} tan\theta_l) \tag{6.2}$$

By differentiating to equation (6.2), the angular speed is given:

$$\omega_k = \frac{1}{1+\left(\frac{1}{cos\beta} tan\theta_l\right)^2} \cdot \frac{1}{cos\beta} \cdot \frac{1}{cos^2\theta_l} \cdot \omega_l \tag{6.3}$$

Which can be simplified to:

$$\omega_k = \frac{cos\beta}{1-(sin\beta)^2(cos\theta_l)^2} \omega_l \tag{6.4}$$

For clarify, equation (6.4) can be expressed as: [156]

$$\frac{\omega_l}{\omega_k} = \frac{1-(sin\beta)^2(cos\theta_l)^2}{cos\beta} = \frac{1+\cos^2\beta}{2cos\beta} + \frac{1-\cos^2\beta}{2cos\beta}\cos(2\theta_l) = K_1 + K_2\cos(2\theta_l) \tag{6.5}$$

To clarify the content introduced by shaft misalignment, equation (6.5) was finally

written in terms of a combination of parameters K_1 and K_2. The load angular displacement is $\theta_l = 2\pi f_r t$, where f_r is the load shaft fundamental rotational frequency $(f_r = \omega_r/2\pi)$. It becomes apparent that the presence of angular misalignment will fundamentally give rise to speed signal pulsations at twice the rotational speed frequency (e.g. $2f_r$), and thus additional spectral contents would be expected to be observed to distinguish shaft misalignment fault. Stator current has been validated in some studies to diagnose shaft misalignment by manifesting a marked change in the $2f_r$ sideband in the spectrum [154] [156]. In this chapter, the DFIG controller signals are evaluated to explore the feasibility of shaft misalignment recognition. The spectral analysis based on DFIG harmonic model is demonstrated in next section.

6.3 Model study of shaft misalignment DFIG harmonic emission

In this section, a comparison model study is undertaken to evaluate how the presence of the shaft misalignment condition can affect the DFIG electrical signals, and particularly those in its controller loops. To introduce shaft misalignment effect in the DFIG harmonic model (based on chapter 4), the universal joint model illustrated in last section is implemented by modulating the DFIG operating speed signal with equation (6.4). Instead of using a constant speed in Simulink model for DFIG healthy operation, the mechanical speed input of DFIG is expressed via equation (6.4) to indicate shaft misalignment effect.

6.3.1 Prediction of DFIG signal spectral a contents

Stator flux oriented control (SFOC) is a commonly used control scheme in DFIG WT

applications [157]. Two cascaded control loops enable independent control of stator active (P) and reactive power (Q) in the outer loop by inner controller loop regulation of the two axis (d and q) rotor current in the stator flux oriented reference frame (I_{dr} and I_{qr}) [22]. This section explores the spectral contents of the following DFIG electrical signals: stator A phase current I_{sa}, rotor A phase current I_{ra} and relevant controller signals (stator active power P_s, stator reactive power Q_s, controller active power error P_{err}, controller reactive power error Q_{err}, rotor controller current I_{dr} and I_{qr} , rotor controller current error I_{drerr} and I_{qrerr}). The signals are calculated in time domain in the established DFIG harmonic model and then post processed with FFT analysis to obtain their respective spectra. Recalling chapter 4, the controller signals have identical spectral content originating from the MMF harmonics, classified as f_{SFOC}. Furthermore, the frequency contents of stator current and rotor currents were labelled as f_{Cs} and f_{Cr}, respectively. As mentioned in previous paragraphs, the shaft misalignment would give rise of $2f_r$ side band components in spectrum. The predicted frequency components for DFIG signals in healthy and fault conditions are summarized in Table 6-1.

Table 6-1 Analytical expressions defining the possible mmf harmonic related spectral content of the DFIG control signals

Signal type	SFOC related	Stator current	Rotor current
Healthy	$\|6k(1-s)\|f_e$	$\|1 \pm 6k(1-s)\|f_e$	$\|s \pm 6k(1-s)\|f_e$
Shaft misalignment	$\|6k(1-s)\|f_e \pm 2f_r$	$\|1 \pm 6k(1-s)\|f_e \pm 2f_r$	$\|s \pm 6k(1-s)\|f_e \pm 2f_r$

In this model study, 2^{15} data points were processed by FFT for each signal to enable frequency domain analysis. The illustrated bandwidth was regulated up to 700Hz to present the frequency components up to and including k=2. To clearly indicate the faulty

DFIG characteristics in electrical signal, the healthy DFIG signal and faulty DFIG signal spectrum were shown in the same plot. For illustration purposed the DFIG rotational speed from load side was set as 1380 rpm while the load active power and reactive power were -10kW and 0Var respectively. A 2.5 degrees angular misalignment severity fault was introduced in the model study to enable fault signature analysis and comparison with signals spectral content in the healthy condition.

6.3.2 DFIG Model study of misalignment fault spectral signature

The stator current is first analysed as it is the most investigated signal for fault diagnosis. The predicted spectra are shown in Figure 6-4; the spectrum plot in healthy condition is labelled in blue while the faulty condition spectrum is shown in orange. As demonstrated, the stator current in healthy condition and 2.5 degrees angular misalignment contain identical slot harmonic contents, i.e. $|6k(1-s)|f_e$ components. For the DFIG with 1380 rpm speed, the corresponding harmonic components are exhibited at 50Hz (k=0), 226Hz and 326Hz (k=1), 502Hz and 602Hz (k=2). Nevertheless, additional $2f_r$ sidebands $(2 \times \frac{1380\,rpm}{60} = 46Hz)$ induced by presence of misalignment fault can be observed in the faulty spectrum: the 4Hz and 96Hz frequency components are the most significant fault related components manifested as sidebands of the fundamental harmonic, which matches with general trends of misalignment fault signature in induction motors reported in previous research previous literature [154] [156]. The higher order spectral effects of misalignment fault, i.e. the possible sidebands on higher order components in the spectrum, such as e.g. 180Hz, 280Hz, 372Hz and others, were seen to be at a very low magnitude and barely identifiable in the predicted fault spectrum.

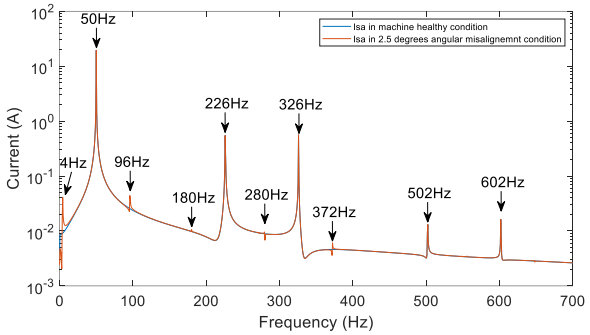

Figure 6-4 Stator Current spectrum

The rotor phase current spectral content has also been investigated. As demonstrated in Figure 6-5, the frequency contents for healthy condition operation are clearly shown, i.e. the $|s \pm 6k(1-s)|f_e$ components are clearly manifested in the spectrum. The corresponding spectral components are located at 4Hz (k=0), 272Hz and 280Hz (k=1), 548Hz and 556Hz (k=2). The fault related components, 42Hz and 50Hz, are visible as side bands of the fundamental component but are not as significant as those in the stator current. Other faulty components like 318Hz and 326Hz are nearly invisible in the faulty spectrum. From the fault diagnosis point of view, the predicted rotor current signal indicates very low diagnostic potential for misalignment fault detection.

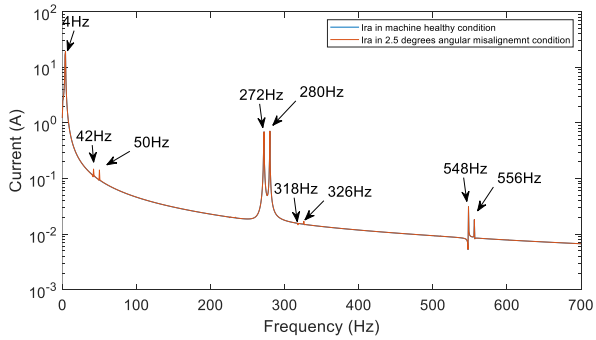

Figure 6-5 Rotor Current spectrum

Shaft misalignment diagnosis in induction motors utilizing electrical signals has been investigated by several researches, with the focus largely place on exploring the diagnostic potential of signals such as stator current and stator active power [154] [61] [156] . However, only a few studies like [158, 159] were reported were vector control enabled induction machines were analysed and no studies could be identified in the literature that explored controller signals potential for providing shaft misalignment condition diagnosis. The following section of this chapter reports a model study of DFIG controller signals spectral content with and without presence of misalignment fault, in an attempt to provide a basic characterisation of possible fault signature nature in these signals. The model results for DFIG controller signals individual spectrums are listed in Figures. 6-6 to 13.

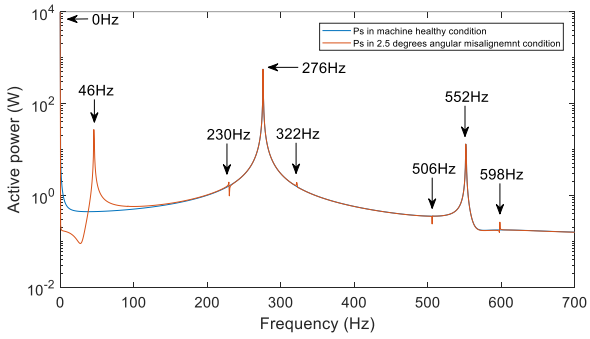

Figure 6-6 Stator active power spectrum

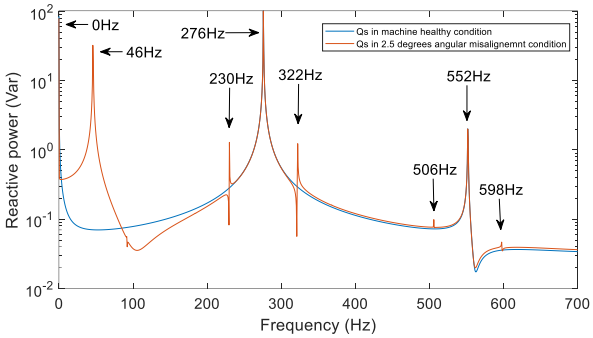

Figure 6-7 Stator reactive power spectrum

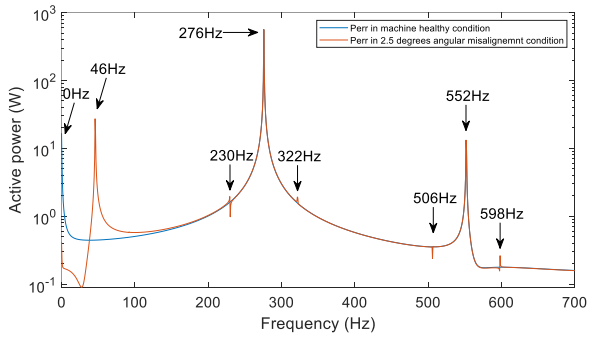

Figure 6-8 Stator active power error signal spectrum

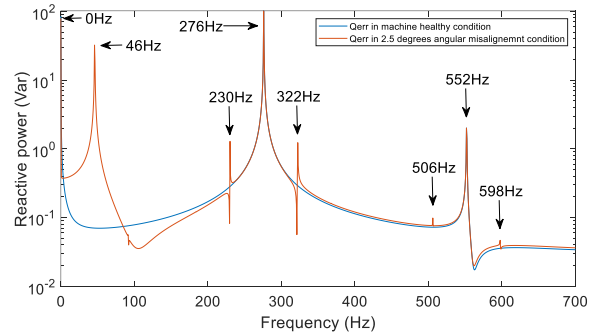

Figure 6-9 Stator reactive power error signal spectrum

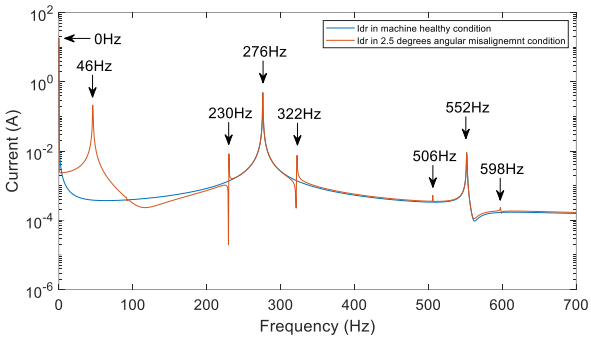

Figure 6-10 Rotor controller current I_{dr} spectrum

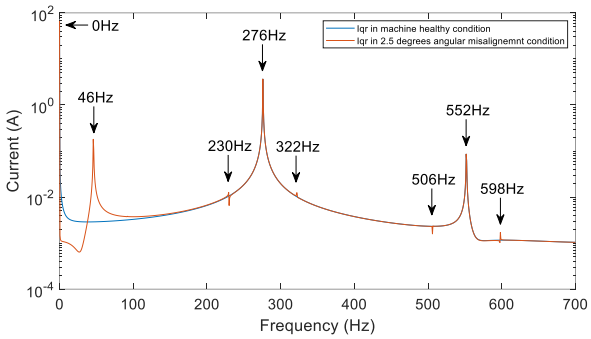

Figure 6-11 Rotor controller current I_{qr} spectrum

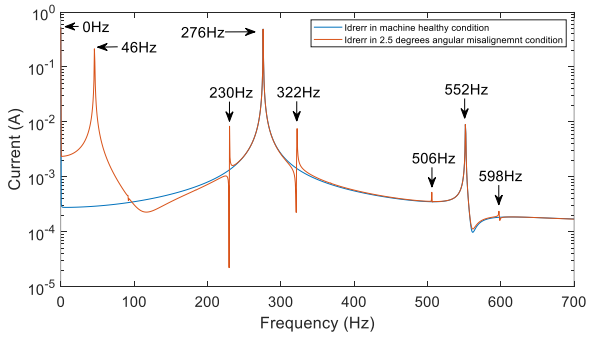

Figure 6-12 Rotor controller error signal I_{drerr} spectrum

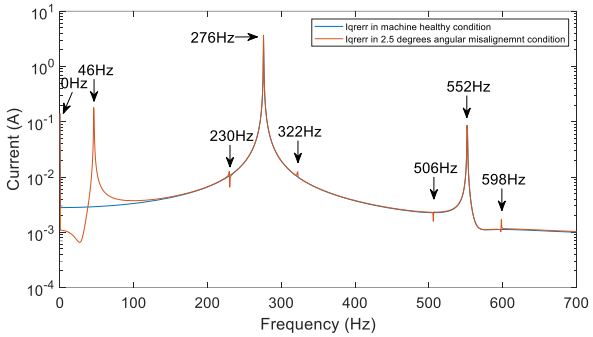

Figure 6-13 Rotor controller error signal I_{drerr} spectrum

For all the controller signals listed above, the MMF harmonic contents for healthy condition are located in the same position in the spectrum, i.e. $|6k(1-s)|f_e$ components are indicated in the figures at: 0Hz (k=0), 276Hz (k=1) and 552Hz (k=2). More interestingly, the additional frequency components induced by presence of the shaft misalignment condition at 46Hz, 230Hz and 322Hz, 506Hz and 598Hz are clearly visible in the results for all controller signals spectra; these components are essentially the $2f_r$ sidebands on the MMF related spectral content (e.g. the 0Hz, 276Hz and 552Hz components for the examined operating conditions). In general, the 46Hz component (the side band of fundamental) is seen to be the most significant among the observable fault related components; the side bands on k=1 and k=2 spectral peaks are of lower magnitude in comparison and thus less compelling as indicators of shaft misalignment presence.

Compared with the stator current signal, which is the conventionally prioritised machine signal for signature analysis based diagnostic purposes, the DFIG controller signals are seen to exhibit an increased sensitivity to shaft misalignment effect for fault recognition purpose. The presented model study results suggest that the $2f_r$ Hz content (k=0) of the DFIG controller signals is the most sensitive to shaft misalignment presence and thus

most suitable for diagnostic application. The relevant experimental study of the observed effects is reported in next section to evaluate their practical manifestation further, as well as their diagnostic potential in realistic operating conditions.

6.4 Shaft misalignment experimental result analysis

Apart from the universal joint model effect introduced before, another theoretical explanation of shaft misalignment was pointed out in [57, 160, 158]: the speed and air-gap eccentricity perturbation caused by the shaft misalignment was shown to have the potential to result in existence of sideband components, which are at integer multiples of the shaft fundamental rotational frequency, i.e. nf_r. To evaluate both effects from experimental result point of view, both f_r and $2f_r$ side bands are investigated in the following experimental study.

A range of experiments were undertaken to examine the manifestation of misalignment fault signature in the DFIG terminal currents and hence the control loop signals in this section. To this end, tests were performed on the aligned and one degree misaligned DFIG at the following typical operating points in both the sub- and the super-synchronous operating regimes: 1340 rpm, 1550 rpm and 1590 rpm. At each considered operating speed tests were performed at 25%, 50% and 100% nominal current.

6.4.1 Study of shaft misalignment signatures

This study focuses on analysis of solely the inner loop two axis rotor controller signals (I_{dr}, I_{drerr}, I_{qr}, I_{qrerr}), since no consistency in fault signature manifestation could be observed in the outer loop controller signals due to spectral noise. For completeness the outer controller signals measured spectra are presented in appendix C1. The typical spectral content observed in the measured DFIG inner loop controller signals and the stator (I_{sa})

and rotor (I_{ra}) phase currents signals spectra for an arbitrary DFIG steady-state operating point (1590 rpm, 50% load) are analysed and presented here for illustrative purposes. Consistent spectral signature effects were also observed at other tested speeds in the operating range of the utilised DFIG test system. A comparative study is undertaken to observe the manifestation of misalignment fault signature in one degree misaligned conditions compared to aligned DFIG operation. All the measured signals were acquired at 5 kHz sampling frequency and processed by Fast Fourier transform (FFT) with a 2^{16} point rectangular window length. The relevant $\boldsymbol{nf_r}$ sideband components are labelled in the spectra to illustrate the typical magnitude levels observed in the measurements.

The wideband spectra of I_{dr} and I_{sa} measured in fault conditions are shown in Figure 6-14 for illustrative purposes, demonstrating the general nature of the observed spectral signature: it can be seen that the measured f_r harmonic content is generally exhibited at a modest magnitude level. Please note that there are two f_r side band harmonic (side bands of 50Hz) could be observed at both left side and right side of stator current I_{sa}.

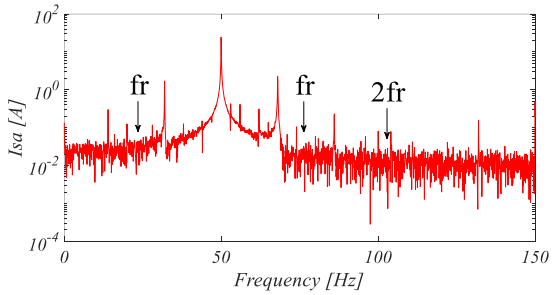

(a)

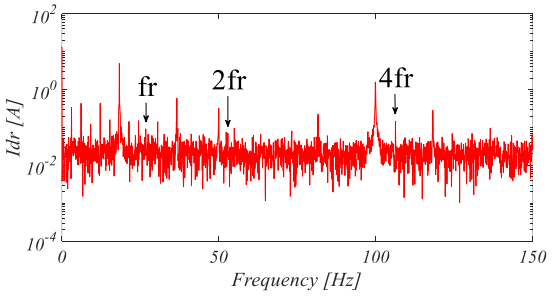

(b)

Figure 6-14 Spectrum of I_{dr} (a) and I_{sa} (b) at 1590 rpm 50% load condition with one degree

To enable a more detailed understanding of the manifestation of possible fault signature, detailed view of the spectral narrow bands containing the first and second order rotational speed sidebands in the examined signals, with and without fault presence, are presented in Figures 6-15 and 6-16, and Figures 6-17 and 6-18, respectively.

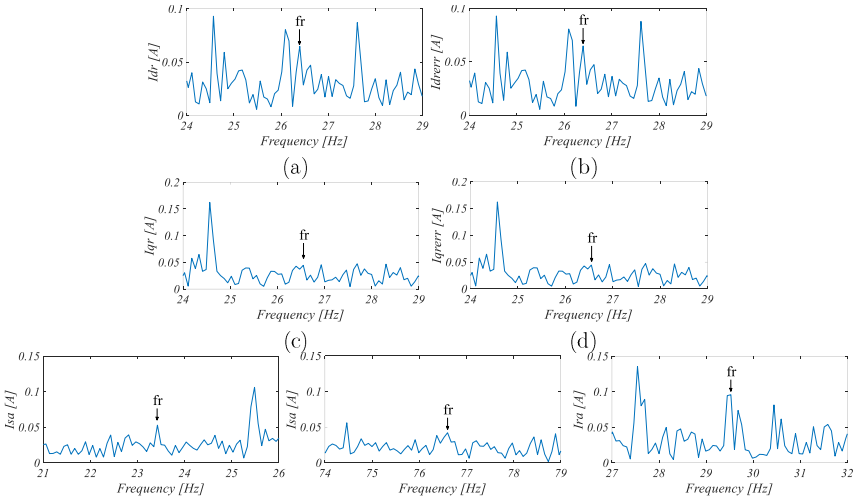

(a) (b) (c) (d) (e) (f) (g)

Figure 6-15 Healthy operating condition zoomed in spectrum at 1590 rpm - 50% load: controller I_{dr} (a), I_{drerr} (b), I_{qr} (c), I_{qrerr} (d) and terminal I_{sa} (e)-(f), I_{ra} (g) signals.

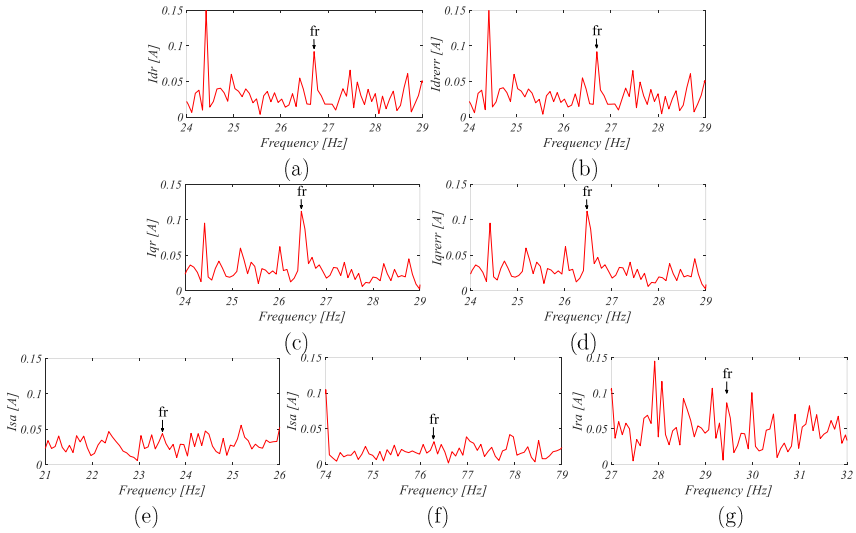

Figure 6-16 One degree operating condition zoomed in spectrum at 1590 rpm - 50% load: controller I_{dr} (a), I_{drerr} (b), I_{qr} (c), I_{qrerr} (d) and terminal I_{sa} (e)-(f), I_{ra} (g) signals.

The detailed views of the narrow bands containing the fault induced first order f_r harmonic effects in Figures 6-15 and 6-16 exhibit a considerable difference between fault signature manifestation in controller and terminal signals. The magnitude change of fundamental order f_r raises with fault in controller signals but only within a low absolute level. In terminal currents however the f_r harmonic components are significantly less responsive to fault presence.

To enable a clearer understanding of the observed fault harmonics relative magnitude change relevance, the measured fault harmonic magnitude values are shown in Table 6-2. The data indicate that a larger relative magnitude increase with fault could be observed in I_{qr} and I_{qrerr} controller signals while little consistency in terminal signals' first order f_r component change could be identified. Referring to the analysis of the first order f_r fault effects at other load and speed conditions considered in next section, not presented for

the sake of brevity in the main body but shown for illustration purposes in appendix C2, it can be noted that no consistent increase could be observed in DFIG signals at these frequencies with shaft misalignment.

Table 6-2 Magnitude of f_r components

Signal Type	Healthy [A]		1 degree [A]	
I_{dr}	0.06478		0.09207	
I_{drerr}	0.06467		0.09188	
I_{qr}	0.0444		0.1123	
I_{qrerr}	0.04443		0.112	
I_{sa}	0.05297	0.04213	0.04408	0.03195
I_{ra}	0.09583		0.08672	

The detailed view of the narrow bands containing the fault induced $2f_r$ harmonic effects in Figure 6-17 and Figure 6-18 indicate that the fault signature manifestation across the examined controller signals is closely similar: the magnitude change at fault frequencies is seen to be manifested at a considerably low level and is not significantly pronounced.

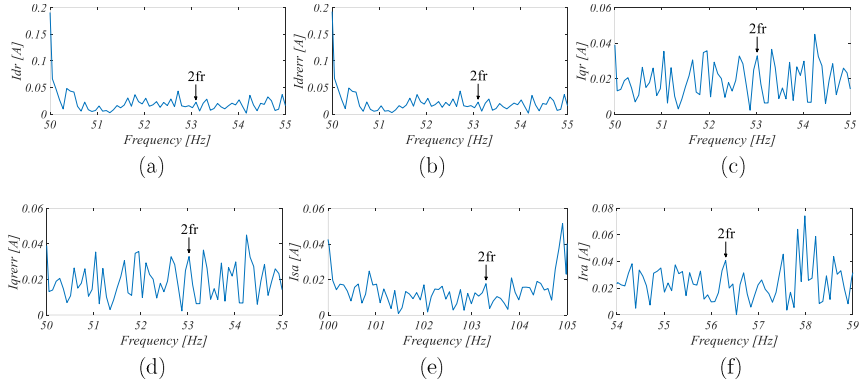

Figure 6-17 Healthy operating condition zoomed in spectrum at 1590 rpm - 50% load: controller I_{dr} (a), I_{drerr} (b), I_{qr} (c), I_{qrerr} (d) and terminal I_{sa} (e), I_{ra} (f) signals.

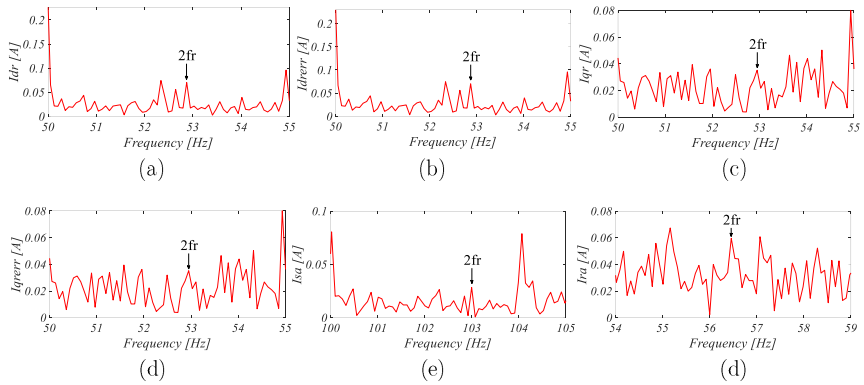

Figure 6-18 One degree operating condition zoomed in spectrum at 1590 rpm - 50% load: controller I_{dr} (a), I_{drerr} (b), I_{qr} (c), I_{qrerr} (d) and terminal I_{sa} (e), I_{ra} (f) signals.

The slight exception can be observed in I_{dr} and I_{drerr} signals in terms of relative magnitude change, however the overall effect is still exhibited at close to noise level magnitude. Compared to the fundamental fr order fault effects explored earlier in this section, the second order f_r harmonics can however be seen to be more responsive to fault presence, albeit still at a reasonably low magnitude level. In fact, the signal spectral harmonic magnitudes are affected by the set SFOC controller loops bandwidth (i.e. 1.8Hz for outer loops and 18Hz for inner loops), which will impose inherent spectrum filtering effects that could obscure some of the relevant components.

For clarity, the measured numerical values of second order f_r fault harmonics' magnitude change are listed in Table 6.3. These further illustrate that the largest relative magnitude increase with fault was observed in the I_{dr} and I_{drerr} signals' $2f_r$ sideband components, which exhibit a more than three-fold relative increase in fault presence.

Table 6-3 Magnitude of $2f_r$ components

Signal Type	Healthy [A]	1 degree [A]
I_{dr}	0.02256	0.07037
I_{drerr}	0.02269	0.07022
I_{qr}	0.03292	0.03523
I_{qrerr}	0.03290	0.03523
I_{sa}	0.01772	0.02843
I_{ra}	0.04076	0.05511

6.4.2 Study of operating condition effects on shaft misalignment signature

This section examines the consistency of $2f_r$ harmonic fault indicator manifestation in the identified higher sensitivity to fault I_{dr} signal's spectrum and for a wider range of generator operating points and loads. For comparison purposes the consistency of $2f_r$ harmonics' manifestation in the terminal current (I_{sa}), which is generally employed for MCSA diagnostic purposes, is also investigated.

The measured fault harmonics' magnitude change is presented in Figure 6-19 and Figure 6-20. These indicate that, in general, the $2f_r$ harmonics in both analysed signals exhibit the tendency of relative magnitude change with fault presence. This however is seen to be manifested at a considerably higher level and consistency in the I_{dr} signal. For the stator current, the $2f_r$ harmonic of stator current is not constantly increasing with fault. i.e. in 1340 rpm 100% load level scenario, the magnitude of healthy condition is larger than that of faulty condition. Moreover, the fault severity change in stator current components is sometimes not evident like the scenarios at 1590 rpm 25% and 50% load conditions. Compared with stator current signal, the controller signal I_{dr} is more capable to indicate the presence of shaft misalignment. Nevertheless, the observed spectral

content is seen to be manifested at considerably less pronounced magnitude than indicated by the presented results in the model study section. A case study is reported in the next subsection to explore and elucidate further the causes of the observed difference in misalignment spectral signature between the model predicted and the measured data sets.

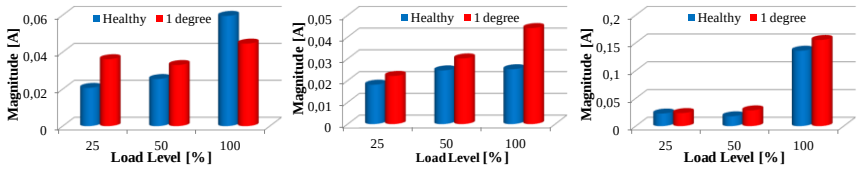

(a) (b) (c)

Figure 6-19 Measured $2f_r$ components magnitude in I_{sa} (a)1340 rpm (b) 1550 rpm (c) 1590 rpm

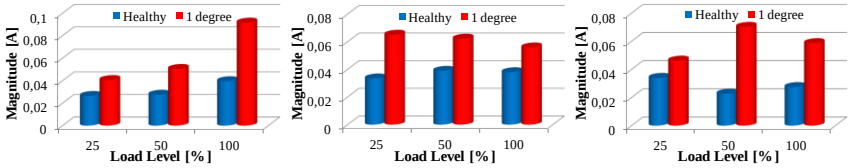

(a) (b) (c)

Figure 6-20 Measured $2f_r$ components magnitude in I_{sa} (a)1340 rpm (b) 1550 rpm (c) 1590 rpm

6.4.3 Investigation of experimental misalignment speed harmonic effect

In the previous sections, the shaft misalignment recognition utilizing DFIG controller signals has been evaluated using a DFIG harmonic model and an experimental DFIG test rig. The findings of the harmonic model study indicated a clear and relatively considerable spectral signature of misalignment fault at $2f_r$ side band away from fundamental spectral content. As for experimental signal analysis, the same tendency could be observed, with the $2f_r$ side band in DFIG I_{dr} current and its error signal

increasing with fault presence, however this was not as significant as presented in the model study and has been observed in the previous section to be of modest diagnostic potential practically. This section will investigate the root cause of the fault spectral signature mitigation in experimental signals and hence explore the possible solution to make fault recognition more evident.

As mentioned in section 6.2, the angular shaft misalignment gives rise to a $2f_r$ side band in electrical signals due to rotational speed pulsation. A case study was undertaken to evaluate the spectral content of an experimentally recorded speed signal. Typically speed signal acquisition is achieved with an incremental encoder: the encoder disk contains a predefined number of pulses, where by counting the number of pulse incensements in a fixed period of time the rotational speed can be obtained. However, recalling Chapter 3, a phase locked loop (PLL) is used in the experimental system to keep the coherence between the input (reference) signal frequency and the output signals via phase comparison. Since the modelling interface of dSPACE is not capable to execute encoder speed estimation directly from a predefined block function (Figure 3-5 Enc delta position) with a high system sample rate, the instantaneous rotational speed is obtained from the PLL. The PLL system contains a PI controller and generally can act as a signal filter, which can potentially reduce the magnitude of higher order harmonic contents. To evaluate this effect, the illustrative experimentally measured speed spectra with and without fault at 1340 rpm and 25% load condition are shown in Figure 6-21.

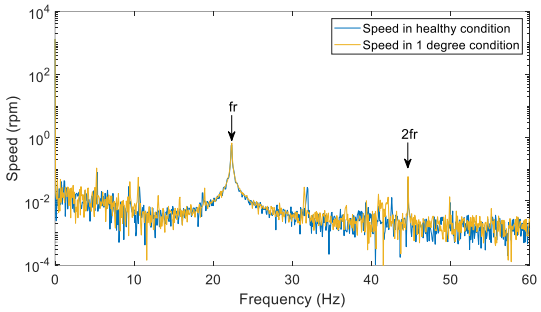

Figure 6-21 PLL estimated speed at 1340 rpm 25% load in healthy and one degree misalignment condition

A detailed view of the measured rotational speed related components (e.g. f_r and $2f_r$) are given in Figure 6-22 to provide a clearer view of harmonic components magnitude difference. For the explored operating speed the harmonic contents of diagnostic interest are located at 22.3Hz (f_r) and 44.6Hz ($2f_r$) in the spectrum.

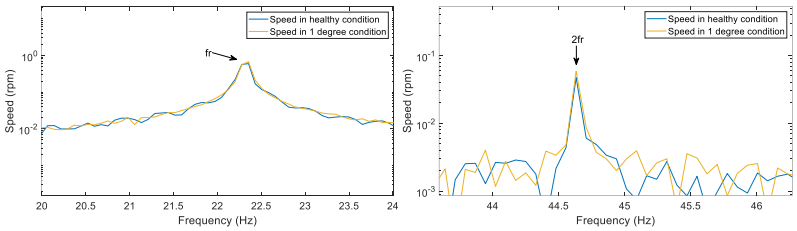

(a) (b)

Figure 6-22 Zoomed in PLL estimated speed spectrum at 1340 rpm condition (a) f_r content (b) $2f_r$ content

The presented data illustrate that the magnitude of f_r components in both healthy and faulty condition are nearly in the same magnitude. In contrast, for the situation of $2f_r$ components, the magnitude of harmonic content in faulty condition is only slightly higher than that of healthy condition. In consequence, with the PLL proceed speed signals, nearly no difference could be observed at rotational frequency related contents in healthy

condition spectra with respect of misalignment condition.

To evaluate how speed harmonic contents are effected by PLL system, a control test was undertaken. The rotational speed estimation was deployed via incremental encoder directly without PLL. It is important to note here that to achieve laboratory DFIG SFOC, a high sample rate was unavoidable and thus disabled the direct speed estimation function in dSPACE real time platform. In this case study, the investigation only focuses on the shaft misalignment effect in the speed spectrum thus no control scheme needed to be applied to evaluate this for the test WRIM. Recalling Figure 3-1 the DC motor was set to rotate in a fixed speed as a prime mover of the WRIM, which only requires a low sample rate for this control. The dSPACE proprietary speed estimation function was utilized in this case study. Tests were undertaken in healthy and 1 degree misalignment conditions, and the corresponding speed spectra are shown in Figure 6-23 with a detailed view of the spectral bandwidths of interest containing the f_r and $2f_r$ harmonic content shown in Figure 6-24.

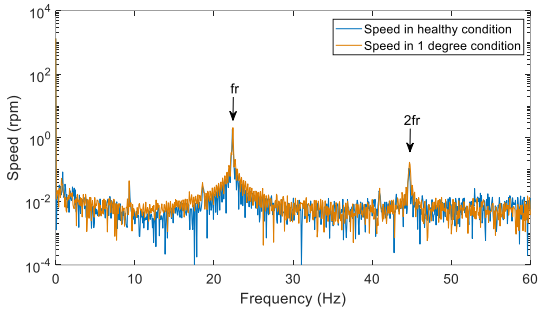

Figure 6-23 Direct estimated speed at 1340 rpm 25% load in healthy and one degree misalignment condition

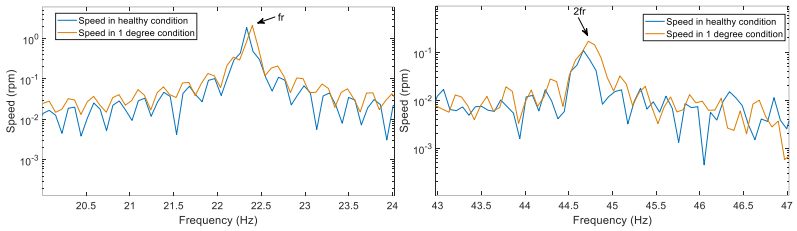

(a) (b)

Figure 6-24 Zoomed in direct estimated speed spectrum at 1340 rpm condition (a) f_r content (b) $2f_r$ content

For a direct estimated speed scenario, no significant magnitude change could be observed in f_r contents. A clear increase is visible with fault in $2f_r$ contents however: the magnitude of the harmonic content in 1 degree misalignment condition is larger than that observed in the healthy condition. To quantify the observed spectral signature magnitude difference between the two speed estimation approaches in more detail, the magnitudes of fault harmonics measured in Figure 6-22 and Figure 6-24 are summarized in Table 6.4.

Table 6-4 Magnitude of speed spectral harmonic contents

Estimation approach	f_r		$2f_r$	
	healthy	1 degree	healthy	1 degree
PLL	0.6	0.5572	0.04738	0.05877
Direct estimation	1.862	2.09	0.1099	0.1707

As demonstrated above, it could be observed that the magnitude of PLL speed estimation harmonic contents are smaller than those from direct speed estimation, largely believed to be caused by the PLL action to attenuate the higher order component contents in the spectrum. Compared to the PLL estimated speed, a considerably more evident increase in the $2f_r$ fault component could be observed in the direct estimated speed spectrum. As a result, the shaft misalignment signature in the DFIG speed and this electrical signals

is believed to be attenuated by PLL speed estimation.

To simulate the influence of the actual misalignment fault effects in the speed signal on DFIG operation a model study was undertaken: the experimental direct estimated speeds in healthy and 1 degree misalignment condition were employed in the DFIG harmonic model and electrical signals then explored for manifestation of fault signature. The outer loop references were set as -3kw for active power and 2kVar for reactive power demand respectively. For illustration purposed the obtained results for the controller signal spectrum are shown in Figure 6-25 left column, with a detailed view of corresponding $2f_r$ harmonic components given in Figure 6-25 right column.

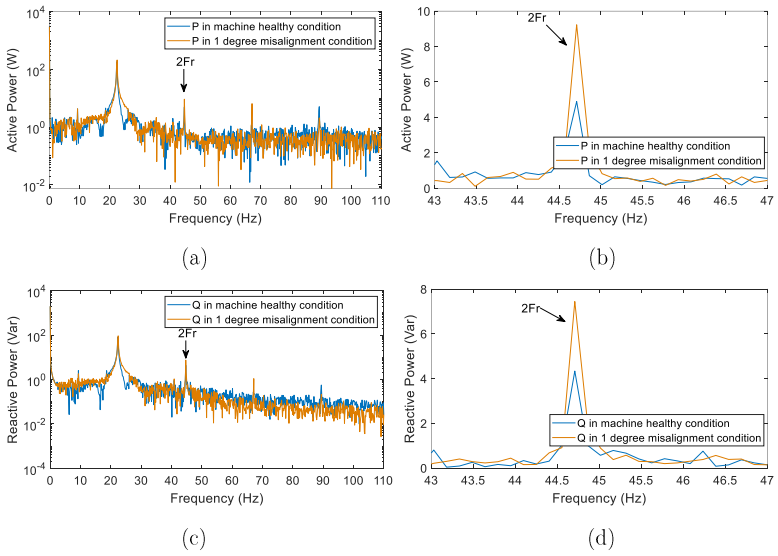

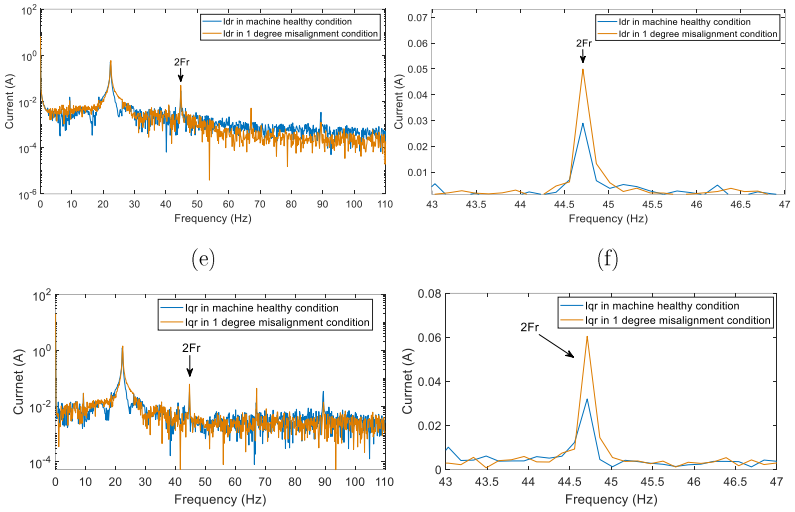

Figure 6-25 DFIG controller signals spectrum and their $2f_r$ component zoomed in view: Active power (a)(b), reactive power (c)(d), I_{dr} (e)(f), I_{qr}(g)(h)

It can be seen from the obtained data that, with the direct estimated speed employed, the DFIG harmonic model indicates that clear recognition of shaft misalignment using the fault signature in the controller signals spectrum is possible. This demonstrates that the shaft misalignment effect in the speed signal is eventually reflected in the DFIG controller signal, contributing to more pronounced fault signature manifestation. However this effect was mitigated in the laboratory SFOC DFIG system due to the limitation of the hardware used: the inability to provide direct speed measurement from encoder outputs wat high sample rate imposes the requirement for application of a PLL as an alternative approach, resulting in inherent mitigation of the relevant fault related spectral contents in the speed signal, and this their counterpart signatures in the electrical signals. To overcome this issue, more advanced hardware is required to enable direct speed estimation in high sample rate conditions.

6.5 Conclusion

This chapter undertakes the analysis of misalignment fault manifestation in a typical WT doubly-fed induction generator (DFIG) topology with a view to exploring the possibility for development of non-invasive and low cost monitoring techniques based on misalignment fault spectral signature trending in the readily available DFIG controller signal loops.

To begin with, the angular shaft misalignment mechanical effect was reviewed using a universal joint model, demonstrating the resultant $2f_r$ frequency component speed signal perturbation with fault presence and mapping this to counterparts $2f_r$ side band spectral signatures in the current but also the DIFG SFOC signals.

In this chapter, the main objective is to explore the feasibility of shaft misalignment recognition utilizing DFIG SFOC controller signals. A model study was thus undertaken to explore the possible spectral signature in the DFIG terminal currents and controller signals It was illustrated that the $2f_r$ side band component spectral signatures are evident in these, and a stronger manifestation of fault induced spectral signature change observed in controller signals when compared to terminal currents. Furthermore, the study verified the proposed understanding of how the misalignment fault signature is mapped in the spectra of DFIG controller signals.

An experimental study of fault effects was then performed on a laboratory DFIG test rig capable of angular shaft misalignment emulation. Tests were undertaken to examine the manifestation of misalignment fault related current spectral signatures and those in the DFIG stator flux oriented controller loops. The DFIG controller signal I_{dr} and its error signal were validated as the most suitable signals among all DFIG electrical signals to indicate shaft misalignment fault. The consistency of the observed phenomena is then

evaluated for a wider range of DFIG operating points. However, while in relative terms the observed fault induced spectral magnitude changes can be significant, they were found to be of low value in absolute terms. Therefore, their application for diagnostic purposes would be challenging and likely of limited effect on the examined test system. Two factors may affect these results: the PLL employment for rotational speed and position acquisition in the available test system and the SFOC controller loop bandwidth. Another case study was performed indicating the magnitude of harmonic contents in the speed spectrum were reduced by the PLL, which can make made the resultant DFIG electrical signal signature less evident compared with direct estimated speed scenario. To improve the practice fault diagnosis efficiently, a more advanced hardware is required to enable direct speed estimation in high sample rate DFIG control system. Further investigation of controller bandwidth effects on fault signature manifestation is needed to ascertain the possibility of enhancing the detectability of controlled signal embedded indices.

Chapter 7 DFIG Shaft misalignment monitoring by FBG Frame strain sensing

Acknowledgement: The research presented in this chapter was published in IEEE Sensors Journal. Some passages have been quoted verbatim from the following source [24].

7.1 Introduction

In this chapter, FBG sensors are utilized to measure distributed relative strain on the generator frame surface to explore the potential of its monitoring to be used as a diagnostic tool for shaft misalignment detection. This chapter first reviews the mechanical model of angular shaft misalignment and its relevant mechanical effects, and then proceeds to illustrate the utilized sensor design and installation procedure, and discuss the considered monitoring points of interest for this application. An experimental study is then undertaken on a purpose built double-fed induction generator (DFIG) test

facility, which allows for controlled introduction of different levels of misalignment in tests.

The distributed FBG sensor suite was installed on the test generator frame and its performance evaluated in a range of tests involving various operating points in healthy and multiple different degrees of angular shaft misalignment operating conditions. The attained results were then analysed, with particular attention to the location and orientation of individual FBG heads' influence on efficacy of capturing the diagnostic content in the measured strain signal. The findings were corroborated with conventional vibration sensing, a widely used standard reference for shaft misalignment monitoring, using a commercial acceleration monitoring platform installed on the test generator. Further tests were also undertaken to ascertain the influence of thermal-cross sensitivity effects caused by the generator frame inherent change of thermal conditions on the analysed strain measurements.

The presented findings demonstrate a strong potential of frame embedded FBG strain sensing application for enabling the recognition of shaft misalignment conditions in the wide operating range of the examined DFIG, and characterise the sensor orientation and placement sensitivity to fault induced excitation.

7.2 Shaft misalignment monitoring

7.2.1 Mechanical effects

As demonstrated in Chapter 6, the angular shaft misalignment mechanical effects can be modelled via a universal joint model representation, which was used to demonstrate that the presence of angular shaft misalignment will fundamentally give rise to speed signal pulsations at twice the rotational speed frequency (e.g. $2f_r$). The relationship between

the misaligned, motor side, shaft speed ω_k and the load side speed, ω_l, was shown in Chapter 6 to be possible to be could be expressed as: [154]

$$\omega_k = \frac{cos\beta}{1-(sin\beta)^2(cos\theta_l)^2}\omega_l \tag{7.1}$$

Assuming invariance of power between the load and the motor side allows the expression relating the load side torque, T_l , and the motor side torque, T_k , and respective shaft speeds to be related as:

$$T_k\omega_k = T_l\omega_l \tag{7.2}$$

The torque transmitted from the load to the motor side via the misaligned universal joint model is then obtained by substitution of equation (7.1) into equation (7.2) to give:

$$T_k = \frac{1-(sin\beta)^2(cos\theta_l)^2}{cos\beta}T_l \tag{7.3}$$

Equation (7.4) can now conveniently be rearranged to the following term:

$$T_k = \left(\frac{1}{cos\beta} - \frac{sin^2\beta}{2cos\beta} - \frac{sin^2\beta}{2cos\beta}cos2\theta_l\right)T_l \tag{7.4}$$

Defining, for clarity, the load angular displacement $\theta_l = 2\pi f_r t$, where f_r is the load shaft fundamental rotational frequency ($f_r = \omega_r/2\pi$, it becomes apparent that the presence of angular misalignment will fundamentally give rise to torque signal pulsations at twice the rotational speed frequency (e.g. $2f_r$). Torque pulsations are usually expected to be transferred into counterpart machine frame vibration at identical frequencies [161] and can thus generally be expected to be possible to manifest as identical frequency frame deformation (i.e. strain) [162] [163]. Furthermore, the general practice and research on angular misalignment monitoring indicates that increased frame vibration at fundamental rotational frequency is also possible with angular misalignment [50] [164].

7.2.2 Monitoring practice

The common industrial practice in monitoring electrical machinery shaft misalignment generally employs two accelerometer sensors, acting at 90^{o} degree spatial displacement [164]. This reflects the fact that the angular misalignment causes axial vibration at fundamental rotational frequency (f_r), while the parallel misalignment produces radial vibration at twice the fundamental rotational speed frequency ($2f_r$): employing two accelerometers, one axially and the other radially mounted on the machine frame, to separately yet synchronously monitor axial and radial vibration signals, allows for identification of effects rooted by both types of misalignment and therefore its diagnosis.

The commercial misalignment detection systems undertake analysis of the captured vibration spectra to extract distinct identifiers of misalignment: it is widely acknowledged that most occurrences of the misalignment condition involve a combination of offset and angular misalignment, hence both the f_r and the $2f_r$ frequency components in both the radial vibration signal and the axial vibration signal are thus observed for misalignment diagnosis purposes [50]. A common approach used in practice is to observe the ratio between the $2f_r$ and f_r components' magnitudes, denoted in further text as M_2f_r and Mf_r respectively, in the frame acceleration signals, and observe its amplitude change. If misalignment is present in the system, a higher than normal (e.g. at healthy system conditions) value of the misalignment diagnostic index, where $m = |M_2f_r / Mf_r|$, is expected [165].

7.3 Principles of FBG strain sensing

An FBG sensor is a small structure imprinted in a single mode optical fiber core. It is fabricated by creating a permanent periodic change (i.e. gratings) in the fiber core's

refractive index by exposure of the fiber core to an interference pattern of UV light [162]. The FBG sensor size is typically really small (i.e standard optical fiber size is ≈ 125 μm in diameter, while FBG head length typically ranges anywhere from 2 to 20 mm depending on the application although other sizes are possible).

In principle, an FBG sensor operates as a light filter that reflects a narrowband light wavelength when a fiber containing an FBG head is illuminated by a broad band light source [166] [167]. The FBG head reflected wavelength is known as the Bragg wavelength, λ_B, and can be defined as: [168]

$$\lambda_B = 2\,\Lambda\, n_{eff} \tag{7.5}$$

where Λ is the grating period and n_{eff} is the FBG's effective refractive index. These parameters are sensitive to the variation in the temperature and strain the FBG structure is exposed to, thus altering the reflected narrowband wavelength. Assuming constant temperature, the variation in λ_B due to strain variation $\Delta\varepsilon$ can be expressed as [168]:

$$\Delta\lambda_B = 2\left(\Lambda\frac{dn_{eff}}{d\varepsilon} + n_{eff}\frac{d\Lambda}{d\varepsilon}\right)\Delta\varepsilon \tag{7.6}$$

The response of the FBG sensor to strain arises due to the change in the grating period (e.g. the physical elongation of the sensor), and the change in the reflective index due to photo-elastic effects [169]. A typical theoretical value of the strain sensitivity of a standard FBG imprinted with the Bragg wavelength of λ_B at 1500 nm is ≈ 1.2 pm/μ strain [162]. This value, however, can vary depending on the FBG sensor embedment and packaging methods.

The performance of surface strain sensing utilizing FBG technology can be affected by the used bonding material and the mounting procedure [170] [171]. Different bonding methods have been explored in the literature, ranging from application of cyanoacrylate

adhesive and epoxy-resin glue [170] [172] to the use of polyamide tape [162] [171]. While the former methods can provide increased rigidity and thus load to sensor transfer, they also impose a generally more complicated installation procedure and are fixed with no flexibility in terms of sensor repositioning and re-application. Polyamide tape bonding application on the other hand has been reported to provide good levels of measured load transfer from the structure to the sensor with advantage of high application flexibility; this method is employed in the feasibility study reported in this work, as detailed further in section 7.5

7.3.1 FBG sensor design

A schematic diagram of the FBG sensor design employed in this study is shown in Figure 7-1. Each used sensor contains a 5 mm FBG head imprinted in a bend-insensitive fiber polyimide single mode optical fiber. The employed FBG sensors' respective central Bragg wavelengths are at 1532 nm, 1539 nm and 1548nm ; their average reflectivity is 80 % and their bandwidth is 0.3 nm.

While the sensor is applied for strain measurement in this work, it is also inherently sensitive to thermal excitation. However, the thermal conditions rate of change in this application (e.g. electric machine frame temperature change rate) is significantly lower than that can be observed in and is typical for the machine frame strain, and should therefore allow clear differentiation of thermal and mechanical effects in the measurements: this will be further studied in experimental work in section 7.5.

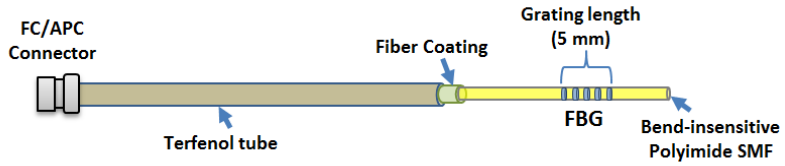

Figure 7-1 FBG sensor schematic diagram

7.4 Experimental set up and FBG strain sensing network scheme design

7.4.1 Description of sensor placement

This study was undertaken on the vector controlled doubly fed induction generator test rig described in Chapter 3. To enable vibration sensing according to accepted practice for misalignment monitoring [165] and its correlation to the explored frame strain analysis, two Bruel &Kjaer (B&K) DT4394 piezoelectric accelerometers were installed on the generator's drive end plate: one in the axial (ACC-A) and the other in the radial (ACC-R) orientation, as illustrated in Figure 7-2. The accelerometer outputs were conditioned and analyzed using the B&K Pulse vibration monitoring platform.

Three different orientations of the frame FBG strain sensing were examined to enable the understanding of optimal sensor positioning for misalignment recognition, as demonstrated in Figure 7-2. The FBG strain gauges were installed on the test machine frame in axial, radial and circumferential orientation, denoted in further text as FBG-A, FBG-R and FBG-C, respectively. All the employed FBG sensors were non-invasively installed on the frame by bonding the respective sensing head to the surface of the frame drive-end cap: FBG-A is placed on the top of end cap oriented parallel to the motor

shaft, FBG-R is mounted on the end cap side in orientation perpendicular to the motor shaft, and FBG-C is fitted along the end cap round external surface. To ensure optimum strain gauge bonding the frame surface in target sensing areas was first stripped of paint, then smoothed by fine sand paper and finally cleaned with Isopropyl alcohol before attaching the FBG sensors, following the procedure applied in [162] [171].The FBG sensing heads were bonded to the treated frame surface by means of Kapton tape [162].

For the purpose of investigating the thermal excitation effects in the explored FBG strain measurements, arising due to the inherent FBG thermo-mechanical cross sensitivity and thermal excitation characteristics inherent to any operating machine frame surface, the frame temperature was estimated by installing a thermo-couple type K on the drive end-cap side of the test machine. The thermocouple output was condition using a Fluke T3000 digital type K thermometer to obtain temperature readings.

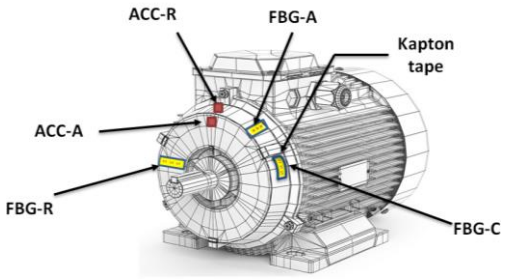

Figure 7-2 Positions of FBG sensors and accelerometers

7.4.2 Examined angular shaft misalignment conditions

For the purpose of this study two different severities of angular shaft misalignment were practically emulated on the experimental test rig: this included operation in aligned conditions, and with one degree and three degrees angular shaft misalignment. The desired misalignment levels were achieved by introducing appropriately dimensioned

shims under the feet of the test motor. A simplified diagram in Figure 7-3 below illustrates the misalignment condition practical recreation process.

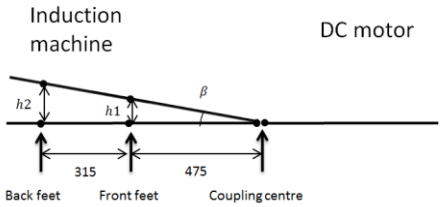

Figure 7-3 Experimental angular shaft misalignment creation layout

In Figure 7-3 $\boldsymbol{\beta}$ is the shaft misalignment angle, and $\boldsymbol{h_1}$ and $\boldsymbol{h_2}$ are the shim thickness dimension for the WRIM front feet and its back feet, respectively; the distance between WRIM's front and back feet is 315mm while the distance between the WRIM front feet and the coupling center is 475mm. The appropriate shim thickness to provide the desired level of misalignment was established by following trigonometric functions arising from the geometry detailed in Figure 7-3:

$$h_1 = 475mm \cdot \sin\beta$$

$$h_2 = (315 + 475)mm \cdot sin\beta$$

Once the shims have been sized and installed on the test system a commercial TKSA 51 laser alignment tool was used to verify the correct amount of misalignment has been achieved. The alignment tool was also used to ascertain there is no offset alignment present in the system during tests.

7.5 Experimental result and discussion

A range of experiments were undertaken to evaluate the proposed FBG frame strain sensing network efficacy in enabling recognition of angular shaft misalignment. To this

end the findings obtained from the FBG sensor measurements were cross compared with those from a commercial vibration monitoring platform.

The laboratory DFIG was tested at the following four typical operating speeds covering both its sub- and super-synchronous operating conditions: 1340 rpm, 1440 rpm 1550 rpm and 1590 rpm. For each considered speed point, three different load levels were examined by performing tests at 25%, 50% and 100% nominal load (current). For each examined speed and load condition three separate test were undertaken, with the DFIG operating with an aligned shaft and 1 and 3 degrees of angular shaft misalignment. A set of thermal tests were also carried out to investigate the FBG thermo-mechanical cross sensitivity effects and ascertain sensors capability for long term online application and how their measurements are affected by the inherent machine surface temperature change.

The findings are presented in the following subsections. Sections 7.5.1 and 7.5.2 focus on exploring the nature of fault related content manifestation in the observed signals spectra for a single operating point, to illustrate the frequency domain content acquired by the strain sensors. Section 7.5.3 then undertakes a consistency study of the identified behavior on a wider range of load and speed operating points. Finally, section 7.5.4 presents the results of the thermo-mechanical cross sensitivity study.

7.5.1 Strain and vibration signals spectral content analysis

The typical spectral content observed in the evaluated frame strain and vibration measurements is shown in detail for an illustrative DFIG operating point (1340 rpm, 25% load) and the examined misalignment conditions in this section to enable understanding of FBG strain monitoring potential.

The measured strain and vibration time domain signals were processed in 2^{17} data point

FFT routines to extract the corresponding spectral content. The resulting data are shown in Figure 7-4 for the 0 to 110 Hz bandwidth to enable a relatively wide band comparison of the spectral content observed by strain and acceleration sensors. While, generally, the fundamental and second order harmonics are typically monitored for misalignment analysis purposes [165], rotational speed harmonics of up to and including the 4^{th} order are examined in this section for the sake of validating the FBG strain sensor capability to register the misalignment induced frame deformation components corresponding to those seen in vibration measurements.

The numeric values of the first four f_r harmonic frequencies at the examined speed (given by: $f_{rk} = k \times n_r / 60$ [Hz], where k=1,2,3… and n_r is the rotor speed in rpm) are: 22.33 Hz, 44.67 Hz, 66.99 Hz and 89.33 Hz. The measured strain and vibration data in Figure 7-4 clearly report the presence of these components, with similar general spectral contents trends observed in healthy and fault conditions. The comparison of the three different orientation frame strain FBG measurements reveals that strong f_{rk} peaks are present in both axial and circumferential strain signals, while the radial strain measurements are considerably less significant in comparison; this suggests lower sensitivity of strain measurements in radial orientation. Compared to the vibration measurements, the FBG strain signals are seen to report more clearly pronounced f_{rk} components in spectra containg a generally lower noise level.

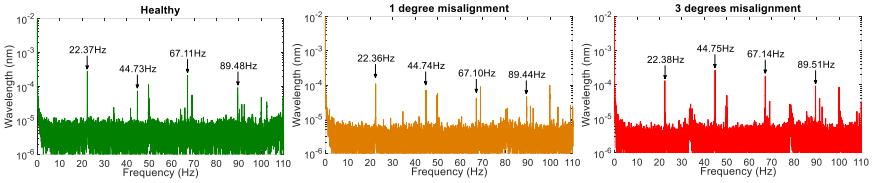

A. FBG axial strain measurement FFT spectrum for different conditions

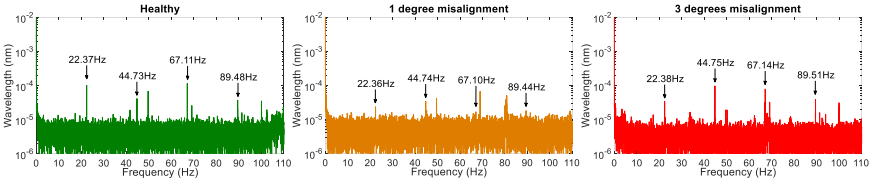

B. FBG circumferential strain measurement FFT spectrum for different conditions

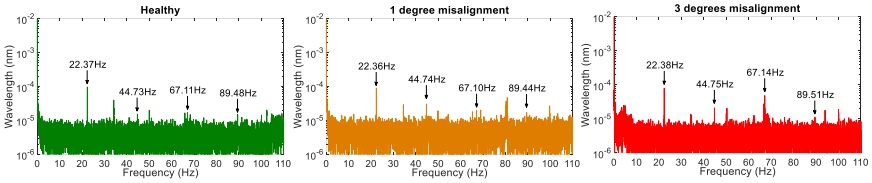

C. FBG radial strain measurement FFT spectrum for different conditions

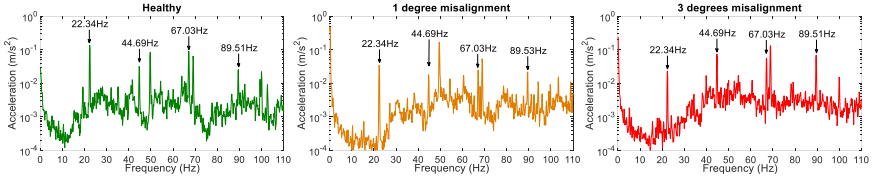

D. Accelerometer axial measurement FFT spectrum for different conditions

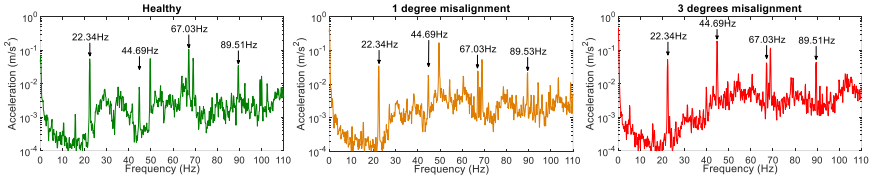

E. Accelerometer radial measurement FFT spectrum for different conditions

Figure 7-4 FBG strain and vibration signals spectrum in different severities of shaft misalignment at DFIG 1340 rpm 25% load condition

7.5.2 Fault related component analysis

This section undertakes a detailed cross correlation study of the strain and vibration signals' key misalignment fault related components, i.e. the fundamental and the second order rotational speed harmonics. To this end, the magnitudes of the strain and vibration signals' f_r and $2f_r$ frequency components measured in Figure 7-4 are summarized in Table 7-1.

Table 7-1 Measured f_r and $2f_r$ frequency components' magnitudes in frame strain and acceleration spectra at 1340 rpm and 25% load

Signal Source	f_r magnitude			$2f_r$ magnitude		
	H	1°	3°	H	1°	3°
FBG-A (nm)	28×10^{-5}	11×10^{-5}	13×10^{-5}	7.3×10^{-5}	7.1×10^{-5}	27×10^{-5}
FBG-C (nm)	10×10^{-5}	2.3×10^{-5}	3.4×10^{-5}	4.2×10^{-5}	3.4×10^{-5}	9.7×10^{-5}
FBG-R (nm)	9.6×10^{-5}	8.9×10^{-5}	8.0×10^{-5}	1.5×10^{-5}	3.0×10^{-5}	2.1×10^{-5}
Axial vibration (m/s^2)	0.13	0.021	0.023	0.031	0.021	0.073
Radial vibration (m/s^2)	0.055	0.034	0.053	0.0079	0.018	0.19

The measurements in Table 7-1 demonstrate that no consistent magnitude change with fault severity level increase can be observed in the FBG measured f_r and $2f_r$ components. As a result, observing the individual magnitude only of these components is not suitable for provision of diagnostic knowledge on angular shaft misalignment. Similarly, the vibration signals exhibit a general inconsistency in the behavior of the observed f_r and $2f_r$ components magnitude at different fault levels making it challenging to utilize these for deriving reliable diagnostic information: while some consistence with fault level propagation can be observed in isolated cases (e.g. the $2f_r$ component in the radial vibration spectrum) this does not hold for other load and speed conditions.

Therefore, the commonly utilized misalignment diagnostic index, based on the magnitude ratio of the 2nd and 1st harmonic (m, as defined in section 7.2.2) has been applied on the measured data and the obtained index values summarized in Table 7-2. The introduction of the ratio index m significantly alters the diagnostic potential of the analysed frame strain and vibration measurements. Regarding the FBG strain signals, it can be observed that the index m continuously increases with fault level rise in both the axial and circumferential direction measurements (FBG-A and FBG-C); nevertheless, this trend could not be monitored in the FBG-R signal, reflecting the observations on the lower sensitivity of the measurement taken in this orientation to fault, as reported in section 7.5.1. Similarly, a continuous growth in the index m value is seen in both the axial and the radial vibration signals 'measurements, as is generally expected [165] [173].

The reported measurements indicate that in-situ frame strain sensing has comparable diagnostic potential to conventional frame vibration monitoring, depending on the sensing orientation: both FBG-A and FBG-C are demonstrated to enable clear recognition of the presence and magnitude of angular shaft misalignment.

Table 7-2 Measured value of diagnostic index m at 1340 rpm and 25% load

Signal source	m		
	H	1°	3°
FBG-A	0.26	0.65	2.03
FBG-C	0.41	1.45	2.83
FBG-R	0.16	0.34	0.26
Axial vibration	0.24	1.02	3.18
Radial vibration	0.14	0.52	3.55

7.5.3 Diagnostic consistency study in the wider operating range

This section examines the consistency of the diagnostic index m manifestation in the

frame strain measurements observed in section 7.5.2 over a wider range of generator operating points and loads, more widely representative of its field application conditions. The misalignment diagnostic index values, obtained from the axial, radial and circumferential direction frame strain measurements for the four investigated speeds at considered load and fault levels detailed in the introduction of section 7.5, are shown in Figures 7-5 to 7-7 The corresponding axial and radial vibration measurements are presented in Figure 7-8 and 7-9.

The index measurements in Figures 7-5 to 7-7 show that, as observed in sections 7.5.1 and 7.5.2, the radial direction strain (Figure 7-6) exhibits an inconsistent m behavior with fault level variation; radial strain would generally be expected to be more sensitive to offset shaft misalignment (which could not be emulated on the test rig due to project limitations), and while, as such, this signal is not of direct use for diagnosis of angular misalignment severity, it could potentially be used to differentiate the type of misalignment observed in the system using frame strain measurements. The axial and circumferential strain measurements on the other hand are seen to report clear increase trends in the value of m for all the examined conditions:

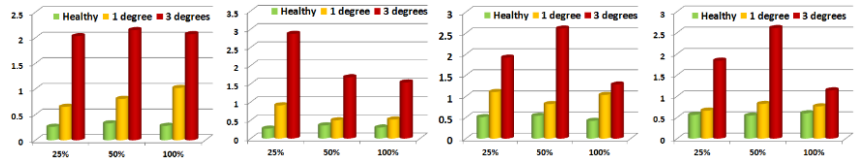

(a) 1340 rpm (b) 1440 rpm (c) 1550 rpm (d) 1590 rpm

Figure 7-5 Measured value of diagnostic index m in axial strain

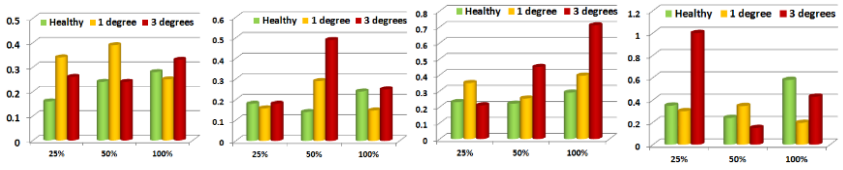

(a) 1340 rpm (b) 1440 rpm (c) 1550 rpm (d) 1590 rpm

Figure 7-6 Measured value of diagnostic index m in radial strain

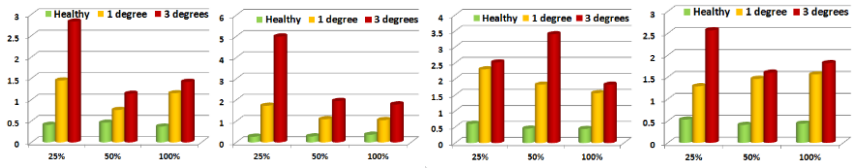

(a) 1340 rpm (b) 1440 rpm (c) 1550 rpm (d) 1590 rpm

Figure 7-7 Measured value of diagnostic index m in circumferential strain

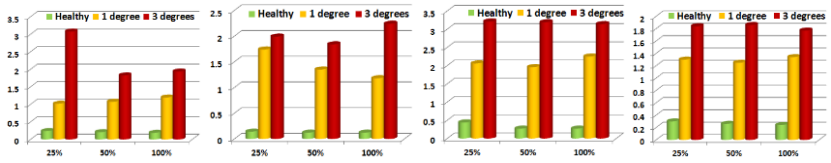

(a) 1340 rpm (b) 1440 rpm (c) 1550 rpm (d) 1590 rpm

Figure 7-8 Measured value of diagnostic index m in axial vibration

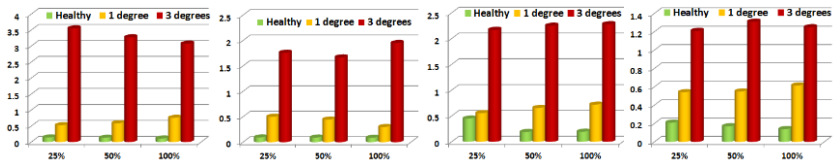

(a) 1340 rpm (b) 1440 rpm (c) 1550 rpm (d) 1590 rpm

Figure 7-9 Measured value of diagnostic index m in radial vibration

both these signals could enable unambiguous detection of angular misalignment presence and monitoring its level propagation. While both signals exhibit strong sensitivity to

fault presence and level, it can be observed that circumferential strain provides increased sensitivity to lower fault levels, while axial strain is more responsive to high level fault. The misalignment diagnosis performance could therefore be strengthened by the joint utilize of these two, allowing for an increased sensitivity across the fault level spectrum. Finally, comparison with the corresponding vibration measurements in Figures 7-8 and Figures 7-9 demonstrates that the diagnostic performance provided by FBG frame strain sensing is comparable to that attainable using conventional frame vibration monitoring.

7.5.4 Thermal cross-sensitivity effects evaluation

The FBG sensors are intrinsically sensitive to both strain and thermal excitation variation. It is thus essential to investigate how the proposed frame FBG strain sensing is affected by machine surface temperature change in long terms tests emulating thermal conditions encountered in practical use. To this end, the test DFIG was operated at 100% nominal current at 1340 rpm in healthy conditions for an extended time period to allow for the machine frame temperature to attain its steady-state nominal load level. The test was run for approximately 150 minutes to ensure the steady-state thermal equilibrium is reached. The frame surface temperature in the vicinity of FBG sensors locations, and the axial and circumferential direction strain demonstrated to enable recognition of angular misalignment in previous sections, were measured at every 30 minutes during the test.

To illustrate the observed strain changes owing to frame temperature change the measured f_r and $2f_r$ components' magnitudes in the axial strain signal spectrum are shown in Figure 7-10 (a) and (b), respectively. The corresponding frame temperature measurements are shown in Figure 7-11: at test start the frame was at ambient temperature (≈26.3℃), reaching a steady-state temperature of ≈41.4℃ at test end. The presented experimental data in Figure 7-10 demonstrate that the f_r and the $2f_r$

componentsexhibit a relatively minor change in magnitude (measured at a maximum of 0.0000573nm for f_r magnitude variation and 0.0000573nm for $2f_r$ variation).

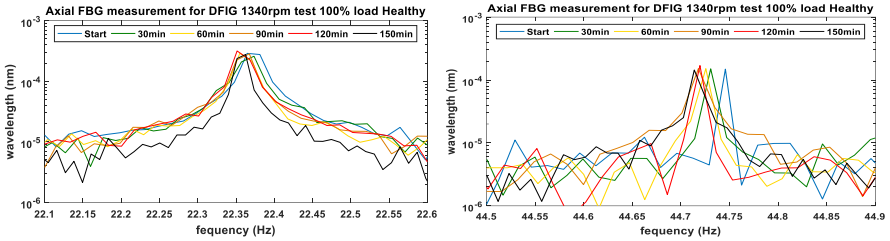

(a) (b)

Figure 7-10 (a) Measured thermal variation caused change in f_r component of FBG-A spectrum (b) Measured thermal variation caused change in $2f_r$ component of FBG-A spectrum

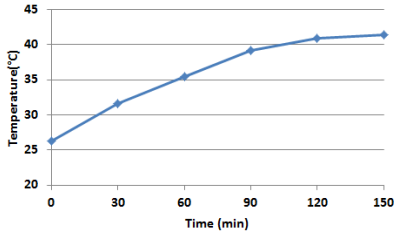

Figure 7-11 Measured generator frame temperature rise from thermal ambient to thermal steady-state value at 1340rpm, 100% load

The estimated maximum variation in the axial and circumferential strain measurements caused by the frame temperature change was used to map the deviation of the corresponding values of diagnostic index m, and the results shown in Figure 7-12. The blue and red bars in Figure 7-12 represent the minimum and maximum observed m values during the 150 minutes test duration. To enable evaluation of the significance of the thermal induced change in the diagnostic index, the value of m measured for 1 degree fault condition in Figure 7-5 is also shown in the figures, and is characterized by a black

line. The measured data report the m variation range for FBG-A of 0.29 to 0.52, which is much lower than the index value for 1 degree fault condition. Similarly, the range of FBG-C variation in m is from 0.38 to 0.5, while the 1 degree fault condition index value is 1.15. In summary, the thermo-mechanical cross-sensitivity test results indicate that no observable detrimental effect can be identified on the diagnostic performance of FBG frame strain measurements for recognition of angular shaft misalignment; while thermal induced changes in the relevant diagnostic index values are present with change in thermal conditions on the frame, these are seen to be of relatively insignificant magnitude and do not compromise the ability of strain measurement to enable recognition of misalignment conditions.

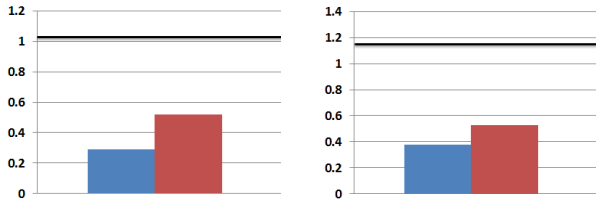

A. FBG-A B. FBG-C

Figure 7-12 Frame temperature variation induced change in m index value measured in ambient to thermal steady-state rise tests at 1340rpm, 100% load.

7.6 Conclusions

This Chapter presents an FBG strain sensor application study for monitoring and diagnosis of misalignment conditions in electric machine drivetrains, based on observation of machine frame relative strain. The proposed method enables straightforward retrofit to existing machinery, and is shown to have the capability to provide an effective means of distributed measurement and monitoring of misalignment induced effects.

The reported technique's performance was evaluated in laboratory tests on a purpose built doubly-fed induction generator test facility, allowing controlled introduction of desired level of angular shaft misalignment. The findings demonstrate that the proposed FBG strain measurements on the generator frame surface can enable recognition and trending of misalignment fault presence and level, and offer diagnostic capability that is commonly obtained through application of more complicated conventional acceleration monitoring systems. It was also found that the FBG sensor innate thermo-mechanical cross sensitivity combined with frame surface temperature variation that is inherent to electric machine operation, has no detrimental effect on the observation of frame signal embedded misalignment signature. The diagnostic potential of differing in-situ FBG strain observation for diagnosis of angular misalignment was assessed, showing that both angular and circumferential direction measurements are strongly responsive to fault presence. Further investigation of optimizing the sensor surface bonding to yield enhanced load to sensor transfer could provide improvements on the reported findings.

Compared to application of accelerometer sensors that exclusively monitor mechanical effects the reported scheme can provide additional thermal monitoring capability using the same hardware platform due to FBG inherent multi-physical sensing capability. Further advantages can also be derived from its ease of installation and positioning, the fact it is power passive, as well as its capability to be integrated into wider FBG multi-sensor systems allowing all-inclusive electrical machine condition monitoring and replacing the current practice where a suite of disparate single-physics sensors is applied for this purpose (e.g., current, temperature, vibration etc.). Finally, the scheme offers full EMI immunity as is inherent to FBG sensing which is important in EMI rich electric machine applications and requires additional measures to achieve in conventional sensor alternatives. While further exploration is needed, the presented principles could enable

the development of electric machinery shaft misalignment detection schemes based on distributed in-situ FBG strain sensing of machine frame, as standalone systems or as part of wider drivetrain FBG monitoring schemes.

The cost of FBG sensor is currently comparable to cost of conventional lower grade piezoelectric accelerometers, and considerably lower than the cost of high end commercial vibration sensors. The required FBG interrogator systems however remain costly, and although more expensive compared to low end charge amplifier/signal conditioning systems for accelerometer platforms they compare favorably in cost to high end accelerometer conditioning systems. The interrogator cost in practical applications could nevertheless potentially be offset by intelligent exploitation of the FBG multi-physical sensing capability and multiplexing to yield an integrated monitoring system with much greater condition monitoring functionality compared to vibration only monitoring platforms.

Chapter 8 Conclusions and recommendations for future work

8.1 Summary

The demand of renewable energy has been steadily increasing in recent years with the rising social awareness of global environmental and climate issues. Wind energy as one of the fastest growing sustainable energy sources is being widely exploited for cost effective power generation. However, the operational and maintenance (O&M) costs of wind turbines (WT) remain significant, and in the recent offshore WT applications in particular, as the turbines are generally remotely situated in harsh ambient locations. Condition monitoring (CM) techniques are essential for detecting early faults and reducing unscheduled downtime thus reducing the associated O&M cost. The doubly fed induction generator (DFIG) is the most widely employed WT generator type due to its partial scale converter design and controllability of generated active and reactive powers,

with vast numbers of units in field application at various stages of lifetime [28, 14],these will need to be maintained and monitored effectively throughout their lifecycle to deliver the ambitious reliability and cost targets expected from large scale wind generation [7]. As consequence, the DFIG drive CM technique investigation is the focus of this PhD research topic. Two major topics were investigated in this project: the improved DFIG shaft misalignment recognition techniques and the DFIG sensorless speed estimation.

Shaft misalignment fault is a common issue in practical WT drive trains contributing to 30% of downtime [52]. Unwanted forces arising due to shaft misalignment condition can lead to damage and destruction of key WT drivetrain components such as bearings, seals, couplings and eventually its gearbox or generator; more generally, the shaft misalignment condition is reported responsible for 50% of all rotating machinery breakdowns [51]. To eliminate the considerable downtime and economic loss, different techniques are investigated to recognize DFIG shaft misalignment for CM.

Traditional machine rotational speed estimation depends on a velocity measurement device such as for example an incremental encoder, which requires additional electronics, extra wiring, extra space, frequent maintenance and careful mounting. Sensorless speed estimation (SSE) offers a low cost, high reliability, better noise immunity and less maintenance approach for machine rotational speed estimation. Additionally, SSE is an alternative solution to keep the generator in operation in case an encoder failure occurs. SSE in DFIG drive thus was selected as one of two main topics of this project.

The implementation of DFIG harmonic model in Simulink platform was firstly focused on in this research project to enable theoretical investigation of machine performance in varieties of operating scenarios. The development of model began with wound rotor induction machine (WRIM) harmonic modelling. The machine higher order harmonic

effects were approved by calculating self and mutual inductances of stator and rotor windings based on conductor distribution function. The DFIG model was implemented based on developed WRIM harmonic model by introducing additional controller model. A standard two-axis (dq) controller model was added to rotor side converter (RSC) to enable stator flux oriented control (SFOC) scheme. DFIG decoupled active power and reactive power control thus could be achieved. While considerable literature explores terminal signal (stator current) based CM and SSE techniques limited research exists on the development of these in DFIG controller signals embedded schemes. With the help of the developed DFIG harmonic model, the spectral contents in controller loops signals could be analyzed and thus provide instrumental underpinning for the analysis and development of CM and SSE techniques in this work.

After developing the DFIG harmonic model, the experimental tests are required to cross-correlate the findings from theoretical study. To this end, a laboratory DFIG test rig was extensively modified to simulate WT generator operation. The test rig consists of a WRIM, a DC machine as a prime mover, a commercial DC drive, a commercial back to back converter, dSPACE real-time platform and sets of sensors. The implementation of DFIG control scheme is challenging since the commercial RSC has inherent limitation to develop a SFOC scheme for DFIG application. With the help of a dedicated resolver signal conditioning module and a real-time platform, following modifications are deployed to the DFIG test rig to accomplish DFIG SFOC with stator directly connected to the grid supply:

- DC motor control implementation
- Rotor side current control scheme investigation
- SFOC scheme inner loops implementation for experimental test rig

- Synchronization of a vector control DFIG with the grid supply
- SFOC scheme outer loops implementation

The validation of DFIG SFOC control was examined by power loop step change test. Moreover, the validation and recognition of experimental DFIG signal significant harmonic contents was also undertaken for SSE investigation.

The investigation of DFIG sensorless speed estimation scheme utilizing controller loop signal began with the theoretical study based on DFIG harmonic model. Since the spectral search based (SSB) approach was selected, the speed dependent harmonic content (MMF) harmonics of DFIG signals needs to be identified. The DFIG signal spectral analysis was firstly undertaken to recognize MMF contents from DFIG harmonic model. The experimental recorded DFIG signals were also investigated to validate the model findings and identify other existing spectral contents beyond that represented by proposed DFIG modelling. The characteristic MMF contents in DFIG controller signals especially inner loop controller signals are stronger manifested in the spectrum and thus less effected by the surrounding spectral contents compared with the traditionally exploited for SSE terminal current spectrum. Additionally, the DFIG signals in different load levels were evaluated to identify the signal most suitable for SSB SSE tracking. To offer a high speed and accuracy harmonic content identification approach, a dedicated parabolic interpolation SSB algorithm was developed. After a theoretical study, the algorithm was validated in MATLAB interface utilizing DFIG test recordings. The estimated speeds from DFIG signals indicated a good match with encoder measured speed in both constant and variable speed conditions. To enable real-time speed estimation, a commercial FPGA platform is employed. The parabolic interpolation algorithm has to be implemented in LabVIEW interface to functionalize the routine in

real-time in a dedicated software routine. The real-time validation of the developed SSE algorithm was conducted in both constant speed and variable speed conditions in different load scenarios. The estimated speed indicated a good match with measured speed in all conditions.

The other major topic is DFIG shaft misalignment fault detection technique development. Typical misalignment online monitoring technique depends on costly vibration sensors and associated signal conditions platforms. To reduce the cost of CM, motor current signature analysis (MCSA) technique was frequently investigated. Stator current was typically selected as the diagnostic signal for MCSA. In DFIG system with SFOC employed, the fault induced harmonics are also expected to be observed in controller loop signals. These signals thus are investigated to explore a new approach for MCSA shaft misalignment diagnostics. The research began with a theoretic model study: shaft misalignment mechanical effect is simulated with a universal joint model and was introduced to the developed DFIG harmonic model. The spectral harmonic contents from DFIG model controller signals were analyzed in both healthy and faulty conditions mapping the possible fault characteristic frequency contents in the controller signals, reported by the model study as a potential misalignment indicator. To validate this finding in a practical setting, experimental tests utilizing laboratory DFIG were undertaken. Varieties of load and speed operating points were tested in both healthy and faulty scenarios. The harmonic component of interest manifested a tendency of increase in magnitude with shaft misalignment however is not as significant as model study indicated. The limitation of the testing facilities were evaluated in the end of the chapter and potential improvement model study was investigated.

The application of fibre optic sensing for CM has been increasingly investigated due to

its features: electromagnetic interference (EMI) immunity, small size and flexibility, multiplexing capability and that of multi-physical sensing. In this study, Fibre Bragg grating (FBG) technique was employed to sense the DFIG frame strain, the nature and practical manifestation of the shaft misalignment fault spectral signatures from frame strain is investigated to develop novel fault diagnostic tool. In this study, three different orientations of frame strain: radial, axial and circumferential were evaluated in a wide range of speed and load operation points. To cross-correlate the performance with typically employed vibration sensor for online monitoring, two orientations of machine vibration were also analyzed. After testing with different severity of faults, a novel approach of shaft misalignment diagnostic enables fault recognition and severity definition utilizing two orientations of strain signal is implemented. Moreover, a thermal cross-sensitivity study was undertaken to prove the developed strain sensing approach is independent to the ambient temperature of sensing locations.

8.2 Summary of major contributions of the work

This thesis reported for the first time that it is possible to utilize controller signal to develop an effective SSE in DFIGs. This was coupled by a dedicated rapid estimation spectral analysis technique based on parabolic estimation, which allowed accurate real time estimation performance in practical tests at improved rates. Furthermore, the algorithm capability could not be fully exploited due to the limitations in hardware available in this research, and is believed to be considerably higher than that could be tested in experiments in this work. Nonetheless, the reported real time estimation results compare favorable to alternative spectral search based techniques for electric machinery reported in the literature.

This thesis work also reported novel techniques for DFIG shaft misalignment recognition:

which based on identification of spectral content of acquired signal sources. Controller embedded signals spectrum were investigated in both model study and acquired DFIG signals. The harmonic component of interest manifested a tendency of increase in magnitude with shaft misalignment however the characteristics in practical signal is not as significant as model study indicated. DFIG frame strain sensing utilizing FBG technique was also employed to monitor shaft misalignment in different orientations. A novel approach for shaft misalignment fault recognition and severity identification was successfully implemented.

- The development of the DFIG harmonic model in Simulink which is capable for both higher order harmonic spectral analysis of machine signals and decoupled active/reactive power control (SFOC scheme). The model signal signature was cross-correlated evaluated with experimental recorded DFIG signals.
- The development of shaft misalignment model and model and analytical characterization DFIG misalignment fault signature in controller signals. Experimental validation was also conducted and investigated utilizing laboratory emulated shaft misalignment DFIG test rig.
- The development of DFIG shaft misalignment monitoring technique utilizing FBG frame strain sensing and experimental evaluation and validation of its performance in practical conditions with an assessment of the sensing thermal cross-sensitivity and orientation
- Investigation of DFIG controller signals based sensorless speed estimation algorithm with improved estimation rate capability, and its experimental validation. The dedicated real time routine was implemented in LabVIEW interface and experimental validation was conducted.

8.3 Recommendations for future work

A number of areas were identified during this PhD research project where further researches could be conducted to develop DFIG condition monitoring techniques. Due to the time constrain, the targets listed in this section were beyond the scope of this PhD project. The identified future works are presented as followings:

- **Sensorless estimation for angular rotor position acquirement**: to enable DFIG sensorless control, the angular rotor position is the essential parameter to obtain. Based on the existing SSE routine, the real-time rotor position thus could be obtained via integration of instantaneous speed. Further development of the algorithm will focus on the real-time integral. Besides, the evaluation of sensorless control performance will be conducted.
- **Investigation of other generator faults:** the developed DFIG harmonic model is adapted to investigate varieties of electrical and mechanical faults by manipulate the machine parameters or characteristics. This could be beneficial to explore the achievability of DFIG control loop signals to identify different generator faults. In this project, researches were undertaken focused on angular shaft misalignment diagnosis. As an extension of the study, the offset and combined shaft misalignment investigation should be achieved from modelling to practical testing. In addition, the study of other mechanical fault such as bearing fault and eccentricity are also important since these have large failure rate faults and responsible for high downtime rates. Therefore, more investigations of control loop signals spectra in different fault conditions could be potentially undertaken.
- **Development of FBG sensing technique for other generator faults:** DFIG frame strain sensing utilizing FBG was employed for shaft misalignment

recognition and has proven an evident mechanical effect signature cross-correlated with vibration spectrum. Therefore, FBG strain sensing could be potentially a diagnostic tool for other mechanical fault such as bearing fault and eccentricity recognition. Further experimental studies could be performed on these topics.

- **Development of Finite element analysis (FEA) model for fault signature analysis**: In this PhD project, DFIG harmonic model was implemented in Simulink interface to investigate electrical signal characteristics in healthy and fault condition. However, the developed model is not capable for some multi-physics signal study such as vibration, surface strain, electromagnetic field and thermos effects. Therefore the FEA model is required to enable model/ theoretical study of multi-physic study. The effect of monitoring operation along with faults could give additional indication of certain fault patterns in these signals and thus could be used for fault diagnosis purpose.
- **Use of more advanced techniques for condition monitoring:** the machine learning based techniques could have the potential to extract the inherent characteristics of DFIG faults. Differ from traditional signal spectral investigation, this technique enables multi-sources condition monitoring and classify the fault patterns beyond traditional characteristic frequency components. The potential of machine learning technique could be employed for available test facilities measured signals. i.e. current, vibration, strain…etc.
- **Investigation of fault mitigation techniques:** Investigations of WT generator electrical and mechanical fault mitigation is important to help to secure the DFIG operation until scheduled maintenance can be deployed. Therefore this research could be extended to implement fault mitigation technique, which is

could be firstly evaluated in developed DFIG harmonic model and then examined in laboratory test rig.

References

Commented [YW3]: Changed reference table frame to make it within regulation

[1] "*Electricity generation and supply in Scotland, Wales, Northern Ireland and England, 2016 to 2019*," Department for Business, Energy & Industrial Strategy, 2020.

[2] "*Renewable Caoacity Statistics 2020*," IRENA , 2020.

[3] N. Panwar, S. Kaushik and S. Kothari, "Role of renewable energy sources in environmental protection: A review," *Renewable and Sustainable Energy Reviews,* vol. 15, no. 3, pp. 1513-1524, 2011.

[4] "*Future of wind*," International Renewable Energy Agency, IRENA, 2019.

[5] J. Lee and F. Zhao, "*GWEC | GLOBAL WIND REPORT 2019*," Global Wind Energy Council, 2020.

[6] "*Offshire Wind Outlook 2019*," International Energy Agency , 2019.

[7] Y. Amirat, M. Benbouzid, B. Bensaker and R. Wamkeue, "Condition Monitoring and Fault Diagnosis in Wind Energy Conversion Systems: A Review," Antalya, 2007.

[8] B. Lu, Y. Li, X. Wu and Z. Yang, "A Review of Recent Advances in Wind Turbine Condition Monitoring and Fault Diagnosis," in *IEEE*, 2009.

[9] C. Walford, "Wind turbine reliability: understanding and minimizing wind turbine operation and maintenance costs," Sandia National Laboratries, 2006.

[10] D. McMillan and G. W. Ault, "Quantification of Condition Monitoring Benefit for Offshore Wind Turbines," *WIND ENGINEERING,* vol. 31, no. 4, pp. 267-285, 2007.

[11] "UpWind-Design limits and solutions for very large turbines," European Wind Energy Association, EWEA, 2011.

[12] Y. Li, C. Zhu, C. Xu and J. Tan, "Fatigue reliability analysis of wind turbine drivetrain

considering strength degradation and load sharing using survival signature and FTA," *Energies,* vol. 13, no. 8, 2020.

[13] C. D. Dao, B. Kazemtabrizi, C. J. Crabtree and P. J. Tavner, "Integrated condition-based maintenance modelling and optimisation for offshore wind turbines," *Wind Energy,* pp. 1-19, 2021.

[14] C. Hernandez, T. Telsnig and A. Pradas, "JRC Wind Energy Status Report 2016 Edition," Luxemburg, 2017.

[15] H. Li and Z. Chen, "Overview of different wind generator systems and their comparisons," *IET Renewable Power Generation,* vol. 2, no. 2, pp. 123-138, 2007.

[16] S. Djurovic, C. J. Crabtree, P. J. Tavner and A. C. Smith, "Condition monitoring of wind turbine induction generators with rotor electrical asymmetry," *IET Renewable Power Generation,* vol. 6, no. 4, pp. 207-216, 2012.

[17] D. Vilchis-Rodriguez, S. Durovic and A. Smith, "Wound rotor induction generator bearing fault modelling and detection using stator current analysis," *IET Renewable Power Generation,* vol. 7, no. 4, pp. 330-340, 2013.

[18] J. Li, D. Wang and L. He, "Study of rotor winding inter-turn short Fault in Doubly Fed Induction Gnenrator Based on Current Signal Spectrum Analysis," in *International Conference on Electrical Machines and Systems*, 2013.

[19] M. Zaggout, P. Tavner, C. Crabtree and L. Ran, "Detection of rotor electrical asymmetry in wind trubine doubly-fed induction generators," *IET Renewable Power Generation,* vol. 8, no. 8, pp. 878-886, 2014.

[20] N. Sarma and S. Durovic, "Modelling, Analysis and Validation of Controller Signal Interharmonic Effects in DFIG Drives," *IEEE Transactions on Sustainable Energy,* vol. 11, no. 2, pp. 713-725, 2019.

[21] N. Sarma, P. M. Tuohy, A. Mohammed and S. Djurovic, "Rotor electrical fault detection in DFIGs using wide-band controller signals," *IEEE Transactions on Sustainable Energy,* vol. 12, no. 1, pp. 623-633, 2021.

[22] N. Sarma, P. M. Touhy and S. Djurovic, "Modeling, Analysis and Validation of Controller Signal Interharmonic Effects in DFIG Drives," *IEEE Transactions on Sustainable Energy,* 2019.

[23] N. Sarma, P. M. Touhy, J. M. Apsley, Y. Wang and S. Djurovic, "DFIG Stator Flux

Oriented Control Scheme Execution for Test Facilities Utilising Commercial Converters," *IET Renewable Power Generation,* vol. 12, no. 12, pp. 1366-1374, 2018.

[24] Y. Wang, A. Mohammed, N. Sarma and S. Djurovic, "Double Fed Induction Generator Shaft Misalignment Monitoring by FBG Frame Strain Sensing," *IEEE Sensors Journal.*

[25] K. Raman, *Fiber bragg gratings*, Acdemic press, 2009.

[26] J. Manwell, J. McGowan and A. Rogers, Wind Energy Explained: Theory, Design and Application, 2nd Edition, John Wiley & Sons Ltd, 2009.

[27] S. Djurovic, "Analysis of Doubly-Fed Induction Generator under Electrical Fault Conditions," Unicersity of Manchester, Manchester, 2007.

[28] G. Abad, J. Lopez, M. Rodriguez, L. Marroyo and G. Iwanski, Doubly Fed Induction Machine : Modelling and Control for Wind Energy Generation, Wiley-IEEE press, 2011.

[29] M. R. Patel, Wind and Solar Power Systems Design, Analysis, and Operation, Second Edition, CRC Press, 2005.

[30] "*RenewableWatch*," July 2017. [Online]. Available: https://renewablewatch.in/2017/07/29/turbine-configuration/. [Accessed 15 April 2020].

[31] J. Fletcher and J. Yang, "Introduction to the Doubly-Fed Induction Generator for Wind Power Applications," in *Paths to Sustainable Energy*, InTech, 2010, pp. 259-278.

[32] M.Ragheb, "Wind energy conversion theory," 2017.

[33] G. Abad, J. Lopez, M. Rodriguze, L. Marroyo and G. Iwanski, "*Doubly Fed Induction Machine- Modeling and Control for Wind Energt Generation*," Wiley, 2011.

[34] B.Hopfensperger, D.J.Atkinson and R.A.Lakin, "Stator-flux-oriented control of a doubly-fed induction machine with and without position encoder," *IEEE Proceedings- Electric Power Applications,* vol. 146, no. 6, pp. 597-605, 1999.

[35] D. Casadei, F. Filippetti, C. Rossi, A. Stefani, G. Capolino and A. Yazidi, "A General Diagnostic Method for Doubly Fed Induction Machine Drives Based on Field Oriented Control," in *IEEE International Symposium on Diagnostics for Electric Machines, Power Electronics and Drives*, Cracow, 2007.

[36] F. Spinato, P. Tavner, G. v. Bussel and E. Koutoulakos, "Reliability of wind turbine subassemblies," *IET Renewable Power Generation,* vol. 3, no. 4, pp. 387-401, 2009.

[37] W. Qiao and D. Lu, "A Survey on Wind Turbine Condition Monitoring and Fault Diagnosis—Part I: Components and Subsystems," *IEEE Transactions on Industrial Electronics,* vol. 62, no. 10, pp. 6536-6545, 2015.

[38] "*Guide to UK Offshore Wind Operations and Maintenance*," Garrad Hassan for the Crown Estate, 2013.

[39] ENTSO-E, "*Preparing the Electricity Grid of the Future – 2050 Electricity Highways*," [Online]. Available: https://www.entsoe.eu/outlooks/ehighways-2050/. [Accessed 05 01 2020].

[40] W. Yang, P. J. Tavner, C. J. Crabtree, Y. Feng and Y. Qiu, "Wind turbine condition monitoring : technical and commercial challenges," *Wind Energy,* vol. 17, no. 5, pp. 673-693, 2017.

[41] "*Cirtification of Condition Monitoring*," Service Specification, June 2016.

[42] S. J. Lacey, "The Roal of Vibration Monitoring in Predictive Maintenance," *Asset Management and Maintenance Journal,* vol. 24, no. 1, pp. 42-51, 2011.

[43] C. J. Crabtree, D. Zappalá and P. J. Tavner, "*Survey of commercially available condition monitoring systems for wind turbines*," Durham Cniversity, Durham, 2014.

[44] S. F. Program, "*Upwind: Dedign limits and solutions for very large wind turbines*," March 2011. [Online]. Available: http://www.ewea.org/fileadmin/files/library/publications/reports/UpWind_Report.pdf. [Accessed 22 June 2017].

[45] N. Sarma, "Investigation of Controller Embedded Condition Monitoring for Doubly Fed Induction Generators," University of Manchester, Manchester, 2017.

[46] P. Tavner, "Review of condition monitoring of rotating electrical machines," *IET Electrical Power Applications,* vol. 2, no. 4, pp. 215-247, 2008.

[47] L. M. Popa, B. Jensen, E. Ritchie and I. Boldea, "Condition Monitoring of Wind Generators," in *38th IEEE Annual Meeting on Conference Record of the Industry Applications Conferences (IAS)*, 2003.

[48] Z. Ye and B. Wu, "A Review on Induction Motor Online Fault Diganosis," in *3rd International Power Electronics and Motion Control Conference (IPEMC)*, 2000.

[49] M. Benbouzid, "A Review of Induction Motors Signature Analysis as a Medium for Faults

Detection," *IEEE transactions on industrial electronics,* vol. 47, no. 5, pp. 984-993, 2000.

[50] "*Vibration Diagnostic Guide*," SKF Reliability Systems, CM5003, 2000.

[51] G. Knitz, "*A Guide to Wind Turbine Alignment*," *Wind system magazine,* pp. 22-25, 6 March 2012.

[52] O. Tonk and Q. Wang, "The detection of wind turbine shaft misalignment using temperature monitoring," *CIRP Journal of Mnaufacturing Science and Technology,* vol. 17, pp. 71-79, 2009.

[53] O. Mankowski and Q. Wang, "Real-time Monitoring of Wind Turbine Generator Shaft Alignment using Laser Measurement," in *International Through-life Engineering Services Conference*, 2013.

[54] "*Guideline for the Certification of Condition Monitoring Systems for Wind turbines*," in *Germanischer Lloyd Renewables Certification*, Hamburg, 2013.

[55] S. Sheng, H. Link, W. LaCava, J. van Dam, B. McNiff, P. Veers, J. Keller, S. Butterfield and F. Oyague, "Wind turbine drivetrain condition monitoring during GRC phase 1 and phase 2 testing," in *National Renewable Energy Lab. (NREL)*, USA, 2011.

[56] "*Maintenance*," European Comission Erasmus+ Programme, 2015, Skill Wind.

[57] R. Obaid, T. Habetler and R. Tallam, "Detecting load unbalance and shaft misalignment using stator current in inverter-driven induction motors," in *IEEE International Electric Machines and Drives Conference*, Madison, 2003.

[58] W. Zhang, J. Yang and a. e. a. L. Chun, "Theoretical and experimental research on turbo-generator shaft alignment using strain gauge method," *Journal of Vibration and Control,* vol. 23, no. 7, pp. 1183-1192, 2017.

[59] A. Simm, Q. Wang, S. Huang and W. Zhao, "Laser based measurement for the monitoring of shaft misalignment," *Elsevier Measurement,* no. 87, pp. 104-116, 2016.

[60] S. B. Chaudhury and S. Gupta, "Online Identification OfAC Motor Misalignment Using Current Signature Analysis and Modified K-Mean Clustering Technique," in *2006 IEEE International Conference on Industrial Technology*, Mumbai, 2006.

[61] A. K. Verma, S. Sarangi and M. H. Kolekar, "Misalignment fault detection in induction motor using rotor shaft vibration and stator current signature analysis," *Int. J. Mechatronics and Manufacturing Systems,* vol. 6, no. 5/6, pp. 422-436, 2013.

[62] J. Bossio, G. Bossio and C. Angelo, "Angular Misalignment in Induction Motors with Flexible Coupling," in *2009 35th Annual Conference of IEEE Industrial Electronics*, Porto, 2009.

[63] M. Blödt, P. Granjon, B. Raison and G. Rostaing, "Models for Bearing Damage Detection in Induction Motors Using Stator Current Monitoring," *IEEE transactions on industrial electronics,* vol. 55, no. 4, pp. 1813-1822, 2008.

[64] S. Nandi, H. A. Toliyat and X. Li, "Condition Monitoring and Fault Diagnosis of Electrical Motors-A Review," *IEEE TRANSACTIONS ON ENERGY CONVERSION,* vol. 20, no. 4, pp. 719-729, 2005.

[65] D. S. Vilchis-Rodriguez and S. Djurovic, "Wound rotor induction generator bearing fault modelling and detection using stator current analysis," *IET Renewable Power Generation,* vol. 7, no. 4, pp. 330-340, 2013.

[66] K. Alewine and W. Chen, "*Wind Turbine Generator Failure Modes Analysis and Occurrence*," in *Windpower 2010*, Texas, 2010.

[67] D. S. Shah and V. N. Patel, "A Review of Dynamic Modelling and Fault Identifications Methods for Rolling Element Bearing," in *2nd International Conference on Innovations in Automation and Mechatronics Engineering*, 2014.

[68] D. S. Vilchis--Rodriguez and S. Djurovic, "Wound rotor induction generator bearing fault modelling and detection using stator current analysis," *IET Renewable Power Generation,* vol. 7, no. 4, pp. 330-340, 2013.

[69] W. Li and C. K. Mechefske, "Detection of Induction Motor Faults: A Comparison of Stator Current, Vibration and Acoustic Methods," *Journal of Vibration and Control,* vol. 12, no. 2, pp. 165-188, 2006.

[70] S. Nandi, H. A. Toliyat and X. Li, "Condition Monitoring and Fault Diagnosis of Electrical Motors-A Review," *IEEE TRANSACTIONS ON ENERGY CONVERSION,* vol. 20, no. 4, pp. 719-729, 2005.

[71] J. Faiz and S. M. Moosavi, "Review of Eccentricity Fault Detection Techniques in IMs Focusing on DFIG," in *IEEE 5th International Conference on Power Engineering, Energy and Electrical Drives*, 2015.

[72] Z. Dogan, B. Kara, C. Emeksiz and L. Gokrem, "The Static Eccentricity Fault Diagnosis in Time Domain at Line Start Permanent Magnet Synchronous Motor," *Journal of New*

Results in Science, pp. 88-95, 2016.

[73] J. Faiz, B. M. Ebrahimi, B. Akin and H. A. Toliyat, "Comprehensive Eccentricity Fault Diagnosis in Induction Motors Using Finite Element Method," *IEEE TRANSACTIONS ON MAGNETICS,* vol. 45, no. 3, pp. 1764-1767, 2009.

[74] H. A. Toliyat, M. S. Arefeen and A. G. Parlos, "A Method for Dynamic Simulation of Air-Gap Eccentricity in Induction Machines," *IEEE TRANSACTIONS ON INDUSTRY APPLICATIONS,* vol. 32, no. 4, pp. 910-918, 1996.

[75] J. Cameron, W. Thomson and A. Dow, "Vibration and current monitoring for detecting airgap eccentricity in large induction motors," *IEE Proceedings B- Electric Power Applications,* vol. 133, no. 3, pp. 155-163, 1986.

[76] J. Faiz and S. M. M. Moosavi, "Detection of mixed eccentricity fault in doubly-fed induction generator based on reactive power spectrum," *IET Electric Power Applications,* vol. 11, no. 6, pp. 1076-1084, 2016.

[77] G. Kliman, W. J. Premerlani, R. A. Koegl and D. Hpeweler, "A New Approach to On-Line Turn Fault Detection in AC Motors," in *Industry Applications Conference*, 1996.

[78] G. Stone and J. Kapler, "Stator winding monitoring," *IEEE Industry Applications Magazine,* vol. 4, no. 5, pp. 15-20, 1998.

[79] M. B. Abadi and S. M. e. a. Cruz, "Detection of Stator and Rotor Faults in a DFIG Based on the Stator Reactive Power Analysis," in *IECON2014-40th Annual Conference of the IEEE*, 2014.

[80] M. Zaggout, P. Tavner and L. R. Christopher Crabtree, "Detœction of rotor electrical asymmetry in wind turbine doubly-fed induction generators," *IET Renewable Power Generator,* vol. 8, no. 8, pp. 878-886, 2014.

[81] P. J. Tavner, "Review of condition monitoring of rotating electrical machines," *Published in IET Electric Power Applications,* vol. 2, no. 4, pp. 215-247, 2007.

[82] M. e. a. Blodt, "Mechanical Fault Detection in Induction Motor Drives through Stator Current Monitoring - Theory and Application Examples," *Fault Detection,* vol. 45, no. 3, pp. 451-487, 2010.

[83] S. Williamson and S. Durovic, "Origins of Stator Current Spectra in DFIGs with Winding Faults and Excitation Asymmetries," in *2009 IEEE International Electric Machines and Drives Conference*, Miami, 2009.

[84] M. E. H. Benbouzid and G. B. Kliman, "What Stator Current Processing-Based Technique to Use for Induction Motor Rotor Fault Diagnosis?," *IEEE TRANSACTIONS ON ENERGY CONVERSION,* vol. 18, no. 2, pp. 238-244, 2003.

[85] A. Othonos, K. Kalli, D. Pureur and A. Mugnier, "*Fibre Bragg gratings*," in *Springer Series in Optical Sciences*, New York & Boston, Goodwin House Publishers, 2006, pp. 189-269.

[86] M. Kreuzer, "*Strain Measurement with Fiber Bragg Grating Sensors*," HBM , Darmstadt, Germany, 2006.

[87] P. Wang, J. Liu, F. Song and H. Zhao, "Quasi-distributed temperature measurement using a single fiber Bragg grating embedded in a composite laminate," *Smart Materials and Structures,* vol. 26, 2017.

[88] C. Kim, S. Park, C. Kim and D. Kang, "*Internal Strain Monitoring of Filament Wound Pressure Tanks using Embedded Fiber Bragg Grating Sensors*," 2005.

[89] K. Sousa, I. Brutkowski Vieira da Costa, E. Maciel, J. Rocha, C. Martelli and J. Cardozo da Silva, "Broken Bar Fault Detection in Induction Motor by Using Optical Fiber Strain Sensors," *IEEE Sensors Journal,* vol. 17, no. 12, pp. 3669-3676, 2017.

[90] K. Sousa, U. Dreyer, C. Martelli and J. Cardozo da Silva, "Dynamic Eccentricity Induced in Induction Motor Detected by Optical Fiber Bragg Grating Strain Sensors," *IEEE Sensors Journal,* vol. 16, no. 12, pp. 4786-4792, 2016.

[91] A. Mohammed, N. Sarma and S. Djurovic, "Fibre optic monitoring of induction machine frame strain as a diagnostic tool," in *IEEE International Electric Machines and Drives Conference (IEMDC)*, Miami, 2017.

[92] A. Mohammed and S. Djurovic, "Stator Winding Internal Thermal Monitoring and Analysis Using In-Situ FBG Sensing Technology," *IEEE Transactions on Energy Conversion,* vol. 33, no. 3, pp. 1508-1518, 2018.

[93] A. Mohammed, J. I. Melecio and S. Djurovic, "Stator Winding Fault Thermal Signature Monitoring and Analysis by In Situ FBG Sensors," *IEEE Transactions on Industrial Electronics,* vol. 66, no. 10, pp. 8082-8092, 2019.

[94] A. Mohammed, J. I. Melecio and S. Djurovic, "Open-Circuit Fault Detection in Stranded PMSM Windings Using Embedded FBG Thermal Sensors," *IEEE Sensors Journal,* vol. 19, no. 9, pp. 3358-3367, 2019.

[95] R. e. a. Joao PV, "Development and field trial of a FBG-based magnetic sensor for large hydrogenerators," in *International Society for Optics and Photonics*, 2016.

[96] B. Geraldo and M. M. Werneck, "A magnetostrictive-fiber Bragg grating sensor for induction motor health monitoring," *Measurement,* vol. 122, pp. 117-127, 2018.

[97] A. Mohammed, J. I. Melecio and S. Djurovic, "Electrical Machine Permanent Magnets Health Monitoring and Diagnosis Using an Air-gap Magnetic Sensor," *IEEE Sensors Journal ,* in press, 2020.

[98] A. Mohammed and S. Djurovic, "In-Situ Thermal and Mechanical Fibre Optic Sensing for In-Service Electric Machinery Bearing Condition Monitoring," in *IEEE International Electric Machines & Drives Conference (IEMDC)*, San Diego, 2019.

[99] M. Fabian, M. Hind, C. Gerada, T. Sun and K. Grattan, "Comprehensive monitoring of electrical machine parameters using an integrated fibre Bragg grating-based sensor system," *Journal of Lightwave Technology,* 2017.

[100] P. Neti, M. Shah and K. Younsi, "Electrical signature analysis based online monitoring of drive-trains for doubly-fed wind generators," in *IECON 2012 - 38th Annual Conference on IEEE Industrial Electronics Society*, 2012.

[101] "*FFT (Fast Fourier Transform) Waveform Analysis*," DATAQ INSTRUMENTS, [Online]. Available: https://www.dataq.com/data-acquisition/general-education-tutorials/fft-fast-fourier-transform-waveform-analysis.html. [Accessed 15 6 2017].

[102] S. Gade and K. Gram-Hansen, "*Non-stationary Signal Analysis using Wavelet Transform, Short-time Fourier Transform and Wigner-Ville Distribution*," in *Technical Review*, Nærum, Denmark., Brüel & Kjær , 1996, pp. 1-28.

[103] Z. Peng, P. W. Tse and F. Chu, "A comparison study of improved Hilbert-Huang transform and wavelet transform: Application to fault diagnosis for rolling bearing," *Mechanical Systems and Signal Processing,* vol. 19, pp. 974-988, 2005.

[104] Y. Amirat, V. Choqueuse and M. E. Benbouzid, "Bearing Fault Detection in DFIG-Based Wind Turbines Using the First Intrinsic Mode Function," in *XIX International Conference on Electrical Machines*, Rome, 2010.

[105] M. Feldman, "Hilbert transform in vibration analysis," *Mechanical Systems and Signal Processing,* vol. 25, pp. 735-802, 2011.

[106] D. Shi, P. Unswirth and R. Gao, "Sensorless speed measurement of induction motor using

Hilbert transform and interpolated fast Fourier transform," *IEEE Transactions on Instrumentation and Measurement,* vol. 55, no. 1, pp. 290-299, 2006.

[107] M. Zaky, M. Khater, H. Yasin and S. Shokralla, "Review of Different Speed Estimation schemes for Sensorless Induction Motor Drives," *J Elect Eng,* 2008.

[108] W. Silva, A. Lima and A. Oliveira, "Speed Estimation of an Induction Motor Operating in the Nonstationary Mode by Using Rotor Slot Harmonics," *IEEE Transactions on Instrumentation and Measurement,* vol. 64, no. 4, pp. 984-994, 2015.

[109] K. Tshiloz, "*Sensorless speed esitmation in wound rotor induction machine drives*," University of Manchester, 2016.

[110] J. Bonet-Jara and J. Pons-Llinares, "Sensorless Speed Estimation. A Review.," in *IEEE 12th International Symposium on Diagnostics for Electrical Machines, Power Electronics and Drives (SDEMPED)*, Toulouse, 2019.

[111] K. Tshiloz and S. Djurovic, "Wide range sensorless speed estimation in wound rotor induction machines by sliding window search of the stator current signal," in *8th IET International Conference on Power Electronics, Machines and Drives (PEMD 2016)*, Glasgow, 2016.

[112] D. Wu and S. Pekarek, "Using Mechanical Vibration to Estimate Rotor Speed in Induction Motor Drives," in *2007 IEEE Power Electronics Specialists Conference*, Orlando, 2007.

[113] K. Tshiloz and S. Djurovic, "Scalar Controlled Induction Motor Drive Speed Estimation by Adaptive Sliding Window Search of the Power Signal," *International Journal of Electrical Power and Energy Systems,* vol. 91, pp. 80-91, 2017.

[114] P. Phumiphak and C. Chat-uthai, "Induction Motor Speed Measurement Using Motor Current Signature Analysis Technique," in *2009 International Conference on Electrical Machines and Systems*, Tokyo, 2009.

[115] M. Ishida and K. Iwata, "Steady-state characteristics of a torque and speed control system of an induction motor utilizing rotor slot harmonics for slip frequency sensing," *IEEE Trans. Power Electron,* Vols. PE-2, no. 3, pp. 257-263, 1987.

[116] K. Hurst and T. Habetler, "Sensorless speed measurement using current harmonic spectral estimation in induction machine drives," *IEEE Transactions on Power Electronics,* vol. 11, no. 1, pp. 66-73, 1996.

[117] N. Sarma, P. Tuohy and S. Djurovic, "Modeling, Analysis and Validation of Controller Signal Interharmonic Effects in DFIG Drives," *IEEE Transactions on Sustainable Energy,* 2019.

[118] N. Sarma, P. Tuohy, J. Apsley, Y. Wang and S. Djurović, "DFIG stator flux-oriented control scheme execution for test facilities utilising commercial converters," *IET Renewable Power Generation,* vol. 12, no. 12, pp. 1366-1374, 2018.

[119] "*Setting up a real-time digital data acquisition and control interface in dSPACE*," [Online]. Available: http://academic.csuohio.edu/richter_h/courses/mce484/dspace_guide.pdf. [Accessed 3 4 2017].

[120] dSPACE, *DS1103 PPC Controller Board Hardware Installation and Configuration, dSPACE*, 2007.

[121] Control Technoques, *User Guide MENTOR II*, Control Techniques Drives Ltd, 2006.

[122] V. F. KROUPA, "PRINCIPLES OF PHASE LOCKED LOOPS," 2000 IEEE Int'l Frequency Control Symposium, Kansas City, 2000.

[123] E. Chester and D. Kinniment, "A digital phase locked loop for power conversion ASICs," in *European Conference on Design Automation with the European Event in ASIC Design*, Paris, 1993.

[124] Control Techniques, "*Advanced User Guide Unidrive SP*," Control Techniques, 2005.

[125] Control Techniques, "*User Guide Unidrive SP*".

[126] N. Sarma, "Investigation of Controller Embedded Condition Monitoring for Doubly Fed Induction Generators," University of Manchester, Manchester, 2017.

[127] N. Aung, C. Bi, A. Al Mamun, C. S. Soh and Y. YinQuan, "A Demodulation Technique for Spindle Rotor Position Detection With Resolver," *IEEE Transactions on Magnetics,* vol. 49, no. 6, pp. 2614-2619, 2013.

[128] W. L.Xu, "Torque and reactive power control of a doubly fed induction machine by position sensorless scheme," *Industry Applications, IEEE Transactions on,* vol. 31, no. 3, pp. 636-642, 1995.

[129] A. Shiri, A. Vahedi and A. Shoulaie, "The effect of parameter variations on the performance of indirect vector controlled induction motor drive," in *2006 CES/IEEE 5th International Power Electronics and Motion Control Conference*, Shanghai, 2006.

[130] N. P. Quang and J.-A. Dittrich, *Vector Control of Three-Phase AC Machines: System Development in the Practice*, Berlin: Springer, 2015.

[131] C.M.Ong, *Dynamic simulation of electric machinery: using MATLAB/SIMULINK*, Prentice Hall, 1998.

[132] S. Williamson and A. Smith, "Field analysis for rotating induction machines and its relationship to the equivalent-circuit method," *IEE Proceedings,* vol. 127 Pt.B, no. 2, 1980 .

[133] R. Datta and V. Ranganathan, "Decoupled control of active and reactive power for a grid-connected doubly-fed wound rotor induction machine without position sensors," in *Conference Record of the 1999 IEEE Industry Applications Conference. Thirty-Forth IAS Annual Meeting* , Phoenix, AZ, USA, 1999.

[134] K. Tshiloz and S. Durovic, "Wide range sensorless speed estimation in wound rotor induction machines by sliding window search of the stator current signal," in *8th IET International Conference on Power Electronics, Machines and Drives (PEMD 2016)*, Glasgow, 2016.

[135] K. Tshiloz and S. Durovic, "Scalar Controlled Induction Motor Drive Speed Estimation by Adaptive Sliding Window Search of the Power Signal," *International Journal of Electrical Power and Energy Systems,* vol. 91, no. Feb, pp. 80-91, 2017.

[136] X. Yang, X. Gong and W. Qiao, "Mechanical sensorless maximum power tracking control for direct-drive PMSG wind turbines," in *Energy Conversion Congress and Exposition (ECCE)*, Atalanta, GA, 2010.

[137] S. Djurovic, D. Vilchis-Rodriguez and A. Smith, "Supply Induced Interharmonic Effects in Wound Rotor and Doubly-Fed Induction Generators," *IEEE Transactions on Energy Conversion,* vol. 30, no. 4, pp. 1397-1408, 2015.

[138] N. Sarma, P. M. Tuohy, A. Mohammed and S. Djurovic, "Rotor electrical fault detection in DFIGs using wide-band controller signals," *IEEE Transactions on Sustainable Energy,* vol. 12, no. 1, pp. 623-633, 2021.

[139] S. Dolatabadi and S. Tohidi, "A Review on Position Sensorless Methods for Wind Generators," *INTERNATIONAL JOURNAL of RENEWABLE ENERGY RESEARCH,* vol. 7, no. 2, pp. 476-488, 2017.

[140] G. Marques and D. M. Sousa, "Air-gap-power-vector-based sensorless method for dfig control without flux estimator," *IEEE Transactions on Industrial Electronics,* vol. 58, no.

10, pp. 4717-4726, 2011.

[141] T. P. a. A. M. S. Djukanović, "Precise sinusoid frequency estimation based on parabolic interpolation," in *24th Telecommunications Forum (TELFOR)*, Belgrade, 2016.

[142] National Instrument, "*NI 9402 DATASHEET*," 2017.

[143] National Instrument, "*NI 9215 Datasheet*".

[144] W. Silva, A. Lima and A. Oliveira, "Speed Estimation of an Induction Motor Operating in the Nonstationary Mode by Using Rotor Slot Harmonics," *IEEE Transactions on Instrumentation and Measurement,* vol. 64, no. 4, pp. 984-994, 2015.

[145] K. Hurst and T. Habetler, "Sensorless speed measurement using current harmonic spectral estimation in induction machine drives," *IEEE Transactions on Power Electronics,* vol. 11, no. 1, 1996.

[146] S. Djurovic, C. J. Crabtree and P. e. a. Tavner, "Condition monitoring of wind turbine induction generators with rotor electrical asymmetry," *IET Renewable Power Generation,* vol. 6, no. 4, pp. 207-216, 2012.

[147] W. Yang, P. Tavner and C. ,. a. Crabtree, "Cost-Effective Condition Monitoring for Wind Turbines," *IEEE Transactions on Industrial Electronics,* vol. 57, no. 1, pp. 263-271, 2010.

[148] K. Tshiloz, D. Vilchis-Rodriguez, S. Djukanović, N. Sarma and S. Djurović, "Sensorless speed estimation in wound rotor induction machines by spectral search of the stator phase power signal," *IET Electric Power Applications,* vol. 10, no. 6, pp. 581-592, 2016.

[149] Y. Wang, N. Sarma, A. Mohammed and S. Djurovic, "DFIG current and controller signals' angular shaft misalignment signature' an experimental case study," in *020 International Conference on Electrical Machines (ICEM)*, Gothenburg, 2020.

[150] J. Piotrowski, *Shaft Misalignment Handbook*, Third edition, 1995.

[151] O. Tonks and Q. Wang, "The detection of wind turbine shaft misalignment using temperature monitoring," *CIRP Journal of Manufacturing Science and Technology,* vol. 17, pp. 71-79, 2009.

[152] G. Knitz, "*A Guide to Wind Turbine Alignment*," *Wind Systems,* pp. 22-25, March 2012.

[153] "*UpWind-Design limits and solutions for very large turbines*," European Wind Enegry Association, 2011.

[154] J. M. Bossio, G. R. Bossio and C. H. D. Angelo, "Angular Misalignment in Induction Motors with Flexible Coupling," in *Industrial Electronics*, 2009.

[155] "*Universal Joint*," [Online]. Available: https://howlingpixel.com/i-en/Universal_joint. [Accessed 23 June 2018].

[156] P. F. S. E. A. Ursula B. Ferraz, "A Simplified Model for Mechanical Loads under Angular Misalignment and Unbalance," *International Journal of Mechanical, Aerospace, Industrial, Mechatronic and Manufacturing Engineering,* vol. 7, no. 7, pp. 1611-1617, 2013.

[157] W. Qiao, W. Zhou, J. Aller and R. Harley, "Wind Speed Estimation Based Sensorless Output Maximization Control for a Wind Turbine Driving a DFIG," *IEEE Transactions on Power Electronics,* vol. 23, no. 3, pp. 1156-1169, 2008.

[158] C. Verucchi, J. Bossio, G. Bossio and G. Acosta, "Misalignment detection in induction motors with flexible coupling by means of estimated torque analysis and MCSA," *Mechanical Systems and Signal Processing,* vol. 80, pp. 570-581, 2016.

[159] M. Salah, S. B. Salem and W. e. a. Touti, "Stator current signature analysis to monitor shaft misalignment in induction motor speed-controlled," in *2017 International Conference on Control, Automation and Diagnosis, ICCAD 2017*, Hammamet, 2017.

[160] G. Kliman and J. Stien, "Induction Motor Fault Detetion via Passive Current Monitoring," in *Proceedings of the International Conference on Electric Machines*, 1990.

[161] S. Djurovic, D. Vilchis-Rodriguez and A. Smith, "Investigation of wound rotor induction machine vibration signal under stator electrical fault conditions," *The Journal of Engineering,* vol. 2014, no. 5, pp. 248-258, 2014.

[162] A. Mohammed, N. Sarma and S. Djurovic, "Fibre optic monitoring of induction machine frame strain as a diagnostic tool," in *2017 IEEE International Electric Machines and Drives Conference,IEMDC 2017*, Miami, 2017.

[163] P. Rodriguez, A. Beclahcen and A. Arkkio, "Signatures of electrical faults in the force distribution and vibration pattern of induction motors," *IEEE Proceedings-Electric Power Applications,* vol. 153, no. 4, pp. 523-529, 2006.

[164] J. Alena Bilosova, *Vibration Diagnostics*, Ostrava: Investments in Education Development book, 2012.

[165] J. S. U. I. Mais, "*Spectrum Analysis, The key features of analysing spectra*," 2012. [Online].

Available: https://www.skf.com/binary/tcm:12-113997/CM5118%20EN%20Spectrum%20Analysis.pdf. [Accessed 22 08 2019].

[166] R. Kashyap, *Fiber bragg gratings*, Acdemic press, 2009.

[167] A. Oyhonos, "*Fiber bragg gratings*," *Review of Scientific Instruments,* vol. 68, no. 12, pp. 4309-4341, 1997.

[168] A. Mohammed, J. I. Melecio and S. Durovic, "Stator Winding Fault Thermal Signature Monitoring and Analysis by In Situ FBG Sensors," *IEEE Transactions on Industrial Electronics,* vol. 66, no. 10, pp. 8082-8092, 2019.

[169] J. Hao, Z. Cai, Y. Gong, J. H. Ng, P. Varghses and S. Takahashi, "A Simple Passive Arc-Shape Temperature Independent Load Sensor Using a Pair of Fiber Bragg Gratings," *International Journal of Optomechatronics,* vol. 2, no. 1, pp. 16-31, 2008.

[170] P. Motwani, N. Perogamvros, S. Taylor, M. Sonebi, A. Laskar and A. Murphy, "Experimental Investigation of Strain Sensitivity for Surface Bonded Fibre Optic Sensors," *Sensors and Actuators A : Physical,* vol. 303, no. 111833, 2020.

[171] I. Grabovac, T. Nuyens and C. Davis, "Packaging and Mounting of In-Fibre Bragg Grating Arrays for Structural Healthy Monitoring of Large Structures," Defence Science and Techology Organisation, 2010.

[172] B. Alalibo, W. Cao, A. Gbadebo, L. Aarniovuori and K. Cai, "Investigation of the Effect of Bonding Points on Metal Surface-Mounted FBG Sensors for Electric Machines," *Progress In Electromagnetics Research,* vol. 97, no. Aug, pp. 255-265, 2019.

[173] P. Pennacchi, A. Vania and S. Chatterton, "Nonlinear effects caused by coupling misalignment in rotors equipped with journal bearings," *Mechanical Systems and Signal Processing,* vol. 30, no. 306-322, 2012.

[174] N. Sarma, "Investigation of Controller Embedded Condition Monitoring for Doubly Fed Induction Generators," The University of Manchester, Manchester, 2017.

[175] S. Durovic, "Analysis of Doubly-fed Induction Generator under Electrical Fault Conditions," The University of Manchester, Manchester, 2007.

[176] "*User Guide Mentor II DC Drives 25A to 1850A output*," Control Techniques, 2006.

[177] "*Current Transducer LA 55-P/SP1*," LEM.

[178] "*Voltage Transducer LV 25-200*," LEM, 2014.

[179] "*Voltage Transducer LV 25-600*," LEM, 2014.

[180] "*Advanced User Guide Unidrive SP: Universal Variable Speed AC Drive for induction and servo motors,*" CONTROL TECHNIQUES.

[181] "*DS1103 PPC Controller Board*," dSPACE, 2008.

[182] "*TECJMOCA; DATASHEET Increamental Encoder RI 32,*" HENGSTLER, 2008.

[183] P. L. Cochran, Polyphase Induction Motors: Analysis, Design, and Application, New York: MARCEL DEKKER, 1989.

[184] A. R. Nejad, Z. Gao and T. Moan, "Fatigue reliability analysis of wind turbine drivetrain considering strength degradation and load sharing using survival signature and FTA," *Energy Procedia,* vol. 53, no. C, pp. 248-257, 2014.

[185] W. T. Thomson and M. Fenger, "Current Signature Analysis to Detect Induction motor faults," IEEE Industry Applications Magazine, 2001.

[186] J. Cameron, W. Thomson and A. Dow, "Vibration and current monitoring for detecting airgap eccentricity in large induction motors," *IEE Proceedings B Electric Power Applications,* vol. 133, no. 3, p. 155, 1986.

[187] M. E. H. Benbouzid and G. B. Kliman, "What stator current processing-based technique to use for induction motor rotor faults diagnosis?," *IEEE Transactions on Energy Conversion,* vol. 18, no. 2, pp. 238-244, 2003.

[188] Control Techniques, "*User Guide SM-Resolver*," 2004.

Appendix A DFIG Test-rig Specification

A1. Wound rotor induction machine parameters

The specification of the wound rotor induction machine (WRIM) in laboratory DFIG test-rig is provided in Table A1.

Table A1 Specification of the WRIM in the DFIG test-rig

Parameter	Value	Nomenclature
Name	*Marelli Motori E4F 225M4*	
Rated Power	$30kW$	
Rated Speed	$1470\ rpm$	
Number of phases	3	q
Number of pole-pairs	2	p
Stator supply voltage (phase)	$120V_{rms}$	
Stator frequency	$50Hz$	f_s
Stator rated current	$59\ A_{rms}$	
Rotor rated current	$56A_{rms}$	
Number of turns per phase (stator)	56	N_s
Number of turns per phase (rotor)	42	N_r
Effective turns ratio	1.33	
Stator winding configuration	Star	
Rotor winding configuration	Star	
Stator resistance	$0.09\Omega/phase$	R_s
Rotor resistance	$0.066\Omega/phase$	R_r
Stator leakage inductance	$0.911 \times 10^{-3}H/phase$	$L_{\sigma s}$
Rotor leakage inductance	$0.459 \times 10^{-3}H/phase$	$L_{\sigma r}$
Magnetizing inductance	$44.6 \times 10^{-3}H/phase$	L_m
Rotor inertia	$0.4\ J/kgm^2$	
Number of stator slots	48	
Number of rotor slots	36	
Stack (axial) length	220 mm	w
Stator slot mouth width	3.6 mm	b_s
Rotor slot mouth width	3 mm	b_r
Mechanical air-gap length	0.63 mm	g_a
Stator inner diameter	214 mm	d_{si}
Stator outer diameter	325 mm	d_{ro}
Rotor inner diameter	80 mm	d_{ri}

Mean air-gap diameter	213.37 mm	d
Number of stator turns per coil	7	N_s
Number of rotor turns per coil	14	N_r
Coil pitch of the stator windings	Fully-pitched in slots: 1-13	
Coil pitch of the rotor windings	Fully-pitched in slots: 1-12, 2-11, 3-9	
Type of stator windings	Double layer, lap	
Type of rotor windings	Single layer, concentric	
Stator winding connection	Series/parallel	
Rotor winding connection	Parallel	
Rotor skew	Rotor slots are skewed by one stator slot pitch	

The parameters listed in Table A.1 are obtained from [174, 175].

A2. WRIM winding layout

The laboratory WRIM coil winding connection details are illustrated in this section, which were referred for conductor distribution function based harmonic model implementation. As mentioned in Appendix A1, the WRIM stator windings could be either connected in series or in parallel. The stator and rotor phase winding terminals are summarized in Tables A2-A3. In this section, the stator series connection is chosen to illustrate in figure, the winding connections are demonstrated in Tables A4-A5 and Figure A1, successive individual coils are presented by number 1 to 48 in the Figure A1. Rotor winding are connected in parallel, its connection is presented in Table A6 and Figure A2.

Table A2 Stator phase windings terminals

Phase A winding	A1,A2,A3,A4,D1,D2,G1,G2,J2,J1
Phase B winding	C1,C2,F1,F2,I1,I2,L2,L1
Phase C winding	E1,E2,H1,H2,K1,K2,B2,B3,B1

Table A3 Rotor phase windings terminals

Phase U winding	Ur1,Xr1,Ur2,Xr2
Phase V winding	Vr1,Yr1,Vr2,Yr2
Phase W winding	Wr1,Zr1,Wr2,Zr2

Table A4 Stator windings series connection

Phase	Terminals connection
Phase A winding	(As_1)A1-A5-D2-D1-G1-G2-J2-J1(As_2)
Phase B winding	(Bs_1)C1-C2-F2-F1-I1-I2-L2-L1(Bs_2)
Phase C winding	(Cs_1)E1-E2-H2-H1-K1-K2-B3-B1(Cs_2)

Table A5 Stator windings parallel connection

Phase	Terminal connection
Phase A winding	(As_1)-A1-A5-D2-D1-(As_2) (As_1)-G1-G2-J2-J1-(As_2)
Phase B winding	(Bs_1)-C1-C2-F2-F1-(Bs_2) (Bs_1)-I1-I2-L2-L1-(Bs_2)
Phase C winding	(Cs_1)-E1-E2-H2-H1-(Cs_2) (Cs_1)-K1-K2-B3-B1-(Cs_2)

Table A6 Rotor winding parallel connection

Phase	Terminal connection
Phase U winding	(Ur)-Ur1-Xr1-(Xr) (Ur)-Ur2-Xr2-(Xr)
Phase V winding	(Vr)-Vr1-Yr1-(Yr) (Vr)-Vr2-Yr2-(Yr)
Phase W winding	(Wr)-Wr1-Zr1-(Zr) (Wr)-Wr2-Zr2-(Zr)

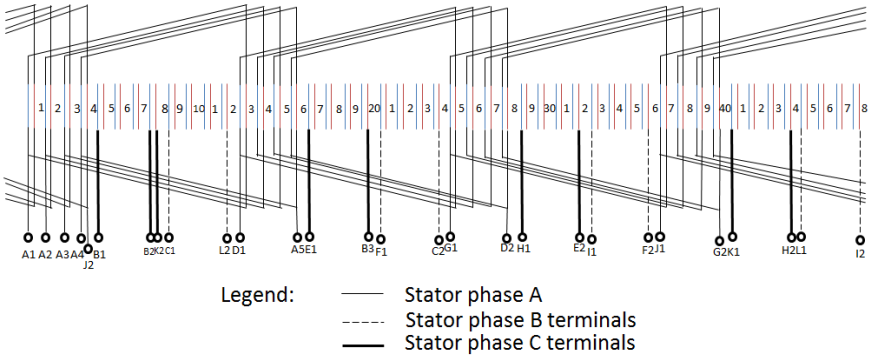

Figure A1 WRIM stator winding diagram (in series)

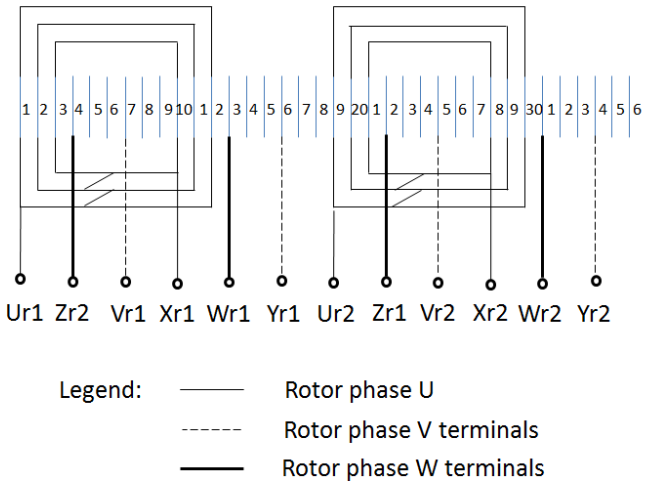

Figure A2 WRIM Rotor winding diagram

A3. Winding parameters for inductance calculation

To obtain the conductor distribution information on stator and rotor thus develop the harmonic model, the winding coil centre, the number of coil series connected conductors and coil pitch are identified, which are demonstrated in Table A7. In this project, the term slot pitch P_{SS} and P_{SR} are designed to express winding coil centres and winding coil pitch [175].

$$P_{SS} = \frac{\pi d}{48}$$

$$P_{SR} = \frac{\pi d}{36}$$

$$\mathrm{d} = d_{si} - g$$

WhereP_{SS} and P_{SR} are stator and rotor slot pitch, respectively, d is the mean air gap diameter, $d_{si}$is the stator inner diameter and g is mechanical air gap length.

Table A7 stator and rotor winding parameters

Winding	Number of Coils in a winding	Winding coils centre	Winding coils pitches	Number of turns per coil
A1-A2	1	$12 \times P_{SS}$	$12 \times P_{SS}$	7
A2-A3	1	$P_{SS} + \frac{12 \times P_{SS}}{2}$	$12 \times P_{SS}$	7
A3-A4	1	$2 \times P_{SS} + \frac{12 \times P_{SS}}{2}$	$12 \times P_{SS}$	7
A4-A5	1	$3 \times P_{SS} + \frac{12 \times P_{SS}}{2}$	$12 \times P_{SS}$	7
D1-D2	4	$12 \times P_{SS} + \frac{12 \times P_{SS}}{2}$ $13 \times P_{SS} + \frac{12 \times P_{SS}}{2}$ $14 \times P_{SS} + \frac{12 \times P_{SS}}{2}$ $15 \times P_{SS} + \frac{12 \times P_{SS}}{2}$	$12 \times P_{SS}$ $12 \times P_{SS}$ $12 \times P_{SS}$ $12 \times P_{SS}$	7 7 7 7
G1-G2	4	$24 \times P_{SS} + \frac{12 \times P_{SS}}{2}$	$12 \times P_{SS}$ $12 \times P_{SS}$	7

		$25 \times P_{ss} + \frac{12 \times P_{ss}}{2}$ $26 \times P_{ss} + \frac{12 \times P_{ss}}{2}$ $27 \times P_{ss} + \frac{12 \times P_{ss}}{2}$	$12 \times P_{ss}$ $12 \times P_{ss}$	7 7 7
J1-J2	4	$\frac{36 \times P_{ss}}{2}$ $P_{ss} + \frac{36 \times P_{ss}}{2}$ $2 \times P_{ss} + \frac{36 \times P_{ss}}{2}$ $3 \times P_{ss} + \frac{36 \times P_{ss}}{2}$	$36 \times P_{ss}$ $36 \times P_{ss}$ $36 \times P_{ss}$ $36 \times P_{ss}$	7 7 7 7
B1-B2	3	$4 \times P_{ss} + \frac{12 \times P_{ss}}{2}$ $5 \times P_{ss} + \frac{12 \times P_{ss}}{2}$ $6 \times P_{ss} + \frac{12 \times P_{ss}}{2}$	$12 \times P_{ss}$ $12 \times P_{ss}$ $12 \times P_{ss}$	7 7 7
B2-B3	1	$7 \times P_{ss} + \frac{12 \times P_{ss}}{2}$	$12 \times P_{ss}$	7
E1-E2	4	$16 \times P_{ss} + \frac{12 \times P_{ss}}{2}$ $17 \times P_{ss} + \frac{12 \times P_{ss}}{2}$ $18 \times P_{ss} + \frac{12 \times P_{ss}}{2}$ $19 \times P_{ss} + \frac{12 \times P_{ss}}{2}$	$12 \times P_{ss}$ $12 \times P_{ss}$ $12 \times P_{ss}$ $12 \times P_{ss}$	7 7 7 7
H1-H2	4	$28 \times P_{ss} + \frac{12 \times P_{ss}}{2}$ $29 \times P_{ss} + \frac{12 \times P_{ss}}{2}$ $30 \times P_{ss} + \frac{12 \times P_{ss}}{2}$ $31 \times P_{ss} + \frac{12 \times P_{ss}}{2}$	$12 \times P_{ss}$ $12 \times P_{ss}$ $12 \times P_{ss}$ $12 \times P_{ss}$	7 7 7 7
K1-K2	4	$4 \times P_{ss} + \frac{36 \times P_{ss}}{2}$ $5 \times P_{ss} + \frac{36 \times P_{ss}}{2}$ $6 \times P_{ss} + \frac{36 \times P_{ss}}{2}$ $7 \times P_{ss} + \frac{36 \times P_{ss}}{2}$	$36 \times P_{ss}$ $36 \times P_{ss}$ $36 \times P_{ss}$ $36 \times P_{ss}$	7 7 7 7
C1-C2	4	$8 \times P_{ss} + \frac{12 \times P_{ss}}{2}$ $9 \times P_{ss} + \frac{12 \times P_{ss}}{2}$	$12 \times P_{ss}$ $12 \times P_{ss}$ $12 \times P_{ss}$ $12 \times P_{ss}$	7 7 7 7

		$10 \times P_{SS} + \frac{12 \times P_{SS}}{2}$ $11 \times P_{SS} + \frac{12 \times P_{SS}}{2}$		
F1-F2	4	$20 \times P_{SS} + \frac{12 \times P_{SS}}{2}$ $21 \times P_{SS} + \frac{12 \times P_{SS}}{2}$ $22 \times P_{SS} + \frac{12 \times P_{SS}}{2}$ $23 \times P_{SS} + \frac{12 \times P_{SS}}{2}$	$12 \times P_{SS}$ $12 \times P_{SS}$ $12 \times P_{SS}$ $12 \times P_{SS}$	7 7 7 7
I1-I2	4	$32 \times P_{SS} + \frac{12 \times P_{SS}}{2}$ $33 \times P_{SS} + \frac{12 \times P_{SS}}{2}$ $34 \times P_{SS} + \frac{12 \times P_{SS}}{2}$ $35 \times P_{SS} + \frac{12 \times P_{SS}}{2}$	$12 \times P_{SS}$ $12 \times P_{SS}$ $12 \times P_{SS}$ $12 \times P_{SS}$	7 7 7 7
L1-L2	4	$8 \times P_{SS} + \frac{36 \times P_{SS}}{2}$ $9 \times P_{SS} + \frac{36 \times P_{SS}}{2}$ $10 \times P_{SS} + \frac{36 \times P_{SS}}{2}$ $11 \times P_{SS} + \frac{36 \times P_{SS}}{2}$	$36 \times P_{SS}$ $36 \times P_{SS}$ $36 \times P_{SS}$ $36 \times P_{SS}$	7 7 7 7
Ur1-Xr1	3	$\frac{11 \times P_{SR}}{2}$ $P_{SR} + \frac{9 \times P_{SR}}{2}$ $2 \times P_{SR} + \frac{7 \times P_{SR}}{2}$	$11 \times P_{SR}$ $9 \times P_{SR}$ $7 \times P_{SR}$	14 14 14
Ur2-Xr2	3	$18 \times P_{SR} + \frac{11 \times P_{SR}}{2}$ $19 \times P_{SR} + \frac{9 \times P_{SR}}{2}$ $20 \times P_{SR} + \frac{7 \times P_{SR}}{2}$	$11 \times P_{SR}$ $9 \times P_{SR}$ $7 \times P_{SR}$	14 14 14
Vr1-Yr1	3	$6 \times P_{SR} + \frac{11 \times P_{SR}}{2}$ $7 \times P_{SR} + \frac{9 \times P_{SR}}{2}$ $8 \times P_{SR} + \frac{7 \times P_{SR}}{2}$	$11 \times P_{SR}$ $9 \times P_{SR}$ $7 \times P_{SR}$	14 14 14
Vr2-Yr2	3	$24 \times P_{SR} + \frac{11 \times P_{SR}}{2}$ $25 \times P_{SR} + \frac{9 \times P_{SR}}{2}$	$11 \times P_{SR}$ $9 \times P_{SR}$ $7 \times P_{SR}$	14 14 14

		$26 \times P_{SR} + \frac{7 \times P_{SR}}{2}$		
Wr1-Zr1	3	$12 \times P_{SR} + \frac{11 \times P_{SR}}{2}$ $13 \times P_{SR} + \frac{9 \times P_{SR}}{2}$ $14 \times P_{SR} + \frac{7 \times P_{SR}}{2}$	$11 \times P_{SR}$ $9 \times P_{SR}$ $7 \times P_{SR}$	14 14 14
Wr2-Zr2	3	$5 \times P_{SR} + \frac{25 \times P_{SR}}{2}$ $4 \times P_{SR} + \frac{27 \times P_{SR}}{2}$ $3 \times P_{SR} + \frac{29 \times P_{SR}}{2}$	$25 \times P_{SR}$ $27 \times P_{SR}$ $29 \times P_{SR}$	14 14 14

A4. DC machine and DC drive

In this PhD project, the DC machine acts as a prime mover in the DFIG test-rig which provides driven rotational speed and torque. The DC machine specification is illustrated in Table A8.

Table A8 Specification of the DC machine

Parameters	Value
Type	K225M
Rated Power	41 kW
Armature voltage	480V
Armature current	95A
Field voltage	342V
Field current	1.75A

The DC motor control is conducted by a commercial DC drive. The specification of DC machine drive is provided in Table A9.

Table A9 Specification of the DC drive

Parameters	Value
Type	M75R
Drive type	4 Quad
Rated power	40 HP
Max armature current	75A
Max armature voltage	480V
Max field current	8A
Max speed	1750 rpm
Max input/output reference	10V, ±5% 10mA

The DC machine operation performance could be adjusted by manipulating settings or parameters in DC drive's menus. These settings could be changed either by DC drive keypad or an external real-time platform. i.e. dSPACE. The settings are generally classified into two groups: "Read and write" settings are accessible to be read and changed to modify the machine performance while the "Read only" settings are only accessible for reading purpose. The external dSPACE real-time platform DAC (Digital to analogue converter) channel connected with analogue input of DC drive enables manipulation of some parameters (i.e. speed and torque) conducted from PC side. More details of DC drive could be found in [176].

A5. Current and voltage sensors

The specification of current Hall sensors utilized in DFIG testing system is illustrated in Table A10.

Table A10 Specification of the current sensors in DFIG test-rig

Parameters	Value
Type	LA 55 − P/SP1
Primary nominal current	50 A_{rms}
Primary current measuring range	0 … ± 100A_{rms}
Measuring resistance	0 … 335Ω
Secondary nominal current	25 mA_{rms}
Conversion ratio	1: 2000
Supply voltage (±5%)	±12 … 15V_{dc}

Two types of voltage sensors were used in DFIG test-rig for stator voltage and grid voltage monitoring purpose, which are demonstrated in Tables A11-12.

Table A11 Specification of the stator voltage sensors in DFIG test-rig

Parameters	Value
Type	LV 25 − 200
Primary nominal voltage	200 V_{rms}
Primary voltage measuring range	0 … ± 300V_{rms}
Primary nominal current	10 mA_{rms}
Measuring resistance	0 … 246Ω
Secondary nominal current	25 mA_{rms}
Conversion ratio	200V: 25mA
Supply voltage (±5%)	±12 … 15V_{dc}

Table A12 Specification of the GRID voltage sensors in DFIG test-rig

Type	LV 25 − 600
Primary nominal voltage	600 V_{rms}
Primary voltage measuring range	0 … ± 900V_{rms}
Primary nominal current	10 mA_{rms}
Measuring resistance	30 … 320Ω
Secondary nominal current	25 mA_{rms}
Conversion ratio	600V: 25mA
Supply voltage (±5%)	±12 … 15V_{dc}

More detailed specifications of sensors could be found in [177, 178, 179].

A6. Back-to-back converter

Back-to-back converter was connected to the rotor windings of the WRIM in the DFIG test rig, which allows bidirectional power flow. The specification of the back-to-back converter utilized is demonstrated in Table A13.

Table A13 Specification of the commercial back-to-back converter in the DFIG test-rig

Parameters	Value	
	GSC	RSC
Type	UNIDRIVE SP 4401	UNIDRIVE SP 4401
Rated power	45kW	45kW
Mode of operation	Regen	Servo
Switching frequency	set to 3kHz	set to 6kHz
Max output current	96 A_{rms}	96 A_{rms}
Max input current	76 A_{rms}	76 A_{rms}
DC link voltage	700 V_{dc}	700 V_{dc}

More detailed descriptions of back-to-back converter could be found in [180].

A7. dSPACE real-time platform

dSPACE real-time platform was employed in this project to conduct real-time DFIG control and signal acquisition. The specification of dSPACE platform is demonstrated in Table A.14 [181, 45].

Table A14 Specification of the dSPACE platform in the DFIG test-rig

Parameters	Value
Type of controller board	DS 1103PPC
Processor type	PPC750GX
Analogue to digital converter (ADC)	16 ADC, 16-bit resolution, 4 µs sampling time 4 parallel ADC, 12-bit resolution, 800 ns sampling time ±10V input voltage range
Digital to analog converter (DAC)	8 DAC, 16-bit resolution 5 µs settling time ±10 V output voltage range
Digital incremental Encoder interface	6 digital inputs Single-ended (TTL) or differential (RS422) input 24-bit position counter Max 1.65 MHz input frequency Encoder supply voltage 5V/1.5 A

In this project, the stator flux oriented control scheme routine and DC motor drive control are conducted via dSPACE real-time platform. The corresponding programming is proceeded by compiling Simulink model, which would be converted to an .sdf file. i.e. with the help of Real-time Interface (RTI) Simulink toolbox associated to dSPACE, the ADC channels (signal acquisition for sensor signal) and DAC channels (reference control signals output for UNIDRIVE\MENTOR drive) from 1103 controller board could be virtualized in Simulink interface. The whole control scheme is implemented via a Simulink model consisting signal inputs and outputs. After the compiling process finished and the .sdf file loaded in dSPACE CONTROL DESK, the real-time execution of the Simulink algorithm could be approved. The execution time of real-time application is identical to the sample rate setting in Simulink file. Generally, to enable on-line control of the program in CONTROL DESK, some essential parameters, pre-defined switches and plotters linked to Simulink blocks are modified accessible in control panel.

A8. Incremental Encoder

Incremental encoder is employed in DFIG test rig to acquire rotor rotational speed and angular position for DFIG control, which is connected to the dSPACE controller board digital incremental encoder port. The specification of the encoder is provided in Table A15 [182].

Table A15 Specification of the encoder in DFIG test-rig

Parameters	Value
Type	RI 32
Supply voltage	5 V_{dc}
Pin assignment	Red-5V, White-A, Green-B, Yellow-Z, Black-GND
Number of pulses	1000

Appendix B Harmonic modelling of WRIM

B1. Mathematical equations of DFIG signals.

The DFIG SFOC signals can be written in the following equations defining the time/frequency domain nature of the DFIG currents and voltage signals [22, 137].

$$V_{sabc}(t) = V_{sM}\cos(\omega_s t + \phi_{vs}) \tag{B.1}$$

$$I_{sabc}(t) = \sum_k I_{sM}^k \cos([1 \mp 6k(1-s)]\omega_s t + \phi_{Is}) \tag{B.2}$$

$$V_{rabc}(t) = \sum_k V_{rM}^k \cos([s \mp 6k(1-s)]\omega_s t + \phi_{Vr}) \tag{B.3}$$

$$I_{rabc}(t) = \sum_k I_{rM}^k \cos([s \mp 6k(1-s)]\omega_s t + \phi_{Ir}) \tag{B.4}$$

Where V_{sM} is the peak value of stator voltage V_{sabc}, I_{sM} is the peak value of stator current I_{sabc}, V_{sM} is the peak value of rotor voltage V_{rabc}, I_{rM} is the peak value of rotor current I_{rabc}, ω_s is the supply frequency, ϕ is the phase shift between the three phase quantities of stator voltage (ϕ_{vs}), stator current (ϕ_{Is}), rotor voltage (ϕ_{Vr}) and rotor current (ϕ_{Ir}). k is the k^{th} harmonic of the signal. s is the slip.

Based on the equations B.1-4, the nature of DFIG stator active power signal and reactive power signal can be derived as follows:

$$P_s(t) = V_{sa}I_{sa} + V_{sb}I_{sb} + V_{sc}I_{sc} \tag{B.5}$$

$$Q_s(t) = \frac{1}{\sqrt{3}}[(V_{sb} - V_{sc})I_{sa} + (V_{sc} - V_{sa})I_{sb} + (V_{sa} - V_{sb})I_{sc}] \tag{B.6}$$

Hence the resultant instantaneous active and reactive power equation can be written as:

$$P_s(t) = \frac{3}{2}\sum_k V_{sM}I_{sM}^k \cos([6k(1-s)]\omega_s t) \tag{B.7}$$

$$Q(t) = \frac{3}{2}\sum_k V_{sM}I_{sM}^k \sin([6k(1-s)]\omega_s t) \tag{B.8}$$

The equations describing the time/frequency nature of the DFIG rotor current controller loop signals in stator flux oriented reference frame is defined as:

$$I_{rd}(t) = \sqrt{\frac{3}{2}}\sum_k I_{rM}^k \cos([6k(1-s)]\omega_s t) \tag{B.9}$$

$$I_{rq}(t) = \sqrt{\frac{3}{2}}\sum_k I_{rM}^k \sin([6k(1-s)]\omega_s t) \tag{B.10}$$

B2. Coupling impedance approach

One of the key purposes of this project is to investigate chrematistics of mechanical faults for DFIG condition monitoring. Typically, the most effective approach to achieve this is by analysing the spectrum of relevant machine signals (current, vibration, torque, etc.) Specific characteristic frequency components can be observed while along with fault. To

investigate the machine signals' higher order harmonic contents, the WRIM harmonic model is developed in this project. In WRIM, the stator and rotor windings are magnetically coupled via air-gap magnetic flux. The calculation of self inductance and mutual inductance consists higher order harmonics for modelling is undertaken by coupling impedance approach. In practice, the machine winding coil conductors are located in slots which generate flux distribution differ from the ideal sinusoidal distribution (dashed line) like illustrated in Figure B1, thus higher order flux density harmonics in airgap are introduced and significantly effects the machine performance [27].

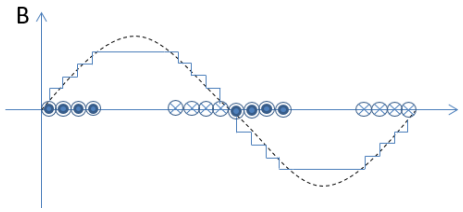

Figure B1 Produced flux density distribution

B3. Conduction distribution theory

The main purpose of conduction distribution theory is to demonstrate the spatial distribution of the rotor and stator conductor on their surface [27]. The electric machine windings consist of sets of connected coils. The coil in a stator or a rotor can be regarded as a group of conductors located at the stator inner surface slot or rotor outer surface slot, respectively. Each coil contains the number of N_n conductors. The spatial distribution of an arbitrary n-th coil can be mathematically expressed as a conductor density function $c_n(y)$ in a linear way like Figure B2 shown [27].

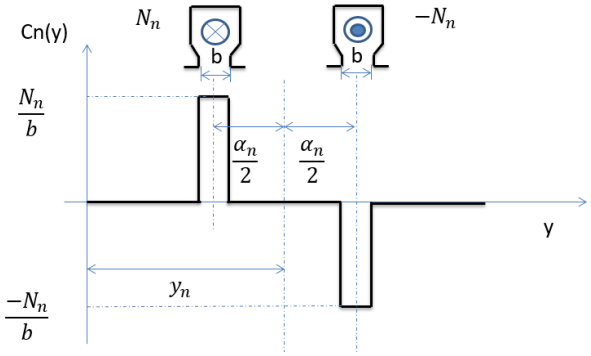

Figure B2 n-th coil conductor distribution function

The conductors in slots are demonstrated as pulses, where the conductors are assumed to be homogenously spread in the length of slot mouth of width b. The current flow directions in conductors are indicated by positive and negative sign. Based on the previous definitions, the n-th conductor distribution density $c_n(y)$ is defined in turns per meter over the mean airgap perimeter. In addition, following definitions are clarified below: [27]:

- α_n is the coil pitch of the n-th coil in the winding
- y_n is n-th coil centre position in the winding

To analyse the conductor distribution space harmonic, the function $c_n(y)$ is resolved by complex Fourier analysis. Therefore the conductor density over mean airgap perimeter is expressed by a series of space harmonics as follows: [27]

$$c_n(y) = \sum_{v=-\infty}^{v=+\infty} \overline{C_n^k}\, e^{-jky} \tag{B.11}$$

where v is the space harmonic integer number, k is defined as wave number of v-th order space harmonic, the expression is: [27]

$$k = \frac{2\pi}{\lambda_v} = \frac{2\pi}{\frac{\pi d}{v}} = \frac{2v}{d} \tag{B.12}$$

where λ_v is the wavelength of the n-th order harmonic and d is the machine mean air gap diameter. The Fourier Coefficient of conductor distribution function $\overline{C_n^k}$ is given as: [27]

$$\overline{C_n^k} = \frac{1}{\pi d}\int_0^{\pi d} c_n(y) e^{jky} dy \tag{B.13}$$

where the n-th coil conductor distribution function $c_n(y)$ plotted in Figure B2 is: [27]

$$c_n(y) = \begin{cases} \frac{N_n}{b} & for \quad y_n - \frac{\alpha_n}{2} - \frac{b}{2} \le y \le y_n - \frac{\alpha_n}{2} + \frac{b}{2} \\ \frac{-N_n}{b} & for \quad y_n + \frac{\alpha_n}{2} - \frac{b}{2} \le y \le y_n + \frac{\alpha_n}{2} + \frac{b}{2} \end{cases} \tag{B.14}$$

The Fourier Coefficient $\overline{C_n^k}$ can be derived based on equation (B.13) and (B.14): [27]

$$\overline{C_n^k} = -j\frac{2N_n}{\pi d} k_{bv} k_{pv} e^{jky_n} \tag{B.15}$$

where k_{pv} is the conventional pitch factor of the n-th coil and k_{bv} is the v-th harmonic slot mouth width factor. By assuming the air gap m.m.f distribution excited by the slot conductor current flow is equivalent to that produced by the surface current flow in the conductors which the distributed width on surface is equal to slot width. The slot mouth factor is defined as: [27]

$$k_{bv} = \frac{sin\left(\frac{kb}{2}\right)}{\frac{kb}{2}} \tag{B.16}$$

while the expression of v-th harmonic coil pitch factor is as following:

$$k_{pv} = \sin\left(\frac{k\alpha_n}{2}\right) \tag{B.17}$$

To enable negative harmonics recognition, the Fourier Coefficient of negative harmonics are derived by [27]:

$$\overline{C_n^{-k}} = \overline{\dot{C}_n^k} \tag{B.18}$$

where $\overline{\dot{C}_n^k}$ is the complex conjugate of $\overline{C_n^k}$.

To clearly demonstrate the theoretical study, an arbitrary coil in stator winding A is analysed. As illustrated in Figures B3-5: the original conductor distribution is shown in blue while the model reconstructed distribution is in orange. Different harmonic numbers (50, 120,150) taken into account were tested.

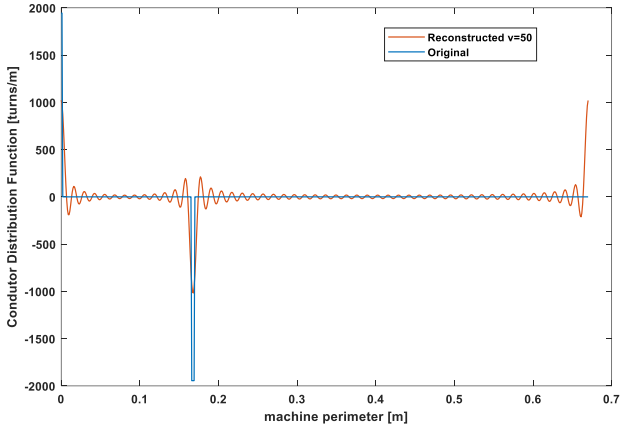

Figure B3 v=50 harmonics reconstruction

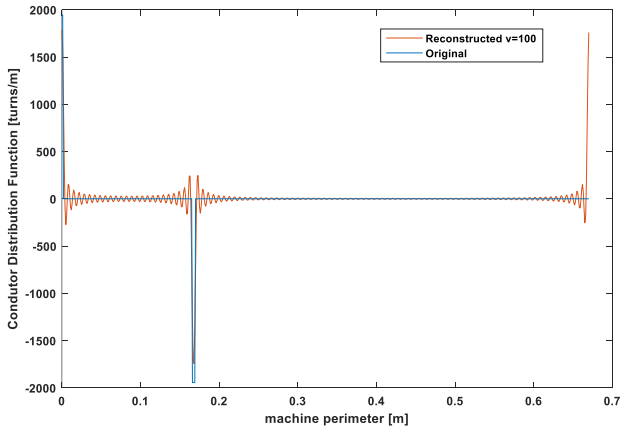

Figure B4 v=120 harmonics reconstruction

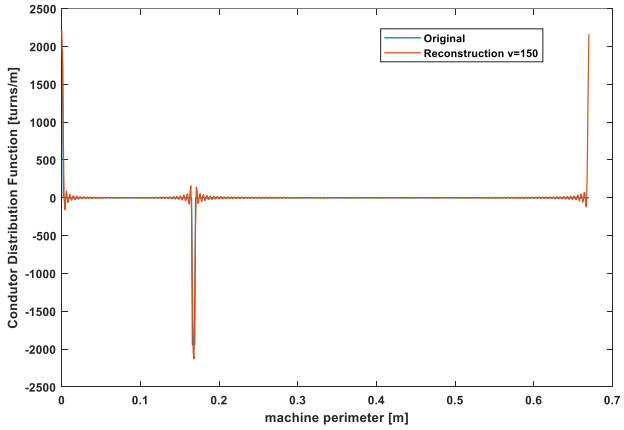

Figure B5 v=150 harmonics reconstruction

As the figures shown, the original conductor distribution function, as equation (B.14) described, should be a square wave signal which only has magnitude at conductor distributed slot width position (blue curve). With the number of harmonics considering

increases, the ripples of reconstructed function are reduced in size and its magnitude gets closer to the assumed distribution. In fact, the stator and rotor slot mouth width are much smaller than machine mean air gap perimeter. To obtain an accurate reconstruction result, a large number of harmonics have to be taken into account in the model [27].

In the machine, each winding consists of a set of coils, the conductor distribution function of a winding is defined as the sum of every individual coil conductor distribution function [27]. One of the stator winding A in the test rig is demonstrated as an example to explain the theory. There are four set of coils existed inside.

$$C_{sa}(y) = c_1(y) + c_2(y) + \cdots + c_4(y) = \sum_{v=-\infty}^{v=+\infty} \overline{C_{sa}^k} e^{-jky} \tag{B.19}$$

where $\overline{C_{sa}^k}$ is the conductor distribution function Fourier Coefficient of the whole winding and $c_{1\ldots4}(y)$ are the conduction distribution function of each coil.

Recalling equations (B.1) and (B.6):

$$\begin{aligned} C_{sa}(y) &= \sum_{v=-\infty}^{v=+\infty} \overline{C_1^k}\, e^{-jky} + \sum_{v=-\infty}^{v=+\infty} \overline{C_2^k}\, e^{-jky} + \cdots + \sum_{v=-\infty}^{v=+\infty} \overline{C_4^k}\, e^{-jky} \\ &= \sum_{v=-\infty}^{v=+\infty} (\overline{C_1^k} + \overline{C_2^k} + \overline{C_3^k} + \overline{C_4^k})\, e^{-jky} \end{aligned} \tag{B.20}$$

So we can define:

$$\overline{C_{sa}^k} = \overline{C_1^k} + \overline{C_2^k} + \overline{C_3^k} + \overline{C_4^k} \tag{B.21}$$

And the complex conductor distribution of wind A is derived in [27]:

$$c_{sa}(y) = \sum_{v=-\infty}^{v=+\infty} \overline{C_{sa}^k}\, e^{-jky} \tag{B.22}$$

which is the sum of all four consisted coil conductor distribution function. By adding the all four reconstructed conductor distribution function together, the plot of winding A conductor distribution function is exhibited below: (200 harmonics are considered)

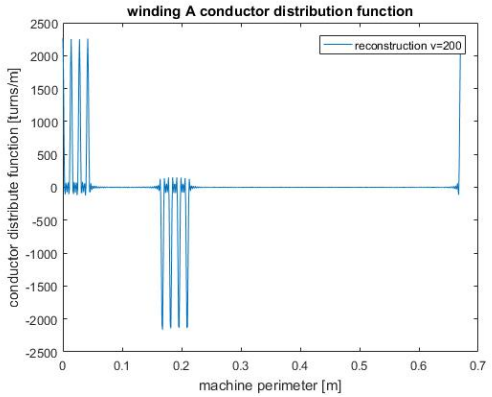

Figure B6 Winding A conductor distribution function

As for DFIG stator phase, each phase winding is constructed by four windings. Using the similar way sum up all windings per phase, the single phase conductor distribution function can be obtained.

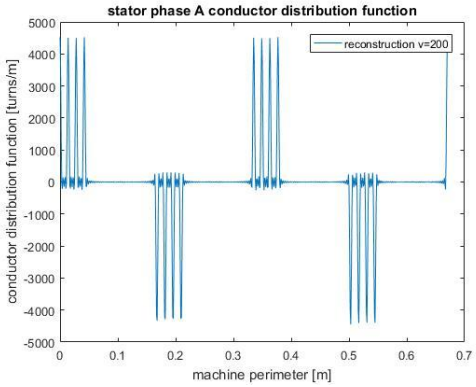

Figure B7 Stator phase A conductor distribution function

As demonstrated in Figure B7, the phase A could be clearly recognized as the construction of four windings illustrated in Figure B6: Two sets of peaks with doubled magnitude of conductor distribution function in phase A. Referring to the winding

connections in Appendix A, the conductor distributed locations have two sets of windings with same current flow direction. In consequence, two sets of doubled peaks are generated by four sets of windings.

The sum of stator three phase conductor distribution function is demonstrated as the Figure B8:

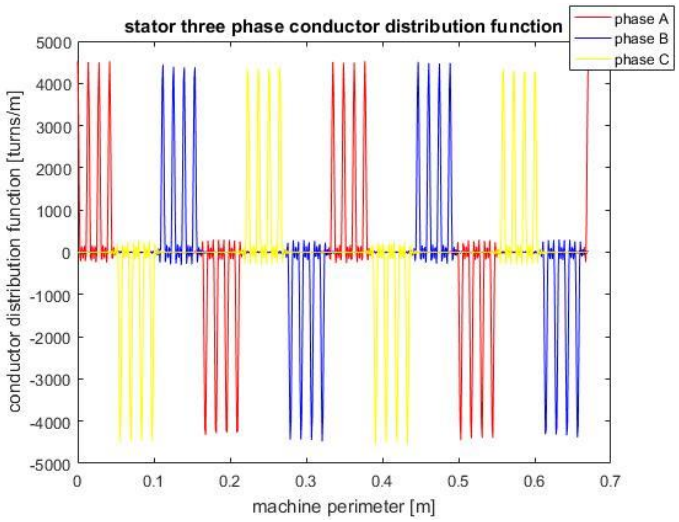

Figure B8 Stator three phase conductor distribution function

B4. Skewing and airgap coefficients

B4.1 Rotor skew

In harmonic model, the skew effect is taken into account while implementing model by introducing skew factor K_{sv} as follows: [183]

$$K_{sv} = \frac{\sin\left(\nu P \frac{\gamma}{2}\right)}{\nu P \frac{\gamma}{2}} \tag{B.23}$$

where ν is the harmonic number, P is the machine pole pair number, γ is radians skew angle.in model development, the skew factor is multiplied into stator/rotor mutual inductance equation: [183]

$$M_{AB} = \frac{w\pi d\mu_0}{g}\sum_{v=-\infty}^{v=+\infty} K_{sv}\frac{\overline{C_A^k}\dot{C_B^k}}{k^2}e^{-jk\beta(t)} \tag{B.24}$$

B4.2 Airgap coefficients.

B4.2.1 Carter's Coefficient

To identify the effective flux path length increase, the Carter's coefficient is introduced for both rotor and stator side, which are defined as follows: [183]

$$K_{CR} = \frac{\tau_R}{\tau_R - \sigma_R w_R} \tag{B.25}$$

$$K_{CS} = \frac{\tau_S}{\tau_S - \sigma_S w_S} \tag{B.26}$$

where τ_R, τ_S are the rotor and stator slot pitch, respectively, w_R, w_s are correspondingly rotor and stator slot mouth widths and σ_R, σ_S are the per unit equivalent change in slot width: [183]

$$\sigma_R = \frac{2}{\pi}\left(\arctan\left(\frac{\tau_R}{2g}\right) - \frac{g}{w_R}\ln\left(1+\left(\frac{w_R}{2g}\right)^2\right)\right) \tag{B.27}$$

$$\sigma_S = \frac{2}{\pi}\left(\arctan\left(\frac{\tau_S}{2g}\right) - \frac{g}{w_S}\ln\left(1+\left(\frac{w_s}{2g}\right)^2\right)\right) \tag{B.28}$$

where g is the airgap length.

The machine airgap Carter's coefficient K_C for testing DFIG is: [27]

$$K_C = K_{CR}K_{CS} \approx 1.27 \tag{B.29}$$

Eventually, the effective airgap length could be worked out: [27]

$$g_{eff} = gK_C \tag{B.30}$$

B4.2.2 Saturation coefficient

The full magnetic path is divided into three sections to analysis: the air gap, the stator and rotor teeth and stator and rotor core yoke sections. The m.m.f drop of each section is calculated separately, the ratio of total ampere-turns/pole to airgap ampere-turns/pole is defined as saturation coefficient *Ks* [183]:

$$K_s = \frac{(NI)_{total}}{(NI)_{gap}} = \frac{(NI)_{gap} + (NI)_{ts} + (NI)_{tr} + (NI)_{cs} + (NI)_{cr}}{(NI)_{gap}} \qquad (B.31)$$

where the sub index t_s, t_r correspondingly represent stator and rotor teeth sections while c_s, c_r stand for stator and rotor core yoke sections.

The m.m.f drop in airgap section can be calculated by following steps.

The average mutual airgap flux value per pole can be calculated via: [27]

$$\psi_m = \frac{V_1}{4.443 K_P K_d N_{st} f} \qquad (B.32)$$

where V_1 is rated stator voltage, K_p is the stator winding pitch factor, K_d is the stator winging distribution function, the stator effective turns number is defined as N_{st} and f is the supply frequency. K_p and K_d are defined as: [27]

$$K_P = sin\frac{y}{\tau}\frac{\pi}{2} \qquad (B.33)$$

$$K_d = \frac{sin\frac{m\pi}{z\,2}}{msin\frac{1\pi}{z2}} \qquad (B.34)$$

where y is the winding coil pitch, τ is the machine pole pitch, z is the slot number per pole and m is the slot number per phase.

The pole area linked by mutual flux can be obtained by: [27]

$$A_{gap} = \frac{\pi d_{si}}{2P} l \qquad (B.35)$$

where d_{si} is the stator core inner diameter, P is the machine pole pair number and l is

the machine length.

Since the maximum flux density is considered for saturation factor calculation, the maximum value of airgap flux density B_{gm} can be obtained from average airgap flux density multiply by $\frac{\pi}{2}$ [27].

$$B_{gm} = \frac{\psi_m}{A_{gap}} \frac{\pi}{2} \tag{B.36}$$

The airgap ampere-turns per pole can be deduced by: [27]

$$(NI)_{gap} = \frac{B_{gm} g_{eff}}{\mu_0} \tag{B.37}$$

where g_{eff} is the effective airgap length derived by Carter's coefficient in the last section, μ_0 is the magnetic permeability of air.

Next is to calculate the m.m.f drop components is stator and rotor teeth in the similar way, the area of stator teeth area A_{ts} and rotor teeth area A_{tr} can be calculated as follows: [27]

$$\mathrm{A_{ts}} = \frac{(d_{si} + D_S)\pi - N_S w_s}{2P} l \times 0.95 \tag{B.38}$$

$$\mathrm{A_{tr}} = \frac{(d_{ro} + D_r)\pi - N_R w_r}{2P} l \times 0.95 \tag{B.39}$$

where D_s is the stator slot depth, D_r is the rotor slot depth, N_s and N_R are the number of stator and rotor slots, respectively. w_s and w_r are the stator and rotor slot width separately. d_{ro} is the rotor core outer diameter. 0.95 is the typical value of the machine stacking factor [27].

Recalling equation (B.20), the magnetic field strength H_{tsm} and H_{trm} can be calculated. Finally, the ampere-turns per pole can be obtained: [27]

$$(NI)_{ts} = H_{tsm} D_S \tag{B.40}$$

$$(NI)_{tr} = H_{trm} D_r \tag{B.41}$$

The same approach can be applied to calculate m.m.f drop in stator and rotor core yokes. The stator core depth D_{SC} and rotor core depth D_{RC} are worked out by: [27]

$$D_{SC} = \frac{d_{so} - (d_{si} + 2D_S)}{2} \tag{B.42}$$

$$D_{RC} = \frac{d_{ro} - (d_{ri} + 2D_R)}{2} \tag{B.43}$$

The stator core yoke area A_{CS} and rotor core yoke area A_{CR} are: [27]

$$A_{CS} = D_{SC} l \times 0.95 \tag{B.44}$$

$$A_{CR} = D_{RC} l \times 0.95 \tag{B.45}$$

Similarly, the ampere-turns per pole components needed for NI_{cs} and NI_{cr} are obtained: [27]

$$(NI)_{cs} = H_{csm} l_s \tag{B.46}$$

$$(NI)_{cr} = H_{crm} l_r \tag{B.47}$$

where H_{csm} and H_{crm} are stator and rotor core yoke magnetic field strength, respectively.

The stator yoke flux path length l_s and rotor yoke flux path length l_r can be deduced by [27]:

$$l_s = \frac{(d_{so} - D_{SC})\pi}{2P} + \frac{\pi D_{SC}}{4} \tag{B.48}$$

$$l_r = \frac{(d_{ri} - D_{RC})\pi}{2P} + \frac{\pi D_{RC}}{4} \tag{B.49}$$

After calculating all m.m.f drop components in machine, the saturation factor is obtained:

$$K_s = \frac{(NI)_{gap} + (NI)_{ts} + (NI)_{tr} + (NI)_{cs} + (NI)_{cr}}{(NI)_{gap}} \approx 1.1 \tag{B.50}$$

B5. Machine parameter calculation

To solve the machine model equations in Chapter 4 (equations 4.1-5), it is necessary to obtain the parameters in the equation: the machine resistance and machine inertia can be looked up from machine parameter datasheet. However, obtaining the machine inductance matrix in equation (4.5) is not straight forward as the inductance consists harmonic information for modelling. Therefore, the inductance matrix obtain is the critical part of implementing harmonic induction machine model.

The inductance values are determined with conductor distribution theory taken into account presented in section 4.2. Self-inductance including stator self-inductance (L_{ss} matrix) and rotor self-inductance (L_{rr} matrix), and the mutual inductance between stator and rotor (L_{sr} and L_{rs} matrix) are worked out.

For any two windings A and B on the stator or the rotor, the self-inductance (i.e.the elements in L_{ss} or L_{rr} matrixes) can be calculated by following formula: [27]

$$M_{AB} = \frac{w\pi d\mu_0}{g} \sum_{v=-\infty}^{v=+\infty} \frac{\overline{C_A^k}\,\dot{\overline{C_B^k}}}{k^2} \qquad (B.51)$$

where w is the machine length, d is the airgap mean diameter, μ_0 is permeability of vacuum, g is the mechanical airgap length, $\overline{C_A^k}$ is the Fourier Coefficient of winding A conductor distribution function which was derived in equation 4.9. $\dot{\overline{C_B^k}}$ is the complex conjugate of Fourier coefficient of winding B. Three elements from stator self-inductance matrix and rotor self-inductance (i.e. stator winding A: L_A, rotor winding *Ur1*: L_{ur1}, and stator winding A and B: L_{AB}) and are listed in Table B.1 below to illustrated the inductance values with different number of harmonics v taken into account.

Table B1 Self-inductance values with different numbers of harmonics taken into account

Number of harmonics taken into account, v	L_A [H]	L_{ur1} [H]	L_{AB} [H]
2	0.117312686174287	0.051321327855764	-0.058656343087143
10	0.123573724417187	0.056179635627318	-0.052715959279744
50	0.124270333966420	0.056174596730978	-0.052682036293602
100	0.124397205986599	0.056173989081828	-0.052630078153066
150	0.124411431834800	0.056173902646617	-0.052622776181291
200	0.124411571686868	0.056173904133509	-0.052622762595701

It can be observed that the self-inductance value are effected by the number of harmonics considered. Take L_A as an example: by increasing harmonic number considered from 2 to 100, the inductance value has an order of 0.1mH variation in table. In consequence, the more orders of harmonics taken into account, the more accurate result could be obtained.

As for calculating mutual inductances between stator and rotor, the physical distance between stator and rotor windings is a time varying value along with machine rotation, therefore the function of rotation is taken into account. The mutual inductance between two windings A and B, which are placed in stator and rotor respectively, can be expressed as follows: [27]

$$M_{AB} = \frac{w\pi d\mu_0}{g}\sum_{v=-\infty}^{v=+\infty}\frac{\overline{C_A^k}\dot{C_B^k}}{k^2}e^{-jk\beta(t)} \tag{B.52}$$

where $\beta(t)$ is the function of displacement in rotor reference frame [27]:

$$\beta(t) = r_{AG}\theta(t) = r_{AG}\omega_t t \tag{B.53}$$

where r_{AG} is the mean airgap radius, θ is the rotor mechanical angle and ω_t is the mechanical speed. The following plot demonstrates how mutual inductance changes with

respect of rotor position. 200 harmonics are taken into account for calculating mutual inductance between stator phase *A* and rotor winding *Ur1*. The mutual inductance value periodically changes with the respect rotor position as illustrated in Figure B9.

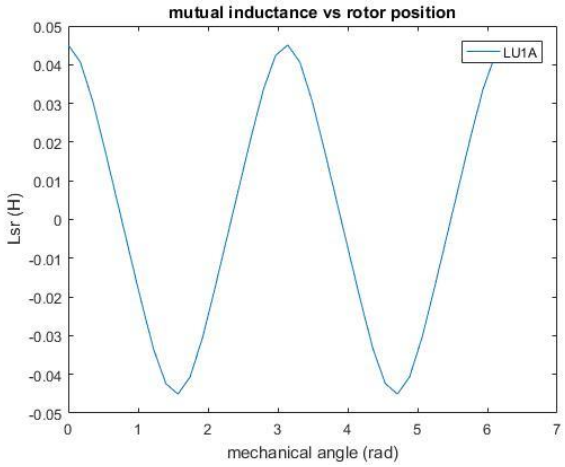

Figure B9 Mutual inductance vs rotor position

Appendix C Additional Spectrum of DFIG embedded controller signals for shaft misalignment analysis

C1. DFIG Outer loop controller signal spectrum

In Chapter 6, the investigation of exploring the feasibility of shaft misalignment diagnosis using DFIG controller signal was demonstrated. The acquired DFIG outer loop signals: Stator active power P, active power error signal P_{err}, stator reactive power Q, reactive power error signal Q_{err} in steady state operating point (1590 rpm, 50% load) are analysed here. The zoomed in FFT results of f_r and $2f_r$ harmonics in healthy and 1 degree misalignment conditions are demonstrated in Figures C1-C4. As demonstrated in the figures, the f_r related harmonic contents in outer loop controller signals are not clearly indicated.

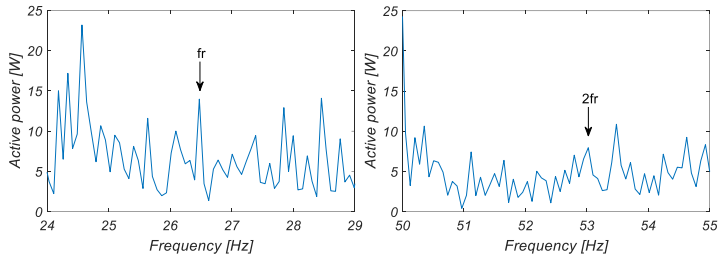

(a) Active power f_r content (b) Active power $2f_r$ content

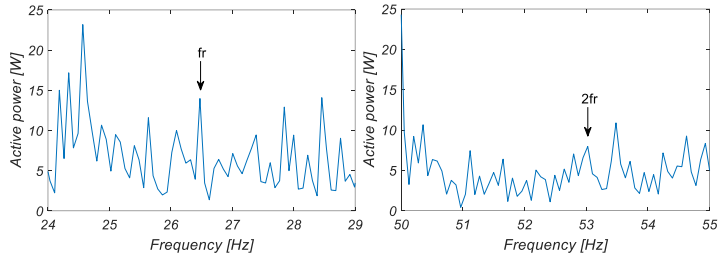

(c) Active power error signal f_r content (d) Active power error signal $2f_r$ content

Figure C1 Healthy operating condition active power and error signal zoomed in spectrum

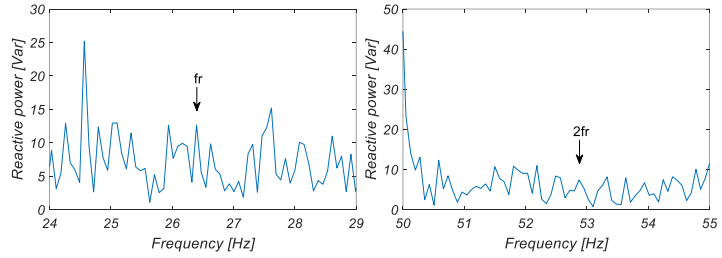

(a) Reactive power f_r content (b) Reactive power $2f_r$ content

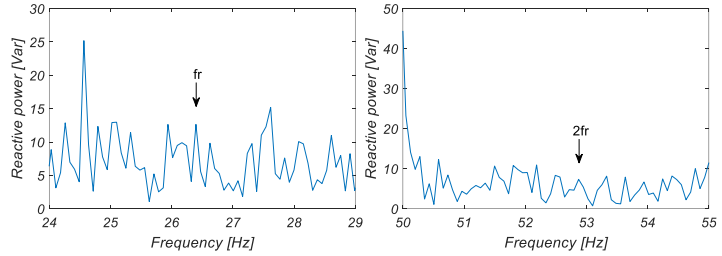

(c) Reactive power error signal f_r content (d) Reactive power error signal $2f_r$ content

Figure C2 Healthy operating condition reactive power and error signal zoomed in spectrum

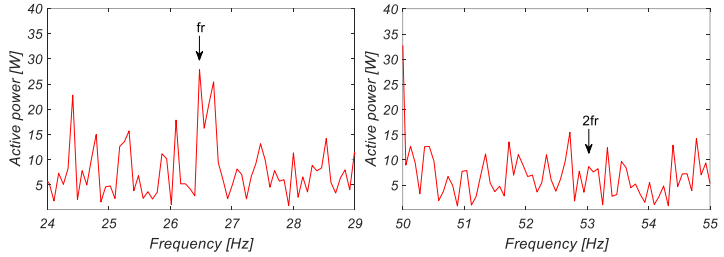

(a) Active power f_r content (b) Active power $2f_r$ content

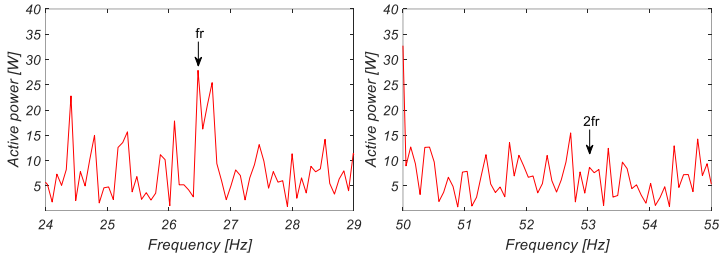

(c) Active power error signal f_r content (d) Active power error signal $2f_r$ content

Figure C3 1 degree misalignment operating condition active power and error signal zoomed in spectrum

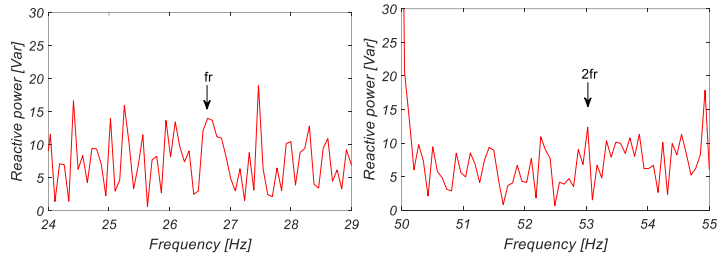

(a) Reactive power f_r content (b) Reactive power $2f_r$ content

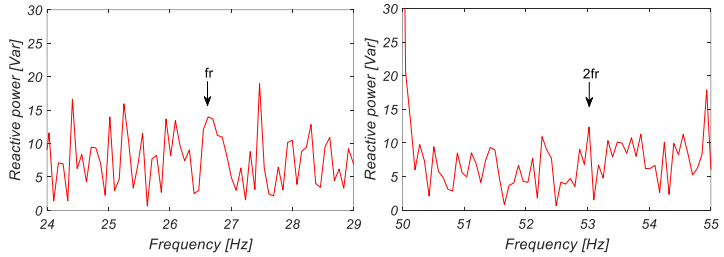

(c) Reactive power error signal f_r content (d) Reactive power error signal $2f_r$ content

Figure C4 1degree misalignment operating condition reactive power and error signal zoomed in spectrum

C2. Additional study of operating condition effects on shaft misalignment signature

In the main chapter, the statistics of $2f_r$ harmonic content of stator current I_{sa} and controller signal I_{dr} in a wide range of generator operating load and speed conditions were demonstrated to unfold the consistency of misalignment fault indication. Similar f_r harmonic component summary of I_{sa} and I_{dr} signals are exhibited in Figures C5-C6.

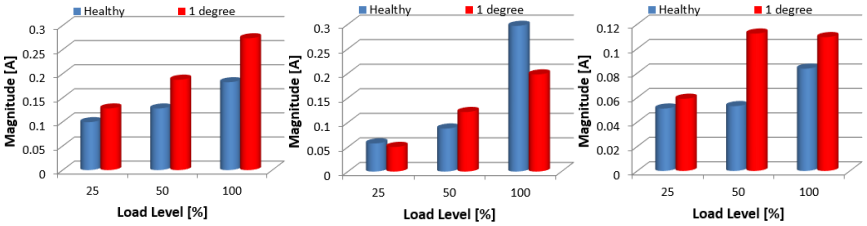

(a) (b) (c)

Figure C5 Measured f_r components magnitude in I_{sa} (a) at 1340 rpm (b) at 1550 rpm (c) at 1590 rpm

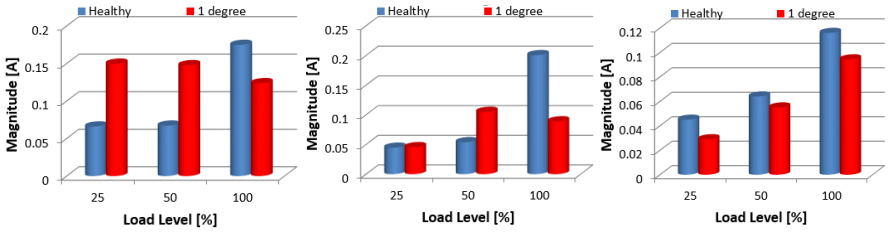

(a) (b) (c)

Figure C6 Measured f_r components magnitude in I_{dr} (a) at 1340 rpm (b) at 1550 rpm (c) at 1590 rpm

As illustrated in the figures, no clear consistency could be observed in the f_r component in I_{sa} and I_{dr} signals with misalignment.